The Dissertation Committee for Panteleimon Lapas
certifies that this is the approved version of the following dissertation:

SPIN ORBIT COUPLING AND MAGNETISM INTERPLAY DRIVEN PHENOMENA

Committee:

Allan H. MacDonald, Supervisor

Gregory A. Fiete

Alexander A. Demkov

Jianshi Zhou

SPIN ORBIT COUPLING AND MAGNETISM INTERPLAY DRIVEN PHENOMENA

by

Panteleimon Lapas

DISSERTATION

Presented to the Faculty of the Graduate School of

The University of Texas at Austin

in Partial Fulfillment

of the Requirements

for the Degree of

DOCTOR OF PHILOSOPHY

THE UNIVERSITY OF TEXAS AT AUSTIN

December 2017

Αφιερωμένη ολόψυχα στον Άγιο Παΐσιο και στους αγαπημένους μου γονείς!

Acknowledgments

This dissertation is the final product of several years of patience and personal effort, a large part of which went into my making the actually tough (at least for me) transition from a zero background in condensed matter physics upon graduating from my local university, to a point where I have something to say in a dissertation submitted to a foreign university. During this journey, a small number (large impact originates from a small number) of people played their own role, the right time, maybe without being aware of their impact on me, whom I would personally like to acknowledge here. These are, prof. Gregory Fiete, who gave me the opportunity to get extensively involved in one of their tough projects, something that at the same time indirectly helped me sharpening my analytical and conceptual skills beyond the course-level ones, Hua Chen, a former post-doc in my group, whose office I visited several times over all those years, discussing various things as well as several naive questions, and my undergraduate fellow and old friend Nikos A., who also helped me with issues of computational nature. I would also like to thank few good friends (especially Zach P. and Yiannis K.-Ch.) that I first met here at Austin, and who made my everyday life abroad more interesting keeping me also in contact with the beyond physics world.

A huge thanks wholeheartedly goes to my supervisor Allan H. Mac-

Donald, who gave me the opportunity of getting familiar with several topics of the condensed matter, patiently answered my questions, steadily guided me whenever I got lost on the way, and generously ingrained to me part of his sharp physical intuition.

A last thanks goes to my family and my wife who, despite the huge distance separating us, patiently and constantly supported me all those years!

Austin, December 2017

SPIN ORBIT COUPLING AND MAGNETISM INTERPLAY DRIVEN PHENOMENA

Publication No. _____

Panteleimon Lapas, Ph.D.
The University of Texas at Austin, 2017

Supervisor: Allan H. MacDonald

Four different projects are presented in this work, where one of them is a collaborative work with a different condensed matter physics group (within my graduate school). The common denominator of all those projects certainly is the atomic spin orbit coupling. In the first two projects, using a mean field theory approach for the electronic degrees of freedom, we study effects that emerge as the result of the proximity of a ferromagnetic metal to a metal with a strong atomic spin orbit coupling. In the third project, using a lowest order many body perturbation theory we try to understand the effect of the interplay between magnetic and lattice degrees of freedom, mediated by the strong atomic spin orbit coupling, on the thermal conductivity of an insulator (with strong spin orbit coupling). In the last project, again relying on lowest order many body perturbation theory, we study the interplay between the Dirac electronic quasiparticles of a thin film topological insulator and the magnetic degrees of freedom of a YIG thin film.

Table of Contents

Acknowledgments **v**

Abstract **vii**

List of Figures **x**

Chapter 1. Bird's eye view **1**

Chapter 2. Interfacial Dzyaloshinskii-Moriya interaction in heavy metal/ferromagnetic metal heterostructures **4**

2.1 Motivation 4
2.2 Atomistic model and model Hamiltonian 7
2.3 Formalism for the itinerant electron antisymmetric exchange interactions 21
2.4 Brief symmetry analysis 31
2.5 Results, discussion and conclusions 36

Chapter 3. Real space anatomy of the spin-orbit torques in heavy metal/ferromagnetic metal heterostructures **48**

3.1 Motivation 48
3.2 Transport theory formalism 49
3.3 Real space anatomy of the spin-orbit torques - Quantum mechanical observables 55
3.3.1 Layer resolved spin accumulation 58
3.3.2 Anomalous Hall effect related charge and spin current density operators 59
3.3.3 Rate of spin accumulation in the ferromagnetic layer . . 61
3.3.4 Rate of spin accumulation in the heavy metal layer . . . 66
3.3.5 Interlayer particle and spin currents 69
3.3.6 Torques transferred to the exchange effective field of the ferromagnet 75

3.3.7 Symmetry arguments for the exchange mediated torques 76
3.4 Results, discussion and conclusions 79

Chapter 4. Thermal conductivity of 2D local moment models with strong spin orbit coupling 97
4.1 Motivation 97
4.2 Overview of the theoretical formalism 98
4.3 Results, discussion and conclusions 103
4.3.1 Boundary scattering dominated/fully ballistic regime . . 103
4.3.2 Phonon dominated heat transport 113
4.3.3 Magnon dominated heat transport 124

Chapter 5. Interfacial effects in YIG - topological insulator heterostructures - enhanced Gilbert damping in YIG 132
5.1 Motivation 132
5.2 Lowest order quantum mechanical spin Hamiltonian for the YIG thin film 134
5.3 Effective Hamiltonians of the decoupled subsystems 158
5.4 Coupling of the Dirac electrons to the long-wavelength dynamics of the YIG magnetization 159
5.5 Matsubara Green's function formalism (low temperature regime) 171
5.6 Application of the developed formalism: Enhanced damping of the FMR mode of a YIG thin film 176

Bibliography 182

List of Figures

2.1 Commensurate bilayer of A-B stacked triangular lattices. The global Oz axis is normal to the interface directed to the reader's eye. The black-colored lattice is the substrate (heavy metal) layer, and the red-colored is the deposited (ferromagnetic) layer. 10

2.2 First Brillouin zone shown together with some high symmetry points. 16

2.3 Two dimensional triangular lattice. The global Oz axis is normal to the single layer directed to the reader's eye, and coincides with the six-fold axis of rotation. The six mirror planes are shown by the coloured straight lines passing through the axes origin O. The angle between two consecutive mirror planes is 30^o. 32

2.4 Two dimensional triangular lattice. The global Oz axis is normal to the single layer directed to the reader's eye. Top left: The broken time reversal symmetry configuration is unaffected by the mirror plane represented by the vertical green line. Top right: The broken time reversal symmetry configuration is unaffected by the mirror plane represented the horizontal green line. Bottom: The broken time reversal symmetry configuration (quenched local moments aligned along the Oz axis) is unaffected by the six-fold axis of rotation normal to the Oxy plane (shown as a thick green dot). Spatial inversion persists in all cases where we've a single layer only. 33

2.5 Two dimensional A-B stacked bilayer lattice structure. The global Oz axis is normal to the Oxy plane directed to the reader's eye, and coincides with the three-fold axis of rotation. The three mirror planes are shown by the coloured straight lines passing through the axes origin O. The angle between two consecutive planes is now 60^o. 34

2.6 Two dimensional A-B stacked bilayer lattice structure. The global Oz axis is normal to the Oxy plane directed to the reader's eye. Top left: The broken time reversal symmetry configuration remains unaffected by the mirror plane represented by the vertical green line. Top right: There is no underlying lattice symmetry to leave the broken time reversal symmetry configuration unaffected. Bottom: The broken time reversal symmetry configuration (quenched local moments aligned along the Oz axis) is unaffected by the three-fold axis of rotation normal to the Oxy plane (shown as a green dot). Spatial inversion is broken in all cases. 35

2.7 X-component of the Dzyaloshinskii-Moriya vector for propagation along the Ox axis (left column) and along the Oy axis (right column). From top to bottom, at each column, the intraband, the interband and the total (intraband+interband) contribution are shown. The only variable parameters are the spin orbit coupling of the heavy metal layer (abscissa), and the 3d-5d atomic orbital offset (adjacent inset). The configuration of the exchange effective field of the ferromagnet is given on top of each subfigure. 39

2.8 Y-component of the Dzyaloshinskii-Moriya vector for propagation along the Ox axis (left column) and along the Oy axis (right column). From top to bottom, at each column, the intraband, the interband and the total (intraband+interband) contribution are shown. The only variable parameters are the spin orbit coupling of the heavy metal layer (abscissa), and the 3d-5d atomic orbital offset (adjacent inset). The configuration of the exchange effective field of the ferromagnet is given on top of each subfigure. 40

2.9 Z-component of the Dzyaloshinskii-Moriya vector for propagation along the Ox axis (left column) and along the Oy axis (right column). From top to bottom, at each column, the intraband, the interband and the total (intraband+interband) contribution are shown. The only variable parameters are the spin orbit coupling of the heavy metal layer (abscissa), and the 3d-5d atomic orbital offset (adjacent inset). The configuration of the exchange effective field of the ferromagnet is given on top of each subfigure. 41

2.10 X-component of the Dzyaloshinskii-Moriya vector for propagation along the Ox axis (left column) and along the Oy axis (right column). From top to bottom, at each column, the intraband, the interband and the total (intraband+interband) contribution are shown. The only variable parameters are the dimensionless ratio $\frac{c}{a}$ (abscissa), and the 3d-5d atomic orbital offset (adjacent inset). The configuration of the exchange effective field of the ferromagnet is given on top of each subfigure. 44

2.11 X-component of the Dzyaloshinskii-Moriya vector for propagation along the Ox axis (left column) and along the Oy axis (right column). From top to bottom, at each column, the intraband, the interband and the total (intraband+interband) contribution are shown. The only variable parameters are the Fermi level position with respect to the 3d atomic orbital on-site effective energy (abscissa), and the 3d-5d atomic orbital offset (adjacent inset). The configuration of the exchange effective field of the ferromagnet is given on top of each subfigure. 46

3.1 Y-component of the transverse (to the order parameter of the ferromagnet) spin accumulation within the heavy metal layer (left column) and the ferromagnetic layer (right column). From top to bottom, at each column, the intraband, the interband and the total (intraband+interband) contribution are shown. The only variable parameters are the effective exchange coupling of the ferromagnet (abscissa), and the spin orbit coupling strength of the heavy metal (adjacent inset). The postulated configuration of the exchange effective field of the ferromagnet is given on top of each subfigure. 81

3.2 Z-component of the transverse (to the order parameter of the ferromagnet) spin accumulation within the heavy metal layer (left column) and the ferromagnetic layer (right column). From top to bottom, at each column, the intraband, the interband and the total (intraband+interband) contribution are shown. The only variable parameters are the effective exchange coupling of the ferromagnet (abscissa), and the spin orbit coupling strength of the heavy metal (adjacent inset). The postulated configuration of the exchange effective field of the ferromagnet is given on top of each subfigure. 82

3.3 X-component of the transverse (to the order parameter of the ferromagnet) spin accumulation within the heavy metal layer (left column) and the ferromagnetic layer (right column). From top to bottom, at each column, the intraband, the interband and the total (intraband+interband) contribution are shown. The only variable parameters are the effective exchange coupling of the ferromagnet (abscissa), and the spin orbit coupling strength of the heavy metal (adjacent inset). The postulated configuration of the exchange effective field of the ferromagnet is given on top of each subfigure. 83

3.4 Z-component of the transverse (to the order parameter of the ferromagnet) spin accumulation within the heavy metal layer (left column) and the ferromagnetic layer (right column). From top to bottom, at each column, the intraband, the interband and the total (intraband+interband) contribution are shown. The only variable parameters are the effective exchange coupling of the ferromagnet (abscissa), and the spin orbit coupling strength of the heavy metal (adjacent inset). The postulated configuration of the exchange effective field of the ferromagnet is given on top of each subfigure. 84

3.5 X-component of the transverse (to the order parameter of the ferromagnet) spin accumulation within the heavy metal layer (left column) and the ferromagnetic layer (right column). From top to bottom, at each column, the intraband, the interband and the total (intraband+interband) contribution are shown. The only variable parameters are the effective exchange coupling of the ferromagnet (abscissa), and the spin orbit coupling strength of the heavy metal (adjacent inset). The postulated configuration of the exchange effective field of the ferromagnet is given on top of each subfigure. 85

3.6 Y-component of the transverse (to the order parameter of the ferromagnet) spin accumulation within the heavy metal layer (left column) and the ferromagnetic layer (right column). From top to bottom, at each column, the intraband, the interband and the total (intraband+interband) contribution are shown. The only variable parameters are the effective exchange coupling of the ferromagnet (abscissa), and the spin orbit coupling strength of the heavy metal (adjacent inset). The postulated configuration of the exchange effective field of the ferromagnet is given on top of each subfigure. 86

3.7 Y-component of the exchange mediated torque onto the exchange effective field of the ferromagnet, for two opposite postulated orientations (left and right column) of the latter along the x direction. From top to bottom, at each column, the intraband, the interband and the total (intraband+interband) contribution are shown. The only variable parameters are the effective exchange coupling of the ferromagnet (abscissa), and the spin orbit coupling strength of the heavy metal (adjacent inset). . . 88

3.8 Z-component of the exchange mediated torque onto the exchange effective field of the ferromagnet, for two opposite postulated orientations (left and right column) of the latter along the x direction. From top to bottom, at each column, the intraband, the interband and the total (intraband+interband) contribution are shown. The only variable parameters are the effective exchange coupling of the ferromagnet (abscissa), and the spin orbit coupling strength of the heavy metal (adjacent inset). . . 89

3.9 X-component of the exchange mediated torque onto the exchange effective field of the ferromagnet, for two opposite postulated orientations (left and right column) of the latter along the y direction. From top to bottom, at each column, the intraband, the interband and the total (intraband+interband) contribution are shown. The only variable parameters are the effective exchange coupling of the ferromagnet (abscissa), and the spin orbit coupling strength of the heavy metal (adjacent inset). . . 90

3.10 Z-component of the exchange mediated torque onto the exchange effective field of the ferromagnet, for two opposite postulated orientations (left and right column) of the latter along the y direction. From top to bottom, at each column, the intraband, the interband and the total (intraband+interband) contribution are shown. The only variable parameters are the effective exchange coupling of the ferromagnet (abscissa), and the spin orbit coupling strength of the heavy metal (adjacent inset). . . 91

3.11 X-component of the exchange mediated torque onto the exchange effective field of the ferromagnet, for two opposite postulated orientations (left and right column) of the latter along the z direction. From top to bottom, at each column, the intraband, the interband and the total (intraband+interband) contribution are shown. The only variable parameters are the effective exchange coupling of the ferromagnet (abscissa), and the spin orbit coupling strength of the heavy metal (adjacent inset) . . 92

3.12 Y-component of the exchange mediated torque onto the exchange effective field of the ferromagnet, for two opposite postulated orientations (left and right column) of the latter along the z direction. From top to bottom, at each column, the intraband, the interband and the total (intraband+interband) contribution are shown. The only variable parameters are the effective exchange coupling of the ferromagnet (abscissa), and the spin orbit coupling strength of the heavy metal (adjacent inset). . . 93

3.13 Spin Hall angle results for different postulated configurations of the exchange effective field of the ferromagnet (shown on the top of each subfigure), for different torque components (the torque component taken into account is denoted by the first superscript of the spin Hall angle notation). The only variable parameters are the effective exchange coupling of the ferromagnet (abscissa), and the spin orbit coupling strength of the heavy metal (adjacent inset). 96

4.1 Lowest order magnon-phonon scattering diagrams used for the calculation of the transport relaxation times in the regime in which thermal transport is magnon-dominated. Straight lines represent magnon propagators whereas wavy lines are phonon propagators. Figures (a) and (b) represent R-processes which involve phonon emissions or absorptions. Fig.(c) represents C-processes which involve phonon emission or absorption. 101

4.2 Lowest order magnon-phonon scattering diagrams used for the calculation of the transport relaxation times in the regime in which thermal transport is phonon-dominated. Wavy lines represent phonon propagators whereas straight lines are magnon propagators. Fig.(a) represents C-processes which involve two magnon creations or annihilations, where-as Fig.(b) represents R-processes that involve phonon emission or absorption. . . . 101

4.3 Zig-zag magnetic phase: A magnetic unit cell consists of four magnetic moments labelled as A, B, C and D, and is represented by the gray-shaded rectangle shown in the figure. The translation vectors of the periodic magnetic structure are the vectors a and b. The translation vectors of the chemical periodic structure are the vectors t_1 and t_2, and a chemical unit cell is represented by any dashed parallelogram. For the Néel and the ferromagnetic states the magnetic unit cell coincides with the chemical unit cell (that is common to all phases). 104

4.4 κ_{xx} component of the total fully ballistic thermal conductivity per unit area, for each ordered phase (see the legend of each subfigure), for different relative strengths of the Debye energy E_D to the magnon characteristic energy SA (given on top of each subfigure), versus temperature. 106

4.5 κ_{yy} component of the total ballistic thermal conductivity per unit area, for each ordered phase (see the legend of each subfigure), for different relative strengths of the Debye energy E_D to the magnon characteristic energy SA (given on top of each subfigure), versus temperature. 107

4.6 Phonon dominated transport: κ_{xx} and κ_{yy} component of the phononic thermal conductivity per unit area, for each ordered phase, for three different subregimes: ballistic, intermediate and diffusive (see the legend of each subfigure) as well as pure boundary scattering, versus temperature. 119

4.7 Phonon dominated transport: κ_{xx}/T^2 and κ_{yy}/T^2 component of the phononic thermal conductivity per unit area, for each ordered phase, for three different subregimes: ballistic, intermediate and diffusive (see the legend of each subfigure) as well as pure boundary scattering, versus temperature. 120

4.8 Magnon dominated transport: κ_{xx} and κ_{yy} component of the magnonic thermal conductivity per unit area, for each ordered phase, for three different subregimes: ballistic, intermediate and diffusive (see the legend of each subfigure) as well as pure boundary scattering, versus temperature. 127

4.9 Magnon dominated transport: κ_{xx}/T^n and κ_{yy}/T^n component of the magnonic thermal conductivity per unit area, for each ordered phase, for three different subregimes: ballistic, intermediate and diffusive (see the legend of each subfigure) as well as pure boundary scattering, versus temperature. The appropriate temperature exponent n that should divide κ_{xx} and κ_{yy} such that the pure boundary scattering results are represented by horizontal straight lines (at least at low temperatures) is given in the nearby yellow inset. 128

5.1 YIG thin film geometry: The global Oxyz coordinate system is shown, as well as the local OXYZ coordinate system with the OZ axis oriented along the equilibrium direction of the order parameter of the YIG insulator. 135

Chapter 1

Bird's eye view

The work presented in this dissertation is broken down into four pieces, all of which have in common a nowadays very widely investigated (and multi-advertised I would supplement) atomic property that bears the name atomic spin orbit coupling. This property is also at the heart of what you are going to read in the following pages, but let me first give you a glimpse of what is going to follow.

The first two projects (or else two chapters) negotiate an equilibrium and a non-equilibrium effect (non-equilibrium because of an applied transport electric field) respectively, both driven by the interplay between spin orbit coupling and magnetism, and both of which in most of this work "reside" in two different materials (the exception is chapter 4). In the second effect (the non-equilibrium one) the applied electric field also plays its own role! Since those turn out to be some kind of messy phenomena, we had better start approaching them step-by-step following the simplest possible route to the reality. To this end, we set out building first a structural toy model (which is developed in chapter 2), which is then followed by the set-up of a mean field Hamiltonian for the electronic degrees of freedom, and in the next step, in each case

(equilibrium effect/non-equilibrium effect) we supplement the so-far build-up with a formalism via which one can study, in one case indirect antisymmetric exchange interaction effects, in the spirit of the Brillouin light scattering experiments, and in the other case, spin-orbit torque effects, motivated by experiments performed on heavy metal/ferromagnetic metal heterostructures.

The forth chapter negotiates the effect of the interplay between the magnetic and the lattice degrees of freedom, mediated by a strong atomic spin-orbit coupling, on the material property called thermal conductivity. However, to study this effect in metallic compounds is a too complicated starting point, and therefore, we turned our attention to insulators, and particularly, the case of the strong spin-orbit driven magnetic insulators. To alleviate the complexity that emerged along the way, a possibly wise choice has been to disconnect the job from real materials (which are highly complicated) and study the aforementioned effect in simple limiting cases, and indeed this is what we finally did (yet having studied one aspect only of this interplay).

In the fifth chapter, a different effect of the interplay between the strong atomic spin orbit coupling and magnetism is studied, in this case motivated by (to the best of my knowledge) yet unpublished experimental efforts. In this last project, a lowest order many body perturbation theory is employed to study the interplay between the Dirac electronic quasiparticles of a thin film topological insulator and the magnetic degrees of freedom of a YIG thin film, which finally led to a toy-model-like analytical result.

Hopefully the reader finally appreciates a different side of the nature,

a side that emerges as a result of very low symmetry!

Chapter 2

Interfacial Dzyaloshinskii-Moriya interaction in heavy metal/ferromagnetic metal heterostructures

2.1 Motivation

Understanding the physics at the interface between a conducting material with large spin orbit coupling and a conducting ferromagnet is of great importance for the design of novel spin-orbitronic logic and memory devices, given the variety of the novel physical phenomena that can transpire at the interface, which range from spin-orbit torques and chiral spin torques to favored chiral spin textures such as magnetic skyrmions (Ref.[12]), spin spirals or domain walls of a particular type. Saying so, and further, in view of the development of recent theories that predict various effects of the interfacial Dzyaloshinskii-Moriya interaction on the spin wave propagation across such interfaces, several experimental efforts of understanding this proximity induced effect have been launched.

In a recent series of experiments, the Brillouin light scattering (BLS) technique is employed to probe the interfacial Dzyaloshinskii-Moriya interaction in sputtered multilayered stacks that incorporate, among other components, a thin ferromagnetic metal adjacent to a metal with strong spin orbit

coupling. In the aforementioned technique (Ref.[61]), a laser beam is focused onto a sample, and photons are inelastically backscattered via interaction with magnons existent in the sample (excited via the ferromagnetic resonance effect). Momentum and energy conservation dictate that if a backscattered photon emerges with increased (decreased) energy, that should have originated from the annihilation of a magnon propagating towards the incoming light beam (from the creation of a magnon propagating opposite to the incoming laser beam). Measurement of the backscattered photon energy can then be related to the frequency difference of two counterpropagating spin wave modes. Approximate analytic expressions for the interfacial Dzyaloshinskii-Moriya induced non-reciprocal spin wave propagation across the interface can be found in the work of Ref.[49].

The strong spin-orbit coupling in conjunction with the lack of inversion symmetry is considered to be responsible for the interfacial Dzyaloshinskii-Moriya effect, which can exist regardless of the crystal symmetry of the component materials, and is further expected to be much stronger than the corresponding bulk effect. As far as the microscopic nature of this effect is concerned, it is considered to be an indirect exchange interaction effect, and various simple mechanisms which lead to such indirect anisotropic exchange interactions were first studied by D.A.Smith. Smith (Ref.[4]), and later on Fert and Levy (Ref.[15, 45, 46]) who studied the scattering of conduction electrons by non-magnetic spin orbit centers diluted in CuMn alloys, concluded that indirect antisymmetric exchange interactions between two magnetic sites can

emerge when a conduction electron that interacts via the exchange interaction with the first magnetic site, propagates to a spin orbit center where its spin is subject to rotation to a different direction, and then continues to a second magnetic site with which it interacts via the exchange interaction mechanism. This indirect magnetic interaction between the initial and the final magnetic site is no longer symmetric under the interchange of the two sites. Furthermore, the work of Smith and that of Fert and Levy, for the systems that they studied, showed that the strength of the aforementioned indirect anisotropic exchange interaction, to lowest order, is proportional to the strength of the spin-orbit coupling of the non-magnetic spin orbit centers.

In this work, motivated by the technological importance as well as the continuing experimental efforts (Ref.[38]), we attempt to shed some light on the nature of the interfacial Dzyaloshinskii-Moriya interaction effect, by using a multiorbital Slater-Koster tight binding mean field theory model that has many of the ingredients shared by the physically realistic systems, and applying it to an A-B stacked commensurate bilayer structure that consists of a triangular lattice of heavy metal atoms on top of which is deposited a triangular lattice of ferromagnetic metal atoms. Within our model, different components of the Dzyaloshinskii-Moriya vector that are relevant to the BLS scattering experiments are studied in terms of the free parameters of the model (to be stressed later on) and different postulated translationally invariant configurations of the exchange effective field of the ferromagnetic material (having in mind the uniformly magnetized strong ferromagnets used in BLS

experiments).

2.2 Atomistic model and model Hamiltonian

As already stated, given the interfacial nature of the induced Dzyaloshinskii-Moriya effect, we use a multiband Slater-Koster tight binding mean field theory model to study the effect on a bilayer of two atomically thin triangular lattices, where the lower layer (termed as the *substrate layer*) is a heavy metal layer, on top of which has been deposited a ferromagnetic metal layer (termed as the *deposited layer*). In reality, of course, both the heavy metal and the ferromagnetic metal crystalline structures can extend several atomic layers beyond the interface. It is presumed that the heavy metal crystalline structure is the FCC structure, which has been cleaved along a plane that is normal to the (111) crystallographic direction. Similarly, the ferromagnetic metal crystalline structure is assumed to be the BCC structure, and the respective crystal is assumed cleaved along a plane normal to the corresponding (111) crystallographic direction. When a crystal is cleaved along a given low order crystallographic plane various bonds between adjacent planes parallel to the corresponding direction are broken. To simplify the situation, we adopt a series of approximations following the work of Yaniv (Refs.[26, 64]). In the first place, any degree of geometrical reconstruction of the cleaved crystal due to the formation of a surface is considered negligible, as a result of which electronic structure related parameters of the corresponding bulk systems are transferred and then used for a qualitative treatment of the interfacial coupling

between the two metals. It is further presumed that any redistribution of the charge degrees of freedom near the surface created upon crystal cleavage can be approximately taken into account as a change in the on-site self-consistent potential felt by the electrons near the outermost surface layer (which is part of the heavy metal – ferromagnetic metal interface as detailed in the following).

Bringing the two so far metal-vacuum surfaces in contact, atomic relaxation effects ensue, followed by the formation of new bonds between the two types of atoms sitting on the two sides of the developing heavy metal – ferromagnetic metal interface. As far as the atomic relaxation effects are concerned, it is assumed that they can reasonably well be described based on the so-called *hard sphere atomistic model*, according to which atoms are treated as hard spheres which have the tendency to get packed as closely as possible. Within that approximation, the heavy metal atoms are assumed closely packed together forming a two-dimensional triangular lattice, and assuming further (for theoretical simplicity) an ideal lattice match between the two materials, the magnetic atoms are considered to relax over various hollow spaces left in the substrate layer, forming a second two-dimensional triangular layer, so that finally the two layers acquire an A-B type of stacking (in the deposited layer the atoms are no more closely packed under such a relaxation process). In real bilayer systems, of course, there is no ideal lattice match between two materials, as a result of which, the last approximation should only be seen as a theoretical simplification of the model. It is also noticed that under such a relaxation process, the lattice constant of the substrate layer, which within

the hard sphere atomistic approximation is defined by the radius of the heavy metal atom, coincides with the lattice constant of the deposited layer, on the one hand inducing some interfacial strain on the deposited layer (which actually somewhat suppresses electronic hopping within that layer), but on the other hand leading to a simple commensurate structure as a result of which the bilayer structure shares the same first Brillouin zone. Possible effects related to any uncompensated bonds created as a result of the crystal cleavage described above are negligible in the context of metal-metal junctions. For an extension of the above model to incommensurate structures, a simple theory for the interlayer interaction is given in Ref.[29].

As soon as the contact is formed, electrons start flowing from the metal with the higher Fermi energy towards the metal with the lower Fermi energy, and this charge flow comes to an end, when the potential energy difference appearing on the two sides of the interface due to a dipole layer developed at the metal-metal interface compensates the Fermi energy difference of the two metals. Under the assumption that the aforementioned (presumably small scale) charge redistribution is confined in the vicinity of the developed interface, this last effect in conjunction with the dipole layer formation at the interface, can both approximately be taken into account (in our model) as an additional renormalization of the on-site self-consistent potential felt by the electrons near the interface.

Saying so, we can now turn our attention to the bilayer structure shown in Fig. 2.1 below. The lattice translation vectors for the substrate layer are $\mathbf{t}_1$

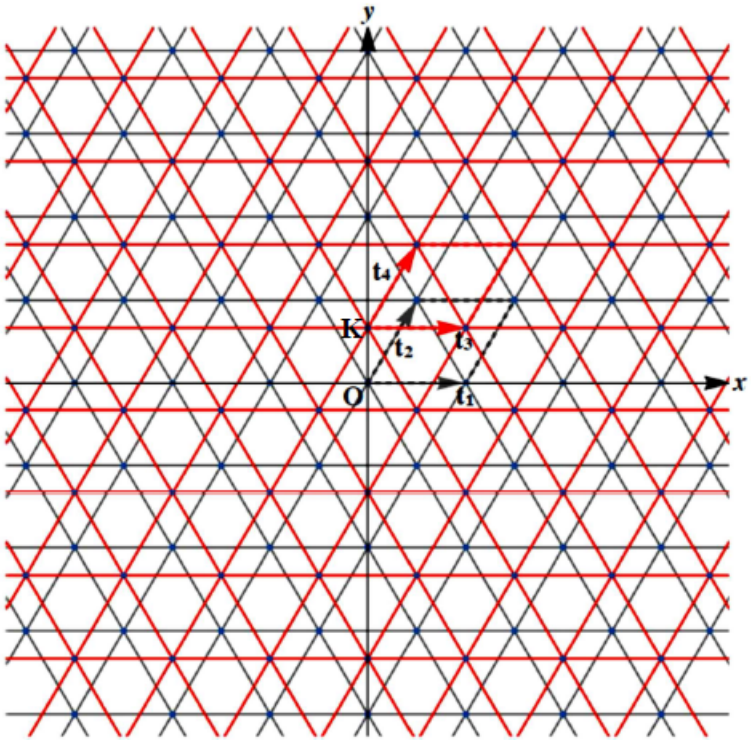

Figure 2.1: Commensurate bilayer of A-B stacked triangular lattices. The global Oz axis is normal to the interface directed to the reader's eye. The black-colored lattice is the substrate (heavy metal) layer, and the red-colored is the deposited (ferromagnetic) layer.

and $\mathbf{t}_2$, and for the deposited layer $\mathbf{t}_3$ and $\mathbf{t}_4$, as shown in the figure. The two layers are at a vertical distance c, but the upper layer is shifted by $\frac{2}{3}\left(\mathbf{t}_2 \cdot \hat{\mathbf{j}}\right)$ along the positive y-direction with respect to the lower layer due to the A-B stacking. The unit cell of the bilayer structure is defined by the vectors $\mathbf{t}_1$, $\mathbf{t}_2$, $\mathbf{t}_\perp = \mathbf{OK} = \frac{\mathbf{2}}{\mathbf{3}}\left(\mathbf{t_2} \cdot \hat{\mathbf{j}}\right)$, and there are two atoms per unit cell (one in each layer). Furthermore, a global Oxyz system is employed in the following analysis oriented as shown in Fig. 2.1, with the Oz axis normal to the bilayer interface (pointing out of the page to the reader's eye).

The Slater-Koster tight binding mean field Hamiltonian of the electronic degrees of freedom in the so-called Wannier-like representation is given by

$$
\begin{aligned}
\hat{\mathcal{H}}_e = & \sum_{i\gamma\sigma} \varepsilon_\gamma \; c^\dagger_{i\gamma\sigma} c_{i\gamma\sigma} + \sum_{i\gamma\sigma} \tilde{\varepsilon}_{\gamma\sigma} \; \tilde{c}^\dagger_{i\gamma\sigma} \tilde{c}_{i\gamma\sigma} + \sum_{\langle ij \rangle} \sum_{\gamma\gamma',\sigma\sigma'} t_{ij}^{\gamma\gamma'} \delta_{\sigma\sigma'} \; c^\dagger_{i\gamma\sigma} c_{j\gamma'\sigma} + \\
& \sum_{\langle ij \rangle} \sum_{\gamma\gamma'} \langle i,\uparrow | \, \tilde{t}_{ij}^{\gamma\gamma'} \, | j,\uparrow \rangle \; \tilde{c}^\dagger_{i\gamma\uparrow} \tilde{c}_{j\gamma'\uparrow} + \sum_{\langle ij \rangle} \sum_{\gamma\gamma'} \langle i,\downarrow | \, \tilde{t}_{ij}^{\gamma\gamma'} \, | j,\downarrow \rangle \; \tilde{c}^\dagger_{i\gamma\downarrow} \tilde{c}_{j\gamma'\downarrow} + \\
& \sum_{\langle ij \rangle} \sum_{\gamma\gamma'} \langle i,\uparrow | \, t'_{ij}{}^{\gamma\gamma'} \, | j,\uparrow \rangle \; \tilde{c}^\dagger_{i\gamma\uparrow} c_{j\gamma'\uparrow} + \sum_{\langle ij \rangle} \sum_{\gamma\gamma'} \langle i,\downarrow | \, t'_{ij}{}^{\gamma\gamma'} \, | j,\downarrow \rangle \; \tilde{c}^\dagger_{i\gamma\downarrow} c_{j\gamma'\downarrow} + \\
& \sum_{\langle ij \rangle} \sum_{\gamma\gamma'} \langle i,\uparrow | \, t'_{ij}{}^{\gamma\gamma'} \, | j,\uparrow \rangle \; c^\dagger_{i\gamma\uparrow} \tilde{c}_{j\gamma'\uparrow} + \sum_{\langle ij \rangle} \sum_{\gamma\gamma'} \langle i,\downarrow | \, t'_{ij}{}^{\gamma\gamma'} \, | j,\downarrow \rangle \; c^\dagger_{i\gamma\downarrow} \tilde{c}_{j\gamma'\downarrow} + \\
& \sum_{i\gamma\gamma'} \sum_{\sigma\sigma'} \left(\tfrac{\lambda_\gamma}{2} \sum_\mu \langle \gamma | \, L_\mu \, | \gamma' \rangle \, (\sigma^\mu)_{\sigma\sigma'} \right) c^\dagger_{i\gamma\sigma} c_{i\gamma'\sigma'} + \\
& \sum_{i\gamma\gamma'} \sum_{\sigma\sigma'} \left(\tfrac{J_\gamma}{2} \delta_{\gamma\gamma'} \, \langle \sigma | \, \vec{\sigma} \, | \sigma' \rangle \cdot \hat{\mathbf{\Omega}} \right) \tilde{c}^\dagger_{i\gamma\sigma} \tilde{c}_{i\gamma'\sigma'}
\end{aligned}
\tag{2.1}
$$

where $c^\dagger_{i\gamma\sigma}(c_{i\gamma\sigma})$ creates (annihilates) an electronic quasiparticle at the i-th lattice site of the heavy metal (substrate) layer, at the γ-th pseudoatomic orbital,

with spin σ, whereas, $\tilde{c}^{\dagger}_{i\gamma\sigma}(\tilde{c}_{i\gamma\sigma})$ are the corresponding creation (annihilation) operators for electronic quasiparticles within the ferromagnetic metallic layer. The first two terms on the right hand side (RHS) of Eq.(2.1) describe the renormalized on-site self-consistent potential energy within the heavy metal and the ferromagnetic metal layer respectively. The next terms up to the forth line of Eq.(2.1) describe the nearest neighbor (NN) hopping of the electronic quasiparticle within the heavy metal layer, the spin-dependent hopping within the ferromagnetic layer, the spin-dependent hopping from the heavy metal to the ferromagnetic layer, and the spin-dependent hopping from the ferromagnetic to the heavy metal layer respectively. The spin-dependent hoppings are introduced on account of the fact that the electronic bands of the majority carriers of a ferromagnetic metal are narrower than the electronic bands of the minority carriers. The terms in the last two lines represent the atomic spin-orbit coupling within the heavy metal layer (defined as on p.420 of Ref.[5]), and the exchange coupling of the electronic quasiparticles to the postulated translationally invariant exchange effective-magnetic-field of the ferromagnet.

To reduce the number of the parameters appearing in the aforementioned model, we dropped the site dependence of the on-site self-consistent potential energies of either layer, and further, considered them identical, for atoms of the same type, for all the pseudoatomic orbitals of a given angular momentum, but spin-dependent as far as the ferromagnetic sites (and only for them) are concerned. Aside that, the spin orbit coupling parameters as well as the on-site exchange coupling parameters (on-site Stoner parameters), de-

fined as $J_{i\gamma} = \tilde{\varepsilon}_{i\gamma\uparrow} - \tilde{\varepsilon}_{i\gamma\downarrow} > 0,\ \forall\, i, \gamma$ according to the Ref.[66], were considered for simplicity site-independent and the same for all the pseudoatomic orbitals of a given angular momentum. It is noted that any possible dependence of the exchange coupling parameters on the orientation of the exchange effective field is not captured in this model. Finally, due to the postulated translational invariance of the exchange effective field of the ferromagnet, we dropped the site index from the spatial orientation of the exchange effective field, denoting it as $\hat{\mathbf{\Omega}} = \sin\theta\cos\phi\ \hat{\mathbf{i}} + \sin\theta\sin\phi\ \hat{\mathbf{j}} + \cos\theta\ \hat{\mathbf{k}}$ in the last term on the RHS of Eq.(2.1).

Within the approximations elaborated above, in this model, the wave vector parallel to the interface of the two metals, denoted as $\mathbf{k}$ in the following (not to be confused with the coordinate unit vector $\hat{\mathbf{k}}$ that always bears a 'hat'), is treated as a good quantum number. In actual systems though, the presence of extensive disorder in conjunction with the lattice mismatch effect could further lead to non-conservation of the electronic 2D momentum $\mathbf{k}$, but in the first place such complications are not treated in our model. Saying so, one can use the following Fourier Transform (FT) convention (assuming N_x lattice points along the x-direction and N_y lattice points along the y-direction)

$$c^{\dagger}_{i\gamma\sigma} = \frac{1}{\sqrt{N_x N_y}} \sum_{\mathbf{k}=(k_x,k_y)} e^{-i\mathbf{k}\cdot\mathbf{R}_i} c^{\dagger}_{\mathbf{k}\gamma\sigma}, \qquad c_{i\gamma\sigma} = \frac{1}{\sqrt{N_x N_y}} \sum_{\mathbf{k}=(k_x,k_y)} e^{i\mathbf{k}\cdot\mathbf{R}_i} c_{\mathbf{k}\gamma\sigma} \quad (2.2)$$

as well as corresponding relationships for the creation and annihilation operators of the electronic quasiparticles within the ferromagnetic layer, with the corresponding in-plane lattice vectors measured from the lattice points O and

K within each layer (as shown Fig. 2.1), and rewrite the electronic mean field Hamiltonian of Eq.(2.1) as below

$$\hat{\mathcal{H}}_e(\mathbf{k}) = \sum_{\gamma\gamma'\sigma\sigma'} \left(\varepsilon_\gamma \delta_{\gamma\gamma'}\delta_{\sigma\sigma'}\right) c^\dagger_{\mathbf{k}\gamma\sigma} c_{\mathbf{k}\gamma'\sigma'} + \sum_{\gamma\gamma'\sigma\sigma'} \left(\tilde{\varepsilon}_{\gamma\sigma} \delta_{\gamma\gamma'}\delta_{\sigma\sigma'}\right) \tilde{c}^\dagger_{\mathbf{k}\gamma\sigma} \tilde{c}_{\mathbf{k}\gamma'\sigma'} +$$

$$\sum_{\gamma\gamma'\sigma\sigma'} \left(\sum_{\Delta\mathbf{R}} t_{\gamma\gamma'} e^{i\mathbf{k}\cdot\Delta\mathbf{R}} \delta_{\sigma\sigma'} \right) c^\dagger_{\mathbf{k}\gamma\sigma} c_{\mathbf{k}\gamma'\sigma'} + \sum_{\gamma\gamma'} \left(\sum_{\Delta\mathbf{R}} \langle\uparrow| \tilde{t}_{\gamma\gamma'} |\uparrow\rangle \, e^{i\mathbf{k}\cdot\Delta\mathbf{R}} \right) \tilde{c}^\dagger_{\mathbf{k}\gamma\uparrow} \tilde{c}_{\mathbf{k}\gamma'\uparrow} +$$

$$\sum_{\gamma\gamma'} \left(\sum_{\Delta\mathbf{R}} \langle\downarrow| \tilde{t}_{\gamma\gamma'} |\downarrow\rangle \, e^{i\mathbf{k}\cdot\Delta\mathbf{R}} \right) \tilde{c}^\dagger_{\mathbf{k}\gamma\downarrow} \tilde{c}_{\mathbf{k}\gamma'\downarrow} + \sum_{\gamma\gamma'} \left(\sum_{\Delta\mathbf{R}} \langle\uparrow| t'_{\gamma\gamma'} |\uparrow\rangle \, e^{i\mathbf{k}\cdot\Delta\mathbf{R}} \right) \tilde{c}^\dagger_{\mathbf{k}\gamma\uparrow} c_{\mathbf{k}\gamma'\uparrow} +$$

$$\sum_{\gamma\gamma'} \left(\sum_{\Delta\mathbf{R}} \langle\downarrow| t'_{\gamma\gamma'} |\downarrow\rangle \, e^{i\mathbf{k}\cdot\Delta\mathbf{R}} \right) \tilde{c}^\dagger_{\mathbf{k}\gamma\downarrow} c_{\mathbf{k}\gamma'\downarrow} + \sum_{\gamma\gamma'} \left(\sum_{\Delta\mathbf{R}} \langle\uparrow| t'_{\gamma\gamma'} |\uparrow\rangle \, e^{i\mathbf{k}\cdot\Delta\mathbf{R}} \right) c^\dagger_{\mathbf{k}\gamma\uparrow} \tilde{c}_{\mathbf{k}\gamma'\uparrow} +$$

$$\sum_{\gamma\gamma'} \left(\sum_{\Delta\mathbf{R}} \langle\downarrow| t'_{\gamma\gamma'} |\downarrow\rangle \, e^{i\mathbf{k}\cdot\Delta\mathbf{R}} \right) c^\dagger_{\mathbf{k}\gamma\downarrow} \tilde{c}_{\mathbf{k}\gamma'\downarrow} + \sum_{\gamma\gamma'\sigma\sigma'} \left(\frac{J_\gamma}{2} \delta_{\gamma\gamma'} \sum_\mu \left(\sigma^\mu\right)_{\sigma\sigma'} \hat{\Omega}_\mu \right) \tilde{c}^\dagger_{\mathbf{k}\gamma\sigma} \tilde{c}_{\mathbf{k}\gamma'\sigma'} +$$

$$\sum_{\gamma\gamma'\sigma\sigma'} \left(\frac{\lambda_\gamma}{2} \sum_\mu \langle\gamma| L_\mu |\gamma'\rangle \left(\sigma^\mu\right)_{\sigma\sigma'} \right) c^\dagger_{\mathbf{k}\gamma\sigma} c_{\mathbf{k}\gamma'\sigma'} \tag{2.3}$$

where $\Delta\mathbf{R} \equiv \mathbf{R}_j - \mathbf{R}_i$ runs over all nearest neighboring (NN) sites of the site i. To proceed with, it is required to truncate the actual Hilbert space of the electronic degrees of freedom down to an effective Hilbert space, which in this model is restricted to including the 3d pseudoatomic orbitals of each atom of the ferromagnetic layer and the 5d pseudoatomic orbitals of each atom of the heavy metal layer. In other words, it is assumed that the conduction band of each material is predominantly of 3d and 5d character respectively (in effect of course they also have s- and maybe a little p-character). Under the last approximation, the electronic quasiparticle Bloch basis states are denoted as $|\ell\mathbf{k}\gamma\sigma\rangle$, where $\ell = \{S,\ D\}$, $\gamma = \{yz,\ zx,\ xy,\ x^2-y^2,\ 3z^2-r^2\}$, $\sigma = \{\uparrow$

, $\downarrow\}$, with S denoting the substrate layer and D denoting the deposited layer. Defining the lattice basis vectors of each layer as below

$$\mathbf{t}_1 = a\hat{\mathbf{i}},\ \ \mathbf{t}_2 = \frac{a}{2}\hat{\mathbf{i}} + \frac{a\sqrt{3}}{2}\hat{\mathbf{j}},\ \ \mathbf{t}_3 = a\hat{\mathbf{i}} = \mathbf{t}_1,\ \ \mathbf{t}_4 = \frac{a}{2}\hat{\mathbf{i}} + \frac{a\sqrt{3}}{2}\hat{\mathbf{j}} = \mathbf{t}_2 \tag{2.4}$$

where a stands for the common (to both layers) lattice constant, the intraplane electronic hoppings to all six NNs are easily derived as

$$\begin{aligned} T_{\gamma\gamma'}(\mathbf{k}) &= t_{\gamma\gamma'}(\hat{\mathbf{e}}_1)\cdot 2\cos(k_x a) + t_{\gamma\gamma'}(\hat{\mathbf{e}}_2)\cdot 2\cos\left(\tfrac{k_x a}{2} + \tfrac{k_y a\sqrt{3}}{2}\right) \\ &\quad + t_{\gamma\gamma'}(\hat{\mathbf{e}}_1 - \hat{\mathbf{e}}_2)\cdot 2\cos\left(\tfrac{k_x a}{2} - \tfrac{k_y a\sqrt{3}}{2}\right) \\ \tilde{T}_{\gamma\gamma'}(\mathbf{k}) &= \tilde{t}_{\gamma\gamma'}(\hat{\mathbf{e}}_1)\cdot 2\cos(k_x a) + \tilde{t}_{\gamma\gamma'}(\hat{\mathbf{e}}_2)\cdot 2\cos\left(\tfrac{k_x a}{2} + \tfrac{k_y a\sqrt{3}}{2}\right) \\ &\quad + \tilde{t}_{\gamma\gamma'}(\hat{\mathbf{e}}_1 - \hat{\mathbf{e}}_2)\cdot 2\cos\left(\tfrac{k_x a}{2} - \tfrac{k_y a\sqrt{3}}{2}\right) \end{aligned} \tag{2.5}$$

where the prefactors $t_{\gamma\gamma'}(\hat{\mathbf{e}}_i)$, $\tilde{t}_{\gamma\gamma'}(\hat{\mathbf{e}}_i)$ encompass the direction and radial-distance dependent Slater-Koster parameters for intraplanar NNs. Similarly, the interplane electronic hoppings to all three NNs are also easily derived as

$$\begin{aligned} {T'}_{\gamma\gamma'}(\mathbf{k}) &= {t'}_{\gamma\gamma'}(\hat{\mathbf{g}}_1)\cdot\exp\left[i\left(\tfrac{k_y a}{\sqrt{3}}\right)\right] + {t'}_{\gamma\gamma'}(\hat{\mathbf{g}}_2)\cdot\exp\left[i\left(-\tfrac{k_x a}{2} - \tfrac{k_y a}{2\sqrt{3}}\right)\right] \\ &\quad + {t'}_{\gamma\gamma'}(\hat{\mathbf{g}}_3)\cdot\exp\left[i\left(\tfrac{k_x a}{2} - \tfrac{k_y a}{2\sqrt{3}}\right)\right] \\ T'_{\gamma\gamma'}(\mathbf{k}) &= t'_{\gamma\gamma'}(\hat{\mathbf{g}}_4)\cdot\exp\left[-i\left(\tfrac{k_y a}{\sqrt{3}}\right)\right] + t'_{\gamma\gamma'}(\hat{\mathbf{g}}_5)\cdot\exp\left[i\left(\tfrac{k_x a}{2} + \tfrac{k_y a}{2\sqrt{3}}\right)\right] \\ &\quad + t'_{\gamma\gamma'}(\hat{\mathbf{g}}_6)\cdot\exp\left[i\left(-\tfrac{k_x a}{2} + \tfrac{k_y a}{2\sqrt{3}}\right)\right] \end{aligned} \tag{2.6}$$

where now the prefactors $t'_{\gamma\gamma'}(\hat{\mathbf{g}}_i)$ encompass the direction and radial-distance dependent Slater-Koster parameters for interplanar NNs. The direction cosines

appearing in Eqs.(2.5)-(2.6) are given by

$$\begin{aligned}
&\hat{\mathbf{e}}_1 = (1,\ 0,\ 0),\ \ \hat{\mathbf{e}}_2 = \left(\tfrac{1}{2},\ \tfrac{\sqrt{3}}{2},\ 0\right),\ \ \hat{\mathbf{e}}_1 - \hat{\mathbf{e}}_2 = \left(\tfrac{1}{2},\ -\tfrac{\sqrt{3}}{2},\ 0\right), \\
&\hat{\mathbf{g}}_1 = \frac{1}{\sqrt{\frac{1}{3}+\left(\frac{c}{a}\right)^2}}\left(0,\ \tfrac{1}{\sqrt{3}},\ \tfrac{c}{a}\right),\ \ \hat{\mathbf{g}}_2 = \frac{1}{\sqrt{\frac{1}{3}+\left(\frac{c}{a}\right)^2}}\left(-\tfrac{1}{2},\ -\tfrac{1}{2\sqrt{3}},\ \tfrac{c}{a}\right), \\
&\hat{\mathbf{g}}_3 = \frac{1}{\sqrt{\frac{1}{3}+\left(\frac{c}{a}\right)^2}}\left(\tfrac{1}{2},\ -\tfrac{1}{2\sqrt{3}},\ \tfrac{c}{a}\right),\ \hat{\mathbf{g}}_4 = \frac{1}{\sqrt{\frac{1}{3}+\left(\frac{c}{a}\right)^2}}\left(0,\ -\tfrac{1}{\sqrt{3}},\ -\tfrac{c}{a}\right), \\
&\hat{\mathbf{g}}_5 = \frac{1}{\sqrt{\frac{1}{3}+\left(\frac{c}{a}\right)^2}}\left(\tfrac{1}{2},\ \tfrac{1}{2\sqrt{3}},\ -\tfrac{c}{a}\right),\ \hat{\mathbf{g}}_6 = \frac{1}{\sqrt{\frac{1}{3}+\left(\frac{c}{a}\right)^2}}\left(-\tfrac{1}{2},\ \tfrac{1}{2\sqrt{3}},\ -\tfrac{c}{a}\right)
\end{aligned} \tag{2.7}$$

where c denotes the vertical distance of the two stacked planes. Furthermore, since we focused on a commensurate bilayer structure, the common (to both layers) first Brillouin zone (1BZ) is shown in Fig. 2.2 below, and the reciprocal

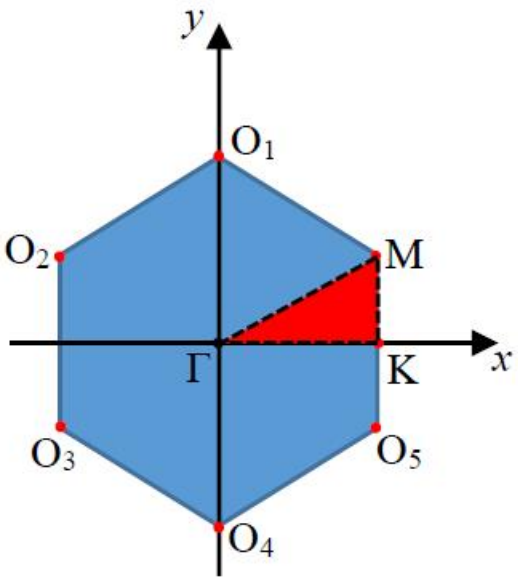

Figure 2.2: First Brillouin zone shown together with some high symmetry points.

lattice basis vectors as well as some high symmetry points of the 1BZ are given

by

$$\mathbf{b}_1 = \left(\tfrac{2\pi}{a},\ -\tfrac{2\pi}{a\sqrt{3}}\right),\ \ \mathbf{b}_2 = \left(0,\ \tfrac{4\pi}{a\sqrt{3}}\right),\ \ \mathbf{G} = m\mathbf{b}_1 + n\mathbf{b}_2,\ \ m,n \in \mathbb{Z}$$

$$\mathrm{M} = \left(\tfrac{2\pi}{a\sqrt{3}},\ \tfrac{2\pi}{3a}\right),\ O_1 = \left(0,\ \tfrac{4\pi}{3a}\right),\ O_2 = \left(-\tfrac{2\pi}{a\sqrt{3}},\ \tfrac{2\pi}{3a}\right),\ O_3 = \left(-\tfrac{2\pi}{a\sqrt{3}},\ -\tfrac{2\pi}{3a}\right),$$

$$O_4 = \left(0,\ -\tfrac{4\pi}{3a}\right),\ O_5 = \left(\tfrac{2\pi}{a\sqrt{3}},\ -\tfrac{2\pi}{3a}\right),\ \Gamma = (0,0),\ \mathrm{M} = \left(\tfrac{2\pi}{a\sqrt{3}},\ \tfrac{2\pi}{3a}\right),$$

$$\mathrm{K} = \left(\tfrac{2\pi}{a\sqrt{3}}, 0\right) \tag{2.8}$$

Before concluding this section, we sketch out some details related to the prefactors appearing on the RHSs of Eqs.(2.5)-(2.6). The dependence of those factors on the bond direction can be immediately read off from page 546 of W. A. Harrison's textbook (Ref.[1]) using the direction cosines given by Eq.(2.7), whereas, for the radial dependence of the Slater-Koster parameters we employ the parametrization of Shi and Papaconstantopoulos (Ref.[53]) who improved Harrison's approach to the two-center Slater-Koster parametrization. W.A. Harrison expressed the two-center Slater-Koster parameters in terms of the interatomic distance and, for the case of the d-orbitals, an effective orbital radius that is characteristic to each transition metal, as well as constants that are universal to all elements and structures. Shi and Papaconstantopoulos improved Harrison's approach in different ways (details can be found in Refs.[53, 66]), suggesting for the d-orbital Slater-Koster parameters the following improved

radial parametrization

$$V_{dd\zeta}(\rho) = \eta_{dd\zeta}\frac{\hbar^2 r_d^3}{m\rho^5},\ \zeta = \{\sigma,\pi,\delta\},\ \ \eta_{dd\sigma} = -21.22,\ \ \eta_{dd\pi} = 12.60,$$
$$\eta_{dd\delta} = -2.29,\ \ \frac{\hbar^2}{m} = 7.62\ \ eV - \mathring{A}^2 \tag{2.9}$$

where ρ denotes the interatomic distance and r_d is a d-orbital effective radius. Within the hard sphere atomistic approximation employed in this work, given the lattice constant $\tilde{a}_{HM}$ (Ref.[53]) of an FCC-structured heavy metal, the lattice constant of the corresponding 2D triangular lattice is $a = 2R_{5d} = 2\frac{\tilde{a}_{HM}\sqrt{2}}{4} = \frac{\tilde{a}_{HM}}{\sqrt{2}}$. Similarly, the 'hard sphere atomic radius' of the ferromagnetic atoms, given the lattice constant $\tilde{a}_{FM}$ of a BCC-structured ferromagnet, is $R_{3d} = \frac{\tilde{a}_{FM}\sqrt{3}}{4}$. Further, within the hard sphere atomistic approximation and the atomic relaxation scheme elaborated previously, the interatomic distance between a ferromagnetic and a heavy metal atom is simply $R_{HM-FM} = a\sqrt{\frac{1}{3} + \left(\frac{c}{a}\right)^2}$, with c denoting the interplanar distance. It should be noted on the way that the parameters read off from Ref.[53] refer to single-element bulk metallic systems.

As already stated previously, in our model the on-site self-consistent potential energies as well as the interatomic hoppings within the ferromagnetic metal layer are assumed exchange-split. The so-called spin-dependent intraplanar hopping is achieved by employing for the two-center Slater-Koster parameters given by Eq.(2.9) a different effective d-orbital radius r_d for the majority and the minority electronic bands, which can be read off from the rightmost column of Table II in the work of Ref.[53]. Given the direction of

the postulated translationally invariant exchange effective field of the ferromagnetic material, $\hat{\mathbf{\Omega}} = \sin\theta\cos\phi\ \hat{\mathbf{i}} + \sin\theta\sin\phi\ \hat{\mathbf{j}} + \cos\theta\ \hat{\mathbf{k}}$ (with the angles θ and ϕ defined with respect to the global Oxyz system of Fig. 2.1), the lower term in Eq.(2.5) is modified as below

$$\begin{aligned}
\tilde{T}^{\uparrow\uparrow}_{\gamma\gamma'}(\mathbf{k}) &= \tilde{t}^{\uparrow\uparrow}_{\gamma\gamma'}(\hat{\mathbf{e}}_1)\cdot 2\cos(k_x a) + \tilde{t}^{\uparrow\uparrow}_{\gamma\gamma'}(\hat{\mathbf{e}}_2)\cdot 2\cos\left(\tfrac{k_x a}{2} + \tfrac{k_y\sqrt{3}}{2}\right) + \\
&\qquad \tilde{t}^{\uparrow\uparrow}_{\gamma\gamma'}(\hat{\mathbf{e}}_1 - \hat{\mathbf{e}}_2)\cdot 2\cos\left(\tfrac{k_x}{2} - \tfrac{k_y\sqrt{3}}{2}\right) \\
\tilde{T}^{\downarrow\downarrow}_{\gamma\gamma'}(\mathbf{k}) &= \tilde{t}^{\downarrow\downarrow}_{\gamma\gamma'}(\hat{\mathbf{e}}_1)\cdot 2\cos(k_x a) + \tilde{t}^{\downarrow\downarrow}_{\gamma\gamma'}(\hat{\mathbf{e}}_2)\cdot 2\cos\left(\tfrac{k_x a}{2} + \tfrac{k_y\sqrt{3}}{2}\right) + \\
&\qquad \tilde{t}^{\downarrow\downarrow}_{\gamma\gamma'}(\hat{\mathbf{e}}_1 - \hat{\mathbf{e}}_2)\cdot 2\cos\left(\tfrac{k_x}{2} - \tfrac{k_y\sqrt{3}}{2}\right)
\end{aligned} \tag{2.10}$$

where the spin-dependent prefactors $\tilde{t}^{\sigma\sigma}_{\gamma\gamma'}(\hat{\mathbf{e}}_i)$ are defined by

$$\begin{aligned}
\tilde{t}^{\uparrow\uparrow}_{\gamma\gamma'}(\hat{\mathbf{e}}_i) &= \cos^2\left(\tfrac{\theta}{2}\right)\ {}_{\hat{\Omega}}\langle\uparrow|\,\tilde{t}_{\gamma\gamma'}(\hat{\mathbf{e}}_i)|\uparrow\rangle_{\hat{\Omega}}\ + \sin^2\left(\tfrac{\theta}{2}\right)\ {}_{\hat{\Omega}}\langle\downarrow|\,\tilde{t}_{\gamma\gamma'}(\hat{\mathbf{e}}_i)|\downarrow\rangle_{\hat{\Omega}} \\
\tilde{t}^{\downarrow\downarrow}_{\gamma\gamma'}(\hat{\mathbf{e}}_i) &= \sin^2\left(\tfrac{\theta}{2}\right)\ {}_{\hat{\Omega}}\langle\uparrow|\,\tilde{t}_{\gamma\gamma'}(\hat{\mathbf{e}}_i)|\uparrow\rangle_{\hat{\Omega}} + \cos^2\left(\tfrac{\theta}{2}\right)\ {}_{\hat{\Omega}}\langle\downarrow|\,\tilde{t}_{\gamma\gamma'}(\hat{\mathbf{e}}_i)|\downarrow\rangle_{\hat{\Omega}}
\end{aligned} \tag{2.11}$$

On the left hand side (LHS) of Eq.(2.11) the spin quantization axis used is the global Oz axis whereas on the RHS the spin quantization axis is defined by the direction of the postulated exchange effective field, and we use the convention that the majority spins are oriented antiparallel to the exchange effective field whereas the minority spins are oriented parallel to it (on account of the fact that in quantum mechanics the spin and the spin magnetic moment, with which the exchange effective field is related, are in opposite directions, and further, this convention is used throughout this work and also in Eq.(2.3)). Based on the last convention, the factors ${}_{\hat{\Omega}}\langle\uparrow|\,\tilde{t}_{\gamma\gamma'}(\hat{\mathbf{e}}_i)|\uparrow\rangle_{\hat{\Omega}}$ depend on the Slater-Koster parameters defined for the minority bands, whereas the factors ${}_{\hat{\Omega}}\langle\downarrow|\,\tilde{t}_{\gamma\gamma'}(\hat{\mathbf{e}}_i)|\downarrow\rangle_{\hat{\Omega}}$ depend on the Slater-Koster parameters defined for the majority bands, to make connection with the previous discussion.

As a consequence of the spin-dependent Slater-Koster parameters used for the magnetic layer, the interlayer electronic hoppings given by Eq.(2.6) are also rendered spin-dependent, since, the corresponding Slater-Koster parameters employed for the interlayer hoppings, are assumed to be given by

$$(dd\zeta)' = \sqrt{(dd\zeta) \cdot (\widetilde{dd\zeta})}, \quad \zeta = \{\sigma, \pi, \delta\}$$

i.e. by the geometric average of the corresponding single-element Slater-Koster parameters (where the single-element Slater-Koster parameters of the ferromagnetic metal ($\widetilde{dd\zeta}$) are spin-dependent as already stated). Values for the atomic spin orbit coupling parameter (that presumably doesn't renormalize significantly during the processes elaborated in the beginning of this section) can be found in Ref.[48], but it is preferable to retain it as a free parameter of the model.

Concluding this section, the calculation that relies on the model elaborated above, presupposes that all the processes prior to the equilibrium state of the combined system (which entail renormalizations of the on-site self-consistent potential energies and so on) have taken effect, and therefore the combined system acquires a common Fermi level that is chosen to lie within the minority bands of the ferromagnet (and the d-bands of the heavy metal) . The exact values of the renormalized on-site self-consistent potentials are not known, neither are they essential for this calculation. Only the relative energy difference between the on-site self-consistent potential energies of the 3d and the 5d pseudoatomic orbitals, and that between the exchange-split on-site self-consistent potential energies of the 3d pseudoatomic orbitals (that defines the

on-site exchange coupling parameter) are of importance, and since unknown, are further considered as free parameters of the model. It goes without saying that uncontrollable uncertainties are introduced during the transference of material parameters from the work of Shi and Papaconstantopoulos to our model. However, the situation is alleviated to some degree by treating crucial parameters of model as free parameters, by incorporating several properties of the corresponding real materials in the Hamiltonian of the model, by targeting to qualitative conclusions, as well as by the consolable conclusion of the work of Ref.[63] which states that electronic structure calculations on metal-metal interfaces conclude that the electronic structure closely resembles the bulk within one or two atomic layers beyond the interface.

2.3 Formalism for the itinerant electron antisymmetric exchange interactions

In this section, we present a simple formalism by which we study the itinerant electron mediated antisymmetric exchange interaction within the magnetic layer of the bilayer system that was described in detail previously.

In the single-particle Bloch basis states employed so far and collectively denoted as $|i,\mathbf{k}\rangle \equiv |\ell\mathbf{k}\gamma\sigma\rangle = |\ell\mathbf{k}\gamma\rangle \otimes |\sigma\rangle$, along with the condition that $\langle i,\mathbf{k}\,|j,\mathbf{k}\rangle = \delta_{ij}$, the mean field Hamiltonian of the electronic quasiparticles given by Eq.(2.3) is not diagonal. So, let us denote as $|n\mathbf{k}\rangle$ and $\varepsilon_{n\mathbf{k}}$ the eigenstates and the respective eigenvalues of the Hamiltonian $\hat{\mathcal{H}}_e(\mathbf{k})$ above, where $n = \{1, ..., 20\}$ is just a band index. Then, the new single-particle basis states

in terms of the initial single-particle basis states are given by

$$|n\mathbf{k}\rangle = \sum_i |i,\mathbf{k}\rangle \langle i,\mathbf{k}|\ n\mathbf{k}\rangle = \sum_i \left(\langle i,\mathbf{k}|\ n\mathbf{k}\rangle\right)|i,\mathbf{k}\rangle$$

where the coefficients $\langle i,\mathbf{k}|\ n\mathbf{k}\rangle$ are the components of the eigenvector that corresponds to the energy eigenvalue $\varepsilon_{n\mathbf{k}}$. In the following calculations the eigenvectors of the mean field electronic quasiparticle Hamiltonian $\hat{\mathcal{H}}_e(\mathbf{k})$ are subject to the condition that $\langle n'\mathbf{k}\,|n\mathbf{k}\rangle = \delta_{nn'}$ (i.e. are taken orthonormalized). To proceed with, we define a new set of creation and annihilation operators $f^\dagger_{n\mathbf{k}}$ and $f_{n\mathbf{k}}$ for the electronic quasiparticles with respect to which, the mean field electronic quasiparticle Hamiltonian admits the following diagonal form (at each point of the quasiparticle k-space)

$$\hat{\mathcal{H}}_e(\mathbf{k}) = \sum_n \varepsilon_{n\mathbf{k}} f^\dagger_{n\mathbf{k}} f_{n\mathbf{k}} \tag{2.12}$$

based on a postulated translationally invariant exchange effective field within the ferromagnet (this approximation is further justified by the fact that in BLS experiments the magnetic moments are forced to alignment via an applied static magnetic field, though not perfectly). Under those conditions, the system of the interfacial electronic quasiparticles is (magnetically) polarized via its interaction with the exchange effective field of the ferromagnet that is treated (as a parameter and) classically in this formalism, and the mean field electronic eigenstates are given by the Hamiltonian of Eq.(2.12).

It is implied that we work at temperatures much lower than the Curie temperature of the ferromagnetic metal, as a result of which we can focus only

on the direction of the magnetization field of the ferromagnet, considering its magnitude unchanged. Saying so, let us now perturb in a transverse manner the postulated translationally invariant exchange effective field of the ferromagnet (a situation that actually arises from the exchange interaction with the polarized interfacial quasiparticles), and then calculate the concomitant energy change of the system of the interfacial electronic quasiparticles using the Rayleigh-Schrodinger perturbation theory. The aforementioned transverse perturbation is supposed to be a small transverse deflection of the exchange effective field at each lattice site (it is believed that for strong ferromagnets at temperatures much lower than the Curie temperature this approach is reasonable, though the actual variation of the exchange effective field might require more complicated calculations such as a DFT calculation). So, to lowest order it is (a contact exchange interaction is implied anywhere, and further, since only the 3d electrons of the ferromagnet are taken into account, we dropped the orbital dependence from the exchange coupling strength in the following analysis)

$$\hat{\mathcal{H}}' = \frac{J}{2N_xN_y}\sum_i\sum_{\gamma\gamma'}\sum_{\sigma\sigma'}\left(\delta_{\gamma\gamma'}\tilde{c}^{\dagger}_{i\gamma\sigma}(\vec{\sigma})_{\sigma\sigma'}\tilde{c}_{i\gamma'\sigma'}\right)\cdot\delta\mathbf{\Omega}_i \tag{2.13}$$

where the summation is restricted to all the magnetic sites only (in real space), and further, $\vec{\sigma}$ is the interfacial electronic quasiparticle spin operator, and $\delta\mathbf{\Omega}_i$ represents the small transverse deviation of the exchange effective field at the i-th atomic magnetic site from an initially (postulated) translationally invariant configuration. The exchange interaction employed in Eq.(2.13)

however, conserves the total spin, as a result of which it can only lead to indirect exchange interactions of the form $\Omega_i^z\Omega_j^z$, $\Omega_i^+\Omega_j^-$ and $\Omega_i^-\Omega_j^+$ that are consistent with the isotropic exchange interaction. In order to obtain indirect anisotropic exchange interactions total spin conservation should somehow be broken by some virtual process (or series of processes). Further, of all the suggested (by D.A.Smith, Ref.[4]) microscopic mechanisms that can lead to indirect anisotropic exchange interactions, in this work, we particularly focus on the mechanism proposed by Smith and Fert and Levy, or more complicated versions of that. According to the work of Smith it is also required that the distribution of the spin-orbit scattering centers around the magnetic sites is of low symmetry, a requirement that is met by the bilayer structure we study. It should also be noted that Smith proposed various microscopic mechanisms which (to lowest order) can lead to anisotropic indirect exchange interactions between (orbitally) quenched localized magnetic moments, and actually his work is motivated by simple or more complex metallic local moment materials with lower than cubic symmetry. In our model, the spontaneously emergent order parameter of the ferromagnet is ascribed to d-electrons whose itinerant character is also taken into account in the model Hamiltonian (the exchange effective field is treated parametrically though). For simplicity, the metallic ferromagnet is treated as elemental (although real experiments usually use alloyed structures).

Saying so, let us now FT to the momentum space the perturbation

given by Eq.(2.13) to get

$$\hat{\mathcal{H}}' = \frac{J}{2N_xN_y}\sum_i\sum_{\gamma\gamma'}\sum_{\sigma\sigma'}\left(\delta_{\gamma\gamma'}\tilde{c}^\dagger_{i\gamma\sigma}(\vec{\sigma})_{\sigma\sigma'}\tilde{c}_{i\gamma'\sigma'}\right)\cdot\delta\mathbf{\Omega}_i \tag{2.14}$$

where the following definition was employed

$$\delta\Omega_\mu(\mathbf{q}) \equiv \frac{1}{N_xN_y}\sum_i e^{-i\mathbf{q}\cdot\mathbf{R}_i}\delta\Omega_i^\mu, \quad \mu = \{x, y, z\} \tag{2.15}$$

Furthermore, it is more convenient to express the perturbation of Eq.(2.14) in the basis in which the unperturbed interfacial electronic quasiparticle Hamiltonian is diagonal, i.e. the $|n\mathbf{k}\rangle$ basis, since as it stands it is expressed with respect to the $|i, \mathbf{k}\rangle$ single particle Bloch basis states. To switch from the $|i, \mathbf{k}\rangle$ basis to the $|n\mathbf{k}\rangle$ single-particle basis, one can employ the following transformations

$$\tilde{c}^\dagger_{\mathbf{k}+\mathbf{q},\gamma\sigma} = \sum_n \langle n, \mathbf{k}+\mathbf{q}|\ D, \mathbf{k}+\mathbf{q}, \gamma, \sigma\rangle\ f^\dagger_{n\mathbf{k}+\mathbf{q}},\ \tilde{c}_{\mathbf{k}\gamma'\sigma'} = \sum_{n'}\langle D\mathbf{k}\gamma'\sigma'|\ n'\mathbf{k}\rangle\ f_{n'\mathbf{k}} \tag{2.16}$$

where the D stands for the deposited (i.e. the ferromagnetic) layer. Using the last transformation in Eq.(2.14) we find that

$$\hat{\mathcal{H}}' = \frac{J}{2N_xN_y}\sum_{n,n'}\sum_{\mathbf{k},\mathbf{q}}\left\{\vec{\sigma}_{n\mathbf{k}+\mathbf{q},n'\mathbf{k}}\cdot\delta\mathbf{\Omega}(\mathbf{q})\right\}f^\dagger_{n\mathbf{k}+\mathbf{q}}f_{n'\mathbf{k}} \tag{2.17}$$

where for convenience we have used the following compact notation

$$\begin{aligned}&\sum_{\gamma\sigma\sigma'}\langle n, \mathbf{k}+\mathbf{q}|\ D, \mathbf{k}+\mathbf{q}, \gamma, \sigma\rangle\,(\sigma^\mu)_{\sigma\sigma'}\,\langle D\mathbf{k}\gamma\sigma'|\ n'\mathbf{k}\rangle \equiv \sigma^\mu_{n\mathbf{k}+\mathbf{q},n'\mathbf{k}} = \\ &\mathrm{Re}[\sigma^\mu_{n\mathbf{k}+\mathbf{q},n'\mathbf{k}}] + i\mathrm{Im}[\sigma^\mu_{n\mathbf{k}+\mathbf{q},n'\mathbf{k}}], \quad \mu = \{x, y, z\}\end{aligned} \tag{2.18}$$

In the next step, using the unperturbed interfacial quasiparticle Hamiltonian of Eq.(2.12) and the perturbative term of Eq.(2.17), we apply the Rayleigh-Schrodinger perturbation theory up to the second order. Specifically, the overall second order correction to the energy of the interfacial electronic quasiparticle system is given by (the first order correction is not relevant for the antisymmetric exchange interaction calculation)

$$\delta E^{(2)} = \frac{1}{2}\sum_{n\mathbf{k}}\sum_{n'\mathbf{k}'}\left(\frac{f_{n\mathbf{k}}-f_{n'\mathbf{k}'}}{\varepsilon_{n\mathbf{k}}-\varepsilon_{n'\mathbf{k}'}}\right)\langle n\mathbf{k}|\,\hat{\mathcal{H}}'\,|n'\mathbf{k}'\rangle\,\langle n'\mathbf{k}'|\,\hat{\mathcal{H}}'\,|n\mathbf{k}\rangle\,[(1-\delta_{nn'})+(1-\delta_{\mathbf{k}\mathbf{k}'})] \tag{2.19}$$

where $f_{n\mathbf{k}} = [1+\exp[(\varepsilon_{n\mathbf{k}}-\varepsilon_F)/k_BT]]^{-1}$ is the Fermi distribution function, $|n\mathbf{k}\rangle$ the basis in which the unperturbed electronic quasiparticle Hamiltonian is diagonal (see Eq.(2.12)), and $\hat{\mathcal{H}}'$ is given by Eq.(2.17). In the last equation, the Pauli exclusion principle is taken into account in the following way: if there is an excitation from the state $|n\mathbf{k}\rangle$ to the state $|n'\mathbf{k}'\rangle$, the initial state is occupied and the final one should be empty, which is taken care of by the inclusion of the term $f_{n\mathbf{k}}(1-f_{n'\mathbf{k}'})$, before ending up to the more symmetric form shown in Eq.(2.19). From Eqs.(2.17) and (2.19) one is led to the following result (for the second order energy correction per magnetic site of the ferromagnetic layer)

$$\delta E^{(2)}(\mathbf{q}) = \frac{1}{N_xN_y}\sum_{\mu\nu}\delta\Omega_\mu(-\mathbf{q})\left\{\frac{J^2}{8N_xN_y}\sum_{\mathbf{k}}\sum_{n,n'}\left(\frac{f_{n'\mathbf{k}+\mathbf{q}}-f_{n\mathbf{k}}}{\varepsilon_{n'\mathbf{k}+\mathbf{q}}-\varepsilon_{n\mathbf{k}}}\right)\times\right.$$
$$\left.[(1-\delta_{nn'})+(1-\delta_{\mathbf{k},\mathbf{k}+\mathbf{q}})]\,\sigma^{\mu}_{n\mathbf{k},n'\mathbf{k}+\mathbf{q}}\sigma^{\nu}_{n'\mathbf{k}+\mathbf{q},n\mathbf{k}}\right\}\delta\Omega_\nu(\mathbf{q}) \tag{2.20}$$

where μ,ν refer to the transverse components of the exchange effective field of the ferromagnet, and further, the following **generalized exchange intera**−

ction kernel can be singled out

$$K_{\mu\nu}(\mathbf{q}) = \frac{J^2}{8N_xN_y}\times$$
$$\sum_{\mathbf{k}}\sum_{n,n'}\left(\frac{f_{n'\mathbf{k}+\mathbf{q}}-f_{n\mathbf{k}}}{\varepsilon_{n'\mathbf{k}+\mathbf{q}}-\varepsilon_{n\mathbf{k}}}\right)\left[(1-\delta_{nn'})+(1-\delta_{\mathbf{k},\mathbf{k}+\mathbf{q}})\right]\sigma^{\mu}_{n\mathbf{k},n'\mathbf{k}+\mathbf{q}}\sigma^{\nu}_{n'\mathbf{k}+\mathbf{q},n\mathbf{k}} \tag{2.21}$$

The effective microscopic mechanism taken account of by Eq.(2.20) is this: small transverse deflections of the exchange effective field from its initial configuration are accompanied by the emission (from a magnetic site) and absorption (at a neighboring magnetic site) of electron-hole pairs. Intraband and interband contributions to the generalized kernel defined by Eq.(2.21) can further be defined in the following sense

$$K^{\text{intra}}_{\mu\nu}(\mathbf{q}) = \frac{J^2}{8N_xN_y}\sum_{\mathbf{k}}\sum_{n}\left(\frac{f_{n\mathbf{k}}-f_{n\mathbf{k}+\mathbf{q}}}{\varepsilon_{n\mathbf{k}}-\varepsilon_{n\mathbf{k}+\mathbf{q}}}\right)(1-\delta_{\mathbf{k},\mathbf{k}+\mathbf{q}})\sigma^{\mu}_{n\mathbf{k},n\mathbf{k}+\mathbf{q}}\sigma^{\nu}_{n\mathbf{k}+\mathbf{q},n\mathbf{k}}$$

$$K^{\text{inter}}_{\mu\nu}(\mathbf{q}) = \frac{J^2}{8N_xN_y}\sum_{\mathbf{k}}\sum_{n,n'}\left(\frac{f_{n\mathbf{k}}-f_{n'\mathbf{k}+\mathbf{q}}}{\varepsilon_{n\mathbf{k}}-\varepsilon_{n'\mathbf{k}+\mathbf{q}}}\right)(1-\delta_{nn'})\sigma^{\mu}_{n\mathbf{k},n'\mathbf{k}+\mathbf{q}}\sigma^{\nu}_{n'\mathbf{k}+\mathbf{q},n\mathbf{k}} \tag{2.22}$$

$$K_{\mu\nu}(\mathbf{q}) = K^{\text{intra}}_{\mu\nu}(\mathbf{q}) + K^{\text{inter}}_{\mu\nu}(\mathbf{q})$$

It is noted that the generalized exchange interaction kernel has the following important properties

$$K_{\mu\nu}(-\mathbf{q}) = K_{\nu\mu}(\mathbf{q}), \quad K_{\mu\nu}(\mathbf{q}=0) = K_{\nu\mu}(\mathbf{q}=0) \tag{2.23}$$

Now, let us look back to Eq.(2.20) carefully, and delineate what we did so far (in case the reader has been lost in the details provided along the way). We viewed the energy of the electronic quasiparticle system as a functional of the exchange effective field of the ferromagnet (actually as a functional of the orientation of the exchange effective field), we then caused a small

transverse deflection to the initially uniform (translationally invariant) configuration of the exchange effective field (presumably capturing the effect of the quasiparticles onto the exchange effective field due the their mutual exchange interaction), switched to the momentum space via a Fourier Transformation, and finally expanded up to the second order over the aforementioned transverse deflection. Doing so, the bilinear form reached in Eq.(2.20) now looks very much like the bilinear form developed in the first pages of the work of Kataoka-Nakanishi-Yanase-Kanamori (Ref.[27]), adjusted to a non-Bravais lattice model (that is appropriate for our case). In the spirit of the work of Kataoka-Nakanishi-Yanase-Kanamori, one can further decompose the generalized interaction kernel defined in Eq.(2.21) (the definition is inspired by the work of Kataoka-Nakanishi-Yanase-Kanamori) into a symmetric and an antisymmetric component, and then perform an expansion of the antisymmetric component in powers of the wavevector $\mathbf{q}$ which lies within the Oxy plane. The constant term of the aforementioned expansion vanishes, and therefore we focus on the next term that is linear in $\mathbf{q}$. Performing the described steps in a careful way (the steps of this derivation are skipped), the Dzyaloshinskii-

Moriya components are finally found to be given by

$$
\begin{aligned}
D_x &= \tfrac{i}{2}\mathrm{Im}\left[\lim_{\mathbf{q}\to 0}\left(\nabla_{\mathbf{q}}K^{\mathrm{intra}}_{yz}(\mathbf{q})-\nabla_{\mathbf{q}}K^{\mathrm{intra}}_{zy}(\mathbf{q})\right)\cdot\hat{\mathbf{e}}_{\mathbf{q}}+\right.\\
&\qquad\left.\lim_{\mathbf{q}\to 0}\left(\nabla_{\mathbf{q}}K^{\mathrm{inter}}_{yz}(\mathbf{q})-\nabla_{\mathbf{q}}K^{\mathrm{inter}}_{zy}(\mathbf{q})\right)\cdot\hat{\mathbf{e}}_{\mathbf{q}}\right]\\
D_y &= \tfrac{i}{2}\mathrm{Im}\left[\lim_{\mathbf{q}\to 0}\left(\nabla_{\mathbf{q}}K^{\mathrm{intra}}_{xz}(\mathbf{q})-\nabla_{\mathbf{q}}K^{\mathrm{intra}}_{zx}(\mathbf{q})\right)\cdot\hat{\mathbf{e}}_{\mathbf{q}}+\right.\\
&\qquad\left.\lim_{\mathbf{q}\to 0}\left(\nabla_{\mathbf{q}}K^{\mathrm{inter}}_{xz}(\mathbf{q})-\nabla_{\mathbf{q}}K^{\mathrm{inter}}_{zx}(\mathbf{q})\right)\cdot\hat{\mathbf{e}}_{\mathbf{q}}\right]\\
D_z &= \tfrac{i}{2}\mathrm{Im}\left[\lim_{\mathbf{q}\to 0}\left(\nabla_{\mathbf{q}}K^{\mathrm{intra}}_{xy}(\mathbf{q})-\nabla_{\mathbf{q}}K^{\mathrm{intra}}_{yx}(\mathbf{q})\right)\cdot\hat{\mathbf{e}}_{\mathbf{q}}+\right.\\
&\qquad\left.\lim_{\mathbf{q}\to 0}\left(\nabla_{\mathbf{q}}K^{\mathrm{inter}}_{xy}(\mathbf{q})-\nabla_{\mathbf{q}}K^{\mathrm{inter}}_{yx}(\mathbf{q})\right)\cdot\hat{\mathbf{e}}_{\mathbf{q}}\right]
\end{aligned}
\tag{2.24}
$$

We will focus only on the components that are relevant to the BLS scattering experiments for which the aforementioned formalism has been developed. The calculation of the partial derivatives of the generalized kernel on the RHSs of Eqs.(2.24) and the ensuing limiting processes are lengthy enough to be given here. We just give the final expressions for the intraband and interband contributions:

$$
\begin{aligned}
&\lim_{\mathbf{q}\to 0}\nabla_{\mathbf{q}}K^{\mathrm{intra}}_{\mu\nu}(\mathbf{q}) = \tfrac{J^2}{16N_xN_y}\sum_{\mathbf{k}}\sum_{n}\tfrac{\partial^2 f_{n\mathbf{k}}}{\partial\varepsilon^2_{n\mathbf{k}}}\left\langle n\mathbf{k}\right|\nabla_{\mathbf{k}}\hat{\mathcal{H}}_e(\mathbf{k})\left|n\mathbf{k}\right\rangle\sigma^{\mu}_{n\mathbf{k},n\mathbf{k}}\sigma^{\nu}_{n\mathbf{k},n\mathbf{k}}-\\
&\tfrac{J^2}{8N_xN_y}\sum_{\mathbf{k}}\sum_{n}\tfrac{\partial f_{n\mathbf{k}}}{\partial\varepsilon_{n\mathbf{k}}}\left\{\sum_{n''}\sigma^{\mu}_{n\mathbf{k},n''\mathbf{k}}\tfrac{\langle n''\mathbf{k}|\nabla_{\mathbf{k}}\hat{\mathcal{H}}_e(\mathbf{k})|n\mathbf{k}\rangle}{\varepsilon_{n''\mathbf{k}}-\varepsilon_{n\mathbf{k}}}(1-\delta_{nn''})\right\}\sigma^{\nu}_{n\mathbf{k},n\mathbf{k}}+\\
&\tfrac{J^2}{8N_xN_y}\sum_{\mathbf{k}}\sum_{n}\tfrac{\partial f_{n\mathbf{k}}}{\partial\varepsilon_{n\mathbf{k}}}\sigma^{\mu}_{n\mathbf{k},n\mathbf{k}}\left\{\sum_{n''}\tfrac{\langle n\mathbf{k}|\nabla_{\mathbf{k}}\hat{\mathcal{H}}_e(\mathbf{k})|n''\mathbf{k}\rangle}{\varepsilon_{n\mathbf{k}}-\varepsilon_{n''\mathbf{k}}}\sigma^{\nu}_{n''\mathbf{k},n\mathbf{k}}(1-\delta_{nn''})\right\}
\end{aligned}
\tag{2.25}
$$

and

$$\lim_{\mathbf{q}\to 0}\nabla_{\mathbf{q}}K^{\text{inter}}_{\mu\nu}(\mathbf{q}) = \tfrac{J^2}{8N_xN_y}\times$$

$$\Bigg[\sum_{\mathbf{k}}\sum_{n,n'}\tfrac{\langle n'\mathbf{k}|\nabla_{\mathbf{k}}\hat{\mathcal{H}}_e(\mathbf{k})|n'\mathbf{k}\rangle}{\varepsilon_{n\mathbf{k}}-\varepsilon_{n'\mathbf{k}}}\left[\tfrac{f_{n\mathbf{k}}-f_{n'\mathbf{k}}}{\varepsilon_{n\mathbf{k}}-\varepsilon_{n'\mathbf{k}}}+\beta f_{n'\mathbf{k}}\left(1-f_{n'\mathbf{k}}\right)\right](1-\delta_{nn'})\sigma^{\mu}_{n\mathbf{k},n'\mathbf{k}}\sigma^{\nu}_{n'\mathbf{k},n\mathbf{k}}$$

$$-\sum_{\mathbf{k}}\sum_{n,n'}\left(\tfrac{f_{n\mathbf{k}}-f_{n'\mathbf{k}}}{\varepsilon_{n\mathbf{k}}-\varepsilon_{n'\mathbf{k}}}\right)(1-\delta_{nn'})\left\{\sum_{n''}\sigma^{\mu}_{n\mathbf{k},n''\mathbf{k}}\tfrac{\langle n''\mathbf{k}|\nabla_{\mathbf{k}}\hat{\mathcal{H}}_e(\mathbf{k})|n'\mathbf{k}\rangle}{\varepsilon_{n''\mathbf{k}}-\varepsilon_{n'\mathbf{k}}}(1-\delta_{n'n''})\right\}\sigma^{\nu}_{n'\mathbf{k},n\mathbf{k}}$$

$$+\sum_{\mathbf{k}}\sum_{n,n'}\left(\tfrac{f_{n\mathbf{k}}-f_{n'\mathbf{k}}}{\varepsilon_{n\mathbf{k}}-\varepsilon_{n'\mathbf{k}}}\right)(1-\delta_{nn'})\sigma^{\mu}_{n\mathbf{k},n'\mathbf{k}}\left\{\sum_{n''}\tfrac{\langle n'\mathbf{k}|\nabla_{\mathbf{k}}\hat{\mathcal{H}}_e(\mathbf{k})|n''\mathbf{k}\rangle}{\varepsilon_{n'\mathbf{k}}-\varepsilon_{n''\mathbf{k}}}\sigma^{\nu}_{n''\mathbf{k},n\mathbf{k}}(1-\delta_{n'n''})\right\}\Bigg] \tag{2.26}$$

where in Eqs.(2.25) and (2.26) the compact notation of Eq.(2.18) was used, and by definition it is $\beta = 1/k_BT$. In Eq.(2.25) the intraband contribution mainly comes from the second and the third term on the RHS of the equation, and further, the dominant contribution comes from those k-space points where other bands lie near the band at issue, provided the latter is cut by the Fermi level. In (2.26), where more band energy difference denominators appear, the dominant contribution comes from those k-space points where two bands come close to each other, provided that the two bands are on opposite sides of the Fermi level (one above and one below the Fermi level). Concluding this section, let us also mention the following properties of the generalized exchange interaction kernel:

$$\begin{aligned}&\nabla_{-\mathbf{q}}K_{\mu\nu}(-\mathbf{q}) = -\nabla_{\mathbf{q}}K_{\nu\mu}(\mathbf{q}),\\ &\nabla_{\mathbf{q}}K_{\mu\nu}(\mathbf{q}) - \nabla_{\mathbf{q}}K_{\nu\mu}(\mathbf{q}) = \nabla_{-\mathbf{q}}K_{\mu\nu}(-\mathbf{q}) - \nabla_{-\mathbf{q}}K_{\nu\mu}(-\mathbf{q})\end{aligned} \tag{2.27}$$

where the second line of the last equation is compatible with the fact that the Dzyaloshinskii-Moriya response is even under the time reversal operation.

2.4 Brief symmetry analysis

In this section, we perform a brief symmetry analysis of the bilayer structure detailed in the previous sections. Particularly, we sketch out the underlying lattice symmetries of the bilayer structure detailed above, and further, check the effect of some of the aforementioned symmetries on the quenched local moments of the ferromagnet (in the other words, we check how the latter are transformed under some of the aforementioned symmetries).

When the two two-dimensional triangular lattices are decoupled from each other, then, for the heavy metal layer there exists time reversal invariance, translational invariance, spatial inversion, and a six-fold rotational symmetry, i.e. six mirror planes (all normal to the layer) and a six-fold axis of rotation that lies along the intersection of the aforementioned mirror planes. The six mirror planes are shown in Fig.2.3 below. As for the (single) ferromagnetic layer, before embellishing it with the quenched local moments, it has the same symmetries as the single heavy metal layer. However, when the quenched local moments are loaded on the lattice sites of the magnetic layer, then the single ferromagnetic layer has fewer symmetries compared to the single heavy metal layer. For instance, the time reversal symmetry is broken for the single ferromagnetic layer. Fig.2.4 below shows cases in which a postulated uniform magnetic configuration (on a single magnetic layer) is unaffected by an underlying lattice symmetry, as detailed in the caption there in. It should be noticed though, that a broken time reversal symmetry configuration that comes out of a linear combination of the two in-plane broken time reversal symmetry

configurations shown on the top left and the top right subfigures of Fig.2.4 below, is no more unaffected by any of the aforementioned mirror planes.

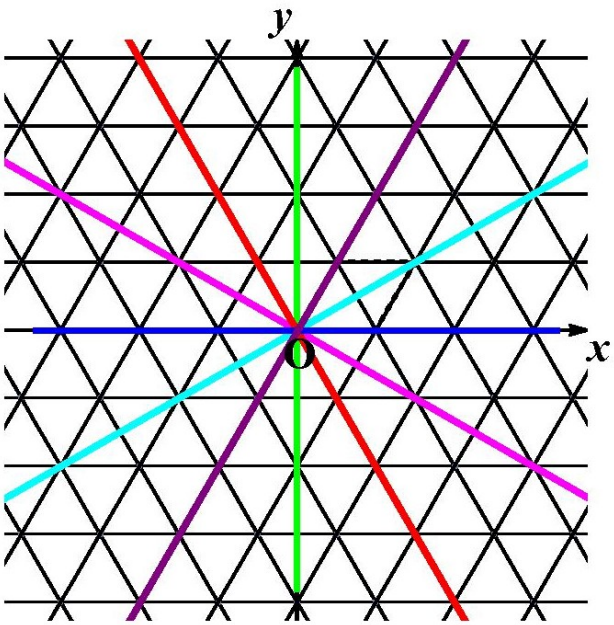

Figure 2.3: Two dimensional triangular lattice. The global Oz axis is normal to the single layer directed to the reader's eye, and coincides with the six-fold axis of rotation. The six mirror planes are shown by the coloured straight lines passing through the axes origin O. The angle between two consecutive mirror planes is 30^o.

Now, when the two layers are coupled to each other, the bilayer structure formed has broken inversion symmetry, broken time reversal symmetry and broken six-fold rotational symmetry in the case of the A-B stacking. The A-B stacked bilayer lattice structure has three mirror planes (normal to the bilayer) and a three-fold axis of rotation along the intersection of the mirror planes, as shown in Fig.2.5 below. Fig.2.6 below, shows the A-B stacked bilayer

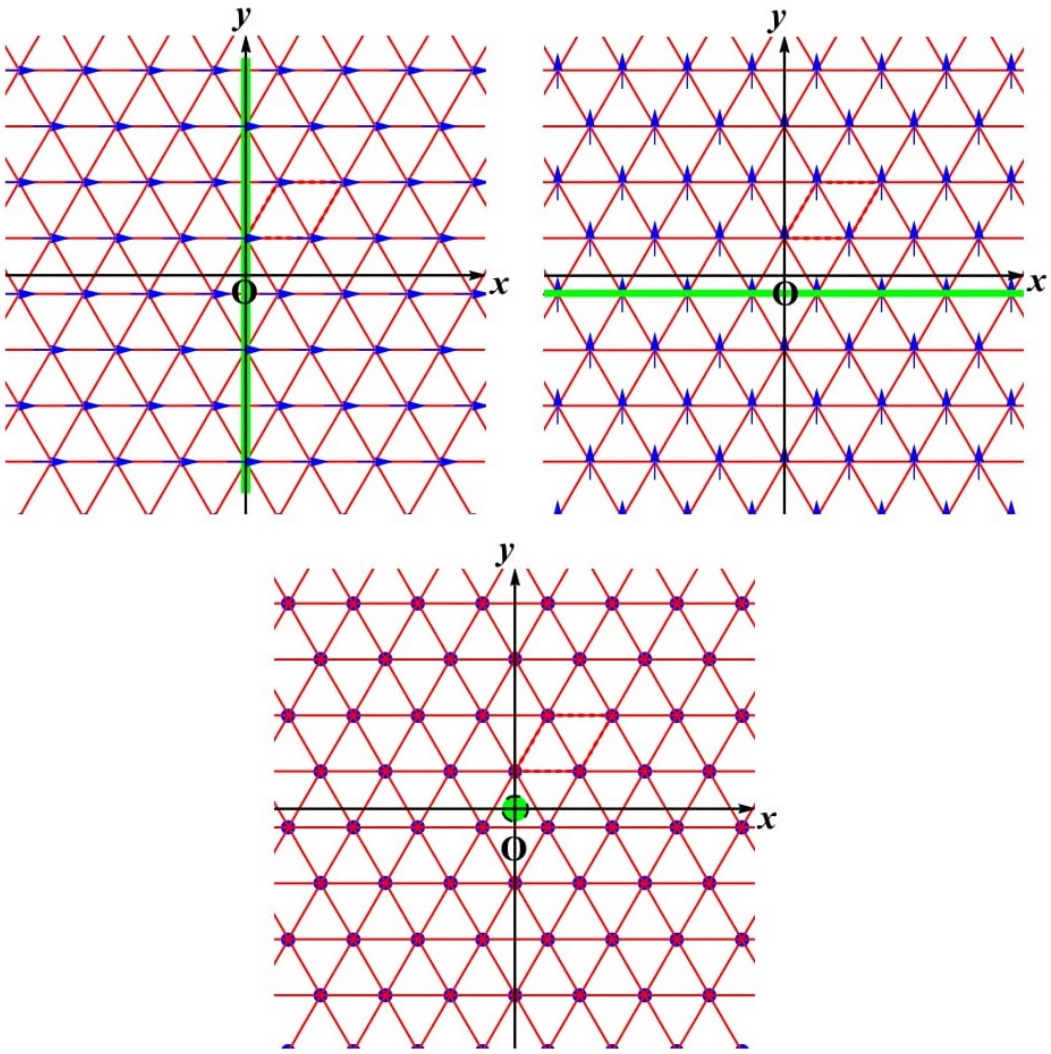

Figure 2.4: Two dimensional triangular lattice. The global Oz axis is normal to the single layer directed to the reader's eye. Top left: The broken time reversal symmetry configuration is unaffected by the mirror plane represented by the vertical green line. Top right: The broken time reversal symmetry configuration is unaffected by the mirror plane represented the horizontal green line. Bottom: The broken time reversal symmetry configuration (quenched local moments aligned along the Oz axis) is unaffected by the six-fold axis of rotation normal to the Oxy plane (shown as a thick green dot). Spatial inversion persists in all cases where we've a single layer only.

structure in conjunction with any one of the three different postulated uniform magnetic configurations examined in this work, with more details given in the caption there in.

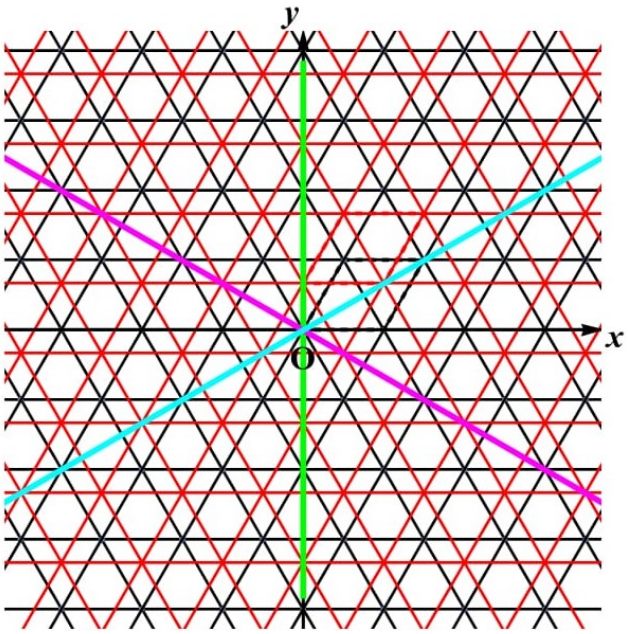

Figure 2.5: Two dimensional A-B stacked bilayer lattice structure. The global Oz axis is normal to the Oxy plane directed to the reader's eye, and coincides with the three-fold axis of rotation. The three mirror planes are shown by the coloured straight lines passing through the axes origin O. The angle between two consecutive planes is now 60^o.

Concluding this section, let us also mention that when the bilayer structure is A-A stacked (meaning that the deposited layer lies right on top of the substrate layer), any lattice symmetries common to the decoupled (single) layers are inherited (by the A-A stacked bilayer), except for the spatial inversion symmetry which now is broken (since the two layers are not identical). Ob-

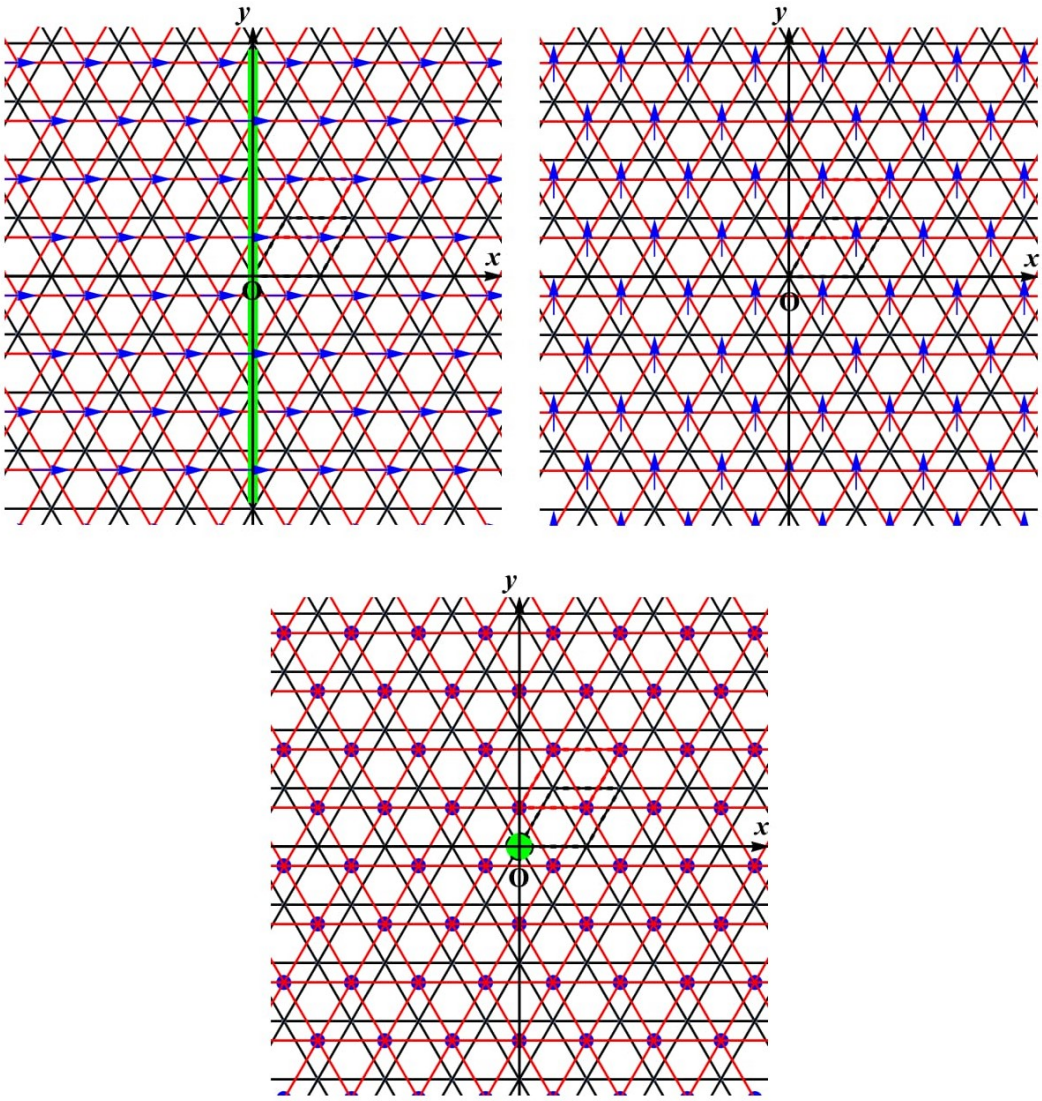

Figure 2.6: Two dimensional A-B stacked bilayer lattice structure. The global Oz axis is normal to the Oxy plane directed to the reader's eye. Top left: The broken time reversal symmetry configuration remains unaffected by the mirror plane represented by the vertical green line. Top right: There is no underlying lattice symmetry to leave the broken time reversal symmetry configuration unaffected. Bottom: The broken time reversal symmetry configuration (quenched local moments aligned along the Oz axis) is unaffected by the three-fold axis of rotation normal to the Oxy plane (shown as a green dot). Spatial inversion is broken in all cases.

viously, by going from a bilayer configuration with the A-A type of stacking to a bilayer configuration with the A-B type of stacking, generally speaking, the symmetry is lowered. As it will be seen in the following, such a symmetry lowering can have important consequences as far as the effects studied in this and the next chapter are concerned.

2.5 Results, discussion and conclusions

In the previous sections, motivated by relevant experiments, we developed a simple formalism for the study of the Dzyaloshinskii-Moriya effect in bilayer structures that lack spatial inversion symmetry, consisting of a ferromagnetic metal film deposited on a heavy metal film. Even though the real materials are three-dimensional structures consisting of several layers each, our starting point has been the interface between the two materials which certainly plays an important role. However, even at the interface between the two materials the situation can be quite messy, as a result of which we had to recourse to some drastic approximations, such as for instance the ideal lattice match approximation. On top of that, several band structure related parameters are not precisely known, and to bypass this impediment, we drastically reduced the number of the band structure related parameters to a minimal set of parameters, which are in turn treated as free parameters of the model. To be explicit, those are, the spin orbit coupling strength of the heavy metal atoms, the effective exchange coupling of the ferromagnet (related to the splitting between its majority and minority bands), the interlayer hybridization (originating from

the strongest Slater-Koster radial parameters), and the 3d-5d atomic orbital on-site effective energy offset. With the help of this minimal edifice, let us now venture to shed light on some aspects of this complex proximity induced effect studied here. We will not attempt to provide any microscopic explanations of the presented results since the situation turns out to be quite complex even under all those simplifications.

First of all, from Eq.(2.24) it is easily seen that any component of the Dzyaloshinskii-Moriya vector, generally speaking, depends also on the direction of propagation of the (uniform) spin wave mode that is excited in a Brillouin light scattering (BLS) experiment. Saying so, for the top left configuration shown in Fig.2.6 above, the quantities $D_X^X,\ D_X^Y$ are relevant to a BLS experiment. For the top right configuration shown in Fig.2.6 above, the quantities D_Y^X and D_Y^Y are only relevant, whereas, for the bottom configuration shown in that figure, the quantities D_Z^X and D_Z^Y are only relevant. In the notation used in the previous lines, the subscript denotes the component of the Dzyaloshinskii-Moriya vector, and the superscript denotes the direction of propagation parallel to the interface, with respect to the global Oxyz system shown in Fig.2.1.

Figures 2.7, 2.8 and 2.9 that follow show the behavior of the relevant (for each configuration of the exchange effective field of the ferromagnet) Dzyaloshinskii-Moriya quantities as a function of the spin orbit coupling strength of the heavy metal layer, for different 3d-5d atomic orbital (on-site effective energy) offsets (with all the other free parameters of the model fixed). Few general

remarks are in the pipeline.

Juxtaposing Figs.2.7, 2.8 and 2.9 below, it is easily seen that along some directions of propagation, certain Dzyaloshinskii-Moriya components do vanish (i.e. both the intraband and the interband contribution to them vanishes), based on symmetry arguments that take into account the fact that the Oyz plane is a mirror plane of the A-B stacked bilayer structure. This then naturally leads to the observation that the Dzyaloshinskii-Moriya effect can drastically depend on the direction of propagation of the induced spin wave mode during a BLS experiment (in other words, it can well be a highly anisotropic effect if the symmetry is not lower enough).

Another thing that is also easily noticed (in Figs.2.7, 2.8 and 2.9) is that in general, a non-vanishing Dzyaloshinskii-Moriya component can have both intraband and interband contributions, which in some cases (for some components) can be comparable to each other. Loosely speaking, intraband contributions are possible if there is sufficient mixing between the conduction bands of the two materials when they are coupled to each other. However, careful inspection shows that the strongest Dzyaloshinskii-Moriya effect is achieved for the case in which the exchange effective field of the ferromagnet is oriented along the Ox axis (normal to the mirror plane Oyz) and the induced spin wave mode propagates along the Oy axis (parallel to the mirror plane Oyz), originating predominantly from interband contributions.

Proceeding a bit further, (from Figs.2.7, 2.8 and 2.9) it is noted that even though the proximity of the ferromagnetic metal to a metal with strong

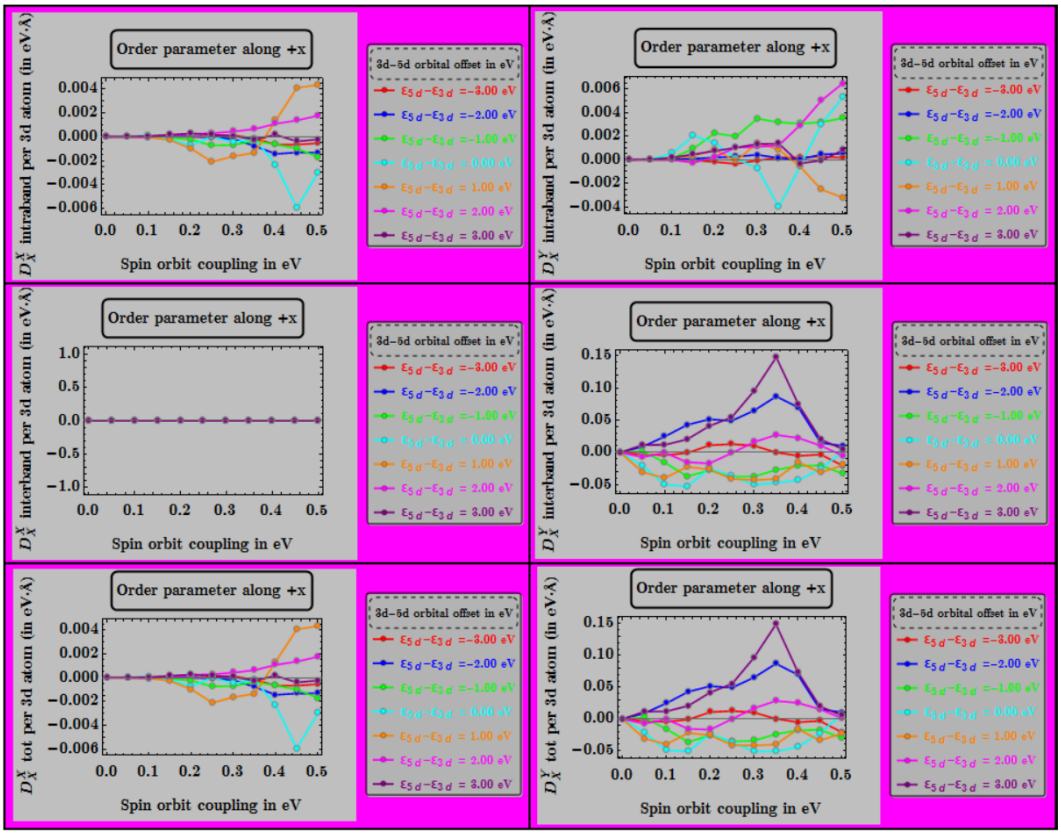

Figure 2.7: X-component of the Dzyaloshinskii-Moriya vector for propagation along the Ox axis (left column) and along the Oy axis (right column). From top to bottom, at each column, the intraband, the interband and the total (intraband+interband) contribution are shown. The only variable parameters are the spin orbit coupling of the heavy metal layer (abscissa), and the 3d-5d atomic orbital offset (adjacent inset). The configuration of the exchange effective field of the ferromagnet is given on top of each subfigure.

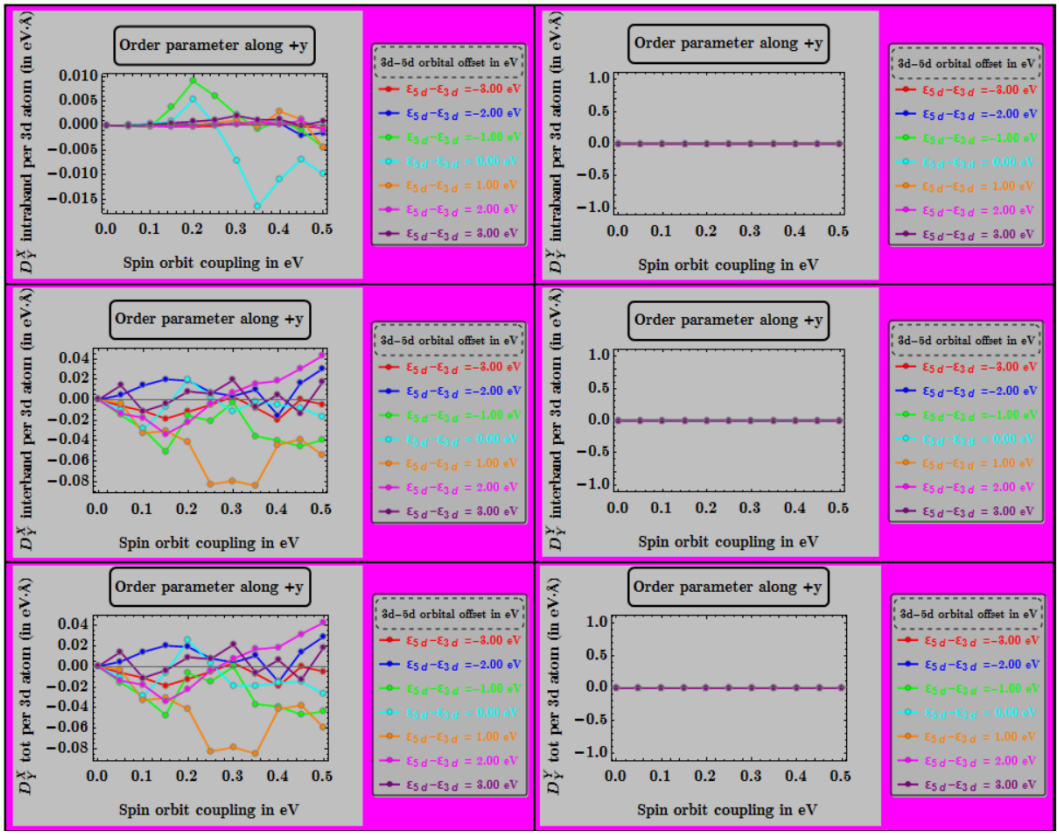

Figure 2.8: Y-component of the Dzyaloshinskii-Moriya vector for propagation along the Ox axis (left column) and along the Oy axis (right column). From top to bottom, at each column, the intraband, the interband and the total (intraband+interband) contribution are shown. The only variable parameters are the spin orbit coupling of the heavy metal layer (abscissa), and the 3d-5d atomic orbital offset (adjacent inset). The configuration of the exchange effective field of the ferromagnet is given on top of each subfigure.

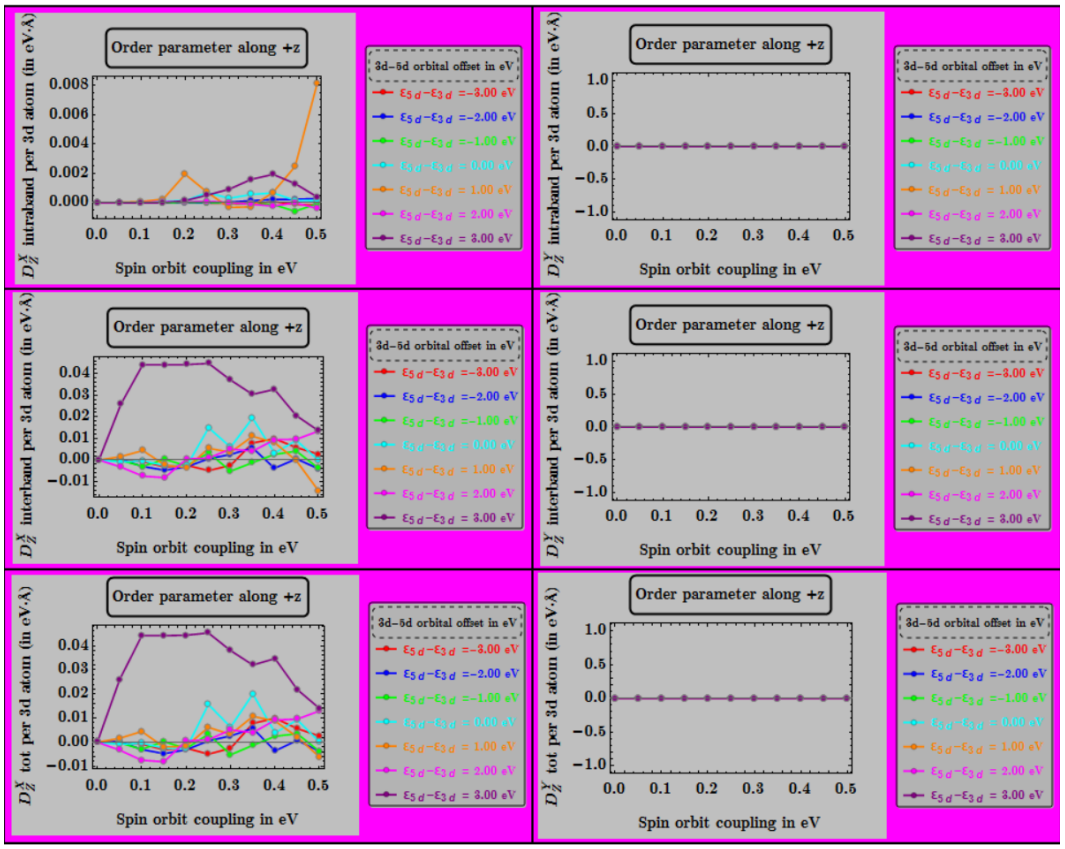

Figure 2.9: Z-component of the Dzyaloshinskii-Moriya vector for propagation along the Ox axis (left column) and along the Oy axis (right column). From top to bottom, at each column, the intraband, the interband and the total (intraband+interband) contribution are shown. The only variable parameters are the spin orbit coupling of the heavy metal layer (abscissa), and the 3d-5d atomic orbital offset (adjacent inset). The configuration of the exchange effective field of the ferromagnet is given on top of each subfigure.

spin orbit coupling certainly enhances the effectiveness of the indirect antisymmetric exchange interaction, the overall effect (both in magnitude and sign) can be dramatically affected by the 3d-5d atomic orbital (on-site effective energy) offset (see for instance the top left panel of Fig.2.8).

Last but not least, from Figs.2.7, 2.8 and 2.9, it is rather obvious that the dependence of the various Dzyaloshinskii-Moriya components on the spin orbit coupling of the heavy metal, generally speaking, is not perturbative (i.e. it doesn't seem to follow any specific power law). It would be interesting to check how the previous quantities behave in the limit in which the spin orbit coupling parameter is artificially switched off down to zero (for instance, if they vanish following some power law), but such a calculation is still in progress, and therefore it is not be presented here.

As already stated previously, in the developed model, for simplicity an ideal lattice match was assumed, as a consequence of which the deposited layer is stretched a bit (and in fact this affects a little bit the direct hopping from one magnetic atom to a neighboring magnetic atom), but in any case, for the effect we study here, the important hopping pathways are the ones from a first magnetic atom to an atom with strong spin orbit coupling and then to a second magnetic atom (let's call such a configuration "trimer configuration"). Saying so, the angle formed by the two separate bonds connecting each magnetic atom to a shared strong spin orbit scattering center (in a trimer configuration) is expected to play a role in the studied effect. Now, in order to check that, we artificially slid the deposited layer (seen as a triangular grid

of smaller spherical atoms at a mutual distance equal to the lattice constant dictated by the closely packed bigger spherical atoms of the substrate layer) along the negative y-direction, until the point K (top layer) of Fig.2.1 comes arbitrarily close to the point O (bottom layer), above it. Reminding the reader that c denotes the interplanar distance and a the common (to both layers) lattice constant, let us turn our attention to the Fig.2.10 below. Fig.2.10 shows the dependence of one component of the Dzyaloshinskii-Moriya vector (specifically the X-component) on the mis-stacking between the two layers, along the negative y direction (of the Oxyz global system). Specifically, starting from the A-B stacking, the two planar grids of hard sphere atoms are gradually mis-stacked (with the substrate layer fixed and the two families of hard sphere atoms always in one-to-one contact with each other), finally approaching arbitrarily close to the case of the A-A stacking (one layer right on top of the other), a process, which (within the hard sphere atomistic model employed here) can be described as a variation of the c/a ratio or equivalently of the 3d-5d-3d bond-to-bond angle. This variation is further shown for several different values of the 3d-5d atomic orbital (on-site effective energy) offset, with all the other free parameters of the model fixed. From Fig.2.10, it is easily seen that the 3d-5d-3d bond-to-bond angle certainly plays an important role since it can affect both the sign (the sign is related to the chirality of the long-wavelength spiraling structures observed in BLS experiments) and the magnitude of the various Dzyaloshinskii-Moriya components, however, in a non-monotonic way. In addition to the above, several other types of numerical

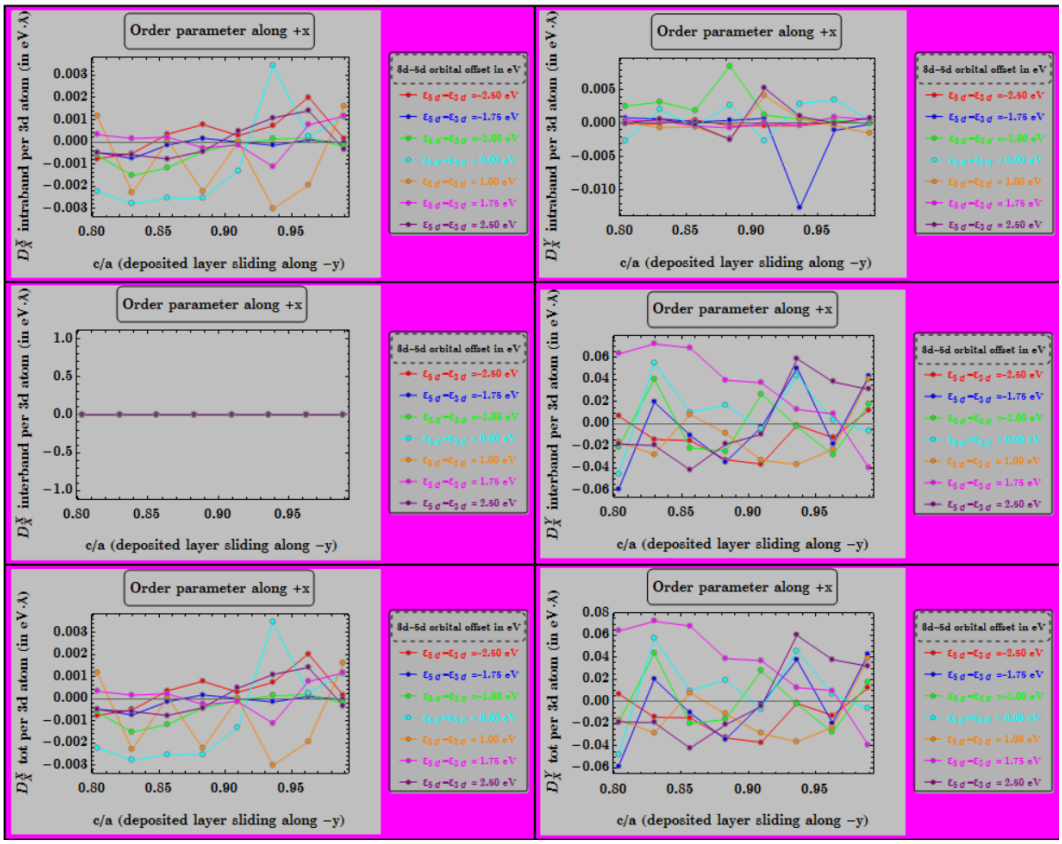

Figure 2.10: X-component of the Dzyaloshinskii-Moriya vector for propagation along the Ox axis (left column) and along the Oy axis (right column). From top to bottom, at each column, the intraband, the interband and the total (intraband+interband) contribution are shown. The only variable parameters are the dimensionless ratio $\frac{c}{a}$ (abscissa), and the 3d-5d atomic orbital offset (adjacent inset). The configuration of the exchange effective field of the ferromagnet is given on top of each subfigure.

calculations were performed, which will be briefly commented in the following lines. In one case, we fixed all the free parameters of the model and varied only the Fermi level position relevant to the 3d atomic orbital on-site effective energy, for different postulated values of the 3d-5d atomic orbital (on-site effective energy) offsets. A result of this calculation is shown in Figure 2.11 below, whereby the conclusion is that a variation of the Fermi level of the ferromagnet can, generally speaking, affect both the magnitude and the sign of the various Dzyaloshinskii-Moriya components.

In another numerical calculation, we introduced a spin orbit coupling for the magnetic atoms as well, choosing a representative realistic value for it, with all the free parameters of the model fixed, except for the 3d-5d atomic orbital (on-site effective energy) offset. The outcome of that calculation is that the atomic spin orbit coupling of the magnetic atoms has negligible effect on the studied phenomenon (which further vindicates the choice not to include it in the minimal set of free parameters of our developed model).

Last but not least, we performed a separate set of numerical calculations for the previously described bilayer heterostructure, this time assuming an ideal A-A type of stacking (instead of the A-B type of stacking considered so far). In those calculations, two only out of the minimal set of free parameters of the model were varied, with the rest kept fixed, and further, the calculation was repeated for several different pairs of variable (and on the other hand fixed) free parameters. The outcome of all those calculations was simply a vanishing Dzyaloshinskii-Moriya effect! The higher symmetry of the A-A type

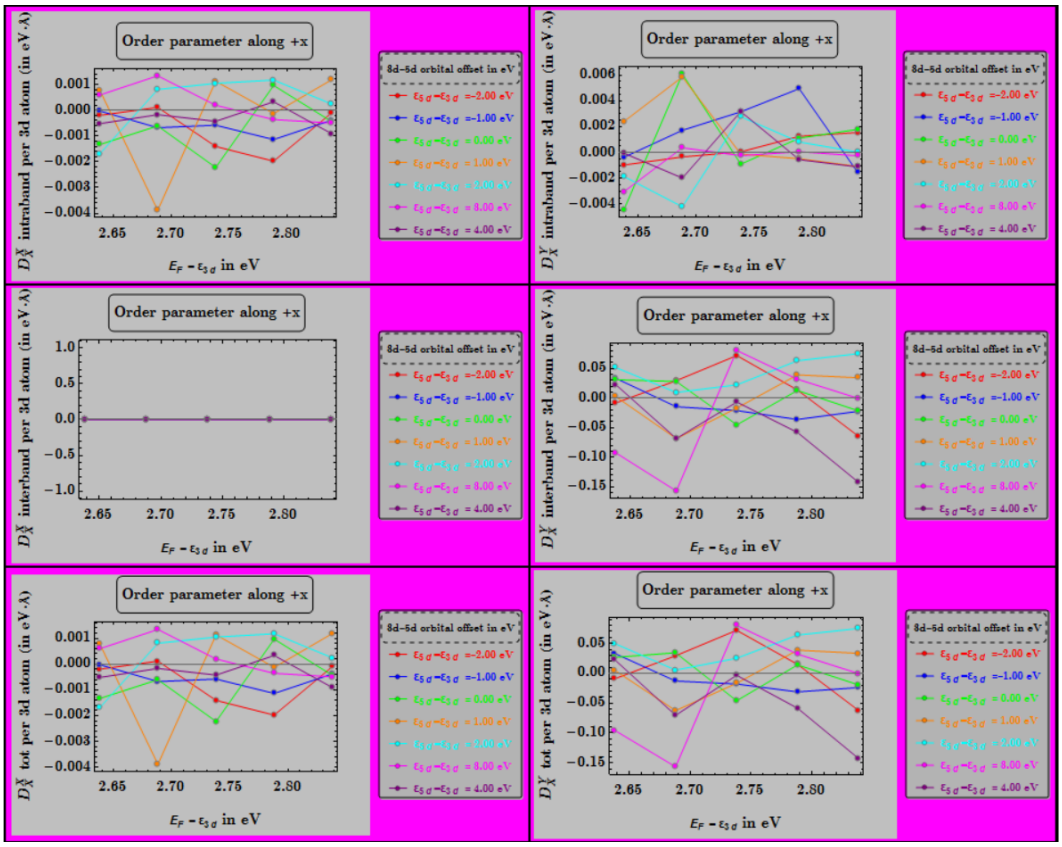

Figure 2.11: X-component of the Dzyaloshinskii-Moriya vector for propagation along the Ox axis (left column) and along the Oy axis (right column). From top to bottom, at each column, the intraband, the interband and the total (intraband+interband) contribution are shown. The only variable parameters are the Fermi level position with respect to the 3d atomic orbital on-site effective energy (abscissa), and the 3d-5d atomic orbital offset (adjacent inset). The configuration of the exchange effective field of the ferromagnet is given on top of each subfigure.

of stacking (compared to the A-B type of stacking), and specifically the six-fold rotational symmetry with the concomitant mirror planes, turns out to be the blocking factor for any indirect antisymmetric exchange interaction effect.

Concluding this chapter, we find that the indirect antisymmetric exchange interaction effect appearing in heavy metal/ferromagnetic metal heterostructures, is as much sensitive to the interfacial microstructure as to various important material parameters, the most significant of which, according to our analysis, seems to be the 3d-5d atomic orbital (on-site effective energy) offset. Having this in mind, a reliable comparison of the indirect Dzyaloshinskii-Moriya effect over heavy metal/ferromagnetic metal heterostructures consisting of different component materials, is a really tough venture, especially if there are less precisely known crucial band structure related parameters (on account of the fact that the heterostructures used in BLS experiments are not epitaxially grown, they have granularities and so on), given the fact that from one component material to the other several parameters change at once! Going beyond the two layers considered above, could maybe unsurprisingly modify the results for the Dzyaloshinskii-Moriya effect, signaling at the same time the fact that the overall effect might not necessarily be localized right at the interface, but such an analysis is beyond this work.

Chapter 3

Real space anatomy of the spin-orbit torques in heavy metal/ferromagnetic metal heterostructures

3.1 Motivation

The manipulation of the magnetic degrees of freedom of very small magnets by electrical means, initially of interest to a smaller scientific community, owing to its several promising technological applications, has by now evolved into a widespread, multifarious, well-established domain of research at the nanoscale. First such attempts, (Refs.[11, 13, 14, 40, 44, 59]) employed the transfer of spin angular momentum (via the exchange interaction) from an injected spin-polarized current to the order parameter of a secondary conducting ferromagnet, but in the meantime, an alternative mechanism was proposed where an electric field induced, spin-orbit coupling mediated emergent spin density (non-collinear with the magnetic order parameter) could interact (via the exchange interaction) with the order parameter of a thin conducting ferromagnet. This secondary mechanism is now at the heart of the domain of the so-called spin orbit torques (SOTs), which can experimentally be observed either in bulk systems or multilayer configurations that lack inversion symmetry (Refs.[18, 39]). In this chapter, using the bilayer structure and the concomitant

model (electronic) Hamiltonian developed previously (under all the approximations elaborated there), we attempt to shed light on the roles played by the various mechanisms suggested for the explanation of the experimentally measured SOTs. Despite the fact that the physics of the spin-orbit torques might not be exclusively dictated by purely interfacial mechanisms, relying on an interfacial model as a first attempt to understanding this complex phenomenon is believed to be a reasonable approach (though the structures used in experiments might be more complicated - they are actually three dimensional structures). Setting up an appropriate (but at the same time simple) transport formalism, we study various hopefully enlightening quantum-mechanical observables in terms of the same free parameters that were explored in the previous chapter.

3.2 Transport theory formalism

The transport theory employed in the following relies on an independent electron approximation, quite generally in the mean field sense, and uses a quantum kinetic equation for the single-particle density matrix to capture both intraband and interband contributions to the non-equilibrium average values of various quantum mechanical observables defined with reference to the bilayer structure detailed in the previous chapter. Any disorder effects are captured within the relaxation time approximation, with the relaxation time, from now on denoted as τ, treated as an additional independent parameter, assumed for simplicity the same for either intraband or interband contributions

(Ref.[42]). Saying so, the non-equilibrium (thermal and quantum mechanical) average value of a quantum mechanical operator $\hat{O}$, to lowest order (in the perturbation of the single-particle density matrix), is given by

$$\left\langle \hat{O} \right\rangle_{noneq} = Tr[\hat{\rho}^{(1)}\hat{O}] = \sum_{n\mathbf{k}} \langle n\mathbf{k}| \hat{\rho}^{(1)}\hat{O} |n\mathbf{k}\rangle =$$

$$\sum_{\mathbf{k}} \sum_{n,n'} \langle n\mathbf{k}| \hat{\rho}^{(1)} |n'\mathbf{k}\rangle \langle n'\mathbf{k}| \hat{O} |n\mathbf{k}\rangle = \sum_{\mathbf{k}} \sum_{n} \langle n\mathbf{k}| \hat{\rho}^{(1)} |n\mathbf{k}\rangle \langle n\mathbf{k}| \hat{O} |n\mathbf{k}\rangle + \tag{3.1}$$

$$\sum_{\mathbf{k}} \sum_{n,n'} \langle n\mathbf{k}| \hat{\rho}^{(1)} |n'\mathbf{k}\rangle \langle n'\mathbf{k}| \hat{O} |n\mathbf{k}\rangle (1 - \delta_{nn'})$$

where $\hat{\rho}^{(1)}$ denotes the linear response correction to the equilibrium (Bloch) band density matrix $\hat{\rho}^{(0)}$, given by

$$\hat{\rho}^{(0)} = \sum_{n\mathbf{k}} f^{(0)}_{n\mathbf{k}} |n\mathbf{k}\rangle \langle n\mathbf{k}| \tag{3.2}$$

where $|n\mathbf{k}\rangle$ are the eigenstates of the band Hamiltonian of Eq.(2.3) and $f^{(0)}_{n\mathbf{k}}$ is the equilibrium Fermi-Dirac distribution function. To proceed further, we need to calculate the matrix elements $\langle n\mathbf{k}| \hat{\rho}^{(1)} |n\mathbf{k}\rangle$ and $\langle n\mathbf{k}| \hat{\rho}^{(1)} |n'\mathbf{k}\rangle$ for the first order correction to the equilibrium density matrix.

Applying a weak static homogeneous electric field on the electronic system in general perturbs the single-particle eigenstates as well as the Fermi-Dirac distribution function. Even within the independent electron approximation, the inclusion of a weak static homogeneous electric field causes difficulties since such a term, on the one hand breaks the translational invariance of the electronic Hamiltonian, but on the other hand, because a uniform electric field grows linearly in space, as far as metals are concerned, it leads to surface

charge build ups that struggle to weaken the interior electric field. To bypass those issues, one can follow the procedure described in Ref.[30], or, recourse to a more elegant treatment of the applied homogeneous electric field, by modifying the quantum kinetic equation of the single-particle density matrix as below

$$\frac{\partial\hat{\rho}}{\partial t} = -\frac{i}{\hbar}[\hat{H},\hat{\rho}] + \frac{1}{\hbar}\nabla_{\mathbf{k}}\hat{\rho}\cdot e\mathbf{E} - \frac{\hat{\rho}-\hat{\rho}^{(0)}}{\tau} \tag{3.3}$$

where from now on $\hat{H}$ represents the band Hamiltonian of Eq.(2.3), e the magnitude of the elementary electric charge, $\mathbf{E}$ the applied homogeneous transport electric field, and further, any relaxation processes are collectively lumped into the rightmost term on the RHS of Eq.(3.3), treated within the relaxation time approximation, with τ denoting the relaxation time parameter (for simplicity chosen as $\mathbf{k}$- and band-independent as already stressed above). In the linear response regime, it is typical to decompose (to lowest order) the density matrix as $\hat{\rho} \approx \hat{\rho}^{(0)} + \hat{\rho}^{(1)}$, and in the steady state, that is of interest in the following, it is $\partial\hat{\rho}/\partial t = 0$, as a result of which one gets

$$\frac{\hat{\rho}^{(1)}}{\tau\hbar^{-1}} \approx -i[\hat{H},\ \hat{\rho}^{(1)}] + \nabla_{\mathbf{k}}\hat{\rho}^{(0)}\cdot e\mathbf{E} \tag{3.4}$$

where the term $\nabla_{\mathbf{k}}\hat{\rho}^{(1)}\cdot e\mathbf{E}$ was neglected being of higher order in the applied electric field which is assumed weak. Considering any two general eigenstates $|m\rangle$ and $|m'\rangle$ of the band Hamiltonian of Eq.(2.3), from the last equation we get

$$\langle m|\,\frac{\hat{\rho}^{(1)}}{\tau\hbar^{-1}}\,|m'\rangle \approx \frac{i\,\langle m|\,\nabla_{\mathbf{k}}\hat{\rho}^{(0)}\,|m'\rangle}{(\varepsilon_{m'}-\varepsilon_m)+i\hbar\tau^{-1}}\cdot e\mathbf{E} \tag{3.5}$$

To calculate the matrix element $\langle m|\,\nabla_{\mathbf{k}}\hat{\rho}^{(0)}\,|m'\rangle$ on the RHS of Eq.(3.5), one needs to use the definition of Eq.(3.2) in conjunction with the following formulae

$$\begin{aligned}\frac{\partial}{\partial\mathbf{k}}\,|n\mathbf{k}\rangle &= \sum_{n'\neq n}\frac{\langle n'\mathbf{k}|\nabla_{\mathbf{k}}\hat{H}(\mathbf{k})|n\mathbf{k}\rangle}{(\varepsilon_{n\mathbf{k}}-\varepsilon_{n'\mathbf{k}})}\,|n'\mathbf{k}\rangle \\ \frac{\partial}{\partial\mathbf{k}}\,\langle n\mathbf{k}| &= \sum_{n'\neq n}\frac{\langle n\mathbf{k}|\nabla_{\mathbf{k}}\hat{H}^{\dagger}(\mathbf{k})|n'\mathbf{k}\rangle}{(\varepsilon_{n\mathbf{k}}-\varepsilon_{n'\mathbf{k}})}\,\langle n'\mathbf{k}|\end{aligned} \tag{3.6}$$

where the summations run over different bands and are subject to the constraint shown explicitly. Doing so, one finally finds

$$\begin{aligned}&\langle n\mathbf{k}|\,\hat{\rho}^{(1)}\,|n\mathbf{k}\rangle \approx -\beta f^{(0)}_{n\mathbf{k}}\left(1-f^{(0)}_{n\mathbf{k}}\right)\langle n\mathbf{k}|\,\nabla_{\mathbf{k}}\hat{H}(\mathbf{k})\,|n\mathbf{k}\rangle\cdot\tfrac{e\mathbf{E}}{\hbar\tau^{-1}} \\ &\langle n\mathbf{k}|\,\hat{\rho}^{(1)}\,|n'\mathbf{k}\rangle \approx (1-\delta_{nn'})\left(\tfrac{f^{(0)}_{n\mathbf{k}}-f^{(0)}_{n'\mathbf{k}}}{\varepsilon_{n\mathbf{k}}-\varepsilon_{n'\mathbf{k}}}\right)\langle n\mathbf{k}|\,\nabla_{\mathbf{k}}\hat{H}(\mathbf{k})\,|n'\mathbf{k}\rangle\cdot \\ &\cdot\left(\tfrac{ie\mathbf{E}}{(\varepsilon_{n'\mathbf{k}}-\varepsilon_{n\mathbf{k}})+i\hbar\tau^{-1}}\right)\end{aligned} \tag{3.7}$$

From Eqs.(3.1) and (3.7), the intraband and the interband contributions to the non-equilibrium average value of a quantum mechanical operator $\hat{O}$ are given by

$$\begin{aligned}&\left\langle\hat{O}\right\rangle^{intra}_{noneq} = \sum_{\mathbf{k}}\sum_{n}\langle n\mathbf{k}|\,\hat{\rho}^{(1)}\,|n\mathbf{k}\rangle\,\langle n\mathbf{k}|\,\hat{O}\,|n\mathbf{k}\rangle = \\ &-\tfrac{\beta e\tau}{\hbar}\sum_{n,\mathbf{k}} f^{(0)}_{n\mathbf{k}}\left(1-f^{(0)}_{n\mathbf{k}}\right)\langle n\mathbf{k}|\,\hat{O}\,|n\mathbf{k}\rangle\,\langle n\mathbf{k}|\,\nabla_{\mathbf{k}}\hat{H}(\mathbf{k})\,|n\mathbf{k}\rangle\cdot\mathbf{E} \\ &\left\langle\hat{O}\right\rangle^{inter}_{noneq} = \sum_{\mathbf{k}}\sum_{n,n'}\langle n\mathbf{k}|\,\hat{\rho}^{(1)}\,|n'\mathbf{k}\rangle\,\langle n'\mathbf{k}|\,\hat{O}\,|n\mathbf{k}\rangle\,(1-\delta_{nn'}) = \\ &ie\sum_{\mathbf{k}}\sum_{n,n'}(1-\delta_{nn'})\left(\tfrac{f^{(0)}_{n\mathbf{k}}-f^{(0)}_{n'\mathbf{k}}}{\varepsilon_{n\mathbf{k}}-\varepsilon_{n'\mathbf{k}}}\right)\langle n'\mathbf{k}|\,\hat{O}\,|n\mathbf{k}\rangle\,\tfrac{\langle n\mathbf{k}|\nabla_{\mathbf{k}}\hat{H}(\mathbf{k})|n'\mathbf{k}\rangle\cdot\mathbf{E}}{(\varepsilon_{n'\mathbf{k}}-\varepsilon_{n\mathbf{k}})+i\hbar\tau^{-1}}\end{aligned} \tag{3.8}$$

whereas, the equilibrium (thermal and quantum-mechanical) average of the operator is given by

$$\left\langle \hat{O} \right\rangle_{eq} = Tr[\hat{\rho}^{(0)}\hat{O}] = \sum_{n\mathbf{k}} f^{(0)}_{n\mathbf{k}} \left\langle n\mathbf{k} \right| \hat{O} \left| n\mathbf{k} \right\rangle \tag{3.9}$$

where $\beta = 1/k_B T$, with T denoting the temperature.

Concluding this section, we mention an important property of the interband contribution to the non-equilibrium value of an operator $\hat{O}$. From the second equation of Eq.(3.8), it is

$$\left\langle \hat{O} \right\rangle^{inter}_{\tau\to\infty} = \sum_{\mathbf{k}} \sum_{n,n'} \left\{ (1-\delta_{nn'}) \left(\frac{f^{(0)}_{n\mathbf{k}} - f^{(0)}_{n'\mathbf{k}}}{\varepsilon_{n\mathbf{k}} - \varepsilon_{n'\mathbf{k}}} \right) \left\langle n'\mathbf{k} \right| \hat{O} \left| n\mathbf{k} \right\rangle \left\langle n\mathbf{k} \right| \nabla_{\mathbf{k}} H(\mathbf{k}) \left| n'\mathbf{k} \right\rangle \cdot \right.$$

$$\left. \cdot \frac{ie\mathbf{E}}{(\varepsilon_{n'\mathbf{k}} - \varepsilon_{n\mathbf{k}})} \right\} \tag{3.10}$$

If the Bloch band Hamiltonian is time reversal invariant then, following the derivation given in Ref.[6] p.38-39 (or the Ref.[56], p.197), the following conditions are valid

$$\begin{aligned} & TH(\mathbf{k})T^{-1} = H(-\mathbf{k}), \\ & T\left|n\mathbf{k}\right\rangle = \left|n_1, -\mathbf{k}\right\rangle, \quad \left\langle n\mathbf{k}\right| T^{-1} = \left\langle n_1, -\mathbf{k}\right|, \quad \varepsilon_{n\mathbf{k}} = \varepsilon_{n_1,-\mathbf{k}}, \\ & T\left|n'\mathbf{k}\right\rangle = \left|n_2, -\mathbf{k}\right\rangle, \quad \left\langle n'\mathbf{k}\right| T^{-1} = \left\langle n_2, -\mathbf{k}\right|, \quad \varepsilon_{n'\mathbf{k}} = \varepsilon_{n_2,-\mathbf{k}} \end{aligned} \tag{3.11}$$

For an operator $\hat{O}$ it is then ($\mathbf{k}$ is also inverted)

$$\left\langle T^{-1}\hat{O}T\right\rangle_{\tau\to\infty}^{inter}=\sum_{\mathbf{k}}\sum_{n,n'}\left\{(1-\delta_{nn'})\left(\frac{f_{n\mathbf{k}}^{(0)}-f_{n'\mathbf{k}}^{(0)}}{\varepsilon_{n\mathbf{k}}-\varepsilon_{n'\mathbf{k}}}\right)\langle n'\mathbf{k}|\,T^{-1}\hat{O}T\,|n\mathbf{k}\rangle\times\right.$$

$$\left.\langle n\mathbf{k}|\,T^{-1}T\nabla_{\mathbf{k}}H(\mathbf{k})T^{-1}T\,|n'\mathbf{k}\rangle\cdot\frac{ie\mathbf{E}}{(\varepsilon_{n'\mathbf{k}}-\varepsilon_{n\mathbf{k}})}\right\}=-\sum_{\mathbf{k}}\sum_{n,n'}\left\{(1-\delta_{nn'})\left(\frac{f_{n\mathbf{k}}^{(0)}-f_{n'\mathbf{k}}^{(0)}}{\varepsilon_{n\mathbf{k}}-\varepsilon_{n'\mathbf{k}}}\right)\right.$$

$$\left.\times\langle n'\mathbf{k}|\,T^{-1}\hat{O}T\,|n\mathbf{k}\rangle\langle n\mathbf{k}|\,T^{-1}\nabla_{\mathbf{k}}H(-\mathbf{k})T\,|n'\mathbf{k}\rangle\cdot\frac{ie\mathbf{E}}{(\varepsilon_{n'\mathbf{k}}-\varepsilon_{n\mathbf{k}})}\right\}=$$

$$-\sum_{\mathbf{k}}\sum_{n_1,n_2}\left\{(1-\delta_{n_1n_2})\left(\frac{f_{n_1,-\mathbf{k}}^{(0)}-f_{n_2,-\mathbf{k}}^{(0)}}{\varepsilon_{n_1,-\mathbf{k}}-\varepsilon_{n_2,-\mathbf{k}}}\right)\langle n_2,-\mathbf{k}|\,\hat{O}\,|n_1,-\mathbf{k}\rangle\times\right.$$

$$\left.\langle n_1,-\mathbf{k}|\,\nabla_{\mathbf{k}}H(-\mathbf{k})\,|n_2,-\mathbf{k}\rangle\cdot\frac{ie\mathbf{E}}{(\varepsilon_{n_2,-\mathbf{k}}-\varepsilon_{n_1,-\mathbf{k}})}\right\}$$

and performing in the last equation the substitutions $\mathbf{k}\to-\mathbf{k},\ n_1\to n,\ n_2\to n'$, we get

$$\left\langle T^{-1}\hat{O}T\right\rangle_{\tau\to\infty}^{inter}=-\sum_{\mathbf{k}}\sum_{n,n'}\left\{(1-\delta_{nn'})\left(\frac{f_{n\mathbf{k}}^{(0)}-f_{n'\mathbf{k}}^{(0)}}{\varepsilon_{n\mathbf{k}}-\varepsilon_{n'\mathbf{k}}}\right)\langle n'\mathbf{k}|\,\hat{O}\,|n\mathbf{k}\rangle\times\right.$$

$$\left.\langle n\mathbf{k}|\,\nabla_{-\mathbf{k}}H(\mathbf{k})\,|n'\mathbf{k}\rangle\cdot\frac{ie\mathbf{E}}{(\varepsilon_{n'\mathbf{k}}-\varepsilon_{n\mathbf{k}})}\right\}=\sum_{\mathbf{k}}\sum_{n,n'}\left\{(1-\delta_{nn'})\left(\frac{f_{n\mathbf{k}}^{(0)}-f_{n'\mathbf{k}}^{(0)}}{\varepsilon_{n\mathbf{k}}-\varepsilon_{n'\mathbf{k}}}\right)\times\right. \quad (3.12)$$

$$\left.\langle n'\mathbf{k}|\,\hat{O}\,|n\mathbf{k}\rangle\,\langle n\mathbf{k}|\,\nabla_{\mathbf{k}}H(\mathbf{k})\,|n'\mathbf{k}\rangle\cdot\frac{ie\mathbf{E}}{(\varepsilon_{n'\mathbf{k}}-\varepsilon_{n\mathbf{k}})}\right\}=\left\langle\hat{O}\right\rangle_{\tau\to\infty}^{inter}$$

Now, if an operator $\hat{O}$ changes signature under the time reversal operation (to follow the terminology of Ref.[51], p.358), i.e. $T\hat{O}T^{-1}=T^{-1}\hat{O}T=-\hat{O}$, then from Eq.(3.12) it is

$$\left\langle T^{-1}\hat{O}T\right\rangle_{\tau\to\infty}^{inter}=\left\langle\hat{O}\right\rangle_{\tau\to\infty}^{inter}\Rightarrow-\left\langle\hat{O}\right\rangle_{\tau\to\infty}^{inter}=\left\langle\hat{O}\right\rangle_{\tau\to\infty}^{inter}\Rightarrow\left\langle\hat{O}\right\rangle_{\tau\to\infty}^{inter}=0 \quad (3.13)$$

The condition of Eq.(3.13), whenever appropriately applicable, was employed as a check for our numerical results.

3.3 Real space anatomy of the spin-orbit torques - Quantum mechanical observables

In this section, we define an appropriate set of real space quantum mechanical operators for the bilayer structure at issue, and study their observable behavior by operating with them on the electronic quasiparticle eigenstates. The aforementioned procedure takes place without and with an applied transport electric field, for various postulated configurations of the exchange effective field of the ferromagnetic metal, by (artificially) varying at the same time crucial (electronic) band structure parameters, with a view to shedding light on the microscopic mechanisms underlying the spin-orbit torques (SOTs) appearing in multilayered metallic structures with structural inversion asymmetry. As expected, the starting point is the A-B stacked bilayer structure elaborated previously, as well as the three different translationally invariant (postulated) configurations for the exchange effective field of the ferromagnet shown in Fig.2.6.

So far, three different microscopic mechanisms have been proposed to explain spin-orbit torque related results in structures that lack inversion symmetry (either bulk systems such as (Ga,Mn)As with the zinc-blende structure Refs.[10, 33], or multilayered systems such as MgO/CoFeB/Ta, Mn/W(001), O/Co/Pt(111) and so on, Refs.[28, 36, 58]). The first one suggests the pumping of spins to the ferromagnet driven by the spin current due to the spin Hall effect (i.e. the conversion of an unpolarized charge current into a chargeless pure spin current transverse to the former) in the heavy metal, and bears

the name "inverse spin pumping effect" (Refs.[18, 62]). The second suggested mechanism ascribes SOTs to current induced nonequilibrium spin accumulation along the so-called Rashba spin-orbit field (Ref.[43], and for the definition of the Rashba SO field Ref.[40] p.872 is suggested). Finally, a third mechanism was proposed by H.Kurebayashi et.al (Refs.[33, 39]) who investigated the current-induced ferromagnetic resonance in a single layer of strained dilute magnetic semiconductor (Ga,Mn)As (deposited on an intrinsic GaAs substrate), where spin-orbit torque effects can emerge due to the lack of inversion symmetry, and further, any spin Hall effect contribution is eliminated by design. Kurebayashi et.al. observed a sizable anti-damping SOT, which attributed to the quantum-mechanical Berry curvature effect, usually thought of as a local magnetic field associated with the geometric phase, acting in the momentum space.

In this study, the main focus is on intrinsic contributions to the spin-orbit torque effects, as opposed to extrinsic contributions, such as those originating from side-jump scattering, skew scattering, and maybe other relaxation mechanisms, with the latter collectively captured by the relaxation time parameter discussed previously (this approximation of course requires refinement at a later stage). Saying so, let us now move on to defining a set of useful quantum mechanical observables that will hopefully help us shed more light on the microscopic origin of the electric field induced (with both layers immersed into the applied electric field) spin orbit torques. Particularly, let me now give an idea of what is going on in this approach, using a less technical but more

vivid language. In the bilayer system at issue, well, we have all those (highly) itinerant quasiparticles, but, we want to describe an observable property related to them at some point (or points) of the real space - how can we do that? The quasiparticle wavefunction is a non-local entity, actually extended over the whole bilayer, therefore, by itself it cannot do our job! Let us see if we can define some sort of real space local operators. Indeed we can! Now, since we attempted to define some sort of real space local operators, I guess, the (temporal) rate of change of those local operators should be dictated by some appropriately defined local Hamiltonian. Going a step further, since we want to describe a quasiparticle property at some point of the real space (e.g. some lattice site), the employed local Hamiltonian should be motivated by what else but the electronic quasiparticle Hamiltonian. Loosely speaking, this is the idea behind the formalism developed in this chapter, and please allow us now to give flesh and bones to it! In the following, the global coordinate system Oxyz shown in Fig. 2.1 is employed, and the SI units are employed everywhere. The hermiticity of the various defined quantum mechanical operators is easily verified (and this step is skipped in the following, but there has been a cross-check during the derivation process). For completeness, it is reminded that the effective Hilbert space used for the calculation of the observables defined in the following is that elaborated below Eq.(2.3).

3.3.1 Layer resolved spin accumulation

At the i-th lattice site of the ferromagnetic (the deposited) layer one can define a local spin accumulation operator as

$$\hat{\mathbf{S}}_i = \hat{S}_{ix}\hat{\mathbf{e}}_x + \hat{S}_{iy}\hat{\mathbf{e}}_y + \hat{S}_{iz}\hat{\mathbf{e}}_z \tag{3.14}$$

with the unit vectors defined with respect to the global Oxyz system of reference, and further, a total spin accumulation operator for the ferromagnetic layer as

$$\begin{aligned}\hat{\mathbf{S}}_{FM} = \sum_i \hat{\mathbf{S}}_i = \left[\sum_i \hat{S}_{ix}\right]\hat{\mathbf{e}}_x + \left[\sum_i \hat{S}_{iy}\right]\hat{\mathbf{e}}_y + \left[\sum_i \hat{S}_{iz}\right]\hat{\mathbf{e}}_z = \\ \left[\frac{\hbar}{2}\sum_{i\gamma}\left(\tilde{c}^{\dagger}_{i\gamma\uparrow}\tilde{c}_{i\gamma\downarrow} + \tilde{c}^{\dagger}_{i\gamma\downarrow}\tilde{c}_{i\gamma\uparrow}\right)\right]\hat{\mathbf{e}}_x + \left[\frac{\hbar}{2i}\sum_{i\gamma}\left(\tilde{c}^{\dagger}_{i\gamma\uparrow}\tilde{c}_{i\gamma\downarrow} - \tilde{c}^{\dagger}_{i\gamma\downarrow}\tilde{c}_{i\gamma\uparrow}\right)\right]\hat{\mathbf{e}}_y + \\ \left[\frac{\hbar}{2}\sum_{i\gamma}\left(\tilde{c}^{\dagger}_{i\gamma\uparrow}\tilde{c}_{i\gamma\uparrow} - \tilde{c}^{\dagger}_{i\gamma\downarrow}\tilde{c}_{i\gamma\downarrow}\right)\right]\hat{\mathbf{e}}_z\end{aligned} \tag{3.15}$$

where the summation over i is summation over the magnetic lattice sites only. Fourier Transforming (FT) the last equation we get

$$\begin{aligned}\hat{\mathbf{S}}_{FM} = \left[\frac{\hbar}{2}\sum_{\mathbf{k},\gamma}\left(\tilde{c}^{\dagger}_{\mathbf{k}\gamma\uparrow}\tilde{c}_{\mathbf{k}\gamma\downarrow} + \tilde{c}^{\dagger}_{\mathbf{k}\gamma\downarrow}\tilde{c}_{\mathbf{k}\gamma\uparrow}\right)\right]\hat{\mathbf{e}}_x + \left[\frac{\hbar}{2i}\sum_{\mathbf{k},\gamma}\left(\tilde{c}^{\dagger}_{\mathbf{k}\gamma\uparrow}\tilde{c}_{\mathbf{k}\gamma\downarrow} - \tilde{c}^{\dagger}_{\mathbf{k}\gamma\downarrow}\tilde{c}_{\mathbf{k}\gamma\uparrow}\right)\right]\hat{\mathbf{e}}_y + \\ \left[\frac{\hbar}{2}\sum_{\mathbf{k},\gamma}\left(\tilde{c}^{\dagger}_{\mathbf{k}\gamma\uparrow}\tilde{c}_{\mathbf{k}\gamma\uparrow} - \tilde{c}^{\dagger}_{\mathbf{k}\gamma\downarrow}\tilde{c}_{\mathbf{k}\gamma\downarrow}\right)\right]\hat{\mathbf{e}}_z\end{aligned} \tag{3.16}$$

Working in a similar way for the heavy metal (substrate) layer, at the end we get

$$\hat{\mathbf{S}}_{HM} = \left[\frac{\hbar}{2}\sum_{\mathbf{k},\gamma}\left(c^{\dagger}_{\mathbf{k}\gamma\uparrow}c_{\mathbf{k}\gamma\downarrow} + c^{\dagger}_{\mathbf{k}\gamma\downarrow}c_{\mathbf{k}\gamma\uparrow}\right)\right]\hat{\mathbf{e}}_x + \left[\frac{\hbar}{2i}\sum_{\mathbf{k},\gamma}\left(c^{\dagger}_{\mathbf{k}\gamma\uparrow}c_{\mathbf{k}\gamma\downarrow} - c^{\dagger}_{\mathbf{k}\gamma\downarrow}c_{\mathbf{k}\gamma\uparrow}\right)\right]\hat{\mathbf{e}}_y + \left[\frac{\hbar}{2}\sum_{\mathbf{k},\gamma}\left(c^{\dagger}_{\mathbf{k}\gamma\uparrow}c_{\mathbf{k}\gamma\uparrow} - c^{\dagger}_{\mathbf{k}\gamma\downarrow}c_{\mathbf{k}\gamma\downarrow}\right)\right]\hat{\mathbf{e}}_z \tag{3.17}$$

The overall equilibrium spin accumulation (i.e. without the applied transport electric field) within the ferromagnetic and the heavy metal layer are found by substituting the operators of Eqs.(3.16) and (3.17) respectively in Eq.(3.9). The overall non-equilibrium spin accumulation within the ferromagnetic and the heavy metal layer, separating intraband and interband contributions, are found by substituting the operators of Eqs.(3.16) and (3.17) respectively in Eqs.(3.8). The difference between the non-equilibrium and the corresponding equilibrium spin accumulation defines the so-called "induced spin accumulation" (for each layer). However, it is customary to talk about the induced spin accumulation per site or per atom, as a result of which, each layer-resolved induced spin accumulation is divided by the number of atoms (lattice sites) of the layer at issue.

3.3.2 Anomalous Hall effect related charge and spin current density operators

In order to investigate any anomalous Hall effects (i.e. no applied magnetic field) in the bilayer structure at issue, we define in the following an

appropriate set of (normal and anomalous Hall effect related) charge and spin current density operators for the studied A-B stacked bilayer structure. Their equilibrium (without any applied electric field) values are respectively given by (based on Eq.(3.9))

$$\begin{aligned}
&\left\langle \hat{j}_\alpha \right\rangle_{eq} = Tr[\hat{\rho}^{(0)}\hat{j}_\alpha] = \sum_{n\mathbf{k}} \langle n\mathbf{k}|\, \hat{\rho}^{(0)}\hat{j}_\alpha \,|n\mathbf{k}\rangle = \\
&(-\tfrac{e}{V}) \sum_{n\mathbf{k}} f^{(0)}_{n\mathbf{k}} \langle n\mathbf{k}|\, \hat{v}_\alpha \,|n\mathbf{k}\rangle, \quad \alpha = \{x, y\} \\
&\left\langle \hat{Q}^\mu_\alpha \right\rangle_{eq} = Tr[\hat{\rho}^{(0)}\hat{Q}^\mu_\alpha] = \sum_{n\mathbf{k}} \langle n\mathbf{k}|\, \hat{\rho}^{(0)}\hat{Q}^\mu_\alpha \,|n\mathbf{k}\rangle = \\
&\tfrac{1}{V} \sum_{n\mathbf{k}} f^{(0)}_{n\mathbf{k}} \langle n\mathbf{k}|\, \hat{S}_\mu \hat{v}_\alpha \,|n\mathbf{k}\rangle, \quad \mu = \{x, y, z\}, \quad \alpha = \{x, y\}
\end{aligned} \tag{3.18}$$

where the α-th component of the Bloch/band velocity operator of the bilayer is defined by $\hat{v}_\alpha = \frac{1}{\hbar}\frac{\partial \hat{\mathcal{H}}_e(\mathbf{k})}{\partial k_\alpha}$, and further, $\hat{S}_\mu = \frac{\hbar}{2}\hat{\sigma}_\mu$ is the μ-th component of the bilayer spin operator (defined in terms of the μ-th Pauli-type spin operator $\hat{\sigma}_\mu$). V denotes the volume of the bilayer structure. The non-equilibrium values of the above operators, separating intraband and interband contributions (based on Eqs.(3.8)), are respectively given by

$$\begin{aligned}
&\left\langle \hat{j}_\alpha \right\rangle^{intra}_{noneq} = \tfrac{1}{V} \sum_\beta \left\{ -\tfrac{e^2}{\hbar^2}\tau \sum_{\mathbf{k}} \sum_n \tfrac{\partial f^{(0)}_{n\mathbf{k}}}{\partial \varepsilon_{n\mathbf{k}}} \langle n\mathbf{k}|\, \tfrac{\partial \hat{\mathcal{H}}_e(\mathbf{k})}{\partial k_\alpha} \,|n\mathbf{k}\rangle \langle n\mathbf{k}|\, \tfrac{\partial \hat{\mathcal{H}}_e(\mathbf{k})}{\partial k_\beta} \,|n\mathbf{k}\rangle \right\} E_\beta, \\
&\left\langle \hat{j}_\alpha \right\rangle^{inter}_{noneq} = \tfrac{1}{V} \sum_\beta \left\{ -i\tfrac{e^2}{\hbar} \sum_{\mathbf{k}} \sum_{n,n'} (1 - \delta_{nn'}) \left(\tfrac{f^{(0)}_{n\mathbf{k}} - f^{(0)}_{n'\mathbf{k}}}{\varepsilon_{n\mathbf{k}} - \varepsilon_{n'\mathbf{k}}} \right) \left(\tfrac{1}{(\varepsilon_{n'\mathbf{k}} - \varepsilon_{n\mathbf{k}}) + i\hbar\tau^{-1}} \right) \times \right. \\
&\qquad \left. \langle n'\mathbf{k}|\, \tfrac{\partial \hat{\mathcal{H}}_e(\mathbf{k})}{\partial k_\alpha} \,|n\mathbf{k}\rangle \langle n\mathbf{k}|\, \tfrac{\partial \hat{\mathcal{H}}_e(\mathbf{k})}{\partial k_\beta} \,|n'\mathbf{k}\rangle \right\} E_\beta
\end{aligned} \tag{3.19}$$

and

$$\left\langle \hat{Q}^{\mu}_{\alpha} \right\rangle^{intra}_{noneq} = \frac{1}{V} \sum_{\beta} \left\{ \frac{e\tau}{2\hbar} \sum_{\mathbf{k}} \sum_{n} \frac{\partial f^{(0)}_{n\mathbf{k}}}{\partial \varepsilon_{n\mathbf{k}}} \left\langle n\mathbf{k} \right| \hat{\sigma}_{\mu} \frac{\partial \hat{\mathcal{H}}_{e}(\mathbf{k})}{\partial k_{\alpha}} \left| n\mathbf{k} \right\rangle \left\langle n\mathbf{k} \right| \frac{\partial \hat{\mathcal{H}}_{e}(\mathbf{k})}{\partial k_{\beta}} \left| n\mathbf{k} \right\rangle \right\} E_{\beta},$$

$$\left\langle \hat{Q}^{\mu}_{\alpha} \right\rangle^{inter}_{noneq} = \frac{1}{V} \sum_{\beta} \left\{ \frac{ie}{2} \sum_{\mathbf{k}} \sum_{n,n'} (1 - \delta_{nn'}) \left(\frac{f^{(0)}_{n\mathbf{k}} - f^{(0)}_{n'\mathbf{k}}}{\varepsilon_{n\mathbf{k}} - \varepsilon_{n'\mathbf{k}}} \right) \left(\frac{1}{(\varepsilon_{n'\mathbf{k}} - \varepsilon_{n\mathbf{k}}) + i\hbar\tau^{-1}} \right) \times \right.$$

$$\left. \left\langle n'\mathbf{k} \right| \hat{\sigma}_{\mu} \frac{\partial \hat{\mathcal{H}}_{e}(\mathbf{k})}{\partial k_{\alpha}} \left| n\mathbf{k} \right\rangle \left\langle n\mathbf{k} \right| \frac{\partial \hat{\mathcal{H}}_{e}(\mathbf{k})}{\partial k_{\beta}} \left| n'\mathbf{k} \right\rangle \right\} E_{\beta} \tag{3.20}$$

where E_{β} denotes the β-th component of the parallel to the interface applied electric field, and also, $\alpha, \beta = \{x, y\}$. The unit of the charge current density operator is $\frac{Coulomb}{sec \times area}$, whereas the unit of the various component spin current density operators is $\frac{eV}{area}$.

3.3.3 Rate of spin accumulation in the ferromagnetic layer

The rate of spin accumulation at the i-th lattice site of the ferromagnetic layer is given by

$$\hat{\tau}^{\mu}_{i} = \frac{d\hat{S}^{\mu}_{i}}{dt} = \frac{1}{i\hbar} \left[\hat{S}^{\mu}_{i}, \hat{\mathcal{H}}_{e} \right] = \frac{1}{i\hbar} \left[\hat{S}^{\mu}_{i}, \sum_{j} \hat{H}_{j} \right] = \frac{1}{i\hbar} \sum_{j} \left[\hat{S}^{\mu}_{i}, \hat{H}_{j} \right] = \frac{1}{i\hbar} \left[\hat{S}^{\mu}_{i}, \hat{H}_{i} \right], \ \forall i, \ \mu = \{x, y, z\} \tag{3.21}$$

where in the third equality on the RHS we decomposed the electronic quasiparticle Hamiltonian into appropriately defined local (single-site) contributions. In addition, the overall rate of spin accumulation within the ferromagnetic layer is given by

$$\hat{\tau}^{\mu} = \sum_{i} \hat{\tau}^{\mu}_{i} = \sum_{i} \frac{d\hat{S}^{\mu}_{i}}{dt} = \frac{1}{i\hbar} \sum_{i} \left[\hat{S}^{\mu}_{i}, \hat{\mathcal{H}}_{e} \right] \Rightarrow \frac{d\hat{S}^{\mu}}{dt} = \frac{1}{i\hbar} \left[\hat{S}^{\mu}, \hat{\mathcal{H}}_{e} \right] \tag{3.22}$$

where the Hamiltonian $\hat{\mathcal{H}}_e$ of the electronic quasiparticle system is given by Eq.(2.1). The part of $\hat{\mathcal{H}}_e$ that is needed for the calculation of the commutator on the RHS of Eq.(3.21) is given by

$$\begin{aligned}
\hat{H}_i = & \sum_{\gamma\sigma} \tilde{\varepsilon}_{\gamma\sigma} \tilde{c}^{\dagger}_{i\gamma\sigma} \tilde{c}_{i\gamma\sigma} + \\
& \tfrac{1}{2} \sum_j \sum_{\gamma\gamma'} \langle i,\uparrow| \, \tilde{t}_{ij}^{\gamma\gamma'} \, |j,\uparrow\rangle \, \tilde{c}^{\dagger}_{i\gamma\uparrow} \tilde{c}_{j\gamma'\uparrow} + \tfrac{1}{2} \sum_j \sum_{\gamma\gamma'} \langle i,\downarrow| \, \tilde{t}_{ij}^{\gamma\gamma'} \, |j,\downarrow\rangle \, \tilde{c}^{\dagger}_{i\gamma\downarrow} \tilde{c}_{j\gamma'\downarrow} + \\
& \tfrac{1}{2} \sum_j \sum_{\gamma\gamma'} \langle j,\uparrow| \, \tilde{t}_{ji}^{\gamma'\gamma} \, |i,\uparrow\rangle \, \tilde{c}^{\dagger}_{j\gamma'\uparrow} \tilde{c}_{i\gamma\uparrow} + \tfrac{1}{2} \sum_j \sum_{\gamma\gamma'} \langle j,\downarrow| \, \tilde{t}_{ji}^{\gamma'\gamma} \, |i,\downarrow\rangle \, \tilde{c}^{\dagger}_{j\gamma'\downarrow} \tilde{c}_{i\gamma\downarrow} + \\
& \sum_j \sum_{\gamma\gamma'} \langle i,\uparrow| \, {t'_{ij}}^{\gamma\gamma'} \, |j,\uparrow\rangle \, \tilde{c}^{\dagger}_{i\gamma\uparrow} c_{j\gamma'\uparrow} + \sum_j \sum_{\gamma\gamma'} \langle i,\downarrow| \, {t'_{ij}}^{\gamma\gamma'} \, |j,\downarrow\rangle \, \tilde{c}^{\dagger}_{i\gamma\downarrow} c_{j\gamma'\downarrow} + \\
& \sum_j \sum_{\gamma\gamma'} \langle j,\uparrow| \, {t'_{ji}}^{\gamma'\gamma} \, |i,\uparrow\rangle \, c^{\dagger}_{j\gamma'\uparrow} \tilde{c}_{i\gamma\uparrow} + \sum_j \sum_{\gamma\gamma'} \langle j,\downarrow| \, {t'_{ji}}^{\gamma'\gamma} \, |i,\downarrow\rangle \, c^{\dagger}_{j\gamma'\downarrow} \tilde{c}_{i\gamma\downarrow} + \\
& \sum_{\gamma\gamma'} \sum_{\sigma\sigma'} \left(\tfrac{J_\gamma}{2} \delta_{\gamma\gamma'} \langle \sigma| \, \vec{\sigma} \, |\sigma'\rangle \cdot \hat{\mathbf{\Omega}} \right) \tilde{c}^{\dagger}_{i\gamma\sigma} \tilde{c}_{i\gamma'\sigma'}
\end{aligned} \tag{3.23}$$

with the index j running over intraplane or interplane nearest neighboring sites only (the $\frac{1}{2}$ factor is inserted to avoid double-counting of the corresponding links in subsequent steps). Calculating the rightmost commutator on the RHS of Eq.(3.21) for each spin component separately, substituting the result in Eq.(3.22) (where the summation runs over all the magnetic sites), and Fourier-

Transforming the last result to the momentum space, we find that

$$\left.\frac{d\hat{S}_x}{dt}\right|_{FM} = \frac{1}{2i}\times$$

$$\sum_{\mathbf{k}\gamma\gamma'}\left\{\left\{\sum_{\Delta\mathbf{R}}\langle i,\downarrow|\,\tilde{t}_{ij}^{\gamma\gamma'}\,|j,\downarrow\rangle\, e^{i\mathbf{k}\cdot\Delta\mathbf{R}} - \sum_{\Delta\mathbf{R}}\langle i,\uparrow|\,\tilde{t}_{ij}^{\gamma\gamma'}\,|j,\uparrow\rangle\, e^{i\mathbf{k}\cdot\Delta\mathbf{R}}\right\}\tilde{c}^{\dagger}_{\mathbf{k}\gamma\uparrow}\tilde{c}_{\mathbf{k}\gamma'\downarrow} +\right.$$

$$\left\{\sum_{\Delta\mathbf{R}}\langle i,\uparrow|\,\tilde{t}_{ij}^{\gamma\gamma'}\,|j,\uparrow\rangle\, e^{i\mathbf{k}\cdot\Delta\mathbf{R}} - \sum_{\Delta\mathbf{R}}\langle i,\downarrow|\,\tilde{t}_{ij}^{\gamma\gamma'}\,|j,\downarrow\rangle\, e^{i\mathbf{k}\cdot\Delta\mathbf{R}}\right\}\tilde{c}^{\dagger}_{\mathbf{k}\gamma\downarrow}\tilde{c}_{\mathbf{k}\gamma'\uparrow} +$$

$$iJ_\gamma \sin\theta\sin\phi\delta_{\gamma\gamma'}\tilde{c}^{\dagger}_{\mathbf{k}\gamma\uparrow}\tilde{c}_{\mathbf{k}\gamma'\uparrow} - J_\gamma\cos\theta\delta_{\gamma\gamma'}\tilde{c}^{\dagger}_{\mathbf{k}\gamma\uparrow}\tilde{c}_{\mathbf{k}\gamma'\downarrow} -$$

$$iJ_\gamma \sin\theta\sin\phi\delta_{\gamma\gamma'}\tilde{c}^{\dagger}_{\mathbf{k}\gamma\downarrow}\tilde{c}_{\mathbf{k}\gamma'\downarrow} + J_\gamma\cos\theta\delta_{\gamma\gamma'}\tilde{c}^{\dagger}_{\mathbf{k}\gamma\downarrow}\tilde{c}_{\mathbf{k}\gamma'\uparrow} +$$

$$\left\{\sum_{\Delta\mathbf{R}}\langle i,\downarrow|\,{t'_{ij}}^{\gamma\gamma'}\,|j,\downarrow\rangle\, e^{i\mathbf{k}\cdot\Delta\mathbf{R}}\right\}\tilde{c}^{\dagger}_{\mathbf{k}\gamma\uparrow}c_{\mathbf{k}\gamma'\downarrow} + \left\{\sum_{\Delta\mathbf{R}}\langle i,\uparrow|\,{t'_{ij}}^{\gamma\gamma'}\,|j,\uparrow\rangle\, e^{i\mathbf{k}\cdot\Delta\mathbf{R}}\right\}\tilde{c}^{\dagger}_{\mathbf{k}\gamma\downarrow}c_{\mathbf{k}\gamma'\uparrow} -$$

$$\left.\left\{\sum_{\Delta\mathbf{R}}\langle i,\uparrow|\,{t'_{ij}}^{\gamma\gamma'}\,|j,\uparrow\rangle\, e^{i\mathbf{k}\cdot\Delta\mathbf{R}}\right\}c^{\dagger}_{\mathbf{k}\gamma\uparrow}\tilde{c}_{\mathbf{k}\gamma'\downarrow} - \left\{\sum_{\Delta\mathbf{R}}\langle i,\downarrow|\,{t'_{ij}}^{\gamma\gamma'}\,|j,\downarrow\rangle\, e^{i\mathbf{k}\cdot\Delta\mathbf{R}}\right\}c^{\dagger}_{\mathbf{k}\gamma\downarrow}\tilde{c}_{\mathbf{k}\gamma'\uparrow}\right\} \tag{3.24}$$

$$\left.\frac{d\hat{S}_y}{dt}\right|_{FM} = \frac{1}{2i^2}\times$$

$$\sum_{\mathbf{k}\gamma\gamma'}\left\{\left\{\sum_{\Delta\mathbf{R}}\langle i,\downarrow|\,\tilde{t}_{ij}^{\gamma\gamma'}\,|j,\downarrow\rangle\, e^{i\mathbf{k}\cdot\Delta\mathbf{R}} - \sum_{\Delta\mathbf{R}}\langle i,\uparrow|\,\tilde{t}_{ij}^{\gamma\gamma'}\,|j,\uparrow\rangle\, e^{i\mathbf{k}\cdot\Delta\mathbf{R}}\right\}\tilde{c}^{\dagger}_{\mathbf{k}\gamma\uparrow}\tilde{c}_{\mathbf{k}\gamma'\downarrow} +\right.$$

$$\left\{\sum_{\Delta\mathbf{R}}\langle i,\downarrow|\,\tilde{t}_{ij}^{\gamma\gamma'}\,|j,\downarrow\rangle\, e^{i\mathbf{k}\cdot\Delta\mathbf{R}} - \sum_{\Delta\mathbf{R}}\langle i,\uparrow|\,\tilde{t}_{ij}^{\gamma\gamma'}\,|j,\uparrow\rangle\, e^{i\mathbf{k}\cdot\Delta\mathbf{R}}\right\}\tilde{c}^{\dagger}_{\mathbf{k}\gamma\downarrow}\tilde{c}_{\mathbf{k}\gamma'\uparrow} +$$

$$J_\gamma \sin\theta\cos\phi\,\delta_{\gamma\gamma'}\tilde{c}^{\dagger}_{\mathbf{k}\gamma\uparrow}\tilde{c}_{\mathbf{k}\gamma'\uparrow} - J_\gamma\cos\theta\,\delta_{\gamma\gamma'}\tilde{c}^{\dagger}_{\mathbf{k}\gamma\uparrow}\tilde{c}_{\mathbf{k}\gamma'\downarrow} - J_\gamma\sin\theta\cos\phi\,\delta_{\gamma\gamma'}\tilde{c}^{\dagger}_{\mathbf{k}\gamma\downarrow}\tilde{c}_{\mathbf{k}\gamma'\downarrow} -$$

$$J_\gamma\cos\theta\,\delta_{\gamma\gamma'}\tilde{c}^{\dagger}_{\mathbf{k}\gamma\downarrow}\tilde{c}_{\mathbf{k}\gamma'\uparrow} + \left\{\sum_{\Delta\mathbf{R}}\langle i,\downarrow|\,{t'_{ij}}^{\gamma\gamma'}\,|j,\downarrow\rangle\, e^{i\mathbf{k}\cdot\Delta\mathbf{R}}\right\}\tilde{c}^{\dagger}_{\mathbf{k}\gamma\uparrow}c_{\mathbf{k}\gamma'\downarrow} -$$

$$\left\{\sum_{\Delta\mathbf{R}}\langle i,\uparrow|\,{t'_{ij}}^{\gamma\gamma'}\,|j,\uparrow\rangle\, e^{i\mathbf{k}\cdot\Delta\mathbf{R}}\right\}\tilde{c}^{\dagger}_{\mathbf{k}\gamma\downarrow}c_{\mathbf{k}\gamma'\uparrow} + \left\{\sum_{\Delta\mathbf{R}}\langle i,\downarrow|\,{t'_{ij}}^{\gamma\gamma'}\,|j,\downarrow\rangle\, e^{i\mathbf{k}\cdot\Delta\mathbf{R}}\right\}c^{\dagger}_{\mathbf{k}\gamma\downarrow}\tilde{c}_{\mathbf{k}\gamma'\uparrow}$$

$$\left.-\left\{\sum_{\Delta\mathbf{R}}\langle i,\uparrow|\,{t'_{ij}}^{\gamma\gamma'}\,|j,\uparrow\rangle\, e^{i\mathbf{k}\cdot\Delta\mathbf{R}}\right\}c^{\dagger}_{\mathbf{k}\gamma\uparrow}\tilde{c}_{\mathbf{k}\gamma'\downarrow}\right\} \tag{3.25}$$

and

$$\left.\frac{d\hat{S}_z}{dt}\right|_{FM} = \frac{1}{2i}\sum_{\mathbf{k}\gamma\gamma'}\left\{\left\{\sum_{\Delta\mathbf{R}}\langle i,\uparrow|\,{t'_{ij}}^{\gamma\gamma'}\,|j,\uparrow\rangle\, e^{i\mathbf{k}\cdot\Delta\mathbf{R}}\right\}\tilde{c}^{\dagger}_{\mathbf{k}\gamma\uparrow}c_{\mathbf{k}\gamma'\uparrow}\right.$$

$$-\left\{\sum_{\Delta\mathbf{R}}\langle i,\uparrow|\,{t'_{ij}}^{\gamma\gamma'}\,|j,\uparrow\rangle\, e^{i\mathbf{k}\cdot\Delta\mathbf{R}}\right\}c^{\dagger}_{\mathbf{k}\gamma\uparrow}\tilde{c}_{\mathbf{k}\gamma'\uparrow} + J_\gamma e^{-i\phi}\sin\theta\,\delta_{\gamma\gamma'}\tilde{c}^{\dagger}_{\mathbf{k}\gamma\uparrow}\tilde{c}_{\mathbf{k}\gamma'\downarrow}$$

$$-J_\gamma e^{i\phi}\sin\theta\,\delta_{\gamma\gamma'}\tilde{c}^{\dagger}_{\mathbf{k}\gamma\downarrow}\tilde{c}_{\mathbf{k}\gamma'\uparrow} + \left\{\sum_{\Delta\mathbf{R}}\langle i,\downarrow|\,{t'_{ij}}^{\gamma\gamma'}\,|j,\downarrow\rangle\, e^{i\mathbf{k}\cdot\Delta\mathbf{R}}\right\}c^{\dagger}_{\mathbf{k}\gamma\downarrow}\tilde{c}_{\mathbf{k}\gamma'\downarrow} \tag{3.26}$$

$$\left.-\left\{\sum_{\Delta\mathbf{R}}\langle i,\downarrow|\,{t'_{ij}}^{\gamma\gamma'}\,|j,\downarrow\rangle\, e^{i\mathbf{k}\cdot\Delta\mathbf{R}}\right\}\tilde{c}^{\dagger}_{\mathbf{k}\gamma\downarrow}c_{\mathbf{k}\gamma'\downarrow}\right\}$$

The x, y, z components (with respect to the global Oxyz system) of the overall rate of spin accumulation within the ferromagnetic layer, under equilibrium

conditions, are found by substituting the operators of Eqs.(3.24) through (3.26) respectively in Eq.(3.9). The non-equilibrium components of the overall rate of spin accumulation within the ferromagnetic layer, separating intraband and interband contributions, are found by substituting Eqs.(3.24) through (3.26) respectively in Eqs.(3.8). The overall rate of spin accumulation per magnetic site is found by dividing the previous results by the number of the magnetic sites.

Concluding this subsection, it is worth mentioning that the quantum mechanical operators defined in Eqs.(3.24) through (3.26) consist, broadly speaking, of three different contributions: (a) Non-local contributions originating from intralayer hoppings (intralayer link currents), which exist owing to the spin-dependent hopping, (b) non-local contributions originating from interlayer hoppings (interlayer link currents), and (c) local (on-site) contributions that are proportional to the strength of the exchange coupling. In any one of those cases, the electronic spin can be maintained or flipped. Even though the above defined operators encompass a whole lot of different local microscopic processes, the issue of which of those processes actually contribute depends also on the content of the quasiparticle wavefunctions, since it is the matrix elements of those operators with respect to the quasiparticle eigenstates that appear in Eqs.(3.8) and (3.9) (that define observable entities).

3.3.4 Rate of spin accumulation in the heavy metal layer

Following the procedure of the previous subsection, the rate of spin accumulation at the i-th lattice site of the heavy metal (substrate) layer is given by

$$\begin{aligned}&\hat{\tau}_i^{\mu}=\frac{d\hat{S}_i^{\mu}}{dt}=\frac{1}{i\hbar}\left[\hat{S}_i^{\mu},\hat{\mathcal{H}}_e\right]=\frac{1}{i\hbar}\left[\hat{S}_i^{\mu},\sum_j\hat{H}_j\right]=\frac{1}{i\hbar}\sum_j\left[\hat{S}_i^{\mu},\hat{H}_j\right]=\\&\frac{1}{i\hbar}\left[\hat{S}_i^{\mu},\hat{H}_i\right],\ \forall i,\ \mu=\{x,y,z\}\end{aligned}\tag{3.27}$$

where in the third equality on the RHS we again decomposed the electronic quasiparticle Hamiltonian into appropriately defined local (lattice site) contributions. In addition to that, the overall rate of spin accumulation within the heavy metal layer is

$$\hat{\tau}^{\mu}=\sum_i\hat{\tau}_i^{\mu}=\sum_i\frac{d\hat{S}_i^{\mu}}{dt}=\frac{1}{i\hbar}\sum_i\left[\hat{S}_i^{\mu},\hat{\mathcal{H}}_e\right]\Rightarrow\frac{d\hat{S}^{\mu}}{dt}=\frac{1}{i\hbar}\left[\hat{S}^{\mu},\hat{\mathcal{H}}_e\right]\tag{3.28}$$

The part of $\hat{\mathcal{H}}_e$ that is needed for the calculation of the commutator on the RHS of Eq.(3.27) is given by

$$\begin{aligned}&\hat{H}_i=\sum_{\gamma\sigma}\varepsilon_{\gamma}c_{i\gamma\sigma}^{\dagger}c_{i\gamma\sigma}+\tfrac{1}{2}\sum_j\sum_{\gamma\gamma',\sigma\sigma'}t_{ij}^{\gamma\gamma'}\delta_{\sigma\sigma'}c_{i\gamma\sigma}^{\dagger}c_{j\gamma'\sigma'}+\tfrac{1}{2}\sum_j\sum_{\gamma\gamma',\sigma\sigma'}t_{ji}^{\gamma'\gamma}\delta_{\sigma\sigma'}c_{j\gamma'\sigma}^{\dagger}c_{i\gamma\sigma'}+\\&\sum_j\sum_{\gamma\gamma'}\langle i,\uparrow|\,{t'_{ij}}^{\gamma\gamma'}\,|j,\uparrow\rangle\,c_{i\gamma\uparrow}^{\dagger}\tilde{c}_{j\gamma'\uparrow}+\sum_j\sum_{\gamma\gamma'}\langle i,\downarrow|\,{t'_{ij}}^{\gamma\gamma'}\,|j,\downarrow\rangle\,c_{i\gamma\downarrow}^{\dagger}\tilde{c}_{j\gamma'\downarrow}+\\&\sum_j\sum_{\gamma\gamma'}\langle j,\uparrow|\,{t'_{ji}}^{\gamma'\gamma}|i,\uparrow\rangle_{i,z}\tilde{c}_{j\gamma'\uparrow}^{\dagger}c_{i\gamma\uparrow}+\sum_j\sum_{\gamma\gamma'}\langle j,\downarrow|\,{t'_{ji}}^{\gamma'\gamma}\,|i,\downarrow\rangle\,\tilde{c}_{j\gamma'\downarrow}^{\dagger}c_{i\gamma\downarrow}+\\&\sum_{\gamma\gamma'}\sum_{\sigma\sigma'}\left(\frac{\lambda_{\gamma}}{2}\sum_{\mu}\langle\gamma|\,L_{\mu}\,|\gamma'\rangle\,(\sigma^{\mu})_{\sigma\sigma'}\right)c_{i\gamma\sigma}^{\dagger}c_{i\gamma'\sigma'}\end{aligned}\tag{3.29}$$

with j running over intraplane or interplane nearest neighboring sites only. Calculating the rightmost commutator on the RHS of Eq.(3.27) for each spin component separately, substituting the result in Eq.(3.28) (where the summation runs over all the heavy metal sites), and Fourier-Transforming the last result to the momentum space, we find that

$$\left.\frac{d\hat{S}_x}{dt}\right|_{HM} = \frac{1}{2i}\times$$

$$\sum_{\mathbf{k}\gamma\gamma'}\left\{\left\{\sum_{\Delta\mathbf{R}}\langle i,\downarrow|\, {t'_{ij}}^{\gamma\gamma'}\,|j,\downarrow\rangle\, e^{i\mathbf{k}\cdot\Delta\mathbf{R}}\right\} c^{\dagger}_{\mathbf{k}\gamma\uparrow}\tilde{c}_{\mathbf{k}\gamma'\downarrow} - \left\{\sum_{\Delta\mathbf{R}}\langle i,\uparrow|\, {t'_{ij}}^{\gamma\gamma'}\,|j,\uparrow\rangle\, e^{i\mathbf{k}\cdot\Delta\mathbf{R}}\right\}\tilde{c}^{\dagger}_{\mathbf{k}\gamma\uparrow}c_{\mathbf{k}\gamma'\downarrow}\right.$$

$$+\left\{\sum_{\Delta\mathbf{R}}\langle i,\uparrow|\, {t'_{ij}}^{\gamma\gamma'}\,|j,\uparrow\rangle\, e^{i\mathbf{k}\cdot\Delta\mathbf{R}}\right\} c^{\dagger}_{\mathbf{k}\gamma\downarrow}\tilde{c}_{\mathbf{k}\gamma'\uparrow} - \left\{\sum_{\Delta\mathbf{R}}\langle i,\downarrow|\, {t'_{ij}}^{\gamma\gamma'}\,|j,\downarrow\rangle\, e^{i\mathbf{k}\cdot\Delta\mathbf{R}}\right\}\tilde{c}^{\dagger}_{\mathbf{k}\gamma\downarrow}c_{\mathbf{k}\gamma'\uparrow}+$$

$$\sum_{\sigma}\left(\frac{\lambda_\gamma}{2}\sum_{\mu}\langle\gamma|\, L_\mu\,|\gamma'\rangle\,(\sigma^\mu)_{\downarrow\sigma}\right) c^{\dagger}_{\mathbf{k}\gamma\uparrow}c_{\mathbf{k}\gamma'\sigma} - \sum_{\sigma}\left(\frac{\lambda_\gamma}{2}\sum_{\mu}\langle\gamma|\, L_\mu\,|\gamma'\rangle\,(\sigma^\mu)_{\sigma\uparrow}\right) c^{\dagger}_{\mathbf{k}\gamma\sigma}c_{\mathbf{k}\gamma'\downarrow}+$$

$$\left.\sum_{\sigma}\left(\frac{\lambda_\gamma}{2}\sum_{\mu}\langle\gamma|\, L_\mu\,|\gamma'\rangle\,(\sigma^\mu)_{\uparrow\sigma}\right) c^{\dagger}_{\mathbf{k}\gamma\downarrow}c_{\mathbf{k}\gamma'\sigma} - \sum_{\sigma}\left(\frac{\lambda_\gamma}{2}\sum_{\mu}\langle\gamma|\, L_\mu\,|\gamma'\rangle\,(\sigma^\mu)_{\sigma\downarrow}\right) c^{\dagger}_{\mathbf{k}\gamma\sigma}c_{\mathbf{k}\gamma'\uparrow}\right\} \tag{3.30}$$

$$\left.\frac{d\hat{S}_y}{dt}\right|_{HM} = \frac{1}{2i^2}\times$$

$$\sum_{\mathbf{k}\gamma\gamma'}\left\{\left\{\sum_{\Delta\mathbf{R}}\left\langle i,\downarrow\right|t'_{ij}{}^{\gamma\gamma'}\left|j,\downarrow\right\rangle e^{i\mathbf{k}\cdot\Delta\mathbf{R}}\right\}c^{\dagger}_{\mathbf{k}\gamma\uparrow}\tilde{c}_{\mathbf{k}\gamma'\downarrow} - \left\{\sum_{\Delta\mathbf{R}}\left\langle i,\uparrow\right|t'_{ij}{}^{\gamma\gamma'}\left|j,\uparrow\right\rangle e^{i\mathbf{k}\cdot\Delta\mathbf{R}}\right\}\tilde{c}^{\dagger}_{\mathbf{k}\gamma\uparrow}c_{\mathbf{k}\gamma'\downarrow}\right.$$

$$-\left\{\sum_{\Delta\mathbf{R}}\left\langle i,\uparrow\right|t'_{ij}{}^{\gamma\gamma'}\left|j,\uparrow\right\rangle e^{i\mathbf{k}\cdot\Delta\mathbf{R}}\right\}c^{\dagger}_{\mathbf{k}\gamma\downarrow}\tilde{c}_{\mathbf{k}\gamma'\uparrow} + \left\{\sum_{\Delta\mathbf{R}}\left\langle i,\downarrow\right|t'_{ij}{}^{\gamma\gamma'}\left|j,\downarrow\right\rangle e^{i\mathbf{k}\cdot\Delta\mathbf{R}}\right\}\tilde{c}^{\dagger}_{\mathbf{k}\gamma\downarrow}c_{\mathbf{k}\gamma'\uparrow} +$$

$$\sum_{\sigma}\left(\frac{\lambda_\gamma}{2}\sum_{\mu}\left\langle\gamma\right|L_\mu\left|\gamma'\right\rangle\left(\sigma^\mu\right)_{\downarrow\sigma}\right)c^{\dagger}_{\mathbf{k}\gamma\uparrow}c_{\mathbf{k}\gamma'\sigma} - \sum_{\sigma}\left(\frac{\lambda_\gamma}{2}\sum_{\mu}\left\langle\gamma\right|L_\mu\left|\gamma'\right\rangle\left(\sigma^\mu\right)_{\sigma\uparrow}\right)c^{\dagger}_{\mathbf{k}\gamma\sigma}c_{\mathbf{k}\gamma'\downarrow}$$

$$\left.-\sum_{\sigma}\left(\frac{\lambda_\gamma}{2}\sum_{\mu}\left\langle\gamma\right|L_\mu\left|\gamma'\right\rangle\left(\sigma^\mu\right)_{\uparrow\sigma}\right)c^{\dagger}_{\mathbf{k}\gamma\downarrow}c_{\mathbf{k}\gamma'\sigma} + \sum_{\sigma}\left(\frac{\lambda_\gamma}{2}\sum_{\mu}\left\langle\gamma\right|L_\mu\left|\gamma'\right\rangle\left(\sigma^\mu\right)_{\sigma\downarrow}\right)c^{\dagger}_{\mathbf{k}\gamma\sigma}c_{\mathbf{k}\gamma'\uparrow}\right\} \tag{3.31}$$

and

$$\left.\frac{d\hat{S}_z}{dt}\right|_{HM} = \frac{1}{2i}\times$$

$$\sum_{\mathbf{k}\gamma\gamma'}\left\{\left\{\sum_{\Delta\mathbf{R}}\left\langle i,\uparrow\right|t'_{ij}{}^{\gamma\gamma'}\left|j,\uparrow\right\rangle e^{i\mathbf{k}\cdot\Delta\mathbf{R}}\right\}c^{\dagger}_{\mathbf{k}\gamma\uparrow}\tilde{c}_{\mathbf{k}\gamma'\uparrow} - \left\{\sum_{\Delta\mathbf{R}}\left\langle i,\uparrow\right|t'_{ij}{}^{\gamma\gamma'}\left|j,\uparrow\right\rangle e^{i\mathbf{k}\cdot\Delta\mathbf{R}}\right\}\tilde{c}^{\dagger}_{\mathbf{k}\gamma\uparrow}c_{\mathbf{k}\gamma'\uparrow}\right.$$

$$-\left\{\sum_{\Delta\mathbf{R}}\left\langle i,\downarrow\right|t'_{ij}{}^{\gamma\gamma'}\left|j,\downarrow\right\rangle e^{i\mathbf{k}\cdot\Delta\mathbf{R}}\right\}c^{\dagger}_{\mathbf{k}\gamma\downarrow}\tilde{c}_{\mathbf{k}\gamma'\downarrow} + \left\{\sum_{\Delta\mathbf{R}}\left\langle i,\downarrow\right|t'_{ij}{}^{\gamma\gamma'}\left|j,\downarrow\right\rangle_{j,z} e^{i\mathbf{k}\cdot\Delta\mathbf{R}}\right\}\tilde{c}^{\dagger}_{\mathbf{k}\gamma\downarrow}c_{\mathbf{k}\gamma'\downarrow}$$

$$+\sum_{\sigma}\left(\frac{\lambda_\gamma}{2}\sum_{\mu}\left\langle\gamma\right|L_\mu\left|\gamma'\right\rangle\left(\sigma^\mu\right)_{\uparrow\sigma}\right)c^{\dagger}_{\mathbf{k}\gamma\uparrow}c_{\mathbf{k}\gamma'\sigma} - \sum_{\sigma}\left(\frac{\lambda_\gamma}{2}\sum_{\mu}\left\langle\gamma\right|L_\mu\left|\gamma'\right\rangle\left(\sigma^\mu\right)_{\sigma\uparrow}\right)c^{\dagger}_{\mathbf{k}\gamma\sigma}c_{\mathbf{k}\gamma'\uparrow}$$

$$\left.-\sum_{\sigma}\left(\frac{\lambda_\gamma}{2}\sum_{\mu}\left\langle\gamma\right|L_\mu\left|\gamma'\right\rangle\left(\sigma^\mu\right)_{\downarrow\sigma}\right)c^{\dagger}_{\mathbf{k}\gamma\downarrow}c_{\mathbf{k}\gamma'\sigma} + \sum_{\sigma}\left(\frac{\lambda_\gamma}{2}\sum_{\mu}\left\langle\gamma\right|L_\mu\left|\gamma'\right\rangle\left(\sigma^\mu\right)_{\sigma\downarrow}\right)c^{\dagger}_{\mathbf{k}\gamma\sigma}c_{\mathbf{k}\gamma'\downarrow}\right\} \tag{3.32}$$

The x, y, z components (with respect to the global Oxyz system) of the overall rate of spin accumulation within the heavy metal layer, under equilibrium conditions, are found by substituting the operators of Eqs.(3.30) through (3.32) respectively in Eq.(3.9). The non-equilibrium components of the overall rate of spin accumulation within the heavy metal layer, separating intraband and interband contributions, are found by substituting Eqs.(3.30) through (3.32) respectively in Eqs.(3.8). The overall rate of spin accumulation per spin-orbit site is found by dividing the previous results by the number of the spin-orbit sites.

Concluding this subsection, it is worth mentioning that the quantum mechanical operators defined in Eqs.(3.30) through (3.32) encompass, broadly speaking, two different contributions: (a) Non-local contributions originating from interlayer hoppings (interlayer link currents), and (b) local (on-site) contributions that are proportional to the strength of the spin-orbit coupling. In any one of those cases, the electronic spin can be maintained or flipped.

3.3.5 Interlayer particle and spin currents

The electronic quasiparticle current at the i-th lattice site of the ferromagnetic layer is given by

$$\frac{d\hat{N}_i}{dt} = \frac{1}{i\hbar}\left[\hat{N}_i, \hat{\mathcal{H}}_e\right] = \frac{1}{i\hbar}\left[\hat{N}_i, \sum_j \hat{H}_j\right] = \frac{1}{i\hbar}\sum_j \left[\hat{N}_i, \hat{H}_j\right] = \frac{1}{i\hbar}\left[\hat{N}_i, \hat{H}_i\right], \quad \forall i \tag{3.33}$$

where in the rightmost commutator on the RHS of the above equation, the on-site Hamiltonian to be used is given by Eq.(3.23). The overall electronic

quasiparticle current at the ferromagnetic layer is given by

$$\frac{d\hat{N}}{dt} = \sum_i \frac{d\hat{N}_i}{dt} = \frac{1}{i\hbar}\sum_i \left[\hat{N}_i, \hat{\mathcal{H}}_e\right] \Rightarrow \frac{d\hat{N}}{dt} = \frac{1}{i\hbar}\left[\hat{N}, \hat{\mathcal{H}}_e\right] \tag{3.34}$$

where by definition it is $\hat{N}_i = \sum_{\gamma\sigma} \tilde{c}^{\dagger}_{i\gamma\sigma}\tilde{c}_{i\gamma\sigma}$. Calculating the rightmost commutator on the RHS of Eq.(3.33), substituting the result in Eq.(3.34) (where the summation runs over all the magnetic sites), and Fourier Transforming the last result to the momentum space, we find that

$$\begin{aligned}\left.\frac{d\hat{N}}{dt}\right|_{FM} = \frac{1}{i\hbar}\sum_{\mathbf{k}}\sum_{\gamma\gamma'}\Bigg[&\left\{\sum_{\Delta\mathbf{R}} \langle i,\uparrow|\, {t'_{ij}}^{\gamma\gamma'}\, |j,\uparrow\rangle\, e^{i\mathbf{k}\cdot\Delta\mathbf{R}}\right\} \tilde{c}^{\dagger}_{\mathbf{k}\gamma\uparrow} c_{\mathbf{k}\gamma'\uparrow} + \\ &\left\{\sum_{\Delta\mathbf{R}} \langle i,\downarrow|\, {t'_{ij}}^{\gamma\gamma'}\, |j,\downarrow\rangle\, e^{i\mathbf{k}\cdot\Delta\mathbf{R}}\right\} \tilde{c}^{\dagger}_{\mathbf{k}\gamma\downarrow} c_{\mathbf{k}\gamma'\downarrow} - \left\{\sum_{\Delta\mathbf{R}} \langle i,\uparrow|\, {t'_{ij}}^{\gamma\gamma'}\, |j,\uparrow\rangle\, e^{i\mathbf{k}\cdot\Delta\mathbf{R}}\right\} c^{\dagger}_{\mathbf{k}\gamma\uparrow}\tilde{c}_{\mathbf{k}\gamma'\uparrow} \\ &- \left\{\sum_{\Delta\mathbf{R}} \langle i,\downarrow|\, {t'_{ij}}^{\gamma\gamma'}\, |j,\downarrow\rangle\, e^{i\mathbf{k}\cdot\Delta\mathbf{R}}\right\} c^{\dagger}_{\mathbf{k}\gamma\downarrow}\tilde{c}_{\mathbf{k}\gamma'\downarrow}\Bigg]\end{aligned} \tag{3.35}$$

By an exactly similar procedure, the overall electronic quasiparticle current at the heavy metal layer, provided one uses the on-site Hamiltonian of Eq.(3.29), is given by

$$\begin{aligned}\left.\frac{d\hat{N}}{dt}\right|_{HM} = \frac{1}{i\hbar}\sum_{\mathbf{k}}\sum_{\gamma\gamma'}\Bigg[&\left\{\sum_{\Delta\mathbf{R}} \langle i,\uparrow|\, {t'_{ij}}^{\gamma\gamma'}\, |j,\uparrow\rangle\, e^{i\mathbf{k}\cdot\Delta\mathbf{R}}\right\} c^{\dagger}_{\mathbf{k}\gamma\uparrow}\tilde{c}_{\mathbf{k}\gamma'\uparrow} + \\ &\left\{\sum_{\Delta\mathbf{R}} \langle i,\downarrow|\, {t'_{ij}}^{\gamma\gamma'}\, |j,\downarrow\rangle\, e^{i\mathbf{k}\cdot\Delta\mathbf{R}}\right\} c^{\dagger}_{\mathbf{k}\gamma\downarrow}\tilde{c}_{\mathbf{k}\gamma'\downarrow} - \left\{\sum_{\Delta\mathbf{R}} \langle i,\uparrow|\, {t'_{ij}}^{\gamma\gamma'}\, |j,\uparrow\rangle\, e^{i\mathbf{k}\cdot\Delta\mathbf{R}}\right\} \tilde{c}^{\dagger}_{\mathbf{k}\gamma\uparrow} c_{\mathbf{k}\gamma'\uparrow} \\ &- \left\{\sum_{\Delta\mathbf{R}} \langle i,\downarrow|\, {t'_{ij}}^{\gamma\gamma'}\, |j,\downarrow\rangle\, e^{i\mathbf{k}\cdot\Delta\mathbf{R}}\right\} \tilde{c}^{\dagger}_{\mathbf{k}\gamma\downarrow} c_{\mathbf{k}\gamma'\downarrow}\Bigg]\end{aligned} \tag{3.36}$$

The equilibrium quasiparticle current within the ferromagnetic and the heavy metal layer respectively are found by substituting the operators of Eqs.(3.35)

and (3.36) respectively in Eq.(3.9). The non-equilibrium quasiparticle current within the ferromagnetic and the heavy metal layer respectively, with the intraband and the interband contributions separated, are found by substituting the operators of Eqs.(3.35) and (3.36) respectively in Eqs.(3.8). Had we defined an interlayer quasiparticle current for the bilayer structure using Eqs.(3.35) and (3.36), the result would be

$$\frac{d\hat{N}}{dt} = \left.\frac{d\hat{N}}{dt}\right|_{FM} + \left.\frac{d\hat{N}}{dt}\right|_{HM} = \hat{0} \tag{3.37}$$

which means that there is no net interlayer quasiparticle current for the bilayer structure (i.e. there is no net charge accumulation within either layer)

In the next step, from the equations that give the components of the overall rate of spin accumulation at the ferromagnetic layer, Eqs.(3.24) through (3.26), one can single out the non-local contributions that originate from interlayer hoppings, the so-called "interlayer link spin currents", and define a net interlayer spin current at the ferromagnetic layer whose components are given by

$$\begin{aligned}
\left.\hat{J}_S^x\right|_{FM} = \tfrac{1}{2i}\sum_{\mathbf{k}\gamma\gamma'}\Bigg[&\left\{\sum_{\Delta\mathbf{R}}\langle i,\downarrow|\, {t'_{ij}}^{\gamma\gamma'}\,|j,\downarrow\rangle\, e^{i\mathbf{k}\cdot\Delta\mathbf{R}}\right\}\tilde{c}^{\dagger}_{\mathbf{k}\gamma\uparrow}c_{\mathbf{k}\gamma'\downarrow} + \\
&\left\{\sum_{\Delta\mathbf{R}}\langle i,\uparrow|\, {t'_{ij}}^{\gamma\gamma'}\,|j,\uparrow\rangle\, e^{i\mathbf{k}\cdot\Delta\mathbf{R}}\right\}\tilde{c}^{\dagger}_{\mathbf{k}\gamma\downarrow}c_{\mathbf{k}\gamma'\uparrow} - \left\{\sum_{\Delta\mathbf{R}}\langle i,\uparrow|\, {t'_{ij}}^{\gamma\gamma'}\,|j,\uparrow\rangle\, e^{i\mathbf{k}\cdot\Delta\mathbf{R}}\right\}c^{\dagger}_{\mathbf{k}\gamma\uparrow}\tilde{c}_{\mathbf{k}\gamma'\downarrow} \\
&- \left\{\sum_{\Delta\mathbf{R}}\langle i,\downarrow|\, {t'_{ij}}^{\gamma\gamma'}\,|j,\downarrow\rangle\, e^{i\mathbf{k}\cdot\Delta\mathbf{R}}\right\}c^{\dagger}_{\mathbf{k}\gamma\downarrow}\tilde{c}_{\mathbf{k}\gamma'\uparrow}\Bigg]
\end{aligned} \tag{3.38}$$

$$\hat{J}_S^y\Big|_{FM} = \tfrac{1}{2i^2}\sum_{\mathbf{k}\gamma\gamma'}\Bigg[\Bigg\{\sum_{\Delta\mathbf{R}}\langle i,\downarrow|\, {t'_{ij}}^{\gamma\gamma'}\,|j,\downarrow\rangle\, e^{i\mathbf{k}\cdot\Delta\mathbf{R}}\Bigg\}\tilde{c}^{\dagger}_{\mathbf{k}\gamma\uparrow}c_{\mathbf{k}\gamma'\downarrow} -$$

$$\Bigg\{\sum_{\Delta\mathbf{R}}\langle i,\uparrow|\, {t'_{ij}}^{\gamma\gamma'}\,|j,\uparrow\rangle\, e^{i\mathbf{k}\cdot\Delta\mathbf{R}}\Bigg\}c^{\dagger}_{\mathbf{k}\gamma\uparrow}\tilde{c}_{\mathbf{k}\gamma'\downarrow} - \Bigg\{\sum_{\Delta\mathbf{R}}\langle i,\uparrow|\, {t'_{ij}}^{\gamma\gamma'}\,|j,\uparrow\rangle\, e^{i\mathbf{k}\cdot\Delta\mathbf{R}}\Bigg\}\tilde{c}^{\dagger}_{\mathbf{k}\gamma\downarrow}c_{\mathbf{k}\gamma'\uparrow}$$

$$+\Bigg\{\sum_{\Delta\mathbf{R}}\langle i,\downarrow|\, {t'_{ij}}^{\gamma\gamma'}\,|j,\downarrow\rangle\, e^{i\mathbf{k}\cdot\Delta\mathbf{R}}\Bigg\}c^{\dagger}_{\mathbf{k}\gamma\downarrow}\tilde{c}_{\mathbf{k}\gamma'\uparrow}\Bigg] \tag{3.39}$$

and

$$\hat{J}_S^z\Big|_{FM} = \tfrac{1}{2i}\sum_{\mathbf{k}\gamma\gamma'}\Bigg[\Bigg\{\sum_{\Delta\mathbf{R}}\langle i,\uparrow|\, {t'_{ij}}^{\gamma\gamma'}\,|j,\uparrow\rangle\, e^{i\mathbf{k}\cdot\Delta\mathbf{R}}\Bigg\}\tilde{c}^{\dagger}_{\mathbf{k}\gamma\uparrow}c_{\mathbf{k}\gamma'\uparrow} -$$

$$\Bigg\{\sum_{\Delta\mathbf{R}}\langle i,\uparrow|\, {t'_{ij}}^{\gamma\gamma'}\,|j,\uparrow\rangle\, e^{i\mathbf{k}\cdot\Delta\mathbf{R}}\Bigg\}c^{\dagger}_{\mathbf{k}\gamma\uparrow}\tilde{c}_{\mathbf{k}\gamma'\uparrow} - \Bigg\{\sum_{\Delta\mathbf{R}}\langle i,\downarrow|\, {t'_{ij}}^{\gamma\gamma'}\,|j,\downarrow\rangle\, e^{i\mathbf{k}\cdot\Delta\mathbf{R}}\Bigg\}\tilde{c}^{\dagger}_{\mathbf{k}\gamma\downarrow}c_{\mathbf{k}\gamma'\downarrow}$$

$$+\Bigg\{\sum_{\Delta\mathbf{R}}\langle i,\downarrow|\, {t'_{ij}}^{\gamma\gamma'}\,|j,\downarrow\rangle\, e^{i\mathbf{k}\cdot\Delta\mathbf{R}}\Bigg\}c^{\dagger}_{\mathbf{k}\gamma\downarrow}\tilde{c}_{\mathbf{k}\gamma'\downarrow}\Bigg] \tag{3.40}$$

In the same spirit, from the equations that give the components of the overall rate of spin accumulation at the heavy metal layer, Eqs.(3.30) through (3.32), one can single out the corresponding interlayer link spin currents again, and define a net interlayer spin current at the heavy metal layer whose com-

ponents are given by

$$\hat{J}_S^x\Big|_{HM} = \tfrac{1}{2i}\sum_{\mathbf{k}\gamma\gamma'}\Bigg[\Bigg\{\sum_{\Delta\mathbf{R}}\langle i,\downarrow|\, {t'_{ij}}^{\gamma\gamma'}\,|j,\downarrow\rangle\, e^{i\mathbf{k}\cdot\Delta\mathbf{R}}\Bigg\} c^\dagger_{\mathbf{k}\gamma\uparrow}\tilde{c}_{\mathbf{k}\gamma'\downarrow} -$$

$$\Bigg\{\sum_{\Delta\mathbf{R}}\langle i,\uparrow|\, {t'_{ij}}^{\gamma\gamma'}\,|j,\uparrow\rangle\, e^{i\mathbf{k}\cdot\Delta\mathbf{R}}\Bigg\}\tilde{c}^\dagger_{\mathbf{k}\gamma\uparrow}c_{\mathbf{k}\gamma'\downarrow} + \Bigg\{\sum_{\Delta\mathbf{R}}\langle i,\uparrow|\, {t'_{ij}}^{\gamma\gamma'}\,|j,\uparrow\rangle\, e^{i\mathbf{k}\cdot\Delta\mathbf{R}}\Bigg\} c^\dagger_{\mathbf{k}\gamma\downarrow}\tilde{c}_{\mathbf{k}\gamma'\uparrow}$$

$$-\Bigg\{\sum_{\Delta\mathbf{R}}\langle i,\downarrow|\, {t'_{ij}}^{\gamma\gamma'}\,|j,\downarrow\rangle\, e^{i\mathbf{k}\cdot\Delta\mathbf{R}}\Bigg\}\tilde{c}^\dagger_{\mathbf{k}\gamma\downarrow}c_{\mathbf{k}\gamma'\uparrow}\Bigg] \tag{3.41}$$

$$\hat{J}_S^y\Big|_{HM} = \tfrac{1}{2i^2}\sum_{\mathbf{k}\gamma\gamma'}\Bigg[\Bigg\{\sum_{\Delta\mathbf{R}}\langle i,\downarrow|\, {t'_{ij}}^{\gamma\gamma'}\,|j,\downarrow\rangle\, e^{i\mathbf{k}\cdot\Delta\mathbf{R}}\Bigg\} c^\dagger_{\mathbf{k}\gamma\uparrow}\tilde{c}_{\mathbf{k}\gamma'\downarrow} -$$

$$\Bigg\{\sum_{\Delta\mathbf{R}}\langle i,\uparrow|\, {t'_{ij}}^{\gamma\gamma'}\,|j,\uparrow\rangle\, e^{i\mathbf{k}\cdot\Delta\mathbf{R}}\Bigg\}\tilde{c}^\dagger_{\mathbf{k}\gamma\uparrow}c_{\mathbf{k}\gamma'\downarrow} - \Bigg\{\sum_{\Delta\mathbf{R}}\langle i,\uparrow|\, {t'_{ij}}^{\gamma\gamma'}\,|j,\uparrow\rangle\, e^{i\mathbf{k}\cdot\Delta\mathbf{R}}\Bigg\} c^\dagger_{\mathbf{k}\gamma\downarrow}\tilde{c}_{\mathbf{k}\gamma'\uparrow}$$

$$+\Bigg\{\sum_{\Delta\mathbf{R}}\langle i,\downarrow|\, {t'_{ij}}^{\gamma\gamma'}\,|j,\downarrow\rangle\, e^{i\mathbf{k}\cdot\Delta\mathbf{R}}\Bigg\}\tilde{c}^\dagger_{\mathbf{k}\gamma\downarrow}c_{\mathbf{k}\gamma'\uparrow}\Bigg] \tag{3.42}$$

and

$$\hat{J}_S^z\Big|_{HM} = \tfrac{1}{2i}\sum_{\mathbf{k}\gamma\gamma'}\Bigg[\Bigg\{\sum_{\Delta\mathbf{R}}\langle i,\uparrow|\, {t'_{ij}}^{\gamma\gamma'}\,|j,\uparrow\rangle\, e^{i\mathbf{k}\cdot\Delta\mathbf{R}}\Bigg\} c^\dagger_{\mathbf{k}\gamma\uparrow}\tilde{c}_{\mathbf{k}\gamma'\uparrow} -$$

$$\Bigg\{\sum_{\Delta\mathbf{R}}\langle i,\uparrow|\, {t'_{ij}}^{\gamma\gamma'}\,|j,\uparrow\rangle\, e^{i\mathbf{k}\cdot\Delta\mathbf{R}}\Bigg\}\tilde{c}^\dagger_{\mathbf{k}\gamma\uparrow}c_{\mathbf{k}\gamma'\uparrow} - \Bigg\{\sum_{\Delta\mathbf{R}}\langle i,\downarrow|\, {t'_{ij}}^{\gamma\gamma'}\,|j,\downarrow\rangle\, e^{i\mathbf{k}\cdot\Delta\mathbf{R}}\Bigg\} c^\dagger_{\mathbf{k}\gamma\downarrow}\tilde{c}_{\mathbf{k}\gamma'\downarrow}$$

$$+\Bigg\{\sum_{\Delta\mathbf{R}}\langle i,\downarrow|\, {t'_{ij}}^{\gamma\gamma'}\,|j,\downarrow\rangle\, e^{i\mathbf{k}\cdot\Delta\mathbf{R}}\Bigg\}\tilde{c}^\dagger_{\mathbf{k}\gamma\downarrow}c_{\mathbf{k}\gamma'\downarrow}\Bigg] \tag{3.43}$$

Had we defined an interlayer spin current for the bilayer structure using Eqs.(3.38) through (3.43), under spin-independent hopping, the net interlayer

spin current would be zero. However, under spin-dependent hopping the net interlayer spin current is in general non-zero, except for its z-component.

Concluding this subsection, again from the equations that give the components of the overall rate of spin accumulation at the ferromagnetic layer, Eqs.(3.24) through (3.26), one can single out the non-local contributions that originate from intralayer hoppings, the so-called "intralayer link spin currents", and define a net intralayer spin current at the ferromagnetic layer whose components are given by

$$\hat{J}_S^x\Big|_{FM}^{intra} = \tfrac{1}{2i}\times$$

$$\sum_{\mathbf{k}\gamma\gamma'}\left[\left\{\sum_{\Delta\mathbf{R}}\langle i,\downarrow|\,\tilde{t}_{ij}^{\gamma\gamma'}\,|j,\downarrow\rangle e^{i\mathbf{k}\cdot\Delta\mathbf{R}} - \sum_{\Delta\mathbf{R}}\langle i,\uparrow|\,\tilde{t}_{ij}^{\gamma\gamma'}\,|j,\uparrow\rangle\, e^{i\mathbf{k}\cdot\Delta\mathbf{R}}\right\}\tilde{c}_{\mathbf{k}\gamma\uparrow}^{\dagger}\tilde{c}_{\mathbf{k}\gamma'\downarrow} + \right.$$

$$\left.\left\{\sum_{\Delta\mathbf{R}}\langle i,\uparrow|\,\tilde{t}_{ij}^{\gamma\gamma'}|j,\uparrow\rangle_{j,z} e^{i\mathbf{k}\cdot\Delta\mathbf{R}} - \sum_{\Delta\mathbf{R}}\langle i,\downarrow|\,\tilde{t}_{ij}^{\gamma\gamma'}\,|j,\downarrow\rangle\, e^{i\mathbf{k}\cdot\Delta\mathbf{R}}\right\}\right]\tilde{c}_{\mathbf{k}\gamma\downarrow}^{\dagger}\tilde{c}_{\mathbf{k}\gamma'\uparrow} \tag{3.44}$$

and

$$\hat{J}_S^y\Big|_{FM}^{intra} = \tfrac{1}{2i^2}\times$$

$$\sum_{\mathbf{k}\gamma\gamma'}\left[\left\{\sum_{\Delta\mathbf{R}}\langle i,\downarrow|\,\tilde{t}_{ij}^{\gamma\gamma'}\,|j,\downarrow\rangle\, e^{i\mathbf{k}\cdot\Delta\mathbf{R}} - \sum_{\Delta\mathbf{R}}\langle i,\uparrow|\,\tilde{t}_{ij}^{\gamma\gamma'}\,|j,\uparrow\rangle\, e^{i\mathbf{k}\cdot\Delta\mathbf{R}}\right\}\tilde{c}_{\mathbf{k}\gamma\uparrow}^{\dagger}\tilde{c}_{\mathbf{k}\gamma'\downarrow} + \right.$$

$$\left.\left\{\sum_{\Delta\mathbf{R}}\langle i,\downarrow|\,\tilde{t}_{ij}^{\gamma\gamma'}|j,\downarrow\rangle_{j,z} e^{i\mathbf{k}\cdot\Delta\mathbf{R}} - \sum_{\Delta\mathbf{R}}\langle i,\uparrow|\,\tilde{t}_{ij}^{\gamma\gamma'}\,|j,\uparrow\rangle\, e^{i\mathbf{k}\cdot\Delta\mathbf{R}}\right\}\right]\tilde{c}_{\mathbf{k}\gamma\downarrow}^{\dagger}\tilde{c}_{\mathbf{k}\gamma'\uparrow} \tag{3.45}$$

The equilibrium spin currents defined by Eqs.(3.38) through (3.45) are found by substituting the corresponding operators in Eq.(3.9). The non-equilibrium spin currents defined by Eqs.(3.38) through (3.45), with the intraband and the

interband contributions separated, are found by substituting the corresponding operators in Eqs.(3.8).

3.3.6 Torques transferred to the exchange effective field of the ferromagnet

Let us now focus on the ferromagnetic layer only and again use the global coordinate system Oxyz defined previously. The torques transferred to the exchange effective field of the ferromagnet at the i-th lattice site of the ferromagnetic layer are given by (following the sign convention of Zhang and Li, Ref.[67])

$$\hat{T}_i^{\mu} = -\frac{1}{i\hbar}\left[\hat{S}_i^{\mu}, \hat{H}_i^{exch}\right],\ \forall i,\ \mu = \{x, y, z\} \tag{3.46}$$

where by definition it is

$$\hat{H}_i^{exch} = \sum_{\gamma\gamma'}\sum_{\sigma\sigma'}\left(\frac{J_{\gamma}}{2}\delta_{\gamma\gamma'}\left\langle\sigma\right|\vec{\sigma}\left|\sigma'\right\rangle\cdot\hat{\mathbf{\Omega}}\right)\tilde{c}_{i\gamma\sigma}^{\dagger}\tilde{c}_{i\gamma'\sigma'} \tag{3.47}$$

and the operators $\tilde{c}_{i\gamma\sigma}^{\dagger}$ ($\tilde{c}_{i\gamma\sigma}$) create (destroy) an electronic quasiparticle within the ferromagnetic layer. The components of the overall torque transferred to the exchange effective field of the ferromagnet are given by

$$\hat{T}^{\mu} = \sum_i \hat{T}_i^{\mu} = -\frac{1}{i\hbar}\sum_i\left[\hat{S}_i^{\mu}, \hat{H}_i^{exch}\right] \Rightarrow \hat{T}^{\mu} = -\frac{1}{i\hbar}\sum_i\left[\hat{S}_i^{\mu}, \hat{H}_i^{exch}\right] \tag{3.48}$$

Calculating the commutator on the RHS of Eq.(3.46) for each torque component separately, substituting the corresponding result in Eq.(3.48) (where the summation runs over all the magnetic sites), and Fourier-Transforming to the

momentum space, we find that

$$\begin{aligned}
\hat{T}^x &= \tfrac{1}{2i}\sum_{\mathbf{k}\gamma\gamma'}\Big[-iJ_\gamma \sin\theta\sin\phi\delta_{\gamma\gamma'}\tilde{c}^\dagger_{\mathbf{k}\gamma\uparrow}\tilde{c}_{\mathbf{k}\gamma'\uparrow} + J_\gamma\cos\theta\delta_{\gamma\gamma'}\tilde{c}^\dagger_{\mathbf{k}\gamma\uparrow}\tilde{c}_{\mathbf{k}\gamma'\downarrow} \\
&\qquad -J_\gamma\cos\theta\delta_{\gamma\gamma'}\tilde{c}^\dagger_{\mathbf{k}\gamma\downarrow}\tilde{c}_{\mathbf{k}\gamma'\uparrow} + iJ_\gamma\sin\theta\sin\phi\delta_{\gamma\gamma'}\tilde{c}^\dagger_{\mathbf{k}\gamma\downarrow}\tilde{c}_{\mathbf{k}\gamma'\downarrow}\Big] \\
\hat{T}^y &= \tfrac{1}{2i^2}\sum_{\mathbf{k}\gamma\gamma'}\Big[-J_\gamma \sin\theta\cos\phi\delta_{\gamma\gamma'}\tilde{c}^\dagger_{\mathbf{k}\gamma\uparrow}\tilde{c}_{\mathbf{k}\gamma'\uparrow} + J_\gamma\cos\theta\delta_{\gamma\gamma'}\tilde{c}^\dagger_{\mathbf{k}\gamma\uparrow}\tilde{c}_{\mathbf{k}\gamma'\downarrow} \\
&\qquad +J_\gamma\sin\theta\cos\phi\delta_{\gamma\gamma'}\tilde{c}^\dagger_{\mathbf{k}\gamma\downarrow}\tilde{c}_{\mathbf{k}\gamma'\downarrow} + J_\gamma\cos\theta\delta_{\gamma\gamma'}\tilde{c}^\dagger_{\mathbf{k}\gamma\downarrow}\tilde{c}_{\mathbf{k}\gamma'\uparrow}\Big] \\
\hat{T}^z &= \tfrac{1}{2i}\sum_{\mathbf{k}\gamma\gamma'}\Big[J_\gamma e^{i\phi}\sin\theta\delta_{\gamma\gamma'}\tilde{c}^\dagger_{\mathbf{k}\gamma\downarrow}\tilde{c}_{\mathbf{k}\gamma'\uparrow} - J_\gamma e^{-i\phi}\sin\theta\delta_{\gamma\gamma'}\tilde{c}^\dagger_{\mathbf{k}\gamma\uparrow}\tilde{c}_{\mathbf{k}\gamma'\downarrow}\Big]
\end{aligned} \tag{3.49}$$

Once again, the equilibrium exchange mediated torques onto the exchange effective field of the ferromagnet defined by Eqs.(3.49) are found by substituting the corresponding operators in Eq.(3.9), whereas, their non-equilibrium counterparts, with the intraband and the interband contributions separated, are found by substituting the corresponding operators in Eqs.(3.8). In the last case, the prefactor of the electric field component is a component of the so-called "torkance tensor" (to use a terminology widely used in the literature).

3.3.7 Symmetry arguments for the exchange mediated torques

As stated above, when Eqs.(3.49) are substituted in Eqs.(3.8) (for the non-equilibrium response), the outcome can be symbolically and compactly written as

$$\begin{aligned}
\left\langle \hat{T}^\alpha \right\rangle^{intra}_{noneq} &= \sum_\beta t^{intra}_{\alpha\beta}(\hat{\mathbf{\Omega}})E_\beta, \quad \alpha=\{x,y,z\}, \;\; \beta=\{x,y\} \\
\left\langle \hat{T}^\alpha \right\rangle^{inter}_{noneq} &= \sum_\beta t^{inter}_{\alpha\beta}(\hat{\mathbf{\Omega}})E_\beta, \quad \alpha=\{x,y,z\}, \;\; \beta=\{x,y\}
\end{aligned} \tag{3.50}$$

where E_β is the β-th component of the applied electric field, and $t_{\alpha\beta}(\hat{\mathbf{\Omega}}) = t^{intra}_{\alpha\beta}(\hat{\mathbf{\Omega}}) + t^{inter}_{\alpha\beta}(\hat{\mathbf{\Omega}})$ is the $\alpha\beta$-th component of the "torkance tensor", which depends on the direction of the postulated (translationally invariant) configuration for the exchange effective field of the ferromagnet. Following Ref.[18], we can decompose the torkance tensor into an even and odd part as below

$$\begin{cases} t^{even}_{\alpha\beta}(\hat{\mathbf{\Omega}})\Big|_{\text{intra}} = \frac{1}{2}\left(t_{\alpha\beta}(\hat{\mathbf{\Omega}})\Big|_{\text{intra}} + t_{\alpha\beta}(-\hat{\mathbf{\Omega}})\Big|_{\text{intra}} \right), \\ t^{odd}_{\alpha\beta}(\hat{\mathbf{\Omega}})\Big|_{\text{intra}} = \frac{1}{2}\left(t_{\alpha\beta}(\hat{\mathbf{\Omega}})\Big|_{\text{intra}} - t_{\alpha\beta}(-\hat{\mathbf{\Omega}})\Big|_{\text{intra}} \right) \end{cases} \\ \begin{cases} t^{even}_{\alpha\beta}(\hat{\mathbf{\Omega}})\Big|_{\text{inter}} = \frac{1}{2}\left(t_{\alpha\beta}(\hat{\mathbf{\Omega}})\Big|_{\text{inter}} + t_{\alpha\beta}(-\hat{\mathbf{\Omega}})\Big|_{\text{inter}} \right), \\ t^{odd}_{\alpha\beta}(\hat{\mathbf{\Omega}})\Big|_{\text{inter}} = \frac{1}{2}\left(t_{\alpha\beta}(\hat{\mathbf{\Omega}})\Big|_{\text{inter}} - t_{\alpha\beta}(-\hat{\mathbf{\Omega}})\Big|_{\text{inter}} \right) \end{cases} \tag{3.51}$$

where the even parts are even under the operation $\hat{\mathbf{\Omega}} \to -\hat{\mathbf{\Omega}}$, whereas the odd parts are odd under the aforementioned operation. According to the Fig.2.5, the Oyz coordinate plane is a mirror plane, and it is also noted that the applied electric field is always chosen to be along the positive Ox axis. Under the aforementioned mirror symmetry, the applied electric field is inverted, and further, a postulated configuration (for the exchange effective field) along the Ox axis remains invariant, whereas, postulated configurations (for the exchange effective field) along the Oy or the Oz axes are inverted. A similar argument can be employed for the components of the exchange-mediated transferred torque (which is also a pseudo-vector).

Now, taking into consideration all the previous analysis of this subsection, it turns out that when the exchange effective field is oriented along the

Ox axis, the $t_{yx}^{intra}(\Omega_x)/t_{yx}^{inter}(\Omega_x)$ as well as the $t_{zx}^{intra}(\Omega_x)/t_{zx}^{inter}(\Omega_x)$ torkance components are not restricted by the Oyz mirror symmetry, in other words, they can have either even or odd parts. Furthermore, when the exchange effective field is oriented along the Oy axis, it turns out that $t_{xx}^{even}(\Omega_y)\big|_{\text{intra}} = t_{xx}^{even}(\Omega_y)\big|_{\text{inter}} = 0$, and also, $t_{zx}^{odd}(\Omega_y)\big|_{\text{intra}} = t_{zx}^{odd}(\Omega_y)\big|_{\text{inter}} = 0$, as a result of the Oyz mirror symmetry. Finally, when the exchange effective field is oriented along the Oz axis, it is found that $t_{xx}^{even}(\Omega_z)\big|_{\text{intra}} = t_{xx}^{even}(\Omega_z)\big|_{\text{inter}} = 0$, and also, $t_{yx}^{odd}(\Omega_z)\big|_{\text{intra}} = t_{yx}^{odd}(\Omega_z)\big|_{\text{inter}} = 0$, as a result of the Oyz mirror symmetry.

Let us then turn our attention to the time reversal operation. It can be easily verified that the intraband contribution to the various components of the exchange-mediated transferred torque (given in Eq.(3.50)) is odd under the time reversal operation. Since the electric field is even under the time reversal operation, the intraband torkance components should be odd under the time reversal operation, and therefore they consist of odd parts only (to use the decomposition of Eq.(3.51)). Since we found that as a result of the Oyz mirror symmetry, it is $t_{zx}^{odd}(\Omega_y)\big|_{\text{intra}} = 0$ and $t_{yx}^{odd}(\Omega_z)\big|_{\text{intra}} = 0$, it is expected that the intraband contribution to the z-component of the transferred torque when the postulated exchange effective field is oriented along the Oy axis, as well as the intraband contribution to the y-component of the transferred torque when the postulated exchange effective field is oriented along the Oz axis, are both zero. A similar line of arguments based on the time reversal operation, leads to the restrictions that $t_{yx}^{even}(\Omega_x)\big|_{\text{intra}} = t_{zx}^{even}(\Omega_x)\big|_{\text{intra}} = 0$. Concluding this subsection, it should be mentioned that the exchange-mediated transferred

torques that are even under the operation $\hat{\mathbf{\Omega}} \rightarrow -\hat{\mathbf{\Omega}}$ are usually referred to as damping/antidamping-like torques, whereas those that are odd under the operation $\hat{\mathbf{\Omega}} \rightarrow -\hat{\mathbf{\Omega}}$ are usually referred to as field-like torques.

3.4 Results, discussion and conclusions

In the previous sections, we developed a simple formalism (which, loosely speaking, looks like a circuit theory) with a view to studying spin orbit torque related effects in bilayer structures that lack spatial inversion symmetry, consisting of a ferromagnetic metal film deposited on a heavy metal film. Even though the real materials are three-dimensional structures consisting of several layers each, and in some cases consisting also of capping layers made of a completely different material, our starting point has been the interface between the heavy metal and the ferromagnetic metal material which certainly plays an important role. However, once again, at the interface between the two materials the situation can easily turn quite messy, and to simplify the overall approach (as already stated) we had to recourse to various drastic approximations elaborated in the previous chapter. On top of that, owing to the uncertainty of the precise values of several band structure related parameters, it was considered prudent to drastically reduce the number of the band structure related parameters to a minimal set of parameters, which are then treated as free (variable) parameters of the model. To remind the reader, those are the spin orbit coupling strength of the heavy metal, the effective exchange coupling of the ferromagnet (related to the energy splitting between its majority and

minority bands), the interlayer hybridization (originating from the strongest Slater-Koster radial parameters), and the 3d-5d atomic orbital on-site effective energy offset. With the help of this minimal edifice, let us now turn our attention to some of the predictions/results of the above developed formalism. We will not attempt to provide any microscopic explanations of the presented results since the situation turns out to be quite complex even under all those simplifications. To avoid overloading the manuscript (although we will overload it a bit) with figures, we focus our attention on the behavior of some of the observable quantities defined in the previous sections as a function of the spin orbit coupling of the heavy metal and the effective exchange coupling of the ferromagnetic metal, with the rest of the parameters of the model fixed (in other words, we artificially see the evolution of various observable quantities to their final values, as the spin-orbit coupling strength of the heavy metal and the exchange effective field of the ferromagnetic metal are gradually switched on up to a representative final value each). In the numerical calculation, the relaxation time parameter was chosen equal to 10^{-13} sec (6.5 meV), and the magnitude of the applied transport electric field equal to 10^{4} V/m. It is also noted that the configurations postulated for the exchange effective field of the ferromagnet are those shown in Fig.2.6 (all of them were taken into account). Brief highlights follow in any case.

Saying so, let us now turn our attention to the Figs.3.1 through 3.6 below. Careful inspection of the aforementioned set of figures first of all shows that the effective exchange coupling of the ferromagnet has a strong suppres-

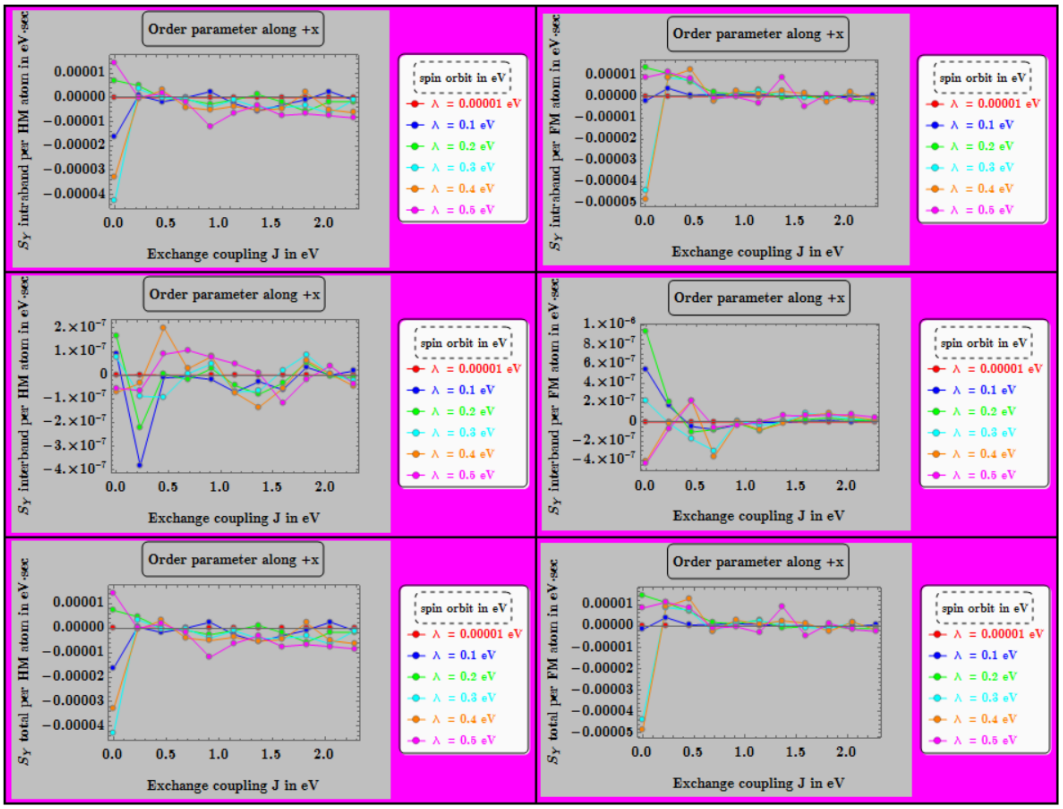

Figure 3.1: Y-component of the transverse (to the order parameter of the ferromagnet) spin accumulation within the heavy metal layer (left column) and the ferromagnetic layer (right column). From top to bottom, at each column, the intraband, the interband and the total (intraband+interband) contribution are shown. The only variable parameters are the effective exchange coupling of the ferromagnet (abscissa), and the spin orbit coupling strength of the heavy metal (adjacent inset). The postulated configuration of the exchange effective field of the ferromagnet is given on top of each subfigure.

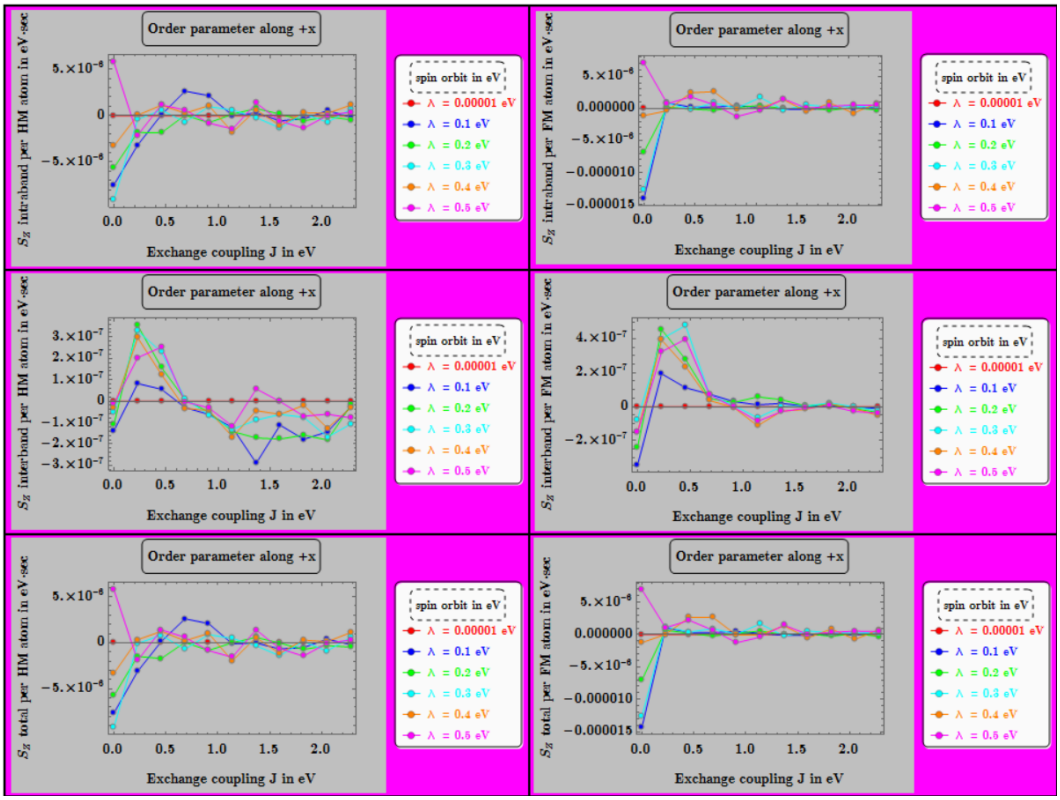

Figure 3.2: Z-component of the transverse (to the order parameter of the ferromagnet) spin accumulation within the heavy metal layer (left column) and the ferromagnetic layer (right column). From top to bottom, at each column, the intraband, the interband and the total (intraband+interband) contribution are shown. The only variable parameters are the effective exchange coupling of the ferromagnet (abscissa), and the spin orbit coupling strength of the heavy metal (adjacent inset). The postulated configuration of the exchange effective field of the ferromagnet is given on top of each subfigure.

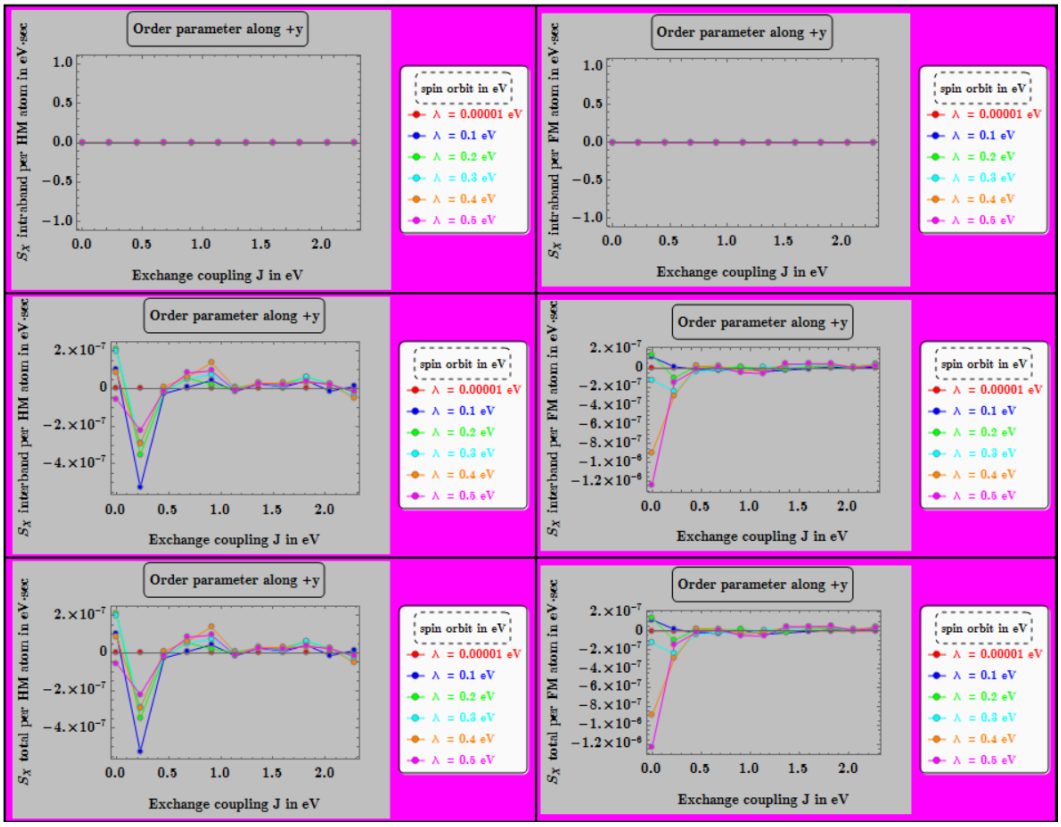

Figure 3.3: X-component of the transverse (to the order parameter of the ferromagnet) spin accumulation within the heavy metal layer (left column) and the ferromagnetic layer (right column). From top to bottom, at each column, the intraband, the interband and the total (intraband+interband) contribution are shown. The only variable parameters are the effective exchange coupling of the ferromagnet (abscissa), and the spin orbit coupling strength of the heavy metal (adjacent inset). The postulated configuration of the exchange effective field of the ferromagnet is given on top of each subfigure.

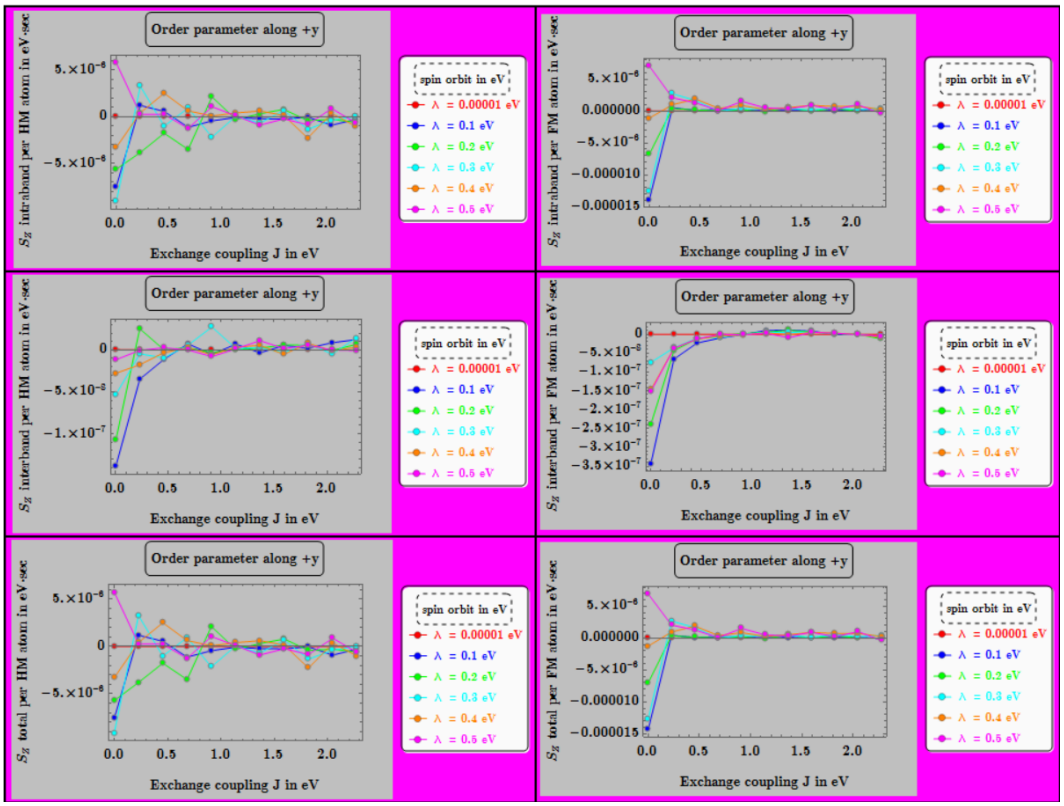

Figure 3.4: Z-component of the transverse (to the order parameter of the ferromagnet) spin accumulation within the heavy metal layer (left column) and the ferromagnetic layer (right column). From top to bottom, at each column, the intraband, the interband and the total (intraband+interband) contribution are shown. The only variable parameters are the effective exchange coupling of the ferromagnet (abscissa), and the spin orbit coupling strength of the heavy metal (adjacent inset). The postulated configuration of the exchange effective field of the ferromagnet is given on top of each subfigure.

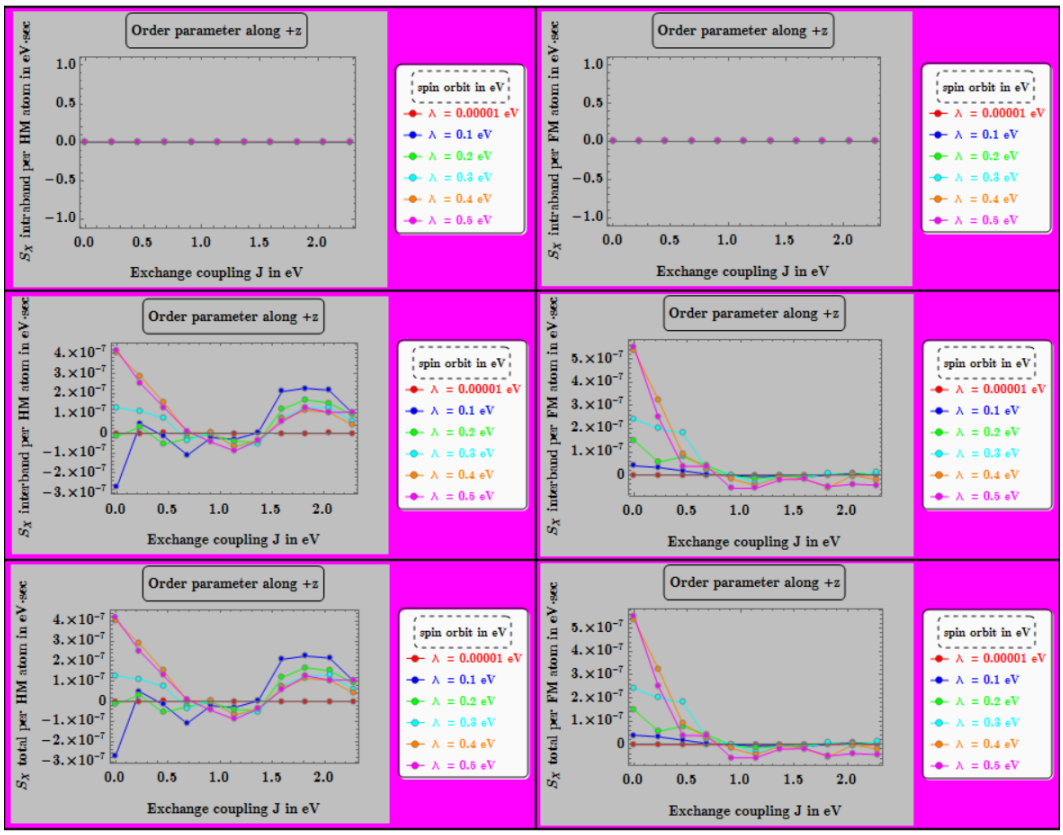

Figure 3.5: X-component of the transverse (to the order parameter of the ferromagnet) spin accumulation within the heavy metal layer (left column) and the ferromagnetic layer (right column). From top to bottom, at each column, the intraband, the interband and the total (intraband+interband) contribution are shown. The only variable parameters are the effective exchange coupling of the ferromagnet (abscissa), and the spin orbit coupling strength of the heavy metal (adjacent inset). The postulated configuration of the exchange effective field of the ferromagnet is given on top of each subfigure.

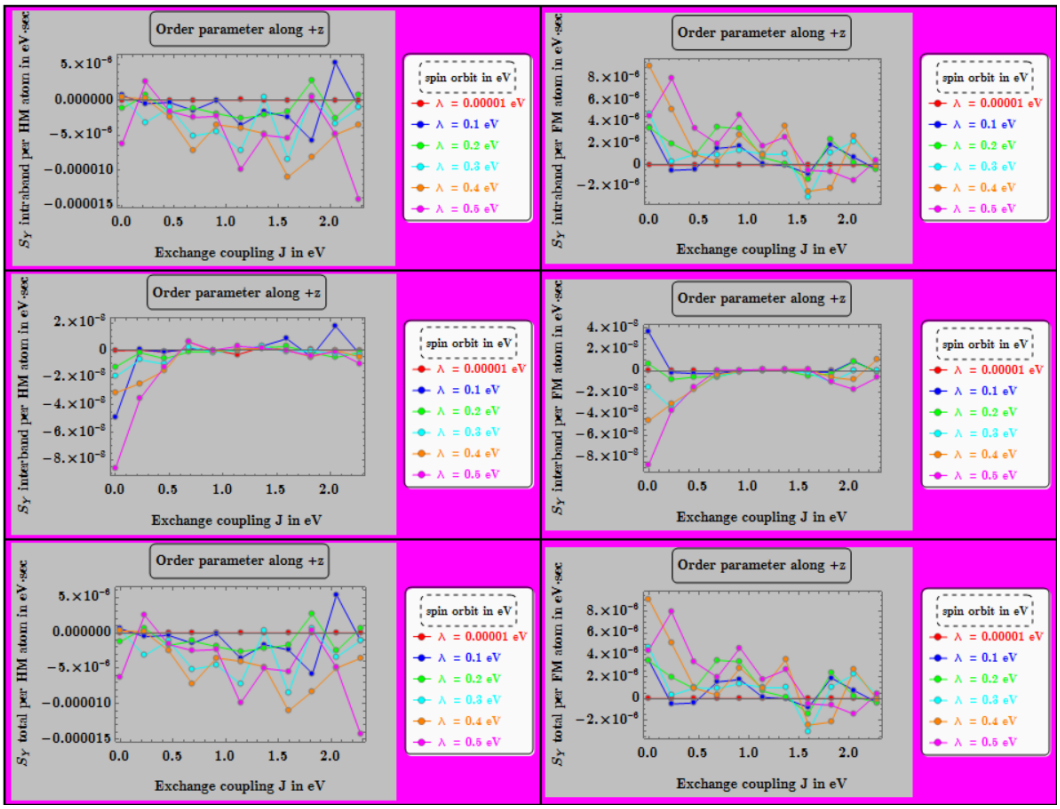

Figure 3.6: Y-component of the transverse (to the order parameter of the ferromagnet) spin accumulation within the heavy metal layer (left column) and the ferromagnetic layer (right column). From top to bottom, at each column, the intraband, the interband and the total (intraband+interband) contribution are shown. The only variable parameters are the effective exchange coupling of the ferromagnet (abscissa), and the spin orbit coupling strength of the heavy metal (adjacent inset). The postulated configuration of the exchange effective field of the ferromagnet is given on top of each subfigure.

sive effect on the transverse (to the exchange effective field) spin accumulation within the magnetic layer. This is in stark contrast to the effect of the spin orbit coupling of the heavy metal, which seems to favor a transverse to the exchange effective field of the ferromagnet spin accumulation, predominantly within the heavy metal layer. In the second place, it is easily verified that the strongest spin accumulation effect is observed along the Oy direction when the exchange effective field of the ferromagnet is oriented along the Oz direction (see Fig.3.6), predominantly originating from intraband responses. Last but not least, it is easily seen that the transverse spin accumulation is, generally speaking, an anisotropic effect, and further, any intraband contribution to it is found to be even under the operation $\hat{\mathbf{\Omega}} \rightarrow -\hat{\mathbf{\Omega}}$. Generally speaking, there can be both intraband and interband contributions to the various components of the transverse to the exchange effective field of the ferromagnet spin accumulation.

A second result of the above developed formalism is given in Figs.3.7 through 3.12 below, which show different components of the exchange-mediated torque transferred to the exchange effective field of the ferromagnet, for different postulated orientations of the latter. The 3d-5d atomic orbital (on-site effective energy) offset as well as the interlayer hybridization are fixed, whereas the strength of the exchange coupling within the ferromagnet and the spin orbit coupling within the heavy metal layer are varied. A careful inspection of the aforementioned set of figures shows first of all that the intraband contribution is in any case odd under the operation $\hat{\mathbf{\Omega}} \rightarrow -\hat{\mathbf{\Omega}}$. An analogous argument

for the corresponding interband contribution cannot be used though.

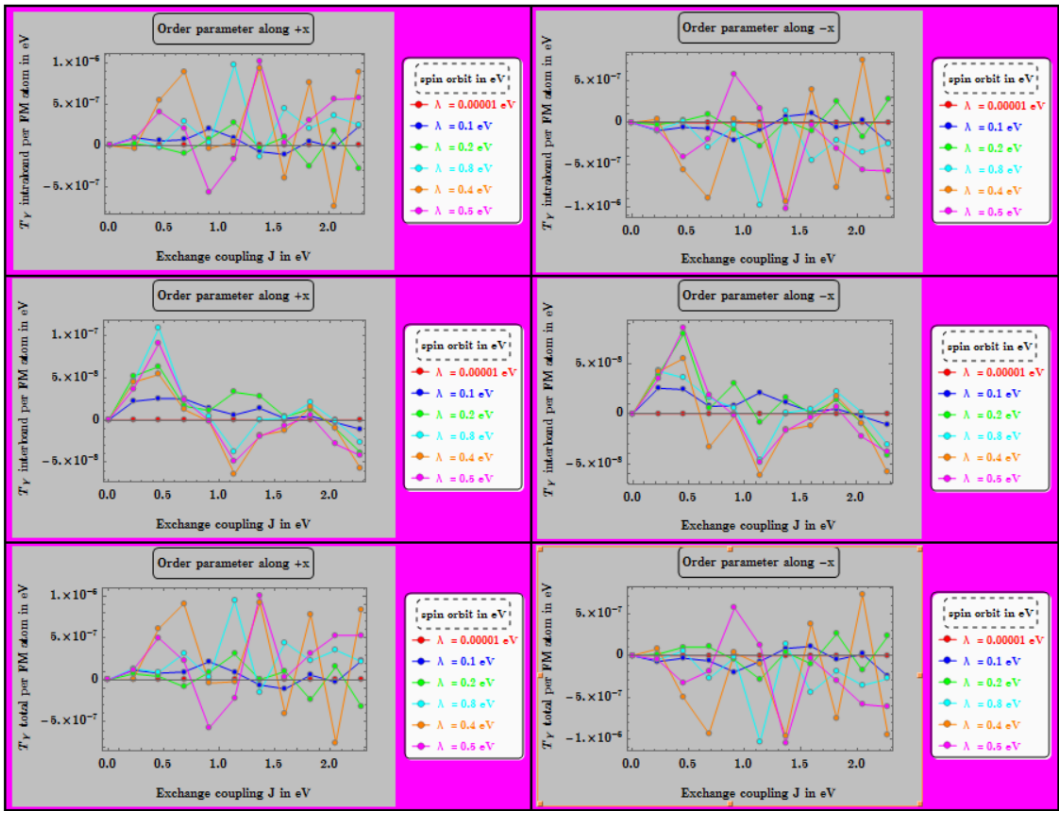

Figure 3.7: Y-component of the exchange mediated torque onto the exchange effective field of the ferromagnet, for two opposite postulated orientations (left and right column) of the latter along the x direction. From top to bottom, at each column, the intraband, the interband and the total (intraband+interband) contribution are shown. The only variable parameters are the effective exchange coupling of the ferromagnet (abscissa), and the spin orbit coupling strength of the heavy metal (adjacent inset).

Aside that, the reader can easily verify the symmetry based predictions detailed in section 3.3.7 for the intraband contributions. For instance, as a result of the Oyz mirror symmetry, it was concluded that the intraband contribution to the z-component of the transferred torque when the postulated

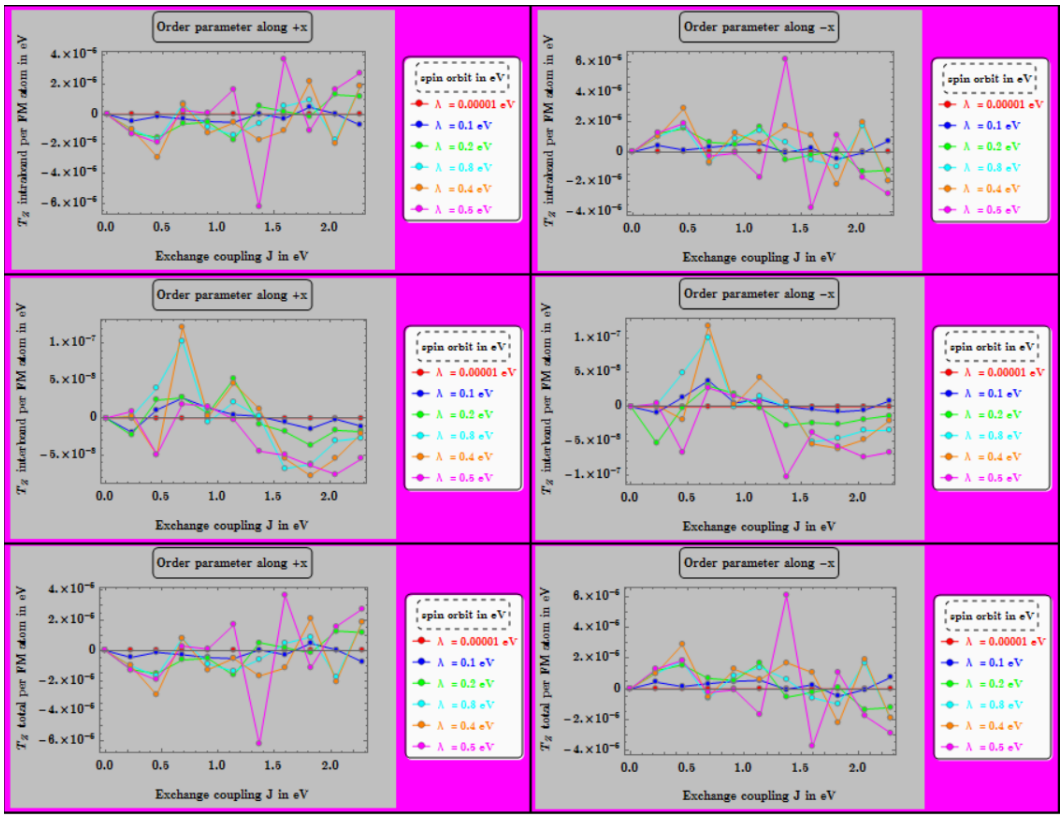

Figure 3.8: Z-component of the exchange mediated torque onto the exchange effective field of the ferromagnet, for two opposite postulated orientations (left and right column) of the latter along the x direction. From top to bottom, at each column, the intraband, the interband and the total (intraband+interband) contribution are shown. The only variable parameters are the effective exchange coupling of the ferromagnet (abscissa), and the spin orbit coupling strength of the heavy metal (adjacent inset).

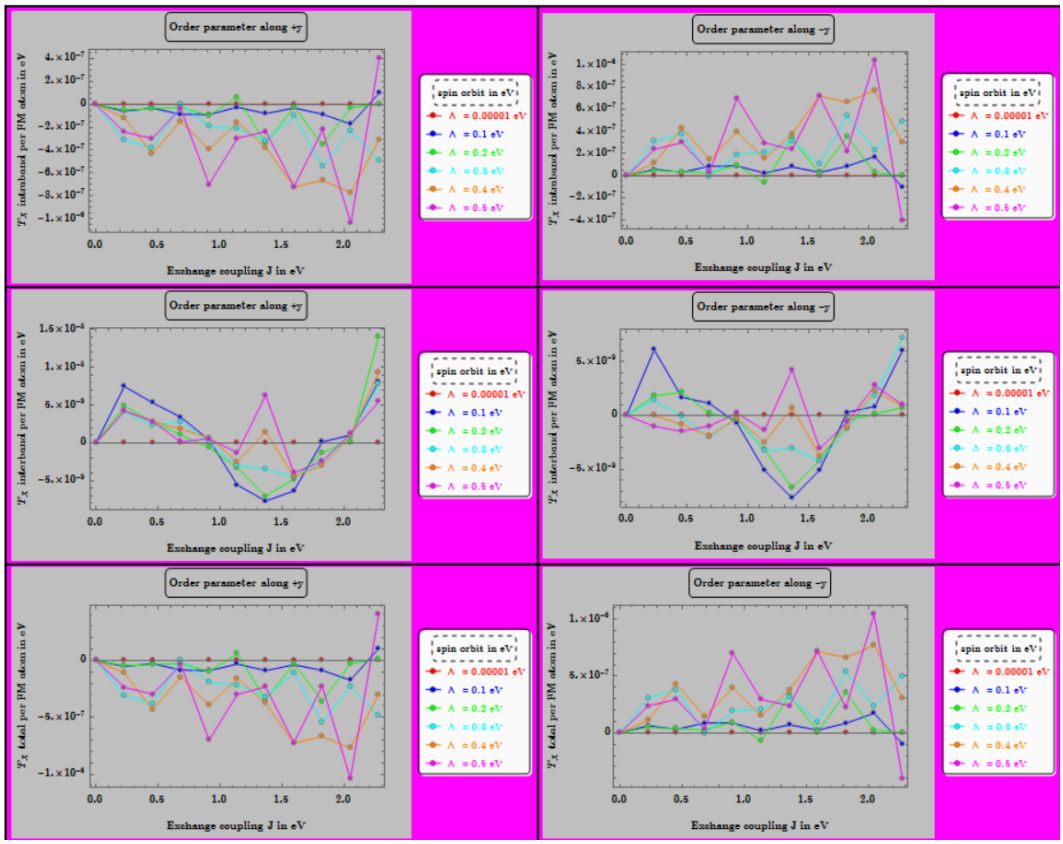

Figure 3.9: X-component of the exchange mediated torque onto the exchange effective field of the ferromagnet, for two opposite postulated orientations (left and right column) of the latter along the y direction. From top to bottom, at each column, the intraband, the interband and the total (intraband+interband) contribution are shown. The only variable parameters are the effective exchange coupling of the ferromagnet (abscissa), and the spin orbit coupling strength of the heavy metal (adjacent inset).

Figure 3.10: Z-component of the exchange mediated torque onto the exchange effective field of the ferromagnet, for two opposite postulated orientations (left and right column) of the latter along the y direction. From top to bottom, at each column, the intraband, the interband and the total (intraband+interband) contribution are shown. The only variable parameters are the effective exchange coupling of the ferromagnet (abscissa), and the spin orbit coupling strength of the heavy metal (adjacent inset).

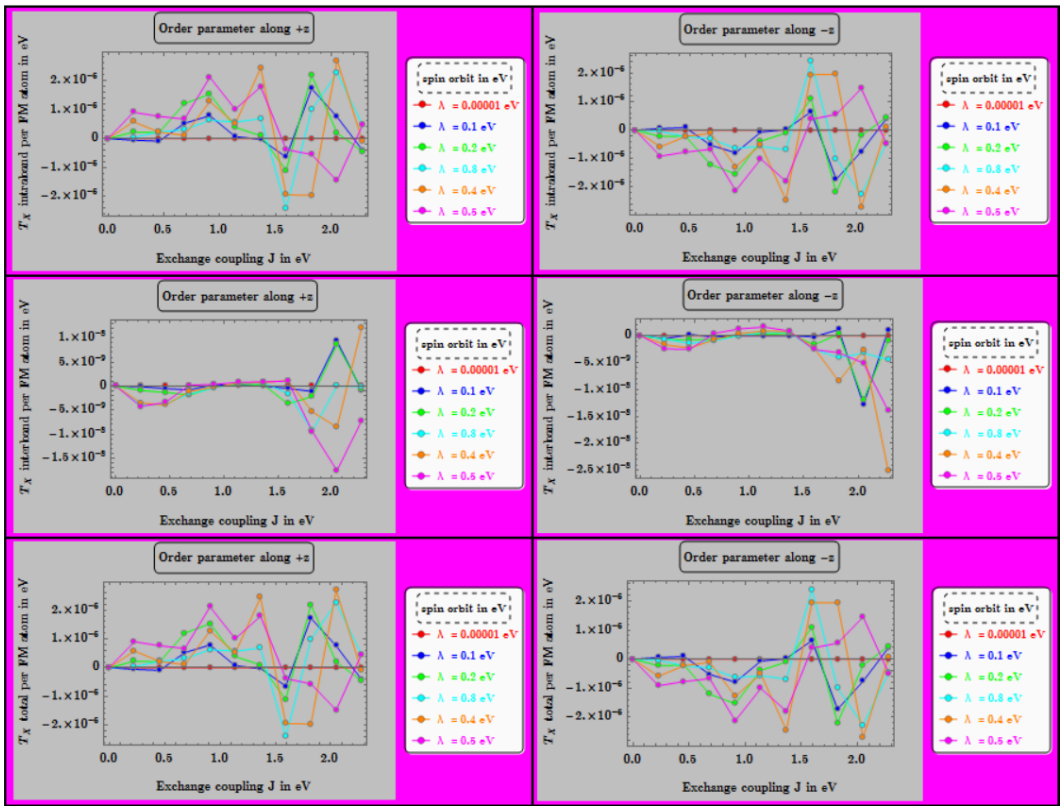

Figure 3.11: X-component of the exchange mediated torque onto the exchange effective field of the ferromagnet, for two opposite postulated orientations (left and right column) of the latter along the z direction. From top to bottom, at each column, the intraband, the interband and the total (intraband+interband) contribution are shown. The only variable parameters are the effective exchange coupling of the ferromagnet (abscissa), and the spin orbit coupling strength of the heavy metal (adjacent inset)

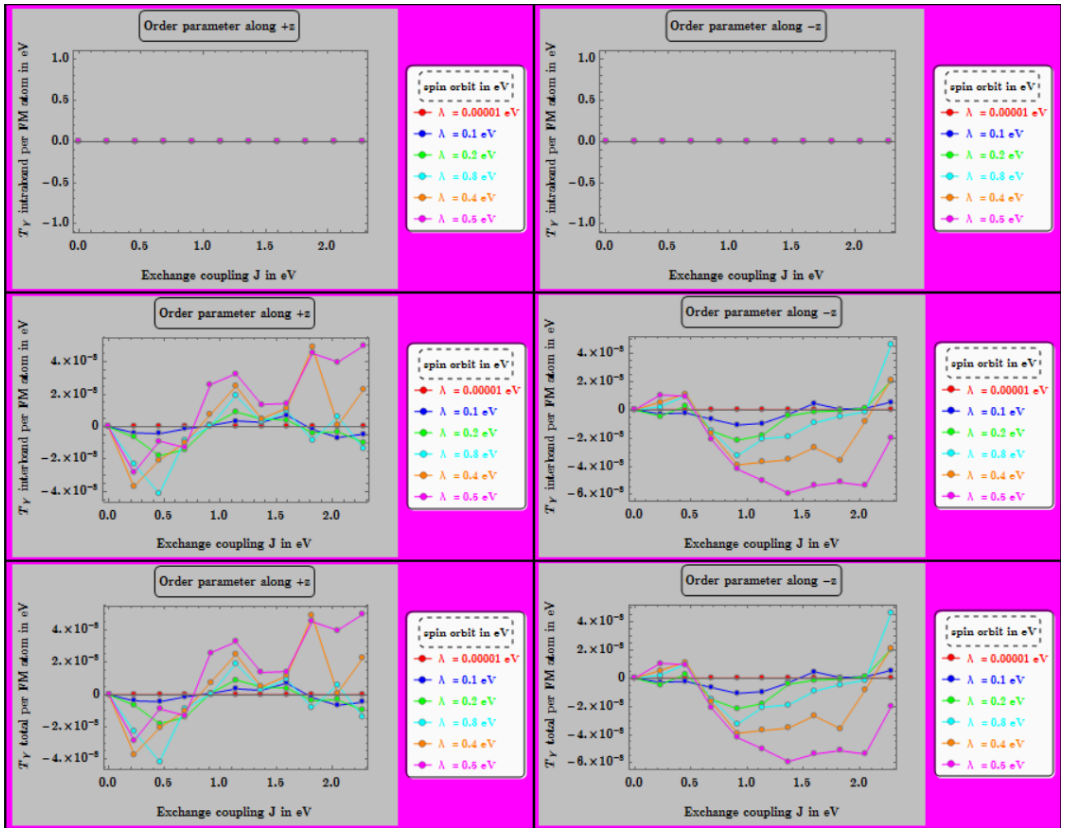

Figure 3.12: Y-component of the exchange mediated torque onto the exchange effective field of the ferromagnet, for two opposite postulated orientations (left and right column) of the latter along the z direction. From top to bottom, at each column, the intraband, the interband and the total (intraband+interband) contribution are shown. The only variable parameters are the effective exchange coupling of the ferromagnet (abscissa), and the spin orbit coupling strength of the heavy metal (adjacent inset).

exchange effective field is oriented along the Oy axis, as well as the intraband contribution to the y-component of the transferred torque when the postulated exchange effective field is oriented along the Oz axis, are both zero, something which is easily seen on the top subfigures of Figs.3.10 and 3.12. From the above figures, it is also noticed that as far as the exchange mediated torques transferred to the exchange effective field of the ferromagnet are concerned, it is possible that an important contribution to them originates from intraband responses. See for example the top subfigures of Figs. 3.7, 3.8 and 3.11.

Several other observables (of those developed in the previous sections) were calculated and sketched as a function of the same parameters as those varied in Figs.3.7 through 3.12 above (with the rest of the minimal set parameters fixed), but to keep the volume of this manuscript reasonable we do not show the relevant results here. Few highlights before concluding this chapter are imperative though. For one thing, a quantity that is of interest in all those experiments with SOTs is the so-called spin Hall angle defined as (c denotes the thickness of the bilayer below, α denotes the torque component and β the postulated spatial orientation of the exchange effective field of the ferromagnet)

$$\theta_{SH}^{\alpha\beta} = \frac{2e}{\hbar}\frac{J_{exch}^{\alpha\beta}}{J_e} = \frac{2e}{\hbar} \times \frac{\left\langle \hat{T}^{\alpha\beta} \right\rangle_{noneq}^{per\ atom}}{J_e} \times c \times N_{unit\ cells},\ \alpha,\beta = \{x,y,z\},\ \alpha \neq \beta \tag{3.52}$$

i.e. as the ratio of the spin current density that via the exchange interaction is manifested as a torque onto the exchange effective field of the ferromagnet

(this current crosses through the interface between the two materials), and the longitudinal charge current density in the bilayer structure (which crosses through a cross section normal to the applied electric field). The prefactor is necessary in order to get a dimensionless result. In our convention, the superscript β denotes the postulated orientation/configuration of the exchange effective field of the ferromagnet, and the superscript α the component of the exchange mediated transferred torque. Saying so, a spin Hall angle result (based on the same series of calculations as those shown in the previous figures) is shown in Fig.3.13 below. As seen from the figure below, certainly the spin-orbit coupling can affect the magnitude of the spin Hall angle, although its effect far from the heavy metal, within the ferromagnet seems to be intercepted by the strong exchange coupling of the ferromagnet. However, the question of what are the optimal band-structure related parameters that could lead to higher values of the various spin Hall angle components is a subtle question that requires harder and deeper investigation (and imagination I would say)! Aside this, we also launched a similar cycle of calculations but this time assuming an A-A type of stacking for the bilayer structure but since not all the results are out we prefer to keep silent about this. Last but not least, same as for the Dzyaloshinskii-Moriya effect, going beyond the two layers considered above, could maybe unsurprisingly modify the outcome for various observables, signaling at the same time the fact that the whole story is not necessarily fully transpired right at the interface, but such an analysis is beyond this work.

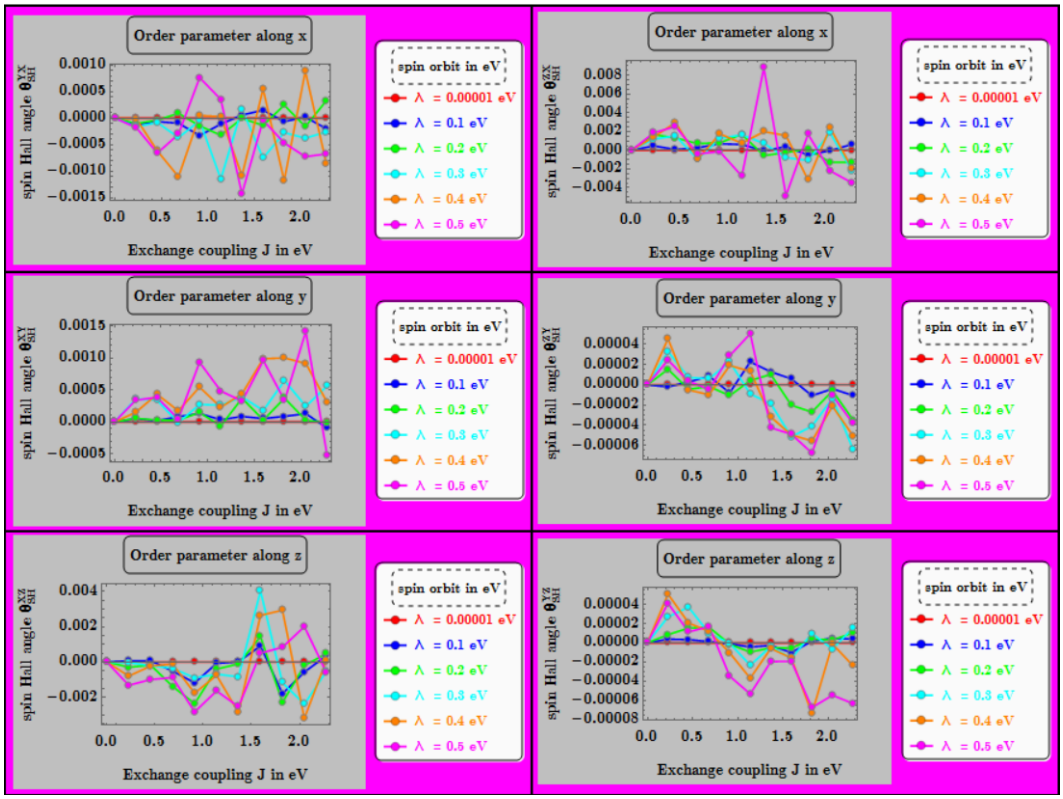

Figure 3.13: Spin Hall angle results for different postulated configurations of the exchange effective field of the ferromagnet (shown on the top of each subfigure), for different torque components (the torque component taken into account is denoted by the first superscript of the spin Hall angle notation). The only variable parameters are the effective exchange coupling of the ferromagnet (abscissa), and the spin orbit coupling strength of the heavy metal (adjacent inset).

Chapter 4

Thermal conductivity of 2D local moment models with strong spin orbit coupling

4.1 Motivation

The influence of the spin-orbit coupling in the solid state is nowadays a very widely explored topic as witnessed by the volume of the papers published about or related to this topic every year, over the last several years [1]. Saying so, this work is actually motivated by studying the effect of the spin-orbit coupling on equally important but less extensively studied up to this day solid state properties, such as the thermal conductivity property. In this work, we focus on the thermal transport properties of two dimensional strong spin-orbit driven magnetic insulators, and more specifically study a magnetic insulator described by the so-called Heisenberg-Kitaev model on a honeycomb lattice (Refs.[7, 8, 23]). Since the theoretical framework of this project is sufficiently developed in the collaborative work of Ref.[57], I will present only the key points of the theoretical set-up of this project (skipping all formulae which one can look up

[1] Part of this chapter appears in Phys.Rev.B 95, 064410 (2017) under the title "Thermal conductivity of local moment models with strong spin orbit coupling", authored by G.L.Stamokostas, P.E.Lapas and G.A.Fiete. The author of this dissertation contributed to the project by setting up the theoretical formalism of the project which is briefly outlined here, but is presented in full detail in the aforementioned publication.

in Ref.[57]), however, paying particular attention to the presentation of the final results.

4.2 Overview of the theoretical formalism

In this work, we actually study the intersite (or two-site) magnetoelastic coupling effect focusing on a magnetic insulator described by the two-parametric nearest neighbor (NN) Heisenberg-Kitaev model on the honeycomb lattice. It should be noted also that intrasite (or single-site) contributions to the magnetoelastic coupling effect cannot be studied by the formalism developed here (they cannot even be captured by such a formalism, Ref.[31]), and further, that the formalism developed here as it is is only appropriate for collinear magnetically ordered states (Refs.[19, 37]). Indeed, the NN Heisenberg-Kitaev model has a rich phase diagram which (among other non-magnetically ordered states) contains several collinear magnetically ordered states: a zig-zag state, a Néel state, a stripy state and a ferromagnetic state. It is only the magnetically ordered states that are of interest in this work (as opposed to, for instance, spin liquid states). Afterwards, given the low energy effective magnetic Hamiltonian stated above, assuming we are at temperatures much lower than an appropriately defined (based on the values of the exchange coupling parameters of the model) magnetic transition temperature, we study the corresponding low energy excitations (magnons) within the linear spin wave approximation. Terms trilinear, quadrilinear and higher order in the magnon operators, which actually lead to a renormalization of the magnon

bands via various magnon-magnon interactions, are assumed to be negligible at temperatures much lower than an appropriately defined magnetic transition temperature.

As far as the lattice degrees of freedom are concerned, assuming temperatures much lower than an appropriately defined Debye temperature for the magnetic insulator, only the energy of the lattice displacements to quadratic order is retained which leads to the phonon spectrum in the standard way. The phonons considered in this work are purely two-dimensional acoustic phonons, which only disperse within the plane of the honeycomb lattice, described by spatially isotropic dispersion relations and subject to the Debye model.

The coupling between the phonons and the magnons enters through the distance dependence of the exchange couplings of the NN Heisenberg-Kitaev model on the dynamic positions of the magnetic ions at two nearest neighboring lattice sites. Assuming a small displacement of the magnetic ions from their equilibrium positions, the aforementioned exchange couplings are Taylor-expanded to lowest order in the displacement of the magnetic ions from their equilibrium positions, which is (to lowest order) the so-called "intersite magnetoelastic coupling" mentioned previously. Now, focusing on temperatures much lower than both an appropriately defined magnetic transition temperature and an appropriately defined Debye temperature, where presumably one-phonon processes are more important than multiple phonon processes, and, under the assumption of a weak magnon-phonon coupling (a hypothesis that should be carefully checked as we elaborate later on), the dominant interac-

tion term for our study is the so-called "one-phonon two-magnon" interaction term. The appropriate form of the one-phonon two-magnon interaction term though, is found after first performing the following steps; we first diagonalize the linear spin wave Hamiltonian, and afterwards, the aforementioned dominant interaction term is expressed in terms of the magnon operators that diagonalize the linear spin wave Hamiltonian. The switch from the old set to a new set of magnon operators is achieved with the help of the eigenvectors of a numerical Bogoliubov-Valatin transformation, for which a standard recipe is clearly described in Ref.[57].

Furthermore, in this work we study two distinct (opposite limit) thermal transport regimes depending on whether the magnon or the phonon energy scale dominates (Refs.[22, 34]). In the case in which the magnon characteristic energy scale dominates, phonons play the role of the bath, and presuming a weak magnon-phonon coupling, the problem translates into a problem of a system weakly interacting with a bath. The relevant lowest order non-equivalent Feynmann diagrams to be used for the calculation of the transport relaxation times are those appearing in Fig.4.1 below. The opposite limit, is the case in which the phonon characteristic energy scale dominates, magnons play the role of the bath, and we again have a problem of a system weakly interacting with a bath. In this case, the relevant lowest order non-equivalent Feynmann diagrams to be used for the calculation of the respective transport relaxation times are those appearing in Fig. 4.2 below.

In either case, given the matrix elements of the one-phonon two-magnon

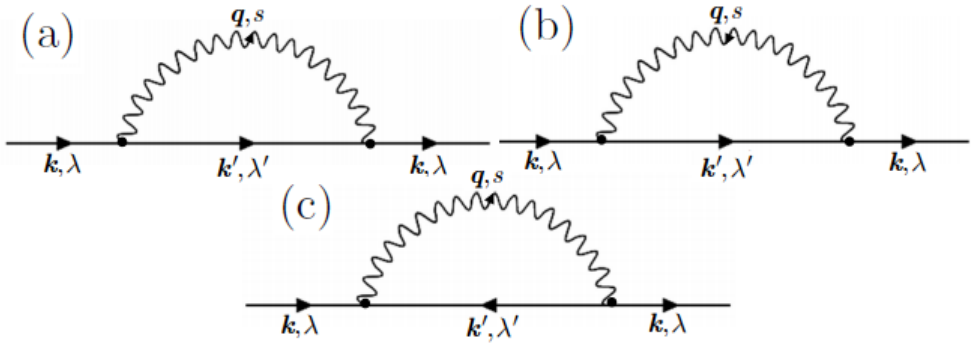

Figure 4.1: Lowest order magnon-phonon scattering diagrams used for the calculation of the transport relaxation times in the regime in which thermal transport is magnon-dominated. Straight lines represent magnon propagators whereas wavy lines are phonon propagators. Figures (a) and (b) represent R-processes which involve phonon emissions or absorptions. Fig.(c) represents C-processes which involve phonon emission or absorption.

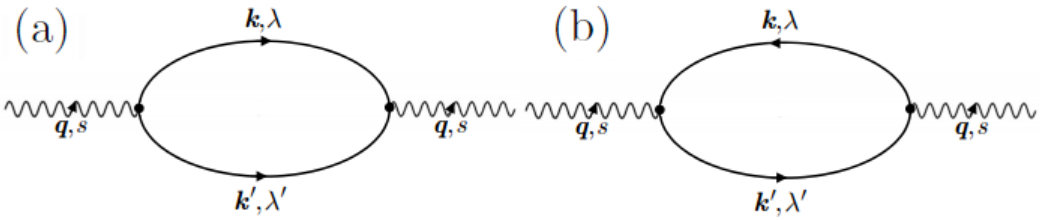

Figure 4.2: Lowest order magnon-phonon scattering diagrams used for the calculation of the transport relaxation times in the regime in which thermal transport is phonon-dominated. Wavy lines represent phonon propagators whereas straight lines are magnon propagators. Fig.(a) represents C-processes which involve two magnon creations or annihilations, where-as Fig.(b) represents R-processes that involve phonon emission or absorption.

scattering processes, one can calculate the respective transport relaxation times by using the Fermi's Golden Rule for each (bare) magnon-phonon interaction vertex, at which momentum conservation (not momentum equivalence as in the *Umklapp processes*) is imposed. Once the transport relaxation times for phonons and magnons are calculated, there comes the final step at which all those results are patched together to compute the diagonal components of the thermal conductivity tensor for each one of the ordered magnetic states of the effective magnetic Hamiltonian mentioned above. The calculation of the thermal conductivity tensor components proceeds via the semiclassical Boltzmann transport theory, within the relaxation time approximation.

In this study, we focus on two only of the various relaxation mechanisms that can appear during thermal transport processes: the magnon-phonon scattering mechanism and the always existent boundary scattering mechanism (for either the phonons or the magnons). The contribution of each of the aforementioned relaxation mechanisms in a corresponding transport relaxation time is presumed to obey a "Matthiessen rule". Furthermore, as already stressed above, depending on the relative strength of the characteristic energy scales of the two types of heat carriers (magnons/phonons), we refer to the two opposite limit thermal transport regimes as the *phonon dominated* regime, and the *magnon dominated* regime, which themselves consist of three subregimes each, the *diffusive*, the *intermediate*, and the *ballistic* subregime. Last but not least, it should be stressed that the more general and experimentally more relevant case, in which both types of carriers participate on an equal footing in the

total thermal conductivity requires a more sophisticated treatment than the one sketched out above, which is beyond this work (Refs.[16, 17]).

4.3 Results, discussion and conclusions

In the following subsections, first the effect of the pure boundary scattering on the heat transport is examined by taking both the magnon and the phonon heat carriers into account. Afterwards, the effect of the magnon-phonon scattering mechanism, particularly of the two-magnon one-phonon scattering mechanism to lowest order, is taken into account on top of the pure boundary scattering. However, in order to simplify the whole treatment, this work focuses on the two simple limiting cases mentioned above, the phonon dominated and the magnon dominated regime, in which only one type of heat carriers dominates the thermal conductivity. Within the two aforementioned regimes, both scattering mechanisms (boundary and magnon-phonon) are examined for the dominant heat carrier. Since in the following analysis we will repeatedly refer to the x and y directions of the honeycomb structure, those are shown in Fig.4.3 below.

4.3.1 Boundary scattering dominated/fully ballistic regime

In this subsection, the *ballistic* behavior of the diagonal components κ_{xx} and κ_{yy} of the thermal conductivity tensor per unit area is studied, for all the magnetically ordered phases of the nearest-neighbor Heisenberg-Kitaev Hamiltonian, versus temperature, for three different relative strengths of the

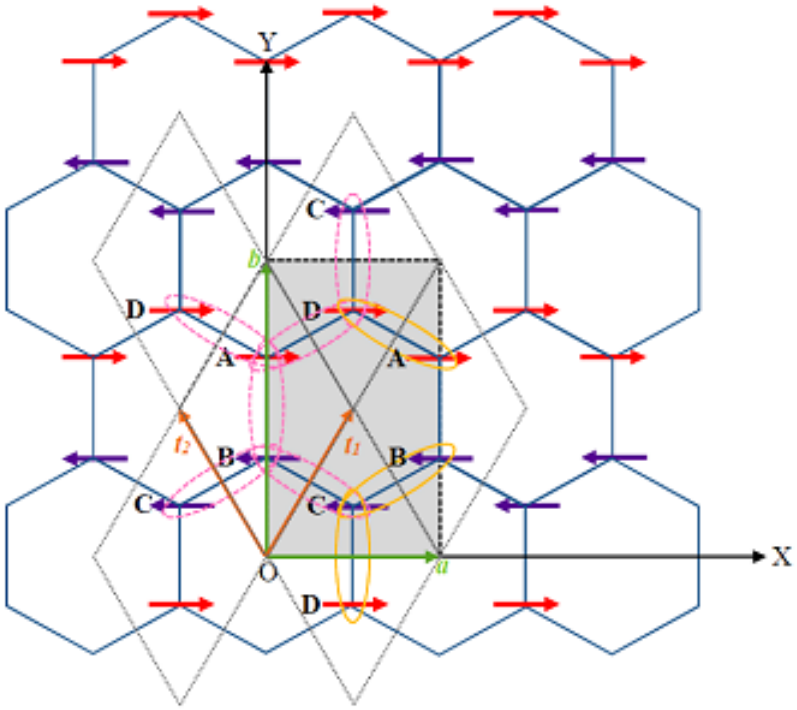

Figure 4.3: Zig-zag magnetic phase: A magnetic unit cell consists of four magnetic moments labelled as A, B, C and D, and is represented by the gray-shaded rectangle shown in the figure. The translation vectors of the periodic magnetic structure are the vectors a and b. The translation vectors of the chemical periodic structure are the vectors t_1 and t_2, and a chemical unit cell is represented by any dashed parallelogram. For the Néel and the ferromagnetic states the magnetic unit cell coincides with the chemical unit cell (that is common to all phases).

magnon and the phonon characteristic energy scales. Temperature is measured in units of $[T] = \frac{SA}{k_B}$, where S is the spin of the local moment at each site, k_B the Boltzmann constant, and A a magnetic energy scale defined in terms of the parameters of the NN Heisenberg-Kitaev Hamiltonian. For the numerical calculations, it is more convenient to convert the ballistic magnon conductivity per unit area to a dimensionless one,

$$\kappa_{mag}^{ball} = \frac{1}{2\pi}\frac{L}{a}\frac{k_B SA}{\hbar} \times \tilde{\kappa}_{mag}^{ball}, \tag{4.1}$$

where $\tilde{\kappa}_{mag}^{ball}$ is the dimensionless ballistic magnon thermal conductivity per unit area, $a = \alpha\sqrt{3}$ with α denoting the interionic distance, and L denotes the length of the crystal (in the direction of the applied temperature gradient), and the same is done for the ballistic phonon conductivity,

$$\kappa_{pho}^{ball} = \left(\frac{E_D}{SA}\right)^3 \frac{1}{2\pi}\frac{L}{a}\frac{k_B SA}{\hbar} \times \tilde{\kappa}_{pho}^{ball}, \tag{4.2}$$

where $\tilde{\kappa}_{pho}^{ball}$ is the dimensionless ballistic phonon thermal conductivity, and $E_D \equiv \hbar v_D q_D = \hbar v_D 2\pi/\alpha\sqrt{3}$ is a Debye energy scale. The total ballistic thermal conductivity is

$$\kappa_{tot}^{ball} = \kappa_{mag}^{ball} + \kappa_{pho}^{ball}. \tag{4.3}$$

Eqs.(4.1), (4.2) and (4.3) are applied to each of the diagonal components of the conductivity tensor independently, and the results are shown in Figs. 4.4 and 4.5 below.

In Figs. 4.4 and 4.5 the temperature region was chosen well below an appropriately defined magnetic transition temperature as well as an appropriately defined Debye temperature, since our system of study is assumed

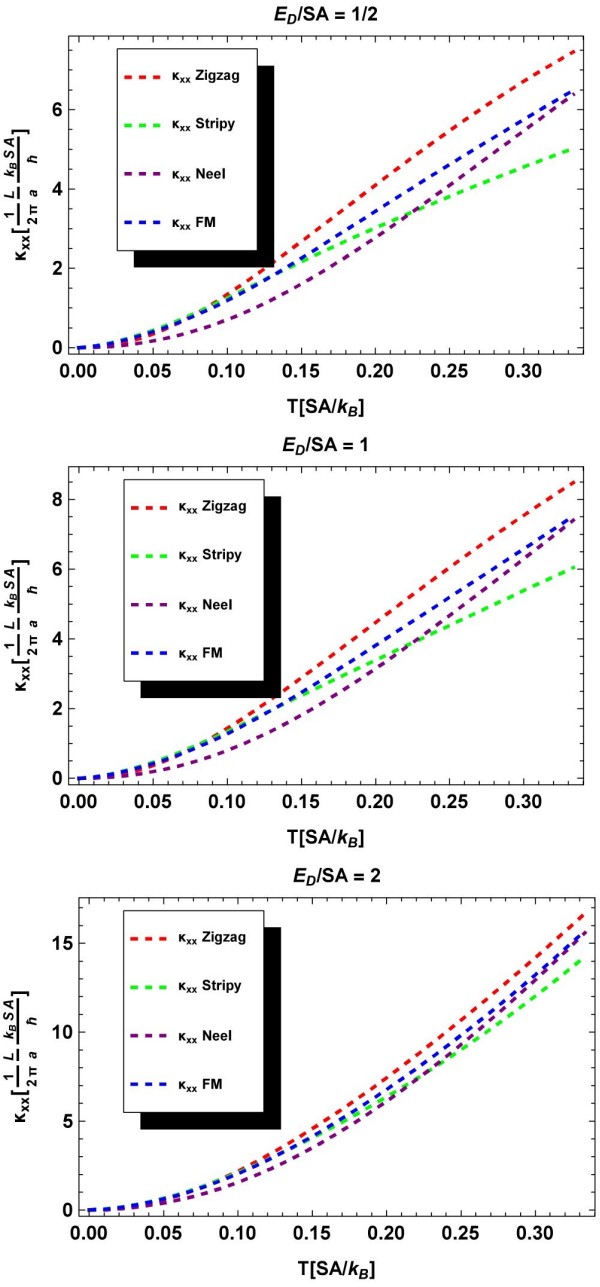

Figure 4.4: κ_{xx} component of the total fully ballistic thermal conductivity per unit area, for each ordered phase (see the legend of each subfigure), for different relative strengths of the Debye energy E_D to the magnon characteristic energy SA (given on top of each subfigure), versus temperature.

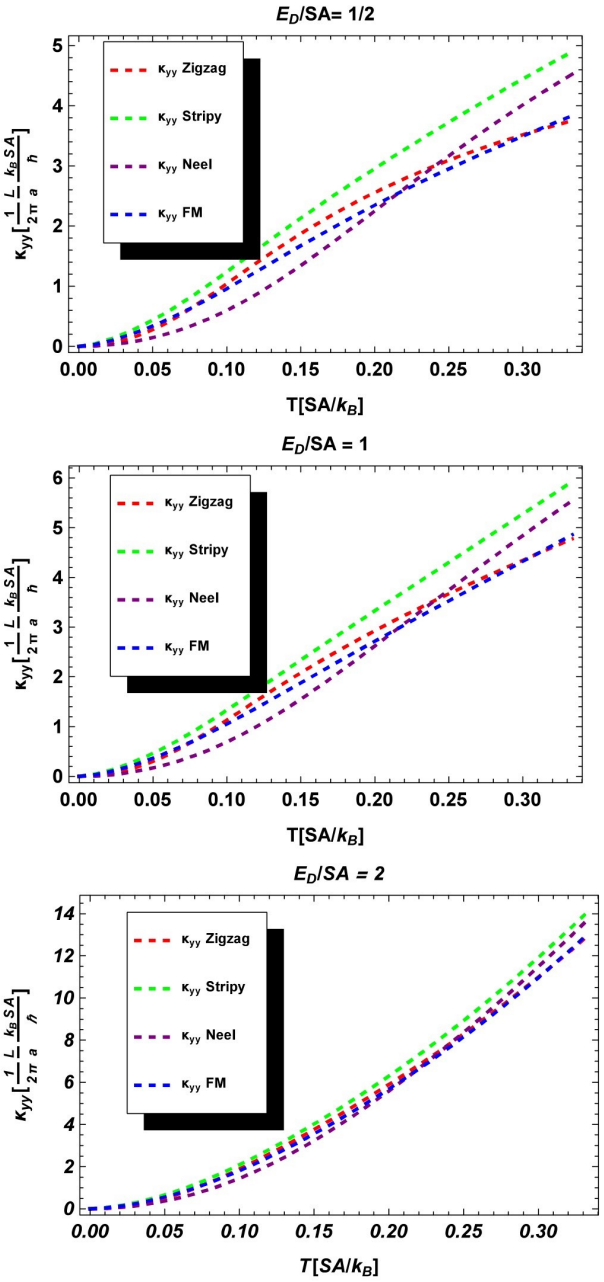

Figure 4.5: κ_{yy} component of the total ballistic thermal conductivity per unit area, for each ordered phase (see the legend of each subfigure), for different relative strengths of the Debye energy E_D to the magnon characteristic energy SA (given on top of each subfigure), versus temperature.

to have well-defined low energy magnetic degrees of freedom (given by the Heisenberg-Kitaev Hamiltonian) as well as low energy magnetic excitations. For sufficiently low temperatures the use of the Debye model in the calculation of the phononic thermal conductivity as well as the neglect of higher order processes (magnon-magnon, phonon-phonon or magnon-phonon) are all well justified. Three distinct characteristic energy relative strengths are considered: (i) magnetic energy half the Debye energy, (ii) magnetic energy equal to the Debye energy, and (iii) magnetic energy twice the Debye energy. In this case, the magnonic and the phononic contribution to the *total fully ballistic* thermal conductivity tensor depends solely on the respective carrier's band structure, via its energy dispersion relation, its group velocity, and its Bose-Einstein occupation factor. Therefore, any differences among the total fully ballistic thermal conductivities directly reflect differences in the carrier band structures, and particularly differences in the magnon band structures, since the phonon band structure is common to all the magnetically ordered phases.

It is noted that for the ferromagnetic and the Néel phases there exist two magnon bands, while for the zig-zag and the stripy phases there exist four bands. In the low temperature region, as far as the magnon contribution is concerned, any gapless magnon bands are more important than any gapped ones, and furthermore, the respective thermal conductivity contribution is dominated by the band structure in the neighborhood of "magnon (energy) valleys". This is because the Bose-Einstein occupation factors decrease rapidly with increasing excitation energies. For a two-dimensional system, there is

one longitudinal and one transverse acoustic phonon (notice that in the fully ballistic regime studied in this section both acoustic phonons are taken into account), both assumed to obey a linear isotropic dispersion relation. Particularly, the two acoustic phonons are treated within the Debye model adjusted to a two dimensional system. It is worth noting that the phononic thermal conductivity within the Debye model in the low temperature regime becomes $\propto T^2$ for a 2D system (in contrast to the T^3 result for a 3D system).

Taking into account the previous discussion, let us now turn our attention to the Figs. 4.4 and 4.5. The bottom diagram of each figure represents phonon dominated total thermal conductivity results. The curves for different phases tend to converge to each other as a result of the common phonon band structure, tend to follow a parabolic dependence on the temperature as a result of the Debye model applied to 2D systems, and tend to become more isotropic due to the smaller difference between the values of the κ_{xx} and κ_{yy} components. The top diagram of each figure represents magnon dominated total thermal conductivity results that differ appreciably from each other over different magnetic phases as a result of the very different magnon band structures of the various phases, deviate significantly from the parabolic dependence on the temperature which is characteristic of the in-plane acoustic phonons, and tend to become significantly anisotropic due to the greater difference between the values of the κ_{xx} and κ_{yy} components. The intermediate diagram of each figure corresponds to an *intermediate fully ballistic subregime* which, as far as the boundary scattering dominated heat transport is concerned, is

characterized by comparable magnonic and phononic contributions (since only the boundary scattering relaxation mechanism is active, there is no coupling between the two subsystems at this point as a result of which the above developed formalism works well for such a case but not beyond that!).

Another point to notice is that, away from the phonon dominated regime, even though as $T \to 0$ all conductivities go to zero, there is a temperature window from $0.05\frac{SA}{k_B}$ up to about $0.11\frac{SA}{k_B}$ within which the Néel total conductivity is markedly lower than the total conductivities of the other three magnetic phases which have higher but nearby values. In addition, the total conductivity of the Néel phase (either component) seems to saturate slower than all the other conductivities within the examined temperature window. This can be traced back to the structure of the lowest magnon bands of the different ordered states. As will be detailed below, the particular feature of the Néel state is that it has a nearly isotropic magnon band whose minimum is located at the center (Γ point) of its corresponding 1BZ. However, let us first introduce some useful terminology to be employed intermittently for the structural description of the various magnon bands.

In the coming analysis (and subsections) we will use the term *stiff anisotropy* to refer to the gapless magnon bands which approach zero energies with non-zero group velocities (as also happens with the acoustic phonons), and the term *soft anisotropy* to refer to the gapless magnon bands which approach zero energies with vanishing group velocities.

For the zig-zag phase, all the four magnon bands are important at low

temperatures (since all of them have magnon energy valleys), and further, half of them are strongly anisotropic whereas the rest half are nearly isotropic (the magnon bands of all the magnetically ordered phases are given in the Appendix A of Ref.[57]). In addition, all four bands have stiff anisotropy, and magnon valleys far from the center of the corresponding 1BZ. For the stripy and the ferromagnetic phase on the other hand, only half of their bands are important at low temperatures. In either case the bands are softly anisotropic, and further, the magnon valleys of the stripy phase are away from the center of the corresponding 1BZ, whereas the ferromagnetic phase has its magnon valley at the center of the corresponding 1BZ. Finally, for the Néel phase, both of its bands are important at low temperatures, and further, both magnon bands have their minima at the center (Γ point) of the corresponding 1BZ, with the one band being stiffly isotropic and the other being stiffly anisotropic around the corresponding valleys.

As will be unfolded in the following discussion, the presence of a stiffly (nearly) isotropic band with a valley (minimum) at the center of the corresponding 1BZ (Γ point) has some special properties. The lowest magnon bands of the ferromagnetic and the stripy phases are *softly anisotropic* which implies that at very low temperatures there can be many more excited magnon quasiparticles compared to the phases which are *stiffly anisotropic*. The zig-zag phase is partially *softly anisotropic* and partially *stiffly anisotropic*, but all of its magnon bands are gapless which implies more spin wave valleys. As a result, there can again be many excited magnon quasiparticles.

The Néel phase, which is a *stiffly anisotropic* phase with half the bands and fewer valleys (1/4) compared to the zig-zag phase, doesn't have any of the aforementioned leeway to increase the population of its low energy magnon quasiparticles (remember that a significant contribution at low temperatures comes from the nearly isotropic valley at the center of the corresponding 1BZ), and this in turn delays the corresponding saturation of its total thermal conductivity (even though it is magnon-dominated).

In continuation of the previous analysis, it seems that the deviation from isotropy (in the magnon bands of interest) leads to a faster saturation of the total conductivity, other than an induced difference between the values of the two diagonal components of the thermal conductivity tensor. It can further be seen from the top and the middle panel of Figs. 4.4 and 4.5 that as the temperature increases above zero, the κ_{xx} component of the stripy phase and the κ_{yy} component of the zig-zag phase seem to saturate first. The reason for this is that for a temperature gradient along the x direction, the stripy phase has its softest magnon modes in that direction, whereas for a temperature gradient along the y direction, the zig-zag phase has its softest magnon modes along that direction.

Before concluding this section, it is worth mentioning that close inspection of the top and the bottom diagrams of the Figs. 4.4 and 4.5 leads to the additional conclusion that the greater heat current (i.e. the greater contribution to the total thermal conductivity) is carried by the heat carriers with the greater characteristic energy scale (and therefore the greater group

velocities). As a measure of the validity of the last statement one can use the low temperature behavior predicted by the two dimensional Debye model (its no saturation sign) as well as the degree of isotropy of the total thermal conductivity that are typical of phonon contributions, and check how the resulting conductivity deviates from the aforementioned typical behavior as one moves toward the magnon dominated side of the fully ballistic regime.

4.3.2 Phonon dominated heat transport

In this subsection we focus on the effect of weak magnon-phonon scattering on the phonon dominated heat transport, using the results of the fully ballistic regime (i.e. of the boundary scattering dominated phononic heat transport) as a reference. A basic reason for using the aforementioned reference is that all the factors appearing in the formula of the thermal conductivity tensor are the same for both the boundary and the magnon-phonon relaxation processes, except for the corresponding transport relaxation time. Therefore, any deviations of the thermal conductivity results from the corresponding pure boundary scattering results are attributed to magnon-phonon scattering (since they originate from transport relaxation times that diverge from the boundary scattering ones). However, before proceeding to the results it would be advisable to first discuss some subtle points that were taken into account in our analysis.

First, the presumed weak magnon-phonon scattering is to a good extent ensured by working at temperatures much lower than the minimum of

an appropriately defined Debye and magnon characteristic temperature, at which the ionic displacements from their equilibrium positions are small (significantly smaller than a typical lattice constant). Given this, provided that phonon induced changes in the bond lengths and bond angles do not lead to any drastic increase of the gradients of the exchange couplings Ref.[31] (if they lead to a drastic decrease as happens in various phenomenological models for the distance dependence of the exchange couplings that does not create any problem), the magnon phonon couplings (superscript H denotes the magnon-phonon coupling originating from the Heisenberg term whereas superscript K denotes the magnon-phonon coupling originating from the Kitaev term) g^H_{mp} and g^K_{mp} are always much smaller than the corresponding exchange couplings. Then, the lowest order perturbative treatment of the magnon-phonon interaction is well justified. Strictly speaking, the distance dependence of the exchange couplings necessitates sophisticated first principle calculations, but keeping in mind that exchange couplings actually originate from electronic exchange paths mediated by neighboring atomic orbital overlaps, an order of magnitude calculation of the gradients of the exchange couplings is feasible and can give an estimate of the strength of the magnon-phonon coupling.

Secondly, as far as the boundary scattering mechanism is concerned, both types of acoustic phonons (transverse and longitudinal) are taken into account via a Debye model adjusted to 2D systems. However, as far as the magnon-phonon scattering mechanism is concerned only the transverse phonon is taken into account for the conductivity calculation. The last approximation

is tied to the assumption that the magnon-phonon scattering is more important for the longitudinal rather than the transverse (acoustic) phonon, which implies that heat conduction is predominantly borne by the transverse phonon (since the other phonon is scattered too much to contribute to the conduction of the heat and is therefore neglected).

Another reason for this approximation is related to the fact that the main effect of the long-wavelength transverse acoustic phonons is to slightly change/perturb the equilibrium angles between neighboring bonds, whereas, the long-wavelength longitudinal acoustic phonons can change both the equilibrium angles between neighboring bonds (actually depending on their direction of propagation they can be more or less effective), and more important the lengths of the interatomic bonds. As a result, in all cases in which the exchange couplings are much more sensitive to perturbations in the bond lengths (i.e. the radial interionic distances) than in the bond angles, the assumption of a stronger magnon-phonon coupling for the longitudinal acoustic phonon should be well justified.

Having in mind the previous discussion, it is noted that the transverse acoustic phonon is subject to magnon-phonon scattering via a much weaker magnon-phonon coupling constant than the one assumed for the longitudinal acoustic phonon, and this is taken computationally into account by using a *reduced coupling constant* $\tilde{g}_{mp}(\vec{k},\vec{q}) = g_{mp}(\vec{k},\vec{q})/\gamma$, where $g_{mp}(\vec{k},\vec{q})$ is the magnon-phonon coupling constant used for the longitudinal acoustic phonons, and γ is a reduction factor such that $\gamma \sim 10$ ($\vec{k}$ and $\vec{q}$ denote the 2D magnon

and the phonon wavevector respectively). Afterwards, the relative strength of the magnon-phonon and boundary scattering, for the (long-wavelength) transverse acoustic phonon assumes, after partitioning it in a dimensional and a dimensionless part, the following form

$$\left.\frac{\tau_b}{\tau_{mp}}\right|_{pho} \simeq \frac{SA}{E_D} \times c_{mag} \times \frac{1}{\gamma^2} \times I, \tag{4.4}$$

where for convenience we've set

$$c_{pho} \equiv \frac{SA}{E_D} \times c_{mag} \times \frac{1}{\gamma^2}. \tag{4.5}$$

and further, the parameter I encapsulates, for a specific material, all the different magnon-phonon scattering processes, whereas c_{mag} is defined as $c_{mag} \equiv 55 \times \frac{1}{\Theta_D(K)} \times \frac{L}{\alpha} \times \frac{1}{N_u \alpha^2}$, with L denoting the length of the crystal in the direction of the applied temperature gradient, and Θ_D representing an appropriately defined Debye temperature in Kelvins.

Thirdly, for the heat transport process to be phonon dominated, it is legitimately required that the phonon and the magnon energy scales are sufficiently different from each other, and it turns out computationally that a ratio of $E_D/SA = 7$ between the phonon and the magnon energy scales suffices to render the thermal conductivity phonon dominated (by order of magnitude). Under those conditions, as already elaborated in the previously, it is sufficient to focus only on one type of heat carriers (in this case the phonons) for an approximate calculation of the thermal conductivity (because *only* the Boltzmann kinetic equation of the dominant heat carriers is employed for the

calculation of the thermal conductivity), treating the much less significant heat carriers as a bath with which the dominant heat carriers can exchange energy quasi-elastically (weak system-bath coupling), as well as momentum. Since the characteristic energy scale ratio E_D/SA was incorporated into the newly-defined parameter c_{pho} of Eq.(4.5), the c_{pho} expressed as $c_{pho} = 10^l$, $l \in \mathbb{Z}$, is treated as a tunable parameter via which one can computationally access the different phonon dominated subregimes: ballistic, intermediate and diffusive, where now, this subcategorization is based on the competition between the boundary and the magnon-phonon relaxation mechanism during the phonon dominated heat transport process.

Finally, it should be stressed one more time that only sufficiently low temperatures are considered in this work for reasons that were described at various points in the previous analysis (well-defined low energy excitations for the lattice and the magnetic degrees of freedom, weak magnon-phonon coupling, negligible higher order phonon-phonon, magnon-magnon and magnon-phonon processes and so on, are all required to simplify the problem). Particularly, for the phonon dominated heat transport since a lower energy scale is set by the magnons, a rather safe upper limit for the temperature range of interest is set by the magnon characteristic energy, by exploring temperatures smaller than $T_{max} = \frac{1}{3}\frac{SA}{k_B}$. Respectively, the units of the thermal conductivity are now naturally expressed in terms of the magnon energy scale SA as well. Particularly, in the phonon dominated ballistic (boundary scattering dominated) subregime where the length L of the crystal plays a significant role, the natural units to

measure the thermal conductivity are $\frac{1}{2\pi}\frac{L}{a}\frac{k_B SA}{\hbar}$. With all the aforementioned details in mind, let us now turn our attention to the Figs. 4.6 and 4.7 below which show the per unit area components of the phononic conductivity tensor κ_{xx} and κ_{yy}, and respectively, the same quantities divided by the temperature squared, for each ordered phase, for the three different subregimes mentioned previously (ballistic, intermediate and diffusive, see the legend of each subfigure) as well as for pure boundary scattering, versus temperature.

As already noted above, both acoustic phonons are subject to boundary as well as magnon-phonon scattering. Since heat conduction is of primary interest, we focus only on the transverse acoustic phonon (the longitudinal one comes in only through boundary scattering, via the 2D Debye model, and its contribution to the heat conduction becomes negligible as one moves away from the purely ballistic deep into the diffusive phonon dominated subregime where it is strongly scattered via the magnon-phonon mechanism). Since the pure boundary scattering for phonons at low temperatures follows exactly the T^2 behavior (as a result of the 2D Debye model), Fig.4.7 actually shows the deviation of the thermal conductivity (due to the transverse long wavelength acoustic phonon) from the T^2 low temperature behavior, as one goes from the fully ballistic deep to the diffusive phonon dominated subregime (by tuning the $c_{pho} = 10^l$ parameter defined above). In Figs.4.6 and 4.7 the black curves correspond to boundary scattering dominated phononic heat transport, whereas the red (and the green in Fig.4.7) curves correspond to the ballistic subregime, where this term now refers to a situation in which the phononic heat trans-

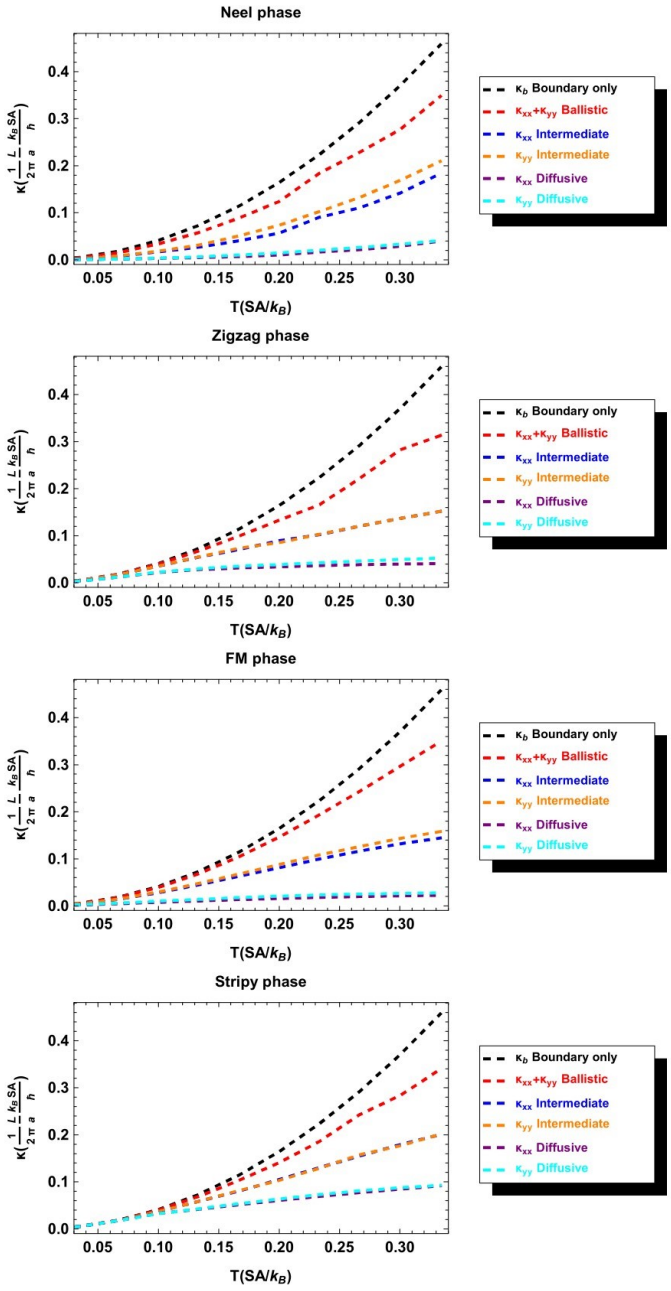

Figure 4.6: Phonon dominated transport: κ_{xx} and κ_{yy} component of the phononic thermal conductivity per unit area, for each ordered phase, for three different subregimes: ballistic, intermediate and diffusive (see the legend of each subfigure) as well as pure boundary scattering, versus temperature.

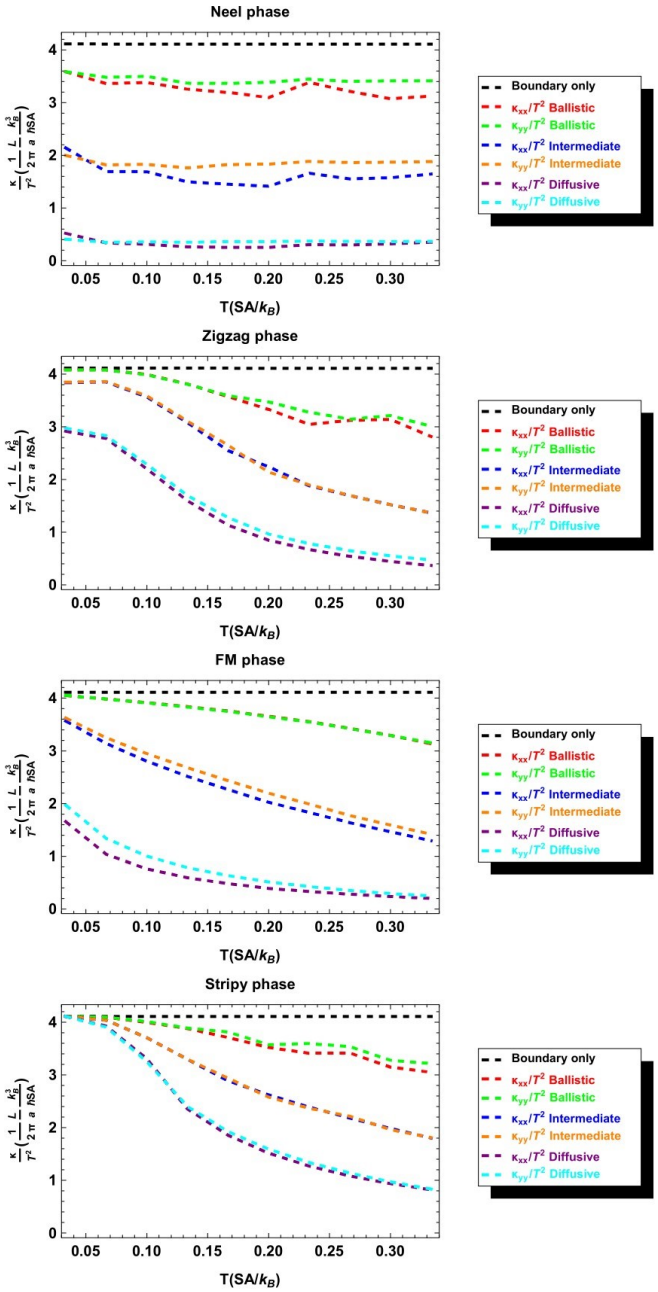

Figure 4.7: Phonon dominated transport: κ_{xx}/T^2 and κ_{yy}/T^2 component of the phononic thermal conductivity per unit area, for each ordered phase, for three different subregimes: ballistic, intermediate and diffusive (see the legend of each subfigure) as well as pure boundary scattering, versus temperature.

port is mostly (but not purely) boundary scattering dominated. In the intermediate subregime, as already stressed above, both scattering mechanisms (boundary and magnon-phonon) affect the transverse long wavelength acoustic phonon. It is worth noting that the cross-over from the purely ballistic to the diffusive subregime takes place by gradually decreasing the strength of the boundary scattering (i.e. by increasing the length of the crystal), and along the way the magnon-phonon scattering mechanism is gradually unmasked until it dominates over the boundary scattering mechanism, deep in the diffusive subregime.

From Figs.4.6 and 4.7, it is easily observed that the thermal conductivity is actually isotropic for *all* subregimes, since the κ_{xx} and the κ_{yy} components almost coincide with each other. This is a consequence of the (intrinsic) isotropic nature of the phonon band structure. Absolute coincidence, upon deviation from the boundary scattering dominated (or fully ballistic) subregime, is not possible because of the interplay with the magnon bath whose band structure is strongly anisotropic. The qualitative conclusion is that in the phonon dominated regime, no matter how anisotropic the band structure of the magnon bath is, the phonon thermal conductivity succeeds in retaining its isotropic character even deeply in the diffusive subregime of the phonon dominated regime.

A second striking aspect of the diagrams of Fig.4.7 (this is hard to be noticed in the diagrams of Fig.4.6) is the fact that for all the magnetic phases, except for the stripy phase, the magnon-phonon scattering mechanism seems

to start taking effect at fairly low temperatures. This can be seen by the fact that at the low temperature limit used in the calculations ($T = 0.05SA/k_B$) passing from the fully ballistic to the diffusive subregime (i.e. from the top to the bottom of each subfigure), the values of the phononic thermal conductivity components deviate significantly from the values of the corresponding top black curve which conforms to the T^2 low temperature behavior, and this of course is indicative of magnon-phonon scatterings at such low temperatures. This last effect, easily seen, is strongest for the Néel phase and weakest for the stripy phase. Saying so, one then is naturally led to the following two qualitative results.

The first qualitative result is that within the phonon dominated regime, at very low temperatures, high energy acoustic phonons can sufficiently effectively be scattered by low energy magnons whose band structure has (at least) a pair of *stiff* gapless magnon bands, of sufficiently different stiffness (the more different the stiffnesses the better). These magnon bands can be isotropic or anisotropic or both (one isotropic, one anisotropic, as happens in the Néel phase), but they must both have their minima (their valleys) at the center of the 1BZ (where the acoustic phonon spectra have their minima as well). This conclusion also agrees with the results of Ref.[19] in which, at very low temperatures (liquid helium temperatures), high energy phonons are scattered (though mildly) by low energy magnons whose band structure consists of a pair of stiff magnon bands, of slightly different stiffness, which are isotropic and both have their minima at the center of the 1BZ.

The second qualitative result is that within the phonon dominated regime, at very low temperatures, high energy acoustic phonons cannot be scattered by low energy magnons whose band structure consists of gapless magnon bands which are soft, and whose minima (magnon energy valleys) are non-degenerate, lying far away from the center of the 1BZ as well as far away from each other. This is exactly the case with the stripy phase, which has two low energy gapless magnon bands on the one hand, but which on the other hand are softly anisotropic, have their valleys far from the center of the 1BZ, and all the valleys are located at different points of the k-space. As a result, there is only one softly anisotropic band around each magnon energy valley whose magnons cannot satisfy energy conservation by interacting with any fast moving phonons.

In conclusion, we mention that as one passes from the fully ballistic deeply into the diffusive subregime, the phononic thermal conductivity keeps decreasing as a result of the stronger and stronger magnon-phonon scattering compared to the boundary scattering (since the magnon-phonon coupling constant is always weak as discussed previously). The last effect is expected within the model we study since the magnon bands of whichever magnetic phase (even the lower energy bands of the phases which have well separated in energy magnon bands) do not saturate within the temperature window employed in this analysis.

4.3.3 Magnon dominated heat transport

In this subsection we focus on the effect of the weak magnon-phonon scattering on the magnon dominated heat transport, using the results of the fully ballistic subregime (i.e of the boundary scattering dominated magnonic heat transport) as a reference. Any deviations of the thermal conductivity results from the respective fully ballistic results are attributed to magnon-phonon scattering (since they originate from transport relaxation times that diverge from the purely ballistic ones). Before proceeding to the results it is helpful to pause and discuss how the arguments presented in the introduction of the previous subsection are modified for the magnon dominated heat transport that is examined in this subsection.

First, the presumed weak magnon-phonon scattering is ensured by working at temperatures much lower than the minimum of an appropriately defined Debye and magnon characteristic temperature. Second, both for the boundary scattering and the magnon-phonon scattering mechanism *all* magnon bands are taken into account (a Debye-like approximation turns out to be a poor one for the magnons due the highly anisotropic nature and non-linear dispersion of the magnon bands). Third, as far as the magnon-phonon scattering mechanism is concerned only the longitudinal phonon is taken into account for the magnon conductivity calculation, since according to the arguments given in the previous section, any magnon-phonon scattering is predominantly caused by the longitudinal rather than the transverse acoustic phonon. Therefore, the approximation that is adopted is that the diffusive regime of the magnon

dominated heat transport originates from the interaction with the longitudinal acoustic phonons. Finally, it should be mentioned that for the heat transport process to be magnon dominated, the phonon and the magnon energy scales must be sufficiently different from each other, and it turns out computationally that a ratio of $SA/E_D = 7$ between the phonon and the magnon energy scales suffices to render the thermal conductivity magnon dominated (by order of magnitude).

Under the aforementioned conditions, it is sufficient to focus only on one type of heat carriers (in this case the magnons) for an approximate calculation of the thermal conductivity (because *only* the Boltzmann kinetic equation of the dominant heat carriers is employed for the calculation of the thermal conductivity). The less significant heat carriers are then treated as a bath (in this case the phonons) with which the dominant heat carriers can exchange energy quasi-elastically (weak system-bath coupling), as well as momentum. The relative strength of the magnon-phonon and the boundary scattering for the case of the magnon-dominated thermal transport, can also be expressed in terms of a corresponding dimensionless (all-scattering encapsulating) parameter I, in sheer analogy with Eq.(4.4), as

$$\left.\frac{\tau_b}{\tau_{mp}}\right|_{mag} \simeq c_{mag} \times \frac{1}{\upsilon_{mag}} \times I, \tag{4.6}$$

where c_{mag} has been defined below Eq.(4.4), and υ_{mag} is the dimensionless magnon group velocity (see Eq.[44] in Ref.[57]). In addition, the tunable parameter via which one can computationally access the different magnon

dominated subregimes (ballistic, intermediate, diffusive) is the parameter c_{mag} (defined right below Eq.(4.4)), which can more conveniently be expressed as $c_{mag} = 10^l$, $l \in \mathbb{Z}$ (to induce order of magnitude changes in the relative strength of the two scattering mechanisms).

We can now turn our attention to the results of Figs.4.8 and 4.9 above, which show the behavior of the components of the magnonic thermal conductivity tensor versus temperature, for all the magnetically ordered phases, for each subregime (ballistic, intermediate, diffusive) as well as pure boundary scattering. In the results of Fig.4.9 there was an attempt to find a power law for the temperature dependence of the pure boundary scattering mechanism (at least in the low temperature limit of the examined temperature window) so that the respective results lie on a horizontal line (and this is important since by doing so, it is much easier to see the deviations in the results caused by the complementary magnon-phonon scattering mechanism). As can be seen from that figure, the temperature exponent can be slightly different for the x and y directions, as happens for the Néel and the FM phase. Further, for all the magnetic phases except for the Néel one, it was possible to find a power of the temperature by which the pure boundary scattering results can be divided so that they all lie along a straight line over the whole examined temperature window (for the Néel phase the given exponents cover only the low temperature limit denoted by the horizontal arrows in the top subfigure of Fig.4.9).

Furthermore, from the Figs.4.8 and 4.9 it is easily seen that the anisotropy of the magnonic conductivity tensor fades away as one moves from the purely

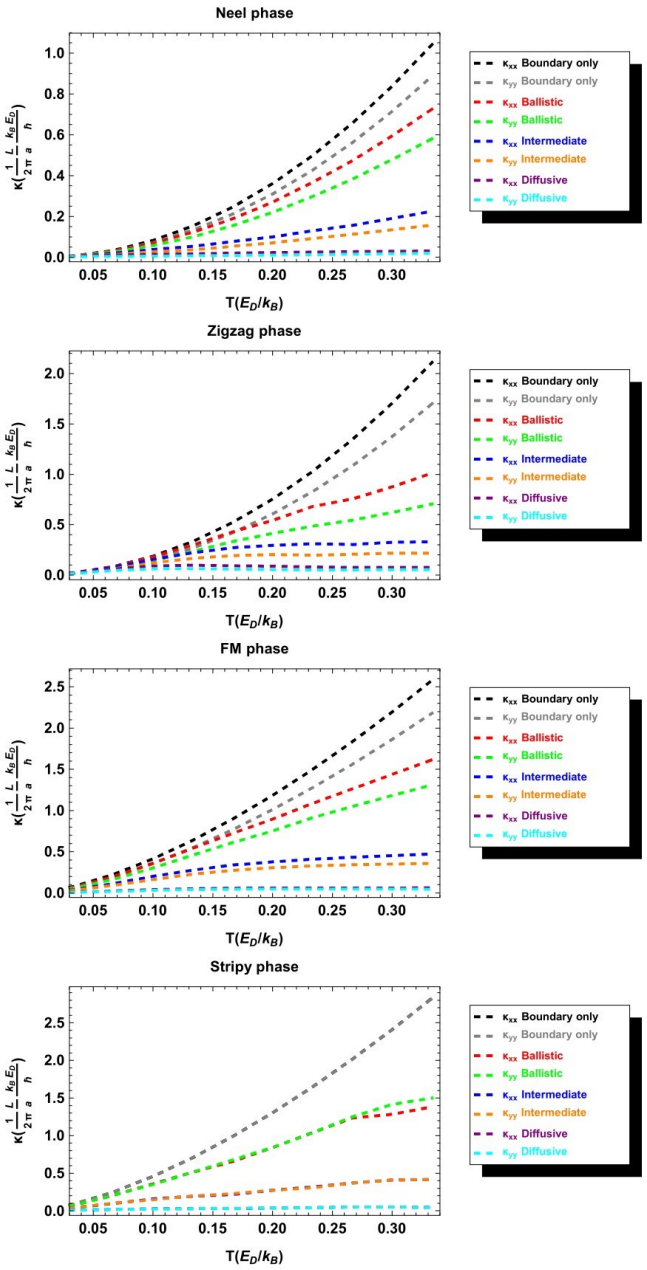

Figure 4.8: Magnon dominated transport: κ_{xx} and κ_{yy} component of the magnonic thermal conductivity per unit area, for each ordered phase, for three different subregimes: ballistic, intermediate and diffusive (see the legend of each subfigure) as well as pure boundary scattering, versus temperature.

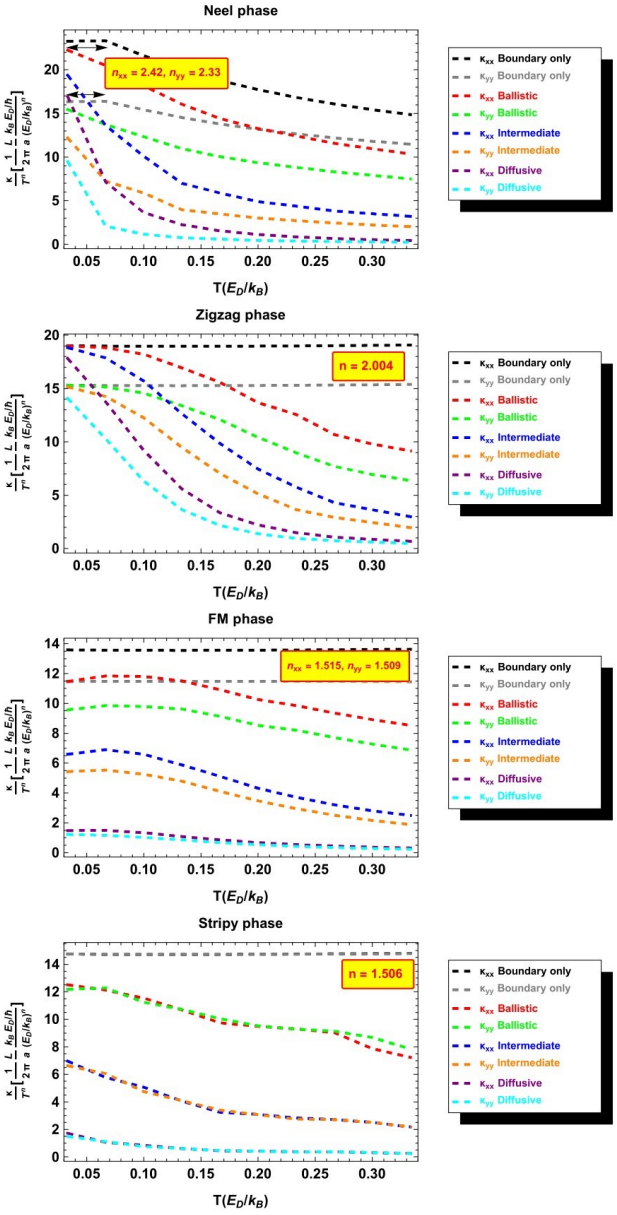

Figure 4.9: Magnon dominated transport: κ_{xx}/T^n and κ_{yy}/T^n component of the magnonic thermal conductivity per unit area, for each ordered phase, for three different subregimes: ballistic, intermediate and diffusive (see the legend of each subfigure) as well as pure boundary scattering, versus temperature. The appropriate temperature exponent n that should divide κ_{xx} and κ_{yy} such that the pure boundary scattering results are represented by horizontal straight lines (at least at low temperatures) is given in the nearby yellow inset.

ballistic deep into the purely diffusive subregime, and this happens because of the stronger and stronger magnon-phonon scattering from the longitudinal phonons (the deeper we enter the diffusive subregime), or to put it differently, stronger and stronger scattering of the (lower energy) magnons by the (low energy) isotropic longitudinal acoustic phonons gradually washes out any residual anisotropic features of the magnon band structure from the magnonic thermal conductivity. It should further be noticed that the aforementioned effect is stronger for soft low energy magnon bands compared to the analogous effect for stiff low energy magnon bands. Saying so, a qualitative argument that can be given here is that for the softly anisotropic phases (the FM and the stripy phase) the anisotropy of the magnonic conductivity tensor starts diminishing earlier with increasing temperature (i.e. for the aforementioned two phases, the anisotropy of the magnonic conductivity is significantly diminished already at very low temperatures), as opposed to the stiffly anisotropic phases (the zigzag and the Néel phase), whose magnon thermal conductivity manages to partially retain the magnon band anisotropies up to higher temperatures. The previous argument is supported by looking at the low temperature side (leftmost side) of each subfigure of Fig.4.9, whereby one can see that due to the intense magnon-phonon scattering, the magnonic conductivity is significantly suppressed compared to its corresponding purely ballistic value. However, the suppression is weaker for the stiffly anisotropic phases (especially for the zigzag phase), where the magnon conductivity is not significantly suppressed from its purely ballistic value unless ones goes to higher temperatures.

Another feature that one can observe by looking at the subfigures of Fig.4.8 is that the magnon conductivity of all the magnetic phases seems to saturate within the temperature window employed in this study, except for the Néel phase which tends to saturation slower than all the other phases. An explanation for this is that, because the low energy magnon band of the Néel phase is stiffly nearly isotropic, with its magnon valley at the center of the 1BZ (where the acoustic phonon bands also have their minima), the strong magnon-phonon scattering mainly affects the lower energy magnons which also have very small wavevectors, whereas the higher energy magnons which are more effective in transporting heat continue to propagate less impeded by the longitudinal acoustic phonons.

Concluding this section, we emphasize that the magnonic conductivies of the various magnetic phases differ more markedly from each other closer to the ballistic subregime (or the pure boundary scattering subregime) compared to the diffusive one. In addition, at very low temperatures (the lower temperature limit of our plots) the boundary scattering mechanism (Fig.4.9, see the yellow insets) seems to approximately follow some particular power law, that varies markedly between the stiffly and the softly anisotropic phases (Néel and zigzag, and stripy and FM, respectively). A further discrimination between the stripy and the FM phase on the one hand, and the zigzag and the Néel phase on the other, deeply within the ballistic subregime, comes from the fact that the values of the two components of the magnon conductivity tensor of the Néel and the FM phase follow slightly different power laws (at

low temperatures) as opposed to the magnon conductivity components of the other two magnetic phases, which can be described by a common power law.

Closing this chapter, a recapitulation of all the previous results can further be found in the conclusions section of Ref.[57].

Chapter 5

Interfacial effects in YIG - topological insulator heterostructures - enhanced Gilbert damping in YIG

5.1 Motivation

The work developed in this chapter is motivated by recent (maybe yet unpublished) experiments on heterostructures in which a very thin film (nanometrically thin) of YIG is deposited on a topological insulator substrate, as a result of which, an enhanced Gilbert damping during the ferromagnetic resonance mode (FMR) is recorded for the YIG insulator.

The discovery of the yttrium iron garnet (YIG) has played a critical role as far as the fundamental understanding of the magnetic materials is concerned, and besides that, it is also a very interesting material from a technological point of view owing to its various applications in the domains of the magnon spintronics, magnonics and spin caloritronics, as well as in microwave devices that can operate at room temperature. (Refs.[24, 25]). Yttrium iron garnet is a ferrimagnetic insulating oxide, (Ref.[25]) with the lowest magnon damping of any known material, and a rather complicated crystal structure, with space group $Ia3d$, and about twenty magnetic ions in the primitive unit cell (Refs.[9, 32]). However, despite the electronic and magnetic complexity of

that material, there is a series of experiments for which the lowest only magnon band suffices for the approximate interpretation of corresponding experimental results. In such cases, as long as the physics is related to long-wavelength properties only, a highly simplified treatment of the YIG insulator is possible, where an effective "block spin" per unit cell is considered, and further, those "block spins" interact with each other predominantly via ferromagnetic exchange interactions. In this work, since only the long-wavelength dynamics of the magnetic degrees of freedom of the YIG is of relevance, on account of the fact that this is the domain probed by the ferromagnetic resonance spectroscopy (FMR), the previous simplified treatment of the YIG insulator is also employed in the formalism to be developed.

Previous theoretical studies on YIG thin films focused either on intrinsic damping mechanisms such as the magnon-phonon scattering processes (Refs.[41, 52]), or non-intrinsic damping mechanisms activated by disorder or inhomogeneities (surface or interfacial), such as the two-magnon scattering processes (Refs.[2, 3, 24, 35, 47]), where the FMR mode decays into finite wave-vector modes of the same energy (same frequency), thus acting as a dephasing mechanism. It should be noted though that as far as the two-magnon scattering mechanism is concerned, it has been found that that mechanism depends on several factors such as the crystalline anisotropy, the sample geometry and dimensions, the nature of the scattering interaction, as well as the external field orientation (the last one actually can have dramatic effects). As opposed to the previous mechanisms, in this work, driven by experimen-

tal results, we microscopically ascribe the enhanced damping of the FMR of the YIG to electron-magnon interactions, in other words, to an interplay between the FMR mode of the YIG and the itinerant electronic quasiparticles at the surface of the topological insulator that is in direct contact with the YIG insulator. Both materials are treated as very thin films (actually they are very thin films but not ultrathin), within the continuum approximation (since only long-wavelength properties are relevant here), and further, the electron-magnon interaction is treated to lowest order via the many body perturbation theory. The following formalism relies on the linear spin wave approximation (LSW) for the YIG, and therefore, the temperature range of validity of the formalism is well below the magnetic transition temperature of the YIG that is close to 600 K.

5.2 Lowest order quantum mechanical spin Hamiltonian for the YIG thin film

In this section, the target is to derive a lowest order quantum mechanical spin Hamiltonian for the YIG thin film, and to this end, we closely follow the method developed in the work of Landeros, Arias and Mills (see Ref.[35]). Minor errors in their derivation are fixed in this treatment, and SI units are used throughout this work. Even though those authors had in mind metallic ferromagnets, treating their magnetism within a local moment picture, their approach is also suited to the system studied in this section (based on the low energy approximate picture for the YIG described in the previous section). To

begin with, let us consider a uniform thin film of YIG with the geometry shown in Fig.5.1 below, where the length and the width of the film are much larger than its thickness d. We further consider two different coordinate systems. The global Oxyz system whose Oxy plane coincides with the plane of the film

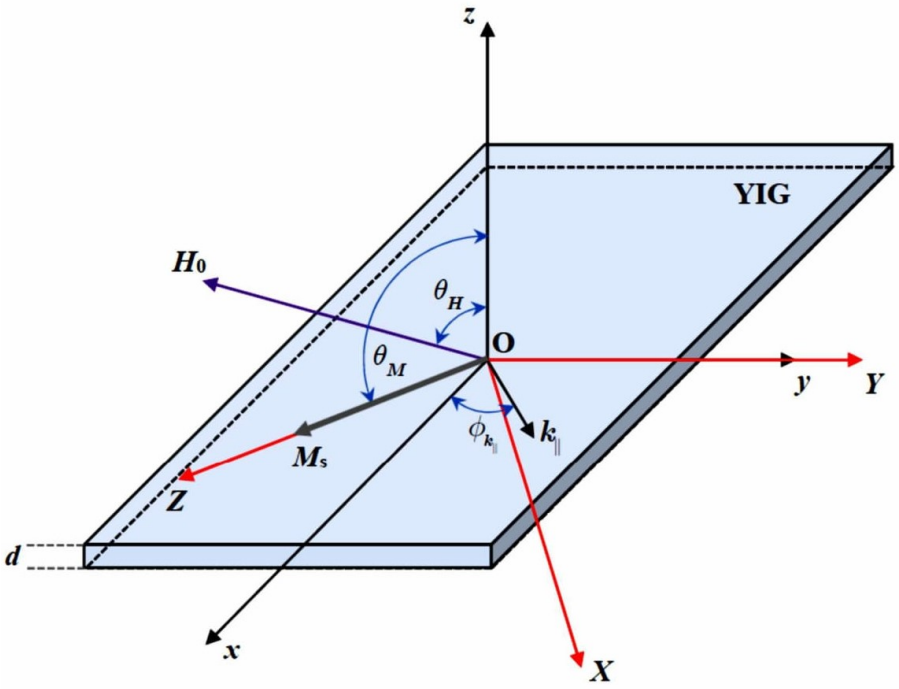

Figure 5.1: YIG thin film geometry: The global Oxyz coordinate system is shown, as well as the local OXYZ coordinate system with the OZ axis oriented along the equilibrium direction of the order parameter of the YIG insulator.

that will later constitute the interface with the topological insulator, with the Oz axis normal to the area of the film, and the local OXYZ system, whose OY axis coincides with the Oy axis, but is rotated by an angle θ_M about the positive y-axis so that the OZ axis lies along the equilibrium direction of the coarse-grained order parameter of the YIG, which quite generally is assumed

tilted out of the plane of the film, by applying an out of plane magnetic field $\vec{H}_0$. The applied magnetic field $\vec{H}_0$ is at an angle θ_H with respect to the global Oz axis, lying for simplicity within the Oxz plane, whereas the order parameter is at an angle θ_M with respect to the same global axis. In the thin film limit (assuming that the film extends from $z = 0$ to $z = d$) any standing waves with nonzero wavevectors perpendicular to the film area, given by $k_{\perp}^{(n)} > \pi/d$, are expected to be shifted by the exchange interaction to frequencies well above those of the FMR range (Ref.[3]). Further, in the aforementioned limit, given that the long-wavelength dynamics of the YIG (coarse-grained) magnetization is of interest here, any spatial variations of the magnetization field across the thickness of the film are averaged out, by approximating the transverse (to the equilibrium orientation) magnetization components $m_X(\mathbf{r}, t)$ and $m_Y(\mathbf{r}, t)$ as below

$$\bar{m}_{\alpha}(x, y, t) = \frac{1}{d} \int_0^d m_{\alpha}(x, y, z, t) dz, \quad \alpha = \{X, Y\} \tag{5.1}$$

i.e. we average them out over the film thickness. Fourier Transforming the above quantities we get

$$\bar{m}_{\alpha}(x, y, t) = \frac{1}{\sqrt{L^2 d}} \sum_{\mathbf{k}_{\parallel}} \bar{m}_{\alpha}(\mathbf{k}_{\parallel}, t) e^{i\mathbf{k}_{\parallel} \cdot \mathbf{r}_{\parallel}} \tag{5.2}$$

where we used the approximation that the length and the width of the film are much larger than the film thickness, as a result of which, translational invariance is preserved within the Oxy plane, and further, we've defined $\mathbf{k}_{\parallel} = k_x \hat{\mathbf{x}} + k_y \hat{\mathbf{y}}$ and $\mathbf{r}_{\parallel} = x\hat{\mathbf{x}} + y\hat{\mathbf{y}}$. L^2 is the basic quantization area to which periodic boundary conditions are applied within the Oxy plane. Notice that the reality

of the averaged transverse magnetization components defined above leads to the condition that $\bar{m}_\alpha(-\mathbf{k}_\parallel, t) = \bar{m}^*_\alpha(\mathbf{k}_\parallel, t)$. In this analysis, a YIG thin film with surface anisotropy of strength K_S is assumed, such that $K_S > 0$, i.e. the normal to the film surface is considered to be a hard axis (such a choice is closer to the experiment we attempt to model here). Given the angle θ_H, the angle θ_M is found from the vanishing net torque condition, where the net torque originates from the combination of the applied external field, the demagnetization field, and the anisotropy field which pulls the order parameter toward an easy direction.

To study the long-wavelength dynamics of the YIG magnetization, we begin by postulating an effective magnetic Hamiltonian for the YIG thin film that consists of the following contributions: (a) the Zeeman interaction with the external applied field, (b) the interaction of the magnetization with the static dipolar field as well as the dynamic dipolar field generated by the dynamics of the magnetization, (c) the exchange interaction between the local moments as well as the dynamic exchange interaction generated by the dynamics of the magnetization, and (d) the interaction with the static and the dynamic (due to the dynamics of the magnetization again) surface anisotropy field. As far as the spin wave dynamics is concerned, it is required to expand the above postulated magnetic effective Hamiltonian up to the second order in the deviation of the magnetization from its equilibrium direction when the system is disturbed. Assuming a small amplitude motion of the order parameter, under the aforementioned approximations, we proceed to decompose the

coarse-grained order parameter of the YIG as

$$\vec{M}(\mathbf{r}_{\parallel}) = \vec{M}^{(0)} + \vec{M}^{(1)}(\mathbf{r}_{\parallel}) + \vec{M}^{(2)}(\mathbf{r}_{\parallel}) + ... \tag{5.3}$$

where by definition it is

$$\vec{M}^{(0)} = M_s \hat{\mathbf{Z}} = M_s \sin\theta_M \hat{\mathbf{x}} + M_s \cos\theta_M \hat{\mathbf{z}} \tag{5.4}$$

where M_s denotes the saturation (coarse-grained) magnetization of the YIG. One can further separate the transverse and the longitudinal components of the coarse-grained order parameter as

$$\vec{M}(\mathbf{r}_{\parallel}) = \left[M_s \sqrt{1 - \left(\frac{\vec{m}(\mathbf{r}_{\parallel})}{M_s} \right)^2} \right] \hat{\mathbf{Z}} + \vec{m}(\mathbf{r}_{\parallel}) = \left[M_s - \frac{1}{2} \frac{\vec{m}^2(\mathbf{r}_{\parallel})}{M_s} + ... \right] \hat{\mathbf{Z}} + \vec{m}(\mathbf{r}_{\parallel}) \tag{5.5}$$

where by definition it is $\vec{m}(\mathbf{r}_{\parallel}) = \bar{m}_X(\mathbf{r}_{\parallel})\hat{\mathbf{X}} + \bar{m}_Y(\mathbf{r}_{\parallel})\hat{\mathbf{Y}}$ and also $\vec{m}(\mathbf{r}_{\parallel}) \perp \vec{M}^{(0)} = M_s \hat{\mathbf{Z}}$. Matching Eqs.(5.3) and (5.5), leads to

$$\begin{aligned} &\vec{M}^{(1)}(\mathbf{r}_{\parallel}) = \vec{m}(\mathbf{r}_{\parallel}) = \bar{m}_X(\mathbf{r}_{\parallel})\hat{\mathbf{X}} + \bar{m}_Y(\mathbf{r}_{\parallel})\hat{\mathbf{Y}} = \\ &\bar{m}_X(\mathbf{r}_{\parallel}) \cos\theta_M \hat{\mathbf{x}} + \bar{m}_Y(\mathbf{r}_{\parallel})\hat{\mathbf{y}} - \bar{m}_X(\mathbf{r}_{\parallel}) \sin\theta_M \hat{\mathbf{z}} \end{aligned} \tag{5.6}$$

and also

$$\begin{aligned} &\vec{M}^{(2)}(\mathbf{r}_{\parallel}) = -\tfrac{1}{2} \tfrac{\vec{m}^2(\mathbf{r}_{\parallel})}{M_s} \hat{\mathbf{Z}} = -\tfrac{\bar{m}_X^2(\mathbf{r}_{\parallel}) + \bar{m}_Y^2(\mathbf{r}_{\parallel})}{2M_s} \hat{\mathbf{Z}} = \\ &-\tfrac{\bar{m}_X^2(\mathbf{r}_{\parallel}) + \bar{m}_Y^2(\mathbf{r}_{\parallel})}{2M_s} \times \{\sin\theta_M \hat{\mathbf{x}} + \cos\theta_M \hat{\mathbf{z}}\} \end{aligned} \tag{5.7}$$

In the next step, we calculate the contribution of each term of the effective magnetic Hamiltonian postulated above, under the small amplitude dynamics of the magnetization field of the YIG.

Zeeman interaction :

$$
\begin{aligned}
&H_Z = -\mu_0 \int\limits_V \vec{H}_0 \cdot \vec{M}(\mathbf{r}_\parallel) d^3r = -\mu_0 \int\limits_V \vec{H}_0 \cdot \vec{M}^{(0)} d^3r \\
&-\mu_0 \int\limits_V \vec{H}_0 \cdot \vec{M}^{(1)}(\mathbf{r}_\parallel) d^3r - \mu_0 \int\limits_V \vec{H}_0 \cdot \vec{M}^{(2)}(\mathbf{r}_\parallel) d^3r - ... = \\
&-\mu_0 M_s H_0 V \cos(\theta_H - \theta_M) - \mu_0 H_0 \sin(\theta_H - \theta_M) \int\limits_V \bar{m}_X(\mathbf{r}_\parallel) d^3r \\
&+\tfrac{\mu_0 H_0}{2M_s} \cos(\theta_H - \theta_M) \int\limits_V \vec{m}^2(\mathbf{r}_\parallel) d^3r
\end{aligned}
\tag{5.8}
$$

Fourier Transforming the last equation and using also Eq.(5.2) we find

$$
\begin{aligned}
&H_Z = -\mu_0 M_s H_0 V \cos(\theta_H - \theta_M) - \mu_0 H_0 \sin(\theta_H - \theta_M) \sqrt{V} \bar{m}_X(\mathbf{k}_\parallel = 0) \\
&+\tfrac{\mu_0 H_0}{2M_s} \cos(\theta_H - \theta_M) \sum_{\mathbf{k}_\parallel} \left\{ \bar{m}_X^*(\mathbf{k}_\parallel) \bar{m}_X(\mathbf{k}_\parallel) + \bar{m}_Y^*(\mathbf{k}_\parallel) \bar{m}_Y(\mathbf{k}_\parallel) \right\}
\end{aligned}
\tag{5.9}
$$

Surface anisotropy :

$$
H_A = \frac{K_s}{M_s^2} \int\limits_S \left(\vec{M}(\mathbf{r}_\parallel) \cdot \hat{\mathbf{z}} \right)^2 d^2S = \frac{K_s}{M_s^2 d} \int\limits_V \left(\vec{M}(\mathbf{r}_\parallel) \cdot \hat{\mathbf{z}} \right)^2 d^3r \tag{5.10}
$$

Using Eqs.(5.3) through (5.7) we get

$$
\begin{aligned}
&\left(\vec{M}(\mathbf{r}_\parallel) \cdot \hat{\mathbf{z}} \right)^2 = \left(\vec{M}^{(0)} \cdot \hat{\mathbf{z}} + \vec{M}^{(1)}(\mathbf{r}_\parallel) \cdot \hat{\mathbf{z}} + \vec{M}^{(2)}(\mathbf{r}_\parallel) \cdot \hat{\mathbf{z}} + ... \right)^2 \approx \\
&M_s^2 \cos^2\theta_M - M_s \sin(2\theta_M) \bar{m}_X(\mathbf{r}_\parallel) - \cos^2\theta_M \bar{m}_Y^2(\mathbf{r}_\parallel) - \cos(2\theta_M) \bar{m}_X^2(\mathbf{r}_\parallel) + ...
\end{aligned}
\tag{5.11}
$$

Let us now define the following parameter

$$
H_s = 2K_s / M_s d \tag{5.12}
$$

where it is reminded that H_s is chosen positive, implying that the z-direction is a hard axis. From Eqs.(5.10) through (5.12) we get

$$\begin{aligned} H_A &= \tfrac{K_s}{M_s^2 d}\int\limits_V \left(\vec{M}(\mathbf{r}_\parallel)\cdot\hat{\mathbf{z}}\right)^2 d^3r \approx ... \approx \tfrac{1}{2}H_s M_s V\cos^2\theta_M \\ &-\tfrac{1}{2}H_s\sin(2\theta_M)\int\limits_V \bar{m}_X(\mathbf{r}_\parallel)d^3r - \tfrac{H_s}{2M_s}\cos^2\theta_M\int\limits_V \bar{m}_Y^2(\mathbf{r}_\parallel)d^3r \\ &-\tfrac{H_s}{2M_s}\cos(2\theta_M)\int\limits_V \bar{m}_X^2(\mathbf{r}_\parallel)d^3r + ... \end{aligned} \tag{5.13}$$

Fourier Transforming (FT) we get

$$\begin{aligned} H_A &\approx \tfrac{1}{2}H_s M_s V\cos^2\theta_M - \tfrac{1}{2}H_s\sin(2\theta_M)\sqrt{V}\bar{m}_X(\mathbf{k}_\parallel=0) \\ &-\tfrac{H_s}{2M_s}\cos^2\theta_M\sum_{\mathbf{k}_\parallel}\bar{m}_Y^*(\mathbf{k}_\parallel)\bar{m}_Y(\mathbf{k}_\parallel) - \tfrac{H_s}{2M_s}\cos(2\theta_M)\sum_{\mathbf{k}_\parallel}\bar{m}_X^*(\mathbf{k}_\parallel)\bar{m}_X(\mathbf{k}_\parallel) + ... \end{aligned} \tag{5.14}$$

Exchange interaction energy :

$$H_{exch} \approx \frac{J}{2M_s^2}\int\limits_V d^3r\left|\nabla\vec{M}(\mathbf{r}_\parallel)\right|^2 \tag{5.15}$$

where the gradient ∇ is calculated with respect to the global Oxyz system. From Eq.(5.5) it is

$$\begin{aligned} \nabla\vec{M}(\mathbf{r}_\parallel) &\approx \nabla\left[M_s - \tfrac{1}{2}\tfrac{\vec{m}^2(\mathbf{r}_\parallel)}{M_s} + ...\right]\hat{\mathbf{Z}} + \nabla\vec{m}(\mathbf{r}_\parallel) = ... = \\ &-\sin\theta_M\tfrac{\vec{m}(\mathbf{r}_\parallel)}{M_s}\cdot\tfrac{\partial\vec{m}(\mathbf{r}_\parallel)}{\partial x} + \cos\theta_M\tfrac{\partial\bar{m}_X(\mathbf{r}_\parallel)}{\partial x} + \tfrac{\partial\bar{m}_Y(\mathbf{r}_\parallel)}{\partial y} \\ &-\cos\theta_M\tfrac{\vec{m}(\mathbf{r}_\parallel)}{M_s}\cdot\tfrac{\partial\vec{m}(\mathbf{r}_\parallel)}{\partial z} - \sin\theta_M\tfrac{\partial\bar{m}_X(\mathbf{r}_\parallel)}{\partial z} \end{aligned} \tag{5.16}$$

and further,

$$\begin{aligned} \left|\nabla\vec{M}(\mathbf{r}_\parallel)\right|^2 &\approx ... \approx \cos^2\theta_M\left(\tfrac{\partial\bar{m}_X(\mathbf{r}_\parallel)}{\partial x}\right)^2 + \left(\tfrac{\partial\bar{m}_Y(\mathbf{r}_\parallel)}{\partial y}\right)^2 + \\ &2\cos\theta_M\tfrac{\partial\bar{m}_X(\mathbf{r}_\parallel)}{\partial x}\tfrac{\partial\bar{m}_Y(\mathbf{r}_\parallel)}{\partial y} \end{aligned} \tag{5.17}$$

where in the last equation, terms proportional to $\vec{m}(\mathbf{r}_\parallel)/M_s$ as well as terms that encompass variation of the coarse-grained order parameter along the z-direction were ignored, in view of the approximations elaborated previously. From Eqs.(5.15) and (5.17) we get

$$H_{exch} \approx \frac{J}{2M_s^2} \int\limits_V d^3r \left| \nabla \vec{M}(\mathbf{r}_\parallel) \right|^2 =$$

$$\frac{J}{2M_s^2} \int\limits_V d^3r \left\{ \cos^2\theta_M \left(\frac{\partial \bar{m}_X(\mathbf{r}_\parallel)}{\partial x} \right)^2 + \left(\frac{\partial \bar{m}_Y(\mathbf{r}_\parallel)}{\partial y} \right)^2 + 2\cos\theta_M \frac{\partial \bar{m}_X(\mathbf{r}_\parallel)}{\partial x} \frac{\partial \bar{m}_Y(\mathbf{r}_\parallel)}{\partial y} \right\} \tag{5.18}$$

Fourier Transforming the last equation we get

$$H_{exch} \approx \frac{D}{2M_s} \sum_{\mathbf{k}_\parallel} \left\{ \cos^2\theta_M k_x^2 \bar{m}_X^*(\mathbf{k}_\parallel)\bar{m}_X(\mathbf{k}_\parallel) + k_y^2 \bar{m}_Y^*(\mathbf{k}_\parallel)\bar{m}_Y(\mathbf{k}_\parallel) + \right.$$

$$\left. \cos\theta_M k_x k_y \bar{m}_Y^*(\mathbf{k}_\parallel)\bar{m}_X(\mathbf{k}_\parallel) + \cos\theta_M k_x k_y \bar{m}_X^*(\mathbf{k}_\parallel)\bar{m}_Y(\mathbf{k}_\parallel) \right\} =$$

$$\frac{1}{2M_s} \sum_{\mathbf{k}_\parallel} Dk_\parallel^2 \left\{ \cos^2\theta_M \cos^2\phi_{\mathbf{k}_\parallel} \bar{m}_X^*(\mathbf{k}_\parallel)\bar{m}_X(\mathbf{k}_\parallel) + \sin^2\phi_{\mathbf{k}_\parallel} \bar{m}_Y^*(\mathbf{k}_\parallel)\bar{m}_Y(\mathbf{k}_\parallel) + \right.$$

$$\left. \tfrac{1}{2}\cos\theta_M \sin(2\phi_{\mathbf{k}_\parallel}) \bar{m}_Y^*(\mathbf{k}_\parallel)\bar{m}_X(\mathbf{k}_\parallel) + \tfrac{1}{2}\cos\theta_M \sin(2\phi_{\mathbf{k}_\parallel}) \bar{m}_X^*(\mathbf{k}_\parallel)\bar{m}_Y(\mathbf{k}_\parallel) \right\} \tag{5.19}$$

where we've defined the so-called "exchange stiffness" as

$$D = J/M_s \tag{5.20}$$

Dipolar interaction energy : The dipolar field $\vec{h}_d(\mathbf{r}, t)$ consists of a static component (which is of zero order in the coarse-grained magnetization deviation) when the coarse-grained order parameter is tilted out of the plane of the

film, and a dynamic component that is generated by the motion of the coarse-grained order parameter of the YIG. The dynamic dipolar component can be expanded in powers of the deviation of the coarse-grained order parameter from its equilibrium direction, analogously to the expansion of the coarse-grained order parameter appearing in Eq.(5.3). In the next steps, following Landeros, Arias and Mills, we keep only the static (zero order) term $\vec{h}_d^{(0)}(\mathbf{r})$ as well as the dynamic first order term denoted as $\vec{h}_d^{(1)}(\mathbf{r},t)$. Saying so, the dipolar contribution to the energy of the system up to the second order in the deviation of the coarse-grained order parameter (from its equilibrium position) is given by (for convenience we skip the time-dependence in the following)

$$H_d = -\tfrac{1}{2}\mu_0 \int_V d^3r \vec{M}(\mathbf{r}_\parallel)\cdot\vec{h}_d(\mathbf{r}) =$$

$$-\tfrac{1}{2}\mu_0 \int_V d^3r \left\{\vec{M}^{(0)} + \vec{M}^{(1)}(\mathbf{r}_\parallel) + \vec{M}^{(2)}(\mathbf{r}_\parallel) + ...\right\}\cdot\left\{\vec{h}_d^{(0)}(\mathbf{r}) + \vec{h}_d^{(1)}(\mathbf{r}) + \vec{h}_d^{(2)}(\mathbf{r}) + ...\right\} =$$

$$-\tfrac{1}{2}\mu_0 \int_V d^3r \left\{\vec{M}^{(0)} + \vec{M}^{(1)}(\mathbf{r}_\parallel) + \vec{M}^{(2)}(\mathbf{r}_\parallel) + ...\right\}\cdot\vec{h}_d^{(0)}(\mathbf{r})$$

$$-\tfrac{1}{2}\mu_0 \int_V d^3r \left\{\vec{M}^{(0)} + \vec{M}^{(1)}(\mathbf{r}_\parallel) + \vec{M}^{(2)}(\mathbf{r}_\parallel) + ...\right\}\cdot\vec{h}_d^{(1)}(\mathbf{r})$$

$$-\tfrac{1}{2}\mu_0 \int_V d^3r \left\{\vec{M}^{(0)} + \vec{M}^{(1)}(\mathbf{r}_\parallel) + \vec{M}^{(2)}(\mathbf{r}_\parallel) + ...\right\}\cdot\vec{h}_d^{(2)}(\mathbf{r}) + ...$$

or

$$
\begin{aligned}
H_d &= -\tfrac{1}{2}\mu_0 \int\limits_V d^3r \left\{ \vec{M}^{(0)} + \vec{M}^{(1)}(\mathbf{r}_\parallel) + \vec{M}^{(2)}(\mathbf{r}_\parallel) + ... \right\} \cdot \vec{h}_d^{(0)}(\mathbf{r}) \\
&-\tfrac{1}{2}\mu_0 \int\limits_V d^3r \left\{ \vec{M}^{(1)}(\mathbf{r}_\parallel) \cdot \vec{h}_d^{(0)}(\mathbf{r}) + \vec{M}^{(1)}(\mathbf{r}_\parallel) \cdot \vec{h}_d^{(1)}(\mathbf{r}) + \underbrace{\vec{M}^{(2)}(\mathbf{r}_\parallel) \cdot \vec{h}_d^{(1)}(\mathbf{r})}_{\propto (spin\ deviation)^3} + ... \right\} \\
&-\tfrac{1}{2}\mu_0 \int\limits_V d^3r \left\{ \vec{M}^{(2)}(\mathbf{r}_\parallel) \cdot \vec{h}_d^{(0)}(\mathbf{r}) + \underbrace{\vec{M}^{(1)}(\mathbf{r}_\parallel) \cdot \vec{h}_d^{(2)}(\mathbf{r})}_{\propto (spin\ deviation)^3} + \underbrace{\vec{M}^{(2)}(\mathbf{r}_\parallel) \cdot \vec{h}_d^{(2)}(\mathbf{r})}_{\propto (spin\ deviation)^4} + ... \right\} + ... \\
&\approx -\tfrac{1}{2}\mu_0 \int\limits_V d^3r \left\{ \vec{M}^{(0)} + 2\vec{M}^{(1)}(\mathbf{r}_\parallel) + 2\vec{M}^{(2)}(\mathbf{r}_\parallel) + ... \right\} \cdot \vec{h}_d^{(0)}(\mathbf{r}) \\
&-\tfrac{1}{2}\mu_0 \int\limits_V d^3r \vec{M}^{(1)}(\mathbf{r}_\parallel) \cdot \vec{h}_d^{(1)}(\mathbf{r}) + ...
\end{aligned}
\tag{5.22}
$$

where a magnetostatics "reciprocity theorem" was used (Ref.[65], section 12.6), as a result of which, the following identity is valid

$$
\mu_0 \int\limits_V d^3r \vec{M}^{(1,\,2)}(\mathbf{r}_\parallel) \cdot \vec{h}_d^{(0)}(\mathbf{r}) = \mu_0 \int\limits_V d^3r \vec{M}^{(0)}(\mathbf{r}_\parallel) \cdot \vec{h}_d^{(1,\,2)}(\mathbf{r}) \tag{5.23}
$$

In the following, we calculate explicitly the dipolar field terms $\vec{h}_d^{(0)}(\mathbf{r})$ and $\vec{h}_d^{(1)}(\mathbf{r})$. The dipolar field is generally given by (see Ref.[65])

$$
\vec{h}_d(\mathbf{r}, t) = -\nabla_{\mathbf{r}} \phi_d(\mathbf{r}, t) \tag{5.24}
$$

where according to the magnetostatics the magnetic scalar potential satisfies the Poisson equation

$$
\nabla^2_{\mathbf{r}} \phi_d(\mathbf{r}, t) = \nabla \cdot \vec{M}(\mathbf{r}_\parallel, t) \tag{5.25}
$$

Using the decomposition of Eq.(5.3), from Eqs.(5.24) and (5.25) we get

$$\begin{array}{l}\vec{h}_d(\mathbf{r},t) = -\nabla_{\mathbf{r}}\phi_d(\mathbf{r},t) \Rightarrow \vec{h}_d^{(0)}(\mathbf{r}) + \vec{h}_d^{(1)}(\mathbf{r},t) + ... = \\ -\nabla_{\mathbf{r}}\phi_d^{(0)}(\mathbf{r}) - \nabla_{\mathbf{r}}\phi_d^{(1)}(\mathbf{r},t) - ... \\ \\ \nabla_{\mathbf{r}}^2\phi_d^{(0)}(\mathbf{r}) + \nabla_{\mathbf{r}}^2\phi_d^{(1)}(\mathbf{r},t) + ... = \nabla\cdot\vec{M}^{(0)} + \nabla\cdot\vec{M}^{(1)}(\mathbf{r}_\parallel,t) + ...\end{array} \tag{5.26}$$

At the zeroth-order we get

$$\nabla_{\mathbf{r}}^2\phi_d^{(0)}(\mathbf{r}) = \nabla\cdot\vec{M}^{(0)} = 0 \tag{5.27}$$

To proceed further with the last equation, we expand the sought magnetic scalar potential as below (the postulated expansion is justified within the thin film approach employed here)

$$\phi_d^{(0)}(\mathbf{r}) = \frac{1}{\sqrt{L^2 d}}\sum_{\mathbf{k}_\parallel}\Phi_{\mathbf{k}_\parallel}^{(0)}(z)\exp\left(i\mathbf{k}_\parallel\cdot\mathbf{r}_\parallel\right) \tag{5.28}$$

Substituting Eq.(5.28) into (5.27) we find

$$\begin{array}{l}\frac{d^2\Phi_{\mathbf{k}_\parallel}^{(0)}(z)}{dz^2} - k_\parallel^2\Phi_{\mathbf{k}_\parallel}^{(0)}(z) = 0, \;\; if\; k_\parallel \neq 0, \\ \\ \frac{d^2\Phi_{\mathbf{k}_\parallel}^{(0)}(z)}{dz^2} = 0, \;\; if\; k_\parallel = 0\end{array} \tag{5.29}$$

Furthermore, we seek solutions of the following form

$$\Phi_{\mathbf{k}_\parallel}^{(0)}(z) = \left\{\begin{array}{l} \left\{\begin{array}{ll} A_{\mathbf{k}_\parallel}e^{-k_\parallel z}, & z > d \\ a_{\mathbf{k}_\parallel}e^{-k_\parallel z} + b_{\mathbf{k}_\parallel}e^{k_\parallel z}, & 0 < z < d \\ B_{\mathbf{k}_\parallel}e^{k_\parallel z}, & z < 0 \end{array}\right\},\; if\; k_\parallel \neq 0 \\ \\ \left\{\begin{array}{ll} A_0 + B_0 z, & z > d \\ a_0 + b_0 z, & 0 < z < d \\ C_0 + D_0 z, & z < 0 \end{array}\right\},\; if\; k_\parallel = 0 \end{array}\right. \tag{5.30}$$

Using appropriate boundary as well as interface conditions for the magnetic scalar potential (that is to say, continuity of the magnetic scalar potential, and

discontinuity of its derivative due to any surface magnetic charge across each interface between the magnetized film and the vacuum), we get the following system of equations (and the corresponding solutions)

$$\left.\begin{array}{l} b_{\mathbf{k}_\parallel} e^{k_\parallel d} + \left(A_{\mathbf{k}_\parallel} - a_{\mathbf{k}_\parallel}\right) e^{-k_\parallel d} = 0 \\ B_{\mathbf{k}_\parallel} - b_{\mathbf{k}_\parallel} + a_{\mathbf{k}_\parallel} = 0 \\ a_{\mathbf{k}_\parallel} + b_{\mathbf{k}_\parallel} = B_{\mathbf{k}_\parallel} \\ a_{\mathbf{k}_\parallel} e^{-k_\parallel d} + b_{\mathbf{k}_\parallel} e^{k_\parallel d} = A_{\mathbf{k}_\parallel} e^{-k_\parallel d} \end{array}\right\} \Leftrightarrow ... \Leftrightarrow$$

$$\left\{\begin{array}{l} a_{\mathbf{k}_\parallel} = 0 \\ b_{\mathbf{k}_\parallel} = 0 \\ A_{\mathbf{k}_\parallel} = 0 \\ B_{\mathbf{k}_\parallel} = 0 \end{array}\right. \quad , \quad if\ k_\parallel \neq 0, \quad and \tag{5.31}$$

$$\left\{\begin{array}{l} b_0 = \sqrt{L^2 d} M_s \cos\theta_M \\ D_0 = 0, \;\; B_0 = 0, \;\; C_0 = 0, \;\; a_0 = 0 \end{array}\right. \quad , \quad if\ k_\parallel = 0$$
$$A_0 = \sqrt{L^2 d} M_s \cos\theta_M d$$

It is noted that the derivative discontinuity across the film-vacuum interface is given by

$$\left.\frac{d\Phi^{(0)}_{\mathbf{k}_\parallel}(z)}{dz}\right|_{z=d^-} - \left.\frac{d\Phi^{(0)}_{\mathbf{k}_\parallel}(z)}{dz}\right|_{z=d^+} = \sqrt{L^2 d} M_s \cos\theta_M \delta_{\mathbf{k}_\parallel,0} \tag{5.32}$$

Combining Eqs.(5.30) and (5.31) one finds

$$\Phi^{(0)}_{\mathbf{k}_\parallel}(z) = \left\{\begin{array}{ll} 0, & z > d \\ 0, & 0 < z < d, \quad if\ k_\parallel \neq 0 \\ 0, & z < 0 \end{array}\right. ,$$

$$\Phi^{(0)}_{\mathbf{k}_\parallel}(z) = \left\{\begin{array}{ll} \sqrt{L^2 d} M_s \cos\theta_M d, & z > d \\ \sqrt{L^2 d} M_s \cos\theta_M z, & 0 < z < d \\ 0, & z < 0 \end{array}\right. , \quad if\ k_\parallel = 0 \tag{5.33}$$

The static dipolar field is given by $\vec{h}_d^{(0)}(\mathbf{r}) = -\nabla_{\mathbf{r}}\phi_d^{(0)}(\mathbf{r})$, therefore, using Eq.(5.33) it is

$$\vec{h}_d^{(0)}(\mathbf{r}) = -\frac{1}{\sqrt{L^2 d}}\nabla_{\mathbf{r}} \sum_{\mathbf{k}_\parallel} \Phi_{\mathbf{k}_\parallel}^{(0)}(z) \exp\left(i\mathbf{k}_\parallel \cdot \mathbf{r}_\parallel\right) =$$

$$-\frac{1}{\sqrt{L^2 d}} \frac{d\Phi_{\mathbf{k}_\parallel=0}^{(0)}(z)}{dz}\hat{\mathbf{z}} - \frac{1}{\sqrt{L^2 d}} \sum_{\mathbf{k}_\parallel \neq 0} \frac{d\Phi_{\mathbf{k}_\parallel \neq 0}^{(0)}(z)}{dz} \exp\left(i\mathbf{k}_\parallel \cdot \mathbf{r}_\parallel\right)\hat{\mathbf{z}} \tag{5.34}$$

$$-\frac{1}{\sqrt{L^2 d}} \sum_{\mathbf{k}_\parallel \neq 0} \left\{ i\mathbf{k}_\parallel \Phi_{\mathbf{k}_\parallel \neq 0}^{(0)}(z) \exp\left(i\mathbf{k}_\parallel \cdot \mathbf{r}_\parallel\right)\right\} = -\frac{1}{\sqrt{L^2 d}} \frac{d\Phi_{\mathbf{k}_\parallel=0}^{(0)}(z)}{dz}\hat{\mathbf{z}}$$

and finally averaging over the film thickness one finds (Landeros, Arias and Mills provide this result without proof)

$$\begin{aligned} \vec{h}_d^{(0)}(\mathbf{r}) &= \frac{1}{d}\int_0^d dz \vec{h}_d^{(0)}(\mathbf{r}) = -\frac{1}{\sqrt{L^2 d}}\frac{1}{d}\int_0^d dz \frac{d\Phi_{\mathbf{k}_\parallel=0}^{(0)}(z)}{dz}\hat{\mathbf{z}} \\ &= -\frac{1}{\sqrt{L^2 d}}\frac{1}{d}\left\{\Phi_{\mathbf{k}_\parallel=0}^{(0)}(d) - \Phi_{\mathbf{k}_\parallel=0}^{(0)}(0)\right\}\hat{\mathbf{z}} = -M_s \cos\theta_M \hat{\mathbf{z}} \end{aligned} \tag{5.35}$$

Now, we proceed to calculate the first contribution to the dipolar interaction energy (the first term in the last line on the RHS of Eq.(5.22))

$$-\frac{1}{2}\mu_0 \int_V d^3 r \left\{\vec{M}^{(0)} + 2\vec{M}^{(1)}(\mathbf{r}_\parallel) + 2\vec{M}^{(2)}(\mathbf{r}_\parallel) + ...\right\} \cdot \vec{h}_d^{(0)}(\mathbf{r}) \approx$$

$$\frac{1}{2}\mu_0 (M_s \cos\theta_M)^2 V - \frac{1}{2}\mu_0 M_s \sin(2\theta_M) \int_V d^3 r \bar{m}_X(\mathbf{r}_\parallel) \tag{5.36}$$

$$-\frac{1}{2}\mu_0 \cos^2\theta_M \int_V d^3 r \left[\bar{m}_X^2(\mathbf{r}_\parallel) + \bar{m}_Y^2(\mathbf{r}_\parallel)\right]$$

which, after Fourier Transforming, finally takes the following form

$$
\begin{aligned}
&-\tfrac{1}{2}\mu_0 \int\limits_V d^3r \left\{ \vec{M}^{(0)} + 2\vec{M}^{(1)}(\mathbf{r}_\parallel) + 2\vec{M}^{(2)}(\mathbf{r}_\parallel) + ... \right\} \cdot \vec{h}_d^{(0)}(\mathbf{r}) = \\
&\tfrac{1}{2}\mu_0 (M_s \cos\theta_M)^2 V - \tfrac{1}{2}\mu_0 M_s \sin(2\theta_M)\sqrt{V}\bar{m}_X(\mathbf{k}_\parallel = 0) \\
&-\tfrac{1}{2}\mu_0 \cos^2\theta_M \sum_{\mathbf{k}_\parallel} \bar{m}_X^*(\mathbf{k}_\parallel)\bar{m}_X(\mathbf{k}_\parallel) - \tfrac{1}{2}\mu_0 \cos^2\theta_M \sum_{\mathbf{k}_\parallel} \bar{m}_Y^*(\mathbf{k}_\parallel)\bar{m}_Y(\mathbf{k}_\parallel)
\end{aligned}
\tag{5.37}
$$

Next, we proceed to the derivation of the lowest order dynamic dipolar field $\vec{h}_d^{(1)}(\mathbf{r}, t)$. At the first-order (we skip the time dependence for convenience) it is

$$
\begin{aligned}
&\nabla_{\mathbf{r}}^2 \phi_d^{(1)}(\mathbf{r}) = \nabla \cdot \vec{M}^{(1)} = \cos\theta_M \tfrac{\partial \bar{m}_X(\mathbf{r}_\parallel)}{\partial x} + \tfrac{\partial \bar{m}_Y(\mathbf{r}_\parallel)}{\partial y} - \sin\theta_M \tfrac{\partial \bar{m}_X(\mathbf{r}_\parallel)}{\partial z} \\
&\approx \cos\theta_M \tfrac{\partial \bar{m}_X(\mathbf{r}_\parallel)}{\partial x} + \tfrac{\partial \bar{m}_Y(\mathbf{r}_\parallel)}{\partial y}
\end{aligned}
\tag{5.38}
$$

To proceed further, we expand the sought magnetic scalar potential as below

$$
\phi_d^{(1)}(\mathbf{r}) = \frac{1}{\sqrt{L^2 d}} \sum_{\mathbf{k}_\parallel} \Phi_{\mathbf{k}_\parallel}^{(1)}(z) \exp\left(i\mathbf{k}_\parallel \cdot \mathbf{r}_\parallel\right) \tag{5.39}
$$

Fourier Transforming (FT) the RHS of Eq.(5.38) using the convention of Eq.(5.2), and then combining the last two equations we get

$$
\begin{aligned}
&\begin{cases}
\frac{d^2\Phi_{\mathbf{k}_\parallel}^{(1)}(z)}{dz^2} - k_\parallel^2 \Phi_{\mathbf{k}_\parallel}^{(1)}(z) = \\
ik_x \bar{m}_X(\mathbf{k}_\parallel)\cos\theta_M + ik_y \bar{m}_Y(\mathbf{k}_\parallel) \equiv f(\mathbf{k}_\parallel), \;\; if\; 0 < z < d \\
\frac{d^2\Phi_{\mathbf{k}_\parallel}^{(1)}(z)}{dz^2} - k_\parallel^2 \Phi_{\mathbf{k}_\parallel}^{(1)}(z) = 0, \;\; if\; z > d \; or \; z < 0
\end{cases}, \quad if\; k_\parallel \neq 0 \\
&\frac{d^2\Phi_{\mathbf{k}_\parallel}^{(1)}(z)}{dz^2} = 0, \quad if\; k_\parallel = 0
\end{aligned}
\tag{5.40}
$$

We proceed seeking solutions of the following form

$$\Phi^{(1)}_{\mathbf{k}_\parallel}(z) = \begin{cases} \left\{ \begin{array}{ll} A_{\mathbf{k}_\parallel} e^{-k_\parallel z}, & z > d \\ a_{\mathbf{k}_\parallel} e^{-k_\parallel z} + b_{\mathbf{k}_\parallel} e^{k_\parallel z} - \frac{f(\mathbf{k}_\parallel)}{k_\parallel^2}, & 0 < z < d \\ B_{\mathbf{k}_\parallel} e^{k_\parallel z}, & z < 0 \end{array} \right\}, \quad if\ k_\parallel \neq 0 \\ \\ \left\{ \begin{array}{ll} A_0 + B_0 z, & z > d \\ a_0 + b_0 z, & 0 < z < d \\ C_0 + D_0 z, & z < 0 \end{array} \right\}, \quad if\ k_\parallel = 0 \end{cases} \tag{5.41}$$

Using again appropriate boundary as well as interface conditions for the magnetic scalar potential (that is to say, continuity of the magnetic scalar potential, and discontinuity of its derivative due to any surface magnetic charge across each interface between the magnetized film and the vacuum), we get the following system of equations (and the corresponding solutions)

$$\left\{ \begin{array}{l} b_{\mathbf{k}_\parallel} e^{k_\parallel d} + \left(A_{\mathbf{k}_\parallel} - a_{\mathbf{k}_\parallel} \right) e^{-k_\parallel d} = -\frac{\bar{m}_X(\mathbf{k}_\parallel) \sin\theta_M}{k_\parallel} \equiv g(\mathbf{k}_\parallel) \\ B_{\mathbf{k}_\parallel} - b_{\mathbf{k}_\parallel} + a_{\mathbf{k}_\parallel} = \frac{\bar{m}_X(\mathbf{k}_\parallel) \sin\theta_M}{k_\parallel} \equiv -g(\mathbf{k}_\parallel) \\ a_{\mathbf{k}_\parallel} + b_{\mathbf{k}_\parallel} - \frac{f(\mathbf{k}_\parallel)}{k_\parallel^2} = B_{\mathbf{k}_\parallel} \\ a_{\mathbf{k}_\parallel} e^{-k_\parallel d} + b_{\mathbf{k}_\parallel} e^{k_\parallel d} - \frac{f(\mathbf{k}_\parallel)}{k_\parallel^2} = A_{\mathbf{k}_\parallel} e^{-k_\parallel d} \end{array} \right\} \Leftrightarrow \ldots \Leftrightarrow$$

$$\left\{ \begin{array}{l} a_{\mathbf{k}_\parallel} = \frac{1}{2} \left[\frac{f(\mathbf{k}_\parallel)}{k_\parallel^2} - g(\mathbf{k}_\parallel) \right] \\ b_{\mathbf{k}_\parallel} = \frac{e^{-k_\parallel d}}{2} \left[\frac{f(\mathbf{k}_\parallel)}{k_\parallel^2} + g(\mathbf{k}_\parallel) \right] \\ A_{\mathbf{k}_\parallel} = \frac{1}{2} \left[-\frac{f(\mathbf{k}_\parallel)}{k_\parallel^2} + g(\mathbf{k}_\parallel) \right] \left(e^{k_\parallel d} - 1 \right) \\ B_{\mathbf{k}_\parallel} = \frac{1}{2} \left[\frac{f(\mathbf{k}_\parallel)}{k_\parallel^2} + g(\mathbf{k}_\parallel) \right] \left(e^{-k_\parallel d} - 1 \right) \end{array} \right. , \quad if\ k_\parallel \neq 0 \tag{5.42}$$

$$\left\{ \begin{array}{l} D_0 = 0, \quad B_0 = 0, \quad C_0 = 0, \quad a_0 = 0 \\ b_0 = -\sin\theta_M \bar{m}_X(\mathbf{k}_\parallel = 0) \\ A_0 = -d \sin\theta_M \bar{m}_X(\mathbf{k}_\parallel = 0) \end{array} \right. , \quad if\ k_\parallel = 0$$

It is noted that the derivative discontinuity across the top film-vacuum interface is given by

$$\left.\frac{d\Phi^{(1)}_{\mathbf{k}_\parallel}(z)}{dz}\right|_{z=d^-} - \left.\frac{d\Phi^{(1)}_{\mathbf{k}_\parallel}(z)}{dz}\right|_{z=d^+} = -\sin\theta_M \bar{m}_X(\mathbf{k}_\parallel) \tag{5.43}$$

and there is an analogous matching condition for the bottom interface at $z = 0$. Combining Eqs.(5.41) and (5.42) we find that

$$\Phi^{(1)}_{\mathbf{k}_\parallel}(z) = \begin{cases} -d\sin\theta_M \bar{m}_X(\mathbf{k}_\parallel = 0), & z > d \\ -\sin\theta_M \bar{m}_X(\mathbf{k}_\parallel = 0) z, & 0 < z < d \\ 0, & z < 0 \end{cases} \quad , \; if \; k_\parallel = 0 \tag{5.44}$$

and also

$$\Phi^{(1)}_{\mathbf{k}_\parallel}(z) = \begin{cases} \frac{1}{2}\left[-\frac{f(\mathbf{k}_\parallel)}{k^2_\parallel} + g(\mathbf{k}_\parallel)\right]\left(e^{k_\parallel d} - 1\right) e^{-k_\parallel z}, & z > d \\ \frac{1}{2}\left[\frac{f(\mathbf{k}_\parallel)}{k^2_\parallel} - g(\mathbf{k}_\parallel)\right] e^{-k_\parallel z} + \frac{e^{-k_\parallel d}}{2}\left[\frac{f(\mathbf{k}_\parallel)}{k^2_\parallel} + g(\mathbf{k}_\parallel)\right] e^{k_\parallel z} & \\ -\frac{f(\mathbf{k}_\parallel)}{k^2_\parallel}, \quad 0 < z < d & \\ \frac{1}{2}\left[\frac{f(\mathbf{k}_\parallel)}{k^2_\parallel} + g(\mathbf{k}_\parallel)\right]\left(e^{-k_\parallel d} - 1\right) e^{k_\parallel z}, & z < 0 \end{cases} \quad , \quad if \; k_\parallel \neq 0 \tag{5.45}$$

The lowest order dynamic dipolar field is given by $\vec{h}_d^{(1)}(\mathbf{r},t) = -\nabla_{\mathbf{r}}\phi_d^{(1)}(\mathbf{r},t)$, and further, using Eq.(5.39) it is

$$\vec{h}_d^{(1)}(\mathbf{r}) = -\tfrac{1}{\sqrt{L^2 d}}\nabla_{\mathbf{r}} \sum_{\mathbf{k}_\parallel} \Phi_{\mathbf{k}_\parallel}^{(1)}(z) \exp\left(i\mathbf{k}_\parallel \cdot \mathbf{r}_\parallel\right) =$$

$$-\tfrac{1}{\sqrt{L^2 d}} \sum_{\mathbf{k}_\parallel} \left\{ i\mathbf{k}_\parallel \Phi_{\mathbf{k}_\parallel}^{(1)}(z) \exp\left(i\mathbf{k}_\parallel \cdot \mathbf{r}_\parallel\right)\right\} - \tfrac{1}{\sqrt{L^2 d}} \sum_{\mathbf{k}_\parallel} \frac{d\Phi_{\mathbf{k}_\parallel}^{(1)}(z)}{dz} \exp\left(i\mathbf{k}_\parallel \cdot \mathbf{r}_\parallel\right) \hat{\mathbf{z}} =$$

$$-\tfrac{1}{\sqrt{L^2 d}} \frac{d\Phi_{\mathbf{k}_\parallel=0}^{(1)}(z)}{dz} \hat{\mathbf{z}} - \tfrac{1}{\sqrt{L^2 d}} \sum_{\mathbf{k}_\parallel \neq 0} \left\{ i\mathbf{k}_\parallel \Phi_{\mathbf{k}_\parallel}^{(1)}(z) \exp\left(i\mathbf{k}_\parallel \cdot \mathbf{r}_\parallel\right)\right\}$$

$$-\tfrac{1}{\sqrt{L^2 d}} \sum_{\mathbf{k}_\parallel \neq 0} \frac{d\Phi_{\mathbf{k}_\parallel}^{(1)}(z)}{dz} \exp\left(i\mathbf{k}_\parallel \cdot \mathbf{r}_\parallel\right) \hat{\mathbf{z}} \tag{5.46}$$

Now, we proceed to calculate the second contribution to the dipolar interaction energy (the second term in the last line on the RHS of Eq.(5.22))

$$-\tfrac{1}{2}\mu_0 \int\limits_V d^3 r \vec{M}^{(1)}(\mathbf{r}_\parallel) \cdot \vec{h}_d^{(1)}(\mathbf{r}) = ... =$$

$$\tfrac{1}{2}\mu_0 \sin^2\theta_M \bar{m}_X^2(\mathbf{k}_\parallel = 0) + \tfrac{1}{2}\mu_0 \sin^2\theta_M \sum_{\mathbf{k}_\parallel \neq 0} \bar{m}_X^*(\mathbf{k}_\parallel)\bar{m}_X(\mathbf{k}_\parallel) \left(\tfrac{1-e^{-k_\parallel d}}{k_\parallel d}\right) +$$

$$\tfrac{1}{2}\mu_0 \sum_{\mathbf{k}_\parallel \neq 0} \left\{ \cos^2\phi_{\mathbf{k}_\parallel} \cos^2\theta_M \bar{m}_X^*(\mathbf{k}_\parallel)\bar{m}_X(\mathbf{k}_\parallel) + \tfrac{1}{2}\sin(2\phi_{\mathbf{k}_\parallel})\cos\theta_M \bar{m}_Y^*(\mathbf{k}_\parallel)\bar{m}_X(\mathbf{k}_\parallel) + \right.$$

$$\left. \tfrac{1}{2}\sin(2\phi_{\mathbf{k}_\parallel})\cos\theta_M \bar{m}_X^*(\mathbf{k}_\parallel)\bar{m}_Y(\mathbf{k}_\parallel) + \sin^2\phi_{\mathbf{k}_\parallel} \bar{m}_Y^*(\mathbf{k}_\parallel)\bar{m}_Y(\mathbf{k}_\parallel) \right\} \left(1 - \tfrac{1-e^{-k_\parallel d}}{k_\parallel d}\right) \tag{5.47}$$

where along the way we Fourier Transformed also (this step is skipped though). Within the thin film approximation it is $k_\parallel d << 1$, as a result of which, from

the last equation we get

$$-\tfrac{1}{2}\mu_0 \int_V d^3r \vec{M}^{(1)}(\mathbf{r}_\parallel)\cdot\vec{h}_d^{(1)}(\mathbf{r}) \approx \tfrac{1}{2}\mu_0 \sin^2\theta_M \bar{m}_X^*(\mathbf{k}_\parallel=0)\bar{m}_X(\mathbf{k}_\parallel=0)+$$

$$\tfrac{1}{2}\mu_0 \sin^2\theta_M \sum_{\mathbf{k}_\parallel\neq 0}\left(1-\tfrac{1}{2}k_\parallel d\right)\bar{m}_X^*(\mathbf{k}_\parallel)\bar{m}_X(\mathbf{k}_\parallel)+$$

$$\tfrac{1}{4}\mu_0 \sum_{\mathbf{k}_\parallel\neq 0} k_\parallel d\left\{\cos^2\phi_{\mathbf{k}_\parallel}\cos^2\theta_M \bar{m}_X^*(\mathbf{k}_\parallel)\bar{m}_X(\mathbf{k}_\parallel)+\tfrac{1}{2}\sin(2\phi_{\mathbf{k}_\parallel})\cos\theta_M \bar{m}_Y^*(\mathbf{k}_\parallel)\bar{m}_X(\mathbf{k}_\parallel)+\right.$$

$$\left.\tfrac{1}{2}\sin(2\phi_{\mathbf{k}_\parallel})\cos\theta_M \bar{m}_X^*(\mathbf{k}_\parallel)\bar{m}_Y(\mathbf{k}_\parallel)+\sin^2\phi_{\mathbf{k}_\parallel}\bar{m}_Y^*(\mathbf{k}_\parallel)\bar{m}_Y(\mathbf{k}_\parallel)\right\}$$

or

$$-\tfrac{1}{2}\mu_0 \int_V d^3r \vec{M}^{(1)}(\mathbf{r}_\parallel)\cdot\vec{h}_d^{(1)}(\mathbf{r}) \approx \tfrac{1}{2}\mu_0 \sin^2\theta_M \sum_{\mathbf{k}_\parallel}\left(1-\tfrac{1}{2}k_\parallel d\right)\bar{m}_X^*(\mathbf{k}_\parallel)\bar{m}_X(\mathbf{k}_\parallel)+$$

$$\tfrac{1}{4}\mu_0 \sum_{\mathbf{k}_\parallel} k_\parallel d\left\{\cos^2\phi_{\mathbf{k}_\parallel}\cos^2\theta_M \bar{m}_X^*(\mathbf{k}_\parallel)\bar{m}_X(\mathbf{k}_\parallel)+\tfrac{1}{2}\sin(2\phi_{\mathbf{k}_\parallel})\cos\theta_M \bar{m}_Y^*(\mathbf{k}_\parallel)\bar{m}_X(\mathbf{k}_\parallel)+\right.$$

$$\left.\tfrac{1}{2}\sin(2\phi_{\mathbf{k}_\parallel})\cos\theta_M \bar{m}_X^*(\mathbf{k}_\parallel)\bar{m}_Y(\mathbf{k}_\parallel)+\sin^2\phi_{\mathbf{k}_\parallel}\bar{m}_Y^*(\mathbf{k}_\parallel)\bar{m}_Y(\mathbf{k}_\parallel)\right\} \tag{5.49}$$

Combining Eqs.(5.22), (5.37) and (5.49) for the dipolar contribution we get

$$
\begin{aligned}
&H_d \approx \tfrac{1}{2}\mu_0 (M_s \cos\theta_M)^2 V - \tfrac{1}{2}\mu_0 M_s \sin(2\theta_M)\sqrt{V}\bar{m}_X(\mathbf{k}_\parallel = 0) + \\
&\tfrac{1}{2}\mu_0 \sum_{\mathbf{k}_\parallel} \left\{ \tfrac{1}{2} k_\parallel d \left\{ \cos^2\phi_{\mathbf{k}_\parallel} \cos^2\theta_M - \sin^2\theta_M \right\} - \cos(2\theta_M) \right\} \bar{m}_X^*(\mathbf{k}_\parallel)\bar{m}_X(\mathbf{k}_\parallel) + \\
&\tfrac{1}{2}\mu_0 \sum_{\mathbf{k}_\parallel} \left\{ \tfrac{1}{2} k_\parallel d \sin^2\phi_{\mathbf{k}_\parallel} - \cos^2\theta_M \right\} \bar{m}_Y^*(\mathbf{k}_\parallel)\bar{m}_Y(\mathbf{k}_\parallel) + \\
&\tfrac{1}{8}\mu_0 \sum_{\mathbf{k}_\parallel} k_\parallel d \sin(2\phi_{\mathbf{k}_\parallel}) \cos\theta_M \bar{m}_Y^*(\mathbf{k}_\parallel)\bar{m}_X(\mathbf{k}_\parallel) + \\
&\tfrac{1}{8}\mu_0 \sum_{\mathbf{k}_\parallel} k_\parallel d \sin(2\phi_{\mathbf{k}_\parallel}) \cos\theta_M \bar{m}_X^*(\mathbf{k}_\parallel)\bar{m}_Y(\mathbf{k}_\parallel)
\end{aligned}
\tag{5.50}
$$

Combining all the aforementioned contributions, it is

$$H_{tot} \approx H_Z + H_A + H_{exch} + H_d = -\mu_0 M_s H_0 V \cos(\theta_H - \theta_M) +$$

$$\tfrac{1}{2}\mu_0 M_s^2 \cos^2\theta_M V + \tfrac{1}{2} H_s M_s V \cos^2\theta_M -$$

$$\left\{\mu_0 H_0 \sin(\theta_H - \theta_M) + \tfrac{1}{2}\mu_0 M_s \sin(2\theta_M) + \tfrac{1}{2} H_s \sin(2\theta_M)\right\} \sqrt{V}\bar{m}_X(\mathbf{k}_\parallel = 0) +$$

$$\tfrac{1}{2M_s} \sum_{\mathbf{k}_\parallel} \Big[\mu_0 H_0 \cos(\theta_H - \theta_M) - H_s \cos(2\theta_M) + D k_\parallel^2 \cos^2\theta_M \cos^2\phi_{\mathbf{k}_\parallel} +$$

$$\mu_0 M_s \left\{\tfrac{1}{2} k_\parallel d \left\{\cos^2\phi_{\mathbf{k}_\parallel} \cos^2\theta_M - \sin^2\theta_M\right\} - \cos(2\theta_M)\right\}\Big] \bar{m}_X^*(\mathbf{k}_\parallel)\bar{m}_X(\mathbf{k}_\parallel) +$$

$$\tfrac{1}{2M_s} \sum_{\mathbf{k}_\parallel} \Big[\mu_0 H_0 \cos(\theta_H - \theta_M) - H_s \cos^2\theta_M + D k_\parallel^2 \sin^2\phi_{\mathbf{k}_\parallel} +$$

$$\mu_0 M_s \left\{\tfrac{1}{2} k_\parallel d \sin^2\phi_{\mathbf{k}_\parallel} - \cos^2\theta_M\right\}\Big] \bar{m}_Y^*(\mathbf{k}_\parallel)\bar{m}_Y(\mathbf{k}_\parallel) +$$

$$\tfrac{1}{2M_s} \sum_{\mathbf{k}_\parallel} \left\{\tfrac{1}{2} D k_\parallel^2 \cos\theta_M \sin(2\phi_{\mathbf{k}_\parallel}) + \tfrac{1}{4}\mu_0 M_s k_\parallel d \sin(2\phi_{\mathbf{k}_\parallel}) \cos\theta_M\right\} \bar{m}_Y^*(\mathbf{k}_\parallel)\bar{m}_X(\mathbf{k}_\parallel) +$$

$$\tfrac{1}{2M_s} \sum_{\mathbf{k}_\parallel} \left\{\tfrac{1}{2} D k_\parallel^2 \cos\theta_M \sin(2\phi_{\mathbf{k}_\parallel}) + \tfrac{1}{4}\mu_0 M_s k_\parallel d \sin(2\phi_{\mathbf{k}_\parallel}) \cos\theta_M\right\} \bar{m}_X^*(\mathbf{k}_\parallel)\bar{m}_Y(\mathbf{k}_\parallel) \tag{5.51}$$

The static contribution is minimized if

$$\frac{\partial}{\partial\theta_M}\left\{-\mu_0 M_s H_0 V \cos(\theta_H - \theta_M) + \frac{1}{2}\mu_0 M_s^2 \cos^2\theta_M V + \frac{1}{2} H_s M_s V \cos^2\theta_M\right\} = 0$$

The last condition leads to the following result

$$\sin(\theta_M - \theta_H) = \frac{\mu_0 M_s + H_s}{2\mu_0 H_0} \sin(2\theta_M) \tag{5.52}$$

Under the condition of Eq.(5.52), further it is

$$-\left\{\mu_0 H_0 \sin(\theta_H - \theta_M) + \tfrac{1}{2}\mu_0 M_s \sin(2\theta_M) + \tfrac{1}{2} H_s \sin(2\theta_M)\right\} \sqrt{V}\bar{m}_X(\mathbf{k}_\parallel = 0)$$

$$= ... = 0$$

i.e. the linear term appearing in Eq.(5.51) vanishes.

To reduce the classical effective magnetic Hamiltonian of the YIG film derived above to a lowest order quantum mechanical magnetic Hamiltonian, we promote the classical magnetization fields to operators via the following prescription (which is acceptable as long as we are at temperatures much lower than the critical temperature of the YIG, Refs.[20, 35])

$$\begin{aligned} &\bar{m}_X^*(\mathbf{k}_\parallel) \to \hat{\bar{m}}_X^\dagger(\mathbf{k}_\parallel), \;\; \bar{m}_X(\mathbf{k}_\parallel) \to \hat{\bar{m}}_X(\mathbf{k}_\parallel), \\ &\bar{m}_Y^*(\mathbf{k}_\parallel) \to \hat{\bar{m}}_Y^\dagger(\mathbf{k}_\parallel), \;\; \bar{m}_Y(\mathbf{k}_\parallel) \to \hat{\bar{m}}_Y(\mathbf{k}_\parallel) \end{aligned} \tag{5.54}$$

Furthermore, the above defined operators obey the following commutation relations (please do not confuse μ_0 which denotes the vaccum permeability with $\tilde{\mu_0}$ that is defined below)

$$\begin{aligned} &\left[\hat{\bar{m}}_X(\mathbf{k}_\parallel),\ \hat{\bar{m}}_Y^\dagger(\mathbf{k'}_\parallel)\right] = i\tilde{\mu}_0 M_s \delta_{\mathbf{k}_\parallel,\mathbf{k'}_\parallel}, \\ &\left[\hat{\bar{m}}_X(\mathbf{k}_\parallel),\ \hat{\bar{m}}_X(\mathbf{k'}_\parallel)\right] = 0, \quad \left[\hat{\bar{m}}_Y(\mathbf{k}_\parallel),\ \hat{\bar{m}}_Y(\mathbf{k'}_\parallel)\right] = 0 \end{aligned} \tag{5.55}$$

where $\tilde{\mu}_0 = -\gamma\hbar$ denotes the effective (coarse-grained) magnetic moment per unit cell of the YIG, and $\gamma = g_J\mu_B/\hbar$ is the corresponding gyromagnetic ratio. Applying the operations of Eq.(5.54) to Eq.(5.51) we find the following neat form for the lowest order quantum mechanical effective magnetic Hamiltonian of the YIG film,

$$\begin{aligned} \hat{H}_{tot} = E_{clas} + \tfrac{1}{2M_s}\sum_{\mathbf{k}_\parallel} \Big[&H_X(\mathbf{k}_\parallel)\hat{\bar{m}}_X^\dagger(\mathbf{k}_\parallel)\hat{\bar{m}}_X(\mathbf{k}_\parallel) + H_Y(\mathbf{k}_\parallel)\hat{\bar{m}}_Y^\dagger(\mathbf{k}_\parallel)\hat{\bar{m}}_Y(\mathbf{k}_\parallel) + \\ &H_{XY}(\mathbf{k}_\parallel)\hat{\bar{m}}_X^\dagger(\mathbf{k}_\parallel)\hat{\bar{m}}_Y(\mathbf{k}_\parallel) + H_{YX}(\mathbf{k}_\parallel)\hat{\bar{m}}_Y^\dagger(\mathbf{k}_\parallel)\hat{\bar{m}}_X(\mathbf{k}_\parallel)\Big] \equiv E_{clas} + \hat{H}_0^{YIG} \end{aligned} \tag{5.56}$$

where for convenience the following definitions were used

$$
\begin{aligned}
&E_{clas} = -\mu_0 M_s H_0 V \cos(\theta_H - \theta_M) + \tfrac{1}{2} M_s V \cos^2\theta_M \left(\mu_0 M_s + H_s\right) \\
&H_X(\mathbf{k}_\parallel) = \underbrace{\mu_0 H_0 \cos(\theta_H - \theta_M) - (H_s + \mu_0 M_s)\cos^2\theta_M + (H_s + \mu_0 M_s)\sin^2\theta_M}_{\equiv H_X(0)} \\
&+ \left\{ D k_\parallel^2 + \tfrac{1}{2}\mu_0 M_s k_\parallel d \right\} \cos^2\phi_{\mathbf{k}_\parallel} \cos^2\theta_M - \tfrac{1}{2}\mu_0 M_s k_\parallel d \sin^2\theta_M \\
&H_Y(\mathbf{k}_\parallel) = \underbrace{\mu_0 H_0 \cos(\theta_H - \theta_M) - (H_s + \mu_0 M_s)\cos^2\theta_M}_{\equiv H_Y(0)} + \left\{ D k_\parallel^2 + \tfrac{1}{2}\mu_0 M_s k_\parallel d \right\} \sin^2\phi_{\mathbf{k}_\parallel} \\
&H_{XY}(\mathbf{k}_\parallel) = H_{YX}(\mathbf{k}_\parallel) = \tfrac{1}{2} \left\{ D k_\parallel^2 + \tfrac{1}{2}\mu_0 M_s k_\parallel d \right\} \cos\theta_M \sin(2\phi_{\mathbf{k}_\parallel})
\end{aligned}
\tag{5.57}
$$

Let us now proceed to derive the spin wave dispersion relation. First of all, it is straightforward to show that

$$
\begin{aligned}
&i\hbar \tfrac{d\hat{\tilde{m}}_X(\mathbf{k'}_\parallel)}{dt} = \left[\hat{\tilde{m}}_X(\mathbf{k'}_\parallel), \hat{H}_{tot} \right] = \left[\hat{\tilde{m}}_X(\mathbf{k'}_\parallel), \hat{H}_0^{YIG} \right] = \tfrac{i\tilde{\mu}_0}{2} \times \\
&\left\{ H_Y(\mathbf{k'}_\parallel)\hat{\tilde{m}}_Y(\mathbf{k'}_\parallel) + H_Y(-\mathbf{k'}_\parallel)\hat{\tilde{m}}_Y(\mathbf{k'}_\parallel) + H_{XY}(-\mathbf{k'}_\parallel)\hat{\tilde{m}}_X(\mathbf{k'}_\parallel) + H_{YX}(\mathbf{k'}_\parallel)\hat{\tilde{m}}_X(\mathbf{k'}_\parallel) \right\} \\
&i\hbar \tfrac{d\hat{\tilde{m}}_Y(\mathbf{k'}_\parallel)}{dt} = \left[\hat{\tilde{m}}_Y(\mathbf{k'}_\parallel), \hat{H}_{tot} \right] = \left[\hat{\tilde{m}}_Y(\mathbf{k'}_\parallel), \hat{H}_0^{YIG} \right] = -\tfrac{i\tilde{\mu}_0}{2} \times \\
&\left\{ H_X(\mathbf{k'}_\parallel)\hat{\tilde{m}}_X(\mathbf{k'}_\parallel) + H_X(-\mathbf{k'}_\parallel)\hat{\tilde{m}}_X(\mathbf{k'}_\parallel) + H_{XY}(\mathbf{k'}_\parallel)\hat{\tilde{m}}_Y(\mathbf{k'}_\parallel) + H_{YX}(-\mathbf{k'}_\parallel)\hat{\tilde{m}}_Y(\mathbf{k'}_\parallel) \right\}
\end{aligned}
\tag{5.58}
$$

Using the following (easily crosschecked) symmetry properties

$$
\begin{aligned}
H_X(-\mathbf{k}_\parallel) &= H_X(\mathbf{k}_\parallel), \\
H_Y(-\mathbf{k}_\parallel) &= H_Y(\mathbf{k}_\parallel), \\
H_{XY}(-\mathbf{k}_\parallel) &= H_{XY}(\mathbf{k}_\parallel)
\end{aligned}
\tag{5.59}
$$

Eqs.(5.58) are simplified as below

$$\begin{aligned}\frac{d\hat{\tilde{m}}_X(\mathbf{k}_\parallel)}{dt} &= \frac{\tilde{\mu}_0}{\hbar} H_Y(\mathbf{k}_\parallel)\hat{\tilde{m}}_Y(\mathbf{k}_\parallel) + \frac{\tilde{\mu}_0}{\hbar} H_{XY}(\mathbf{k}_\parallel)\hat{\tilde{m}}_X(\mathbf{k}_\parallel) \\ \frac{d\hat{\tilde{m}}_Y(\mathbf{k}_\parallel)}{dt} &= -\frac{\tilde{\mu}_0}{\hbar} H_X(\mathbf{k}_\parallel)\hat{\tilde{m}}_X(\mathbf{k}_\parallel) - \frac{\tilde{\mu}_0}{\hbar} H_{XY}(\mathbf{k}_\parallel)\hat{\tilde{m}}_Y(\mathbf{k}_\parallel)\end{aligned} \tag{5.60}$$

Taking the time derivative on both sides of the last set of equations, using the last set of equations to substitute for the first order time derivatives appearing along the way, and switching to the frequency domain, we end up to the following result

$$\left\{ \begin{array}{l} \left\{\Omega^2 - \gamma^2 H_X(\mathbf{k}_\parallel)H_Y(\mathbf{k}_\parallel) + \gamma^2 H_{XY}^2(\mathbf{k}_\parallel)\right\}\hat{\tilde{m}}_X(\mathbf{k}_\parallel) = 0 \\ \left\{\Omega^2 - \gamma^2 H_X(\mathbf{k}_\parallel)H_Y(\mathbf{k}_\parallel) + \gamma^2 H_{XY}^2(\mathbf{k}_\parallel)\right\}\hat{\tilde{m}}_Y(\mathbf{k}_\parallel) = 0 \end{array} \right\} \Rightarrow \tag{5.61}$$

$$\Omega(\mathbf{k}_\parallel) = |\gamma| \sqrt{H_X(\mathbf{k}_\parallel)H_Y(\mathbf{k}_\parallel) - H_{XY}^2(\mathbf{k}_\parallel)}$$

provided that $H_X(\mathbf{k}_\parallel)H_Y(\mathbf{k}_\parallel) \geq H_{XY}^2(\mathbf{k}_\parallel)$. The so-called "ferromagnetic resonance frequency" is given by

$$\begin{aligned}\Omega_{FMR} = \Omega(\mathbf{k}_\parallel = 0) &= |\gamma| \sqrt{H_X(0)H_Y(0) - H_{XY}^2(0)} = \\ &= |\gamma| \sqrt{H_X(0)H_Y(0)}, \qquad H_X(0)H_Y(0) \geq H_{XY}^2(0)\end{aligned} \tag{5.62}$$

Concluding this section, to check if there exist any finite wavevector magnons degenerate with the ferromagnetic resonance mode, one should check if the following condition can be satisfied

$$\begin{aligned}H_X(\mathbf{k}_\parallel)H_Y(\mathbf{k}_\parallel) - H_{XY}^2(\mathbf{k}_\parallel) = H_X(0)H_Y(0) \Rightarrow \\ H_X(\mathbf{k}_\parallel)H_Y(\mathbf{k}_\parallel) - H_X(0)H_Y(0) = H_{XY}^2(\mathbf{k}_\parallel)\end{aligned} \tag{5.63}$$

Defining for convenience the parameters $\xi_{\mathbf{k}_\parallel} \equiv Dk_\parallel + \zeta$ and $\zeta = \frac{1}{2}\mu_0 M_s d$, the

last equation leads to

$$H_X(\mathbf{k}_\parallel)H_Y(\mathbf{k}_\parallel) - H_X(0)H_Y(0) = H_{XY}^2(\mathbf{k}_\parallel) \Rightarrow ... \Rightarrow k_\parallel \Big[k_\parallel \xi_{k_\parallel} \zeta \sin^2\theta_M \sin^2\phi_{\mathbf{k}_\parallel} -$$

$$\xi_{k_\parallel} \Big\{ H_X(0)\sin^2\phi_{\mathbf{k}_\parallel} + H_Y(0)\cos^2\phi_{\mathbf{k}_\parallel}\cos^2\theta_M \Big\} + H_Y(0)\zeta\sin^2\theta_M \Big] = 0$$

where one solution is the $k_\parallel = 0$ solution (that corresponds to the FMR mode), whereas the rest of the solutions, if existent, are solutions to the following equation

$$\begin{aligned} &\Big\{ \zeta^2 \sin^2\theta_M \sin^2\phi_{\mathbf{k}_\parallel} - D \Big\{ H_X(0)\sin^2\phi_{\mathbf{k}_\parallel} + H_Y(0)\cos^2\phi_{\mathbf{k}_\parallel}\cos^2\theta_M \Big\} \Big\} k_\parallel + \\ &\zeta \Big\{ H_Y(0)\sin^2\theta_M - H_Y(0)\cos^2\phi_{\mathbf{k}_\parallel}\cos^2\theta_M - H_X(0)\sin^2\phi_{\mathbf{k}_\parallel} \Big\} + \\ &\Big\{ D\zeta\sin^2\theta_M\sin^2\phi_{\mathbf{k}_\parallel} \Big\} k_\parallel^2 = 0 \end{aligned} \tag{5.65}$$

A way to solve the above equation is this: Given the angle θ_H, we find from Eq.(5.52) the angle θ_M. Afterwards, all the possible values for the angle $\phi_{\mathbf{k}_\parallel} \in [0,\ 2\pi)$ are swept through, where at each step the trinomial equation with respect to $k_\parallel$ (Eq.(5.65)) is checked for non-trivial real solutions. If such non-trivial real solutions do exist this means that there are finite wavevector magnons degenerate with the ferromagnetic resonance mode! In the following, driven by pertinent experimental results we set aside the above described scenario.

Units:

$$\begin{aligned} &[K_s] = \tfrac{eV}{m^2},\ \ [J] = \tfrac{eV}{m},\ \ [D] = \tfrac{eV\cdot m^2}{moment},\ \ [H_0] = \tfrac{A(Ampere)}{m}, \\ &[\mu_0] = \tfrac{eV}{m\cdot A^2},\ \ [M_s] = \tfrac{moment}{m^3},\ \ moment = A\cdot m^2 \end{aligned} \tag{5.66}$$

The magnetic moment SI unit is $1\ Ampere\cdot m^2 = 1\ J/T \rightarrow 1\ eV/T,\ \ T = Tesla$. Notice once again that μ_0 denotes the free space permeability.

5.3 Effective Hamiltonians of the decoupled subsystems

In the previous analysis, we derived the low energy effective Hamiltonian of the magnetic degrees of freedom of the YIG which is just quoted for completeness below

$$\tilde{H}_{YIG} = E_{clas} + \hat{H}_0^{YIG} = E_{clas} + \frac{1}{2M_s}\sum_{\mathbf{k}_\parallel}\Big[H_X(\mathbf{k}_\parallel)\hat{\tilde{m}}_X^\dagger(\mathbf{k}_\parallel)\hat{\tilde{m}}_X(\mathbf{k}_\parallel)+$$

$$H_Y(\mathbf{k}_\parallel)\hat{\tilde{m}}_Y^\dagger(\mathbf{k}_\parallel)\hat{\tilde{m}}_Y(\mathbf{k}_\parallel) + H_{XY}(\mathbf{k}_\parallel)\hat{\tilde{m}}_X^\dagger(\mathbf{k}_\parallel)\hat{\tilde{m}}_Y(\mathbf{k}_\parallel) + H_{YX}(\mathbf{k}_\parallel)\hat{\tilde{m}}_Y^\dagger(\mathbf{k}_\parallel)\hat{\tilde{m}}_X(\mathbf{k}_\parallel)\Big] \tag{5.67}$$

The unit of the Hamiltonian is the eV. (Notice that the magnetization field in the real space is measured in units of $^{moment}/_{volume}$ whereas the same field in the momentum space is measured in units of $^{moment}\Big/\sqrt{volume}$.) Notice also that in the aforementioned Hamiltonian the transverse magnetization operators are written with respect to the local OXYZ system of each local magnetic moment.

Let us now proceed to the subsystem of the topological insulator which is used as a substrate. Retaining the previously chosen global coordinate system Oxyz, the positive Oz axis is now directed from the bottom surface of the TI towards the interface between the top surface of the TI and the YIG insulator. As a further simplification, we assume that the topological insulator substrate is sufficiently thick so that its top and bottom surface are decoupled from each other. Assuming so, the YIG insulator is considered coupled only to the surface of the TI that is adjacent to it, i.e. the top surface of the TI. Under the aforementioned approximations, the low energy mean field Hamiltonian for

the top surface Dirac electrons in the continuum limit, is given by (Ref.[60])

$$H_{TI}^{top} = \sum_{0\leq\left|\mathbf{q}_{\parallel}\right|\leq q_c} \left[\begin{array}{c} \hat{c}_{t\uparrow}^{\dagger}(\mathbf{q}_{\parallel}) \\ \hat{c}_{t\downarrow}^{\dagger}(\mathbf{q}_{\parallel}) \end{array} \right]^T \left[\begin{array}{cc} -E_F & iBq_{\parallel}^{-} \\ -iBq_{\parallel}^{+} & -E_F \end{array} \right] \left[\begin{array}{c} \hat{c}_{t\uparrow}(\mathbf{q}_{\parallel}) \\ \hat{c}_{t\downarrow}(\mathbf{q}_{\parallel}) \end{array} \right] = \\ \sum_{0\leq\left|\mathbf{q}_{\parallel}\right|\leq q_c} \sum_{\alpha\beta} h_{\alpha\beta}(\mathbf{q}_{\parallel}) \hat{c}_{t\alpha}^{\dagger}(\mathbf{q}_{\parallel}) \hat{c}_{t\beta}(\mathbf{q}_{\parallel}) \tag{5.68}$$

where $B > 0$ (in $eV \cdot m$) is an electronic band structure parameter, E_F (in eV) is the Fermi energy, and $q_{\parallel}^{\pm} = q_{\parallel}^{x} \pm i q_{\parallel}^{y}$. The subscript condition $0 \leq \left|\mathbf{q}_{\parallel}\right| \leq q_c$ is there to remind us that this low energy effective Hamiltonian is a good approximation close to the $\mathbf{q}_{\parallel} = 0$ point of the q-space. The spin quantization axis is the Oz axis that is normal to the interface. Further, $\hat{c}_{t\sigma}^{\dagger}(\mathbf{q}_{\parallel})(\hat{c}_{t\sigma}(\mathbf{q}_{\parallel}))$, with $\sigma = \{\uparrow, \downarrow\}$, denotes a Dirac electron creation (annihilation) operator at the top surface of the TI with momentum $\mathbf{q}_{\parallel}$ and spin σ. In the following we couple the Dirac electron system to the YIG magnetic degrees of freedom. It is easily seen that the mean field Hamiltonian of Eq.(5.68) is measured in eV.

5.4 Coupling of the Dirac electrons to the long-wavelength dynamics of the YIG magnetization

Our ultimate target is to study the effect of the electron-magnon interaction on the ferromagnetic resonance of the YIG insulator, but before doing so, let us first elaborate on the coupling of the two subsystems, the YIG and the TI substrate. The coupling of the Dirac electrons of the topological insulator (TI) to the magnetization field of the YIG takes place as below (care is

taken to measure the interfacial coupling energy in eV)

$$H_{TI-YIG} = -\frac{1}{g_J \mu_B} \sum_{\alpha\beta} \int d^2\mathbf{r}_\parallel \int d^3\mathbf{r}' \; J_t(\mathbf{r}_\parallel - \mathbf{r}') \hat{c}^\dagger_{t\alpha}(\mathbf{r}_\parallel) \hat{c}_{t\beta}(\mathbf{r}_\parallel) \vec{\sigma}_{\alpha\beta} \cdot \vec{M}(\mathbf{r}') \tag{5.69}$$

where the integral over $\mathbf{r}_\parallel$ is performed over the top surface of the TI, whereas the integral over $\mathbf{r}'$ is performed over the volume of the YIG thin film. The exchange coupling strength $J_t(\mathbf{r}_\parallel - \mathbf{r}')$ is assumed to be measured in eV, and the aforementioned Hamiltonian couples the Dirac electron spin density per unit area to the magnetization per unit volume of the YIG. Driven by experimental results, the exchange coupling between the two subsystems is modelled as $J_t(\mathbf{r}_\parallel - \mathbf{r}') \approx J_t \delta(\mathbf{r}_\parallel - \mathbf{r}_\parallel{}') \delta(z')$ (i.e. it is restricted right at the interface Oxy between the two subsystems). Notice that the unit of J_t should be $eV \cdot volume$. Forcing the aforementioned model for the exchange coupling to the Hamiltonian of Eq.(5.69) we finally get

$$H_{TI-YIG} \approx -\frac{J_t}{g_J \mu_B} \sum_{\alpha\beta} \int d^2\mathbf{r}_\parallel \hat{c}^\dagger_{t\alpha}(\mathbf{r}_\parallel) \hat{c}_{t\beta}(\mathbf{r}_\parallel) \vec{\sigma}_{\alpha\beta} \cdot \vec{M}(\mathbf{r}_\parallel) \tag{5.70}$$

where in the last equation, the Dirac electron spin density is coupled to the averaged over the thickness of the film magnetization per unit volume of the YIG film, which is the same anywhere along the thickness of the thin film. We note in passing that even though the exchange interaction between the electrons of the TI and the local moments of the YIG is significant right at the interface between the two materials, given that the local moments of the YIG are coupled to each other, during the ferromagnetic resonance (FMR) mode the electron system is indirectly coupled to the whole YIG insulator

(seeing it as a giant magnetic moment during the FMR mode). Performing the decomposition described in Eqs.(5.3) through (5.7) on the RHS of Eq.(5.70), it is

$$
\begin{aligned}
&H_{TI-YIG} \approx -\tfrac{J_t}{g_J\mu_B}\sum_{\alpha\beta}\int d^2\mathbf{r}_\parallel \hat{c}^\dagger_{t\alpha}(\mathbf{r}_\parallel)\hat{c}_{t\beta}(\mathbf{r}_\parallel)\vec{\sigma}_{\alpha\beta}\cdot\vec{M}(\mathbf{r}_\parallel) \approx \\
&-\tfrac{J_t}{g_J\mu_B}\sum_{\alpha\beta}\int d^2\mathbf{r}_\parallel \hat{c}^\dagger_{t\alpha}(\mathbf{r}_\parallel)\hat{c}_{t\beta}(\mathbf{r}_\parallel)\vec{\sigma}_{\alpha\beta}\cdot\vec{M}^{(0)} \\
&-\tfrac{J_t}{g_J\mu_B}\sum_{\alpha\beta}\int d^2\mathbf{r}_\parallel \hat{c}^\dagger_{t\alpha}(\mathbf{r}_\parallel)\hat{c}_{t\beta}(\mathbf{r}_\parallel)\vec{\sigma}_{\alpha\beta}\cdot\vec{M}^{(1)}(\mathbf{r}_\parallel) \\
&-\tfrac{J_t}{g_J\mu_B}\sum_{\alpha\beta}\int d^2\mathbf{r}_\parallel \hat{c}^\dagger_{t\alpha}(\mathbf{r}_\parallel)\hat{c}_{t\beta}(\mathbf{r}_\parallel)\vec{\sigma}_{\alpha\beta}\cdot\vec{M}^{(2)}(\mathbf{r}_\parallel) + ...
\end{aligned}
\tag{5.71}
$$

or further

$$
\begin{aligned}
&H_{TI-YIG} \approx -\tfrac{J_t}{g_J\mu_B}\sum_{\alpha\beta}\int d^2\mathbf{r}_\parallel \hat{c}^\dagger_{t\alpha}(\mathbf{r}_\parallel)\hat{c}_{t\beta}(\mathbf{r}_\parallel)\vec{\sigma}_{\alpha\beta}\cdot\vec{M}(\mathbf{r}_\parallel) \approx \\
&-\tfrac{J_t}{g_J\mu_B}\sum_{\alpha\beta}\int d^2\mathbf{r}_\parallel \hat{c}^\dagger_{t\alpha}(\mathbf{r}_\parallel)\left\{\sigma^x_{\alpha\beta}M_s\sin\theta_M + \sigma^z_{\alpha\beta}M_s\cos\theta_M\right\}\hat{c}_{t\beta}(\mathbf{r}_\parallel) \\
&-\tfrac{J_t}{g_J\mu_B}\sum_{\alpha\beta}\int d^2\mathbf{r}_\parallel \hat{c}^\dagger_{t\alpha}(\mathbf{r}_\parallel)\left\{\sigma^x_{\alpha\beta}\cos\theta_M - \sigma^z_{\alpha\beta}\sin\theta_M\right\}\hat{c}_{t\beta}(\mathbf{r}_\parallel)\bar{m}_X(\mathbf{r}_\parallel) \\
&-\tfrac{J_t}{g_J\mu_B}\sum_{\alpha\beta}\int d^2\mathbf{r}_\parallel \hat{c}^\dagger_{t\alpha}(\mathbf{r}_\parallel)\sigma^y_{\alpha\beta}\hat{c}_{t\beta}(\mathbf{r}_\parallel)\bar{m}_Y(\mathbf{r}_\parallel) \\
&+\tfrac{J_t}{2M_sg_J\mu_B}\sum_{\alpha\beta}\int d^2\mathbf{r}_\parallel \hat{c}^\dagger_{t\alpha}(\mathbf{r}_\parallel)\left\{\sigma^x_{\alpha\beta}\sin\theta_M + \sigma^z_{\alpha\beta}\cos\theta_M\right\}\hat{c}_{t\beta}(\mathbf{r}_\parallel)\bar{m}^2_X(\mathbf{r}_\parallel) + \\
&\tfrac{J_t}{2M_sg_J\mu_B}\sum_{\alpha\beta}\int d^2\mathbf{r}_\parallel \hat{c}^\dagger_{t\alpha}(\mathbf{r}_\parallel)\left\{\sigma^x_{\alpha\beta}\sin\theta_M + \sigma^z_{\alpha\beta}\cos\theta_M\right\}\hat{c}_{t\beta}(\mathbf{r}_\parallel)\bar{m}^2_Y(\mathbf{r}_\parallel) + ...
\end{aligned}
\tag{5.72}
$$

In the last equation, the zeroth order term in the deviation of the YIG magnetization field from its equilibrium configuration represents the modification of the band structure of the Dirac electrons due to the coupling of the TI to

the YIG insulator. This term is preferably absorbed into the Dirac electron effective Hamiltonian of Eq.(5.68), and leads to the following modified effective Dirac electron Hamiltonian

$$\tilde{H}_{TI}^{top} = \sum_{0 \leq \left|\mathbf{q}_{\parallel}\right| \leq q_c} \sum_{\alpha\beta} \tilde{h}_{\alpha\beta}(\mathbf{q}_{\parallel}) \hat{c}_{t\alpha}^{\dagger}(\mathbf{q}_{\parallel}) \hat{c}_{t\beta}(\mathbf{q}_{\parallel}) \tag{5.73}$$

where the following definition is employed

$$\tilde{h}_{\alpha\beta}(\mathbf{q}_{\parallel}) = \begin{bmatrix} -E_F - \frac{J_t}{g_J \mu_B} M_s \cos\theta_M & iBq_{\parallel}^{-} - \frac{J_t}{g_J \mu_B} M_s \sin\theta_M \\ -iBq_{\parallel}^{+} - \frac{J_t}{g_J \mu_B} M_s \sin\theta_M & -E_F + \frac{J_t}{g_J \mu_B} M_s \cos\theta_M \end{bmatrix} \tag{5.74}$$

Furthermore, the first order terms in the deviation of the YIG magnetization field from its equilibrium configuration (Eq.(5.72)) represent one-electron one-magnon creation or annihilation processes, and those are the processes that are of interest in this analysis. The next terms represent one-electron two-magnon processes and so on and so forth. Using the following convention for the electron creation and annihilation operators

$$\hat{c}_{t\alpha}(\mathbf{r}_{\parallel}) = \frac{1}{\sqrt{A}} \sum_{\mathbf{q}_{\parallel}} \hat{c}_{t\alpha}(\mathbf{q}_{\parallel}) e^{i\mathbf{q}_{\parallel}\cdot\mathbf{r}_{\parallel}}, \;\; \hat{c}_{t\alpha}^{\dagger}(\mathbf{r}_{\parallel}) = \frac{1}{\sqrt{A}} \sum_{\mathbf{q}_{\parallel}} \hat{c}_{t\alpha}^{\dagger}(\mathbf{q}_{\parallel}) e^{-i\mathbf{q}_{\parallel}\cdot\mathbf{r}_{\parallel}}, \;\; \alpha = \{\uparrow, \downarrow\} \tag{5.75}$$

where A denotes the basic quantization area to which periodic boundary conditions are applied for the TI within the interfacial plane, the Fourier Transform convention of Eq.(5.2), promoting the transverse magnetization components to corresponding quantum mechanical operators via the prescription detailed previously, and symmetrizing with respect to the magnon creation and anni-

hilation, we finally get

$$
\begin{aligned}
&H^{el}_{1mag} = \\
&-\tfrac{J_t}{2g_J\mu_B}\tfrac{1}{\sqrt{L^2d}}\sum_{\mathbf{k}_\parallel,\mathbf{q}_\parallel}\sum_{\alpha\beta}\hat{c}^\dagger_{t\alpha}(\mathbf{k}_\parallel+\mathbf{q}_\parallel)\left\{\sigma^x_{\alpha\beta}\cos\theta_M-\sigma^z_{\alpha\beta}\sin\theta_M\right\}\hat{c}_{t\beta}(\mathbf{q}_\parallel)\hat{\bar{m}}_X(\mathbf{k}_\parallel)\\
&-\tfrac{J_t}{2g_J\mu_B}\tfrac{1}{\sqrt{L^2d}}\sum_{\mathbf{k}_\parallel,\mathbf{q}_\parallel}\sum_{\alpha\beta}\hat{c}^\dagger_{t\alpha}(-\mathbf{k}_\parallel+\mathbf{q}_\parallel)\left\{\sigma^x_{\alpha\beta}\cos\theta_M-\sigma^z_{\alpha\beta}\sin\theta_M\right\}\hat{c}_{t\beta}(\mathbf{q}_\parallel)\hat{\bar{m}}^\dagger_X(\mathbf{k}_\parallel)\\
&-\tfrac{J_t}{2g_J\mu_B}\tfrac{1}{\sqrt{L^2d}}\sum_{\mathbf{k}_\parallel,\mathbf{q}_\parallel}\sum_{\alpha\beta}\hat{c}^\dagger_{t\alpha}(\mathbf{k}_\parallel+\mathbf{q}_\parallel)\sigma^y_{\alpha\beta}\hat{c}_{t\beta}(\mathbf{q}_\parallel)\hat{\bar{m}}_Y(\mathbf{k}_\parallel)\\
&-\tfrac{J_t}{2g_J\mu_B}\tfrac{1}{\sqrt{L^2d}}\sum_{\mathbf{k}_\parallel,\mathbf{q}_\parallel}\sum_{\alpha\beta}\hat{c}^\dagger_{t\alpha}(-\mathbf{k}_\parallel+\mathbf{q}_\parallel)\sigma^y_{\alpha\beta}\hat{c}_{t\beta}(\mathbf{q}_\parallel)\hat{\bar{m}}^\dagger_Y(\mathbf{k}_\parallel)
\end{aligned}
\tag{5.76}
$$

In this study, we treat the interaction Hamiltonian of Eq.(5.76) perturbatively. However, to apply the many body perturbation theory and treat the aforementioned one-electron one-magnon interaction in the same spirit as the electron-phonon interaction, the form of the interaction given in Eq.(5.76) is not appropriate since it contains operators (the YIG magnetization field operators) that satisfy the commutation algebra of the spin. To be able to take advantage of the conventional Wick's decoupling later on, the aforementioned Hamiltonian should be written in terms of boson and fermion creation and annihilation operators. Provided we are at temperatures much lower than the magnetic critical temperature of the YIG insulator, we can proceed as below.

In the first place, notice that the commutators given in Eq.(5.55) actually obey spin commutation relations as already stressed. Adjusting the convention of Refs.[21, 54] to our case, the magnetic moment density satisfies the following commutation relations (we skip the 'hat' from the YIG mag-

netization field operators from now on since there is no point of confusion I guess)

$$
\begin{aligned}
&[m_X(\mathbf{r},t),\ m_Y(\mathbf{r}',t)] = i\tilde{\mu}_0 m_Z(\mathbf{r},t)\delta(\mathbf{r}-\mathbf{r}') \approx i\tilde{\mu}_0 M_s\delta(\mathbf{r}-\mathbf{r}'),\\
&[m_X(\mathbf{r},t),\ m_X(\mathbf{r}',t)] = 0,\ \ [m_Y(\mathbf{r},t),\ m_Y(\mathbf{r}',t)] = 0,\\
&[m^+(\mathbf{r},t),\ m^-(\mathbf{r}',t)] \approx 2\tilde{\mu}_0 M_s\delta(\mathbf{r}-\mathbf{r}')
\end{aligned}
\tag{5.77}
$$

where $\tilde{\mu}_0 = -\gamma\hbar$ was defined below Eq.(5.55), and further, by definition it is $m^{\pm}(\mathbf{r},t) = m_X(\mathbf{r},t) \pm i m_Y(\mathbf{r},t)$. We then introduce a new set of operators $b(\mathbf{r},t)$ and $b^\dagger(\mathbf{r},t)$ that satisfy the following commutation relations

$$
\begin{aligned}
&\left[b(\mathbf{r},t),\ b^\dagger(\mathbf{r}',t)\right] = \delta(\mathbf{r}-\mathbf{r}'),\\
&[b(\mathbf{r},t),\ b(\mathbf{r}',t)] = \ \left[b^\dagger(\mathbf{r},t),\ b^\dagger(\mathbf{r}',t)\right] = 0
\end{aligned}
\tag{5.78}
$$

which are related to the operators $m^+(\mathbf{r},t),\ m^-(\mathbf{r},t)$ defined above via the following relationships

$$
\begin{aligned}
m^-(\mathbf{r},t) &= \sqrt{2\tilde{\mu}_0 M_s}\, b^\dagger(\mathbf{r},t)\left[\sqrt{1-\tfrac{\tilde{\mu}_0}{2M_s}b^\dagger(\mathbf{r},t)b(\mathbf{r},t)}\right]\\
m^+(\mathbf{r},t) &= \sqrt{2\tilde{\mu}_0 M_s}\left[\sqrt{1-\tfrac{\tilde{\mu}_0}{2M_s}b^\dagger(\mathbf{r},t)b(\mathbf{r},t)}\right] b(\mathbf{r},t)
\end{aligned}
\tag{5.79}
$$

Provided that $\frac{\tilde{\mu}_0}{2M_s}b^\dagger(\mathbf{r},t)b(\mathbf{r},t) = \frac{\tilde{\mu}_0}{2M_s}n(\mathbf{r},t) << 1$ (which is acceptable as long as we are in the temperature range mentioned previously), Eqs.(5.79) reduce to

$$
\begin{aligned}
&m^-(\mathbf{r},t) = \sqrt{2\tilde{\mu}_0 M_s}\, b^\dagger(\mathbf{r},t)\left[\sqrt{1-\tfrac{\tilde{\mu}_0}{2M_s}b^\dagger(\mathbf{r},t)b(\mathbf{r},t)}\right] \approx \sqrt{2\tilde{\mu}_0 M_s}\, b^\dagger(\mathbf{r},t)\\
&m^+(\mathbf{r},t) = \sqrt{2\tilde{\mu}_0 M_s}\left[\sqrt{1-\tfrac{\tilde{\mu}_0}{2M_s}b^\dagger(\mathbf{r},t)b(\mathbf{r},t)}\right] b(\mathbf{r},t) \approx \sqrt{2\tilde{\mu}_0 M_s}\, b(\mathbf{r},t)
\end{aligned}
\tag{5.80}
$$

and therefore it is

$$\begin{aligned}\bar{m}_X(\mathbf{k}_\parallel,t) &\approx \tfrac{1}{2}\sqrt{2\mu_0 M_s}\left\{\bar{b}(\mathbf{k}_\parallel,t)+\bar{b}^\dagger(-\mathbf{k}_\parallel,t)\right\}\\ \bar{m}_Y(\mathbf{k}_\parallel,t) &\approx \tfrac{1}{2i}\sqrt{2\mu_0 M_s}\left\{\bar{b}(\mathbf{k}_\parallel,t)-\bar{b}^\dagger(-\mathbf{k}_\parallel,t)\right\}\end{aligned} \tag{5.81}$$

First we write the YIG effective Hamiltonian of Eq.(5.67) in terms of boson operators using Eqs.(5.81). The result is

$$\begin{aligned}\tilde{H}_{YIG} = E_{clas} + \tfrac{1}{2M_s}\tfrac{\tilde{\mu}_0 M_s}{2}\sum_{\mathbf{k}_\parallel}\Big[&\left\{H_X(\mathbf{k}_\parallel)+H_Y(\mathbf{k}_\parallel)\right\}\bar{b}^\dagger(\mathbf{k}_\parallel)\bar{b}(\mathbf{k}_\parallel)+\\ &\left\{H_X(\mathbf{k}_\parallel)+H_Y(\mathbf{k}_\parallel)\right\}\bar{b}(-\mathbf{k}_\parallel)\bar{b}^\dagger(-\mathbf{k}_\parallel)+\\ &\left\{H_X(\mathbf{k}_\parallel)-H_Y(\mathbf{k}_\parallel)+2iH_{XY}(\mathbf{k}_\parallel)\right\}\bar{b}^\dagger(\mathbf{k}_\parallel)\bar{b}^\dagger(-\mathbf{k}_\parallel)+\\ &\left\{H_X(\mathbf{k}_\parallel)-H_Y(\mathbf{k}_\parallel)-2iH_{XY}(\mathbf{k}_\parallel)\right\}\bar{b}(-\mathbf{k}_\parallel)\bar{b}(\mathbf{k}_\parallel)\Big]\end{aligned} \tag{5.82}$$

where we've used the following (already stated) symmetry properties

$$H_X(-\mathbf{k}_\parallel)=H_X(\mathbf{k}_\parallel),\ H_Y(-\mathbf{k}_\parallel)=H_Y(\mathbf{k}_\parallel),\ H_{XY}(-\mathbf{k}_\parallel)=H_{XY}(\mathbf{k}_\parallel)$$

However, even after the bosonization prescription, the Hamiltonian of Eq.(5.82) is still not diagonal. Let us then check when the last Hamiltonian is diagonalizable. Using the mathematical theory developed in Ref.[**?**], the eigenvalues of the so-called dynamical matrix defined in Ref.[**?**] are

$$\omega_{1,2}(\mathbf{k}_\parallel)=\pm 2\sqrt{H_X(\mathbf{k}_\parallel)H_Y(\mathbf{k}_\parallel)-H_{XY}^2(\mathbf{k}_\parallel)}$$

The effective YIG Hamiltonian is diagonalizable when the aforementioned eigenvalues are real, i.e. under the condition that $H_X(\mathbf{k}_\parallel)H_Y(\mathbf{k}_\parallel)\geq H_{XY}^2(\mathbf{k}_\parallel)$, $\forall\ \mathbf{k}_\parallel$. Under the stated condition, we proceed to diagonalize the secondary

quantized YIG Hamiltonian via the following Bogoliubov-Valatin Transformation (BVT)

$$\bar{b}(\mathbf{k}_\parallel) = u(\mathbf{k}_\parallel)\bar{\beta}(\mathbf{k}_\parallel) + v(\mathbf{k}_\parallel)\bar{\beta}^\dagger(-\mathbf{k}_\parallel),\ \bar{b}^\dagger(\mathbf{k}_\parallel) = u^*(\mathbf{k}_\parallel)\bar{\beta}^\dagger(\mathbf{k}_\parallel) + v^*(\mathbf{k}_\parallel)\bar{\beta}(-\mathbf{k}_\parallel) \tag{5.83}$$

where for the new operators it holds that

$$\begin{aligned} \left[\bar{\beta}(\mathbf{k}_\parallel),\ \bar{\beta}^\dagger(\mathbf{k'}_\parallel)\right] &= \delta_{\mathbf{k}_\parallel \mathbf{k'}_\parallel}, \\ \left[\bar{\beta}(\mathbf{k}_\parallel),\ \bar{\beta}(\mathbf{k'}_\parallel)\right] &= 0, \\ \left[\bar{\beta}^\dagger(\mathbf{k}_\parallel),\ \bar{\beta}^\dagger(\mathbf{k'}_\parallel)\right] &= 0 \end{aligned} \tag{5.84}$$

For simplicity, we assume that the coefficients of the transformation have the following symmetry property

$$u(\mathbf{k}_\parallel) = u(-\mathbf{k}_\parallel), \quad v(\mathbf{k}_\parallel) = v(-\mathbf{k}_\parallel) \tag{5.85}$$

Forcing the Bogoliubov-Valatin Transformation of Eq.(5.83) to Eq.(5.82) the final result is

$$\begin{aligned} &\tilde{H}_{YIG} = E_{clas} + \tfrac{\tilde{\mu}_0}{4} \times \\ &\sum_{\mathbf{k}_\parallel} \Big[\Big\{ \tfrac{\zeta(\mathbf{k}_\parallel)}{2} \Big\{ \left|u(\mathbf{k}_\parallel)\right|^2 + \left|v(\mathbf{k}_\parallel)\right|^2 \Big\} + \gamma(\mathbf{k}_\parallel) u^*(\mathbf{k}_\parallel) v^*(\mathbf{k}_\parallel) + \gamma^*(\mathbf{k}_\parallel) u(\mathbf{k}_\parallel) v(\mathbf{k}_\parallel) \Big\} \bar{\beta}^\dagger(\mathbf{k}_\parallel)\bar{\beta}(\mathbf{k}_\parallel) \\ &+ \Big\{ \tfrac{\zeta(\mathbf{k}_\parallel)}{2} \Big\{ \left|v(\mathbf{k}_\parallel)\right|^2 + \left|u(\mathbf{k}_\parallel)\right|^2 \Big\} + \gamma(\mathbf{k}_\parallel) u^*(\mathbf{k}_\parallel) v^*(\mathbf{k}_\parallel) + \gamma^*(\mathbf{k}_\parallel) u(\mathbf{k}_\parallel) v(\mathbf{k}_\parallel) \Big\} \bar{\beta}(-\mathbf{k}_\parallel)\bar{\beta}^\dagger(-\mathbf{k}_\parallel) \\ &+ \Big\{ \zeta(\mathbf{k}_\parallel) u(\mathbf{k}_\parallel) v^*(\mathbf{k}_\parallel) + \gamma(\mathbf{k}_\parallel) \big(v^*(\mathbf{k}_\parallel)\big)^2 + \gamma^*(\mathbf{k}_\parallel) \big(u(\mathbf{k}_\parallel)\big)^2 \Big\} \bar{\beta}(-\mathbf{k}_\parallel)\bar{\beta}(\mathbf{k}_\parallel) \\ &+ \Big\{ \zeta(\mathbf{k}_\parallel) u^*(\mathbf{k}_\parallel) v(\mathbf{k}_\parallel) + \gamma(\mathbf{k}_\parallel) \big(u^*(\mathbf{k}_\parallel)\big)^2 + \gamma^*(\mathbf{k}_\parallel) \big(v(\mathbf{k}_\parallel)\big)^2 \Big\} \bar{\beta}^\dagger(\mathbf{k}_\parallel)\bar{\beta}^\dagger(-\mathbf{k}_\parallel) \Big] \end{aligned} \tag{5.86}$$

where the following definitions were used

$$\begin{aligned}
\zeta(\mathbf{k}_\parallel) &= 2\left\{H_X(\mathbf{k}_\parallel) + H_Y(\mathbf{k}_\parallel)\right\} \\
\gamma(\mathbf{k}_\parallel) &= H_X(\mathbf{k}_\parallel) - H_Y(\mathbf{k}_\parallel) + 2iH_{XY}(\mathbf{k}_\parallel) \\
\gamma^*(\mathbf{k}_\parallel) &= H_X(\mathbf{k}_\parallel) - H_Y(\mathbf{k}_\parallel) - 2iH_{XY}(\mathbf{k}_\parallel)
\end{aligned} \tag{5.87}$$

After some algebra, it is found that with the following choice

$$\begin{cases}
u(\mathbf{k}_\parallel) = \frac{1}{\sqrt{2}}\left\{\sqrt{\frac{\left|\zeta(\mathbf{k}_\parallel)\right|}{\sqrt{\zeta^2(\mathbf{k}_\parallel) - 4\left|\gamma(\mathbf{k}_\parallel)\right|^2}} + 1}\right\} e^{\frac{i}{2}\left(\psi(\mathbf{k}_\parallel) - \pi\right)}, \\
\qquad\qquad\qquad\qquad\qquad\qquad\qquad\qquad , \quad for\ \zeta(\mathbf{k}_\parallel) > 0 \\
v(\mathbf{k}_\parallel) = \frac{1}{\sqrt{2}}\left\{\sqrt{\frac{\left|\zeta(\mathbf{k}_\parallel)\right|}{\sqrt{\zeta^2(\mathbf{k}_\parallel) - 4\left|\gamma(\mathbf{k}_\parallel)\right|^2}} - 1}\right\} e^{\frac{i}{2}\left(\psi(\mathbf{k}_\parallel) - \pi\right)}
\end{cases} \tag{5.88}$$

where $\psi(\mathbf{k}_\parallel)$ is defined by $\gamma(\mathbf{k}_\parallel) = \left|\gamma(\mathbf{k}_\parallel)\right| e^{i\psi(\mathbf{k}_\parallel)}$, the effective YIG Hamiltonian turns out to get the following diagonal form

$$H'_{YIG} = E_{clas} + \frac{1}{2}\hbar\Omega(\mathbf{k}_\parallel) + \hbar\sum_{\mathbf{k}_\parallel}\Omega(\mathbf{k}_\parallel)\bar{\beta}^\dagger(\mathbf{k}_\parallel)\bar{\beta}(\mathbf{k}_\parallel) \tag{5.89}$$

where by definition it is

$$\Omega(\mathbf{k}_\parallel) = |\gamma|\sqrt{H_X(\mathbf{k}_\parallel)H_Y(\mathbf{k}_\parallel) - H^2_{XY}(\mathbf{k}_\parallel)}, \qquad for\ \zeta(\mathbf{k}_\parallel) > 0 \tag{5.90}$$

The additional condition of $\zeta(\mathbf{k}_\parallel) > 0$, $\forall\ \mathbf{k}_\parallel$ used above is imposed by (spin wave) stability requirements.

The next step is to bring the modified effective Dirac electron Hamiltonian of Eq.(5.73) in diagonal form by using a new set of fermionic operators. It is not hard to see that the Hamiltonian of Eq.(5.73) is a so-called "normal Hamiltonian", to follow the jargon of Ref.[**?**], which can be diagonalized

via a unitary Bogoliubov-Valatin transformation (UBVT) that is symbolically written as

$$C(\mathbf{q}_{\parallel}) = T(\mathbf{q}_{\parallel})F(\mathbf{q}_{\parallel}) \tag{5.91}$$

where, by definition it is

$$C(\mathbf{q}_{\parallel}) = \begin{bmatrix} \hat{c}_{t\uparrow}(\mathbf{q}_{\parallel}) \\ \hat{c}_{t\downarrow}(\mathbf{q}_{\parallel}) \end{bmatrix}, \;\; F(\mathbf{q}_{\parallel}) = \begin{bmatrix} \hat{f}_1(\mathbf{q}_{\parallel}) \\ \hat{f}_2(\mathbf{q}_{\parallel}) \end{bmatrix}, \;\; T(\mathbf{q}_{\parallel}) = \begin{bmatrix} t_{11}(\mathbf{q}_{\parallel}) & t_{12}(\mathbf{q}_{\parallel}) \\ t_{21}(\mathbf{q}_{\parallel}) & t_{22}(\mathbf{q}_{\parallel}) \end{bmatrix} \tag{5.92}$$

and also, $\hat{f}_i^{\dagger}(\mathbf{q}_{\parallel}),\ \hat{f}_i(\mathbf{q}_{\parallel})$ are a new set of fermionic operators that fully diagonalize the Hamiltonian of Eq.(5.73), with $i = \{1, 2\}$ being just a 'band index'. For a unitary Bogoliubov-Valatin transformation it holds that $T^{\dagger}(\mathbf{q}_{\parallel})T(\mathbf{q}_{\parallel}) = T(\mathbf{q}_{\parallel})T^{\dagger}(\mathbf{q}_{\parallel}) = 1,\ \forall\ \mathbf{q}_{\parallel}$. For simplicity, we first define the following complex function of the electronic wavevector $\mathbf{q}_{\parallel}$

$$g(q_{\parallel,x}, q_{\parallel,y}) = \frac{J_t}{g_J\mu_B}M_s \sin\theta_M + iBq_{\parallel}^{+} = \frac{J_t}{g_J\mu_B}M_s \sin\theta_M + iB(q_{\parallel,x} + iq_{\parallel,y}) \tag{5.93}$$

The eigenvalues of the coefficient matrix $\tilde{h}_{\alpha\beta}(\mathbf{q}_{\parallel})$ in Eq.(5.73) are easily found

$$\begin{aligned} \varepsilon_1(\mathbf{q}_{\parallel}) &= -E_F - \sqrt{\left\{\tfrac{J_t}{g_J\mu_B}M_s\cos\theta_M\right\}^2 + B^2q_{\parallel,x}^2 + \left\{\tfrac{J_t}{g_J\mu_B}M_s\sin\theta_M - Bq_{\parallel,y}\right\}^2} \\ &= -E_F - \sqrt{g_1^2 + \left|g(q_{\parallel,x}, q_{\parallel,y})\right|^2} \\ \varepsilon_2(\mathbf{q}_{\parallel}) &= -E_F + \sqrt{\left\{\tfrac{J_t}{g_J\mu_B}M_s\cos\theta_M\right\}^2 + B^2q_{\parallel,x}^2 + \left\{\tfrac{J_t}{g_J\mu_B}M_s\sin\theta_M - Bq_{\parallel,y}\right\}^2} \\ &= -E_F + \sqrt{g_1^2 + \left|g(q_{\parallel,x}, q_{\parallel,y})\right|^2} \end{aligned} \tag{5.94}$$

whereas, the matrix elements of the $T(\mathbf{q}_\parallel)$ matrix are given by

$$
\begin{aligned}
t_{11}(\mathbf{q}_\parallel) &= \frac{g^*(q_{\parallel,x},q_{\parallel,y})\left\{g_1+\sqrt{g_1^2+\left|g(q_{\parallel,x},q_{\parallel,y})\right|^2}\right\}}{\left|g(q_{\parallel,x},q_{\parallel,y})\right|\sqrt{2}\sqrt{\left|g(q_{\parallel,x},q_{\parallel,y})\right|^2+g_1\left(g_1+\sqrt{g_1^2+\left|g(q_{\parallel,x},q_{\parallel,y})\right|^2}\right)}} \\
t_{12}(\mathbf{q}_\parallel) &= \frac{g^*(q_{\parallel,x},q_{\parallel,y})\left\{g_1-\sqrt{g_1^2+\left|g(q_{\parallel,x},q_{\parallel,y})\right|^2}\right\}}{\left|g(q_{\parallel,x},q_{\parallel,y})\right|\sqrt{2}\sqrt{\left|g(q_{\parallel,x},q_{\parallel,y})\right|^2+g_1\left(g_1-\sqrt{g_1^2+\left|g(q_{\parallel,x},q_{\parallel,y})\right|^2}\right)}} \\
t_{21}(\mathbf{q}_\parallel) &= \frac{\left|g(q_{\parallel,x},q_{\parallel,y})\right|}{\sqrt{2}\sqrt{\left|g(q_{\parallel,x},q_{\parallel,y})\right|^2+g_1\left(g_1+\sqrt{g_1^2+\left|g(q_{\parallel,x},q_{\parallel,y})\right|^2}\right)}} \\
t_{22}(\mathbf{q}_\parallel) &= \frac{\left|g(q_{\parallel,x},q_{\parallel,y})\right|}{\sqrt{2}\sqrt{\left|g(q_{\parallel,x},q_{\parallel,y})\right|^2+g_1\left(g_1-\sqrt{g_1^2+\left|g(q_{\parallel,x},q_{\parallel,y})\right|^2}\right)}}
\end{aligned}
\tag{5.95}
$$

where we've defined the parameter $g_1 \equiv \frac{J_t}{g_J\mu_B} M_s \cos\theta_M$. Forcing the UBVT to the modified effective Dirac electron Hamiltonian of Eq.(5.73) we finally get

$$
H'_{TI} = \sum_{0\leq\left|\mathbf{q}_\parallel\right|\leq q_c} \sum_i \varepsilon_i(\mathbf{q}_\parallel)\hat{f}_i^\dagger(\mathbf{q}_\parallel)\hat{f}_i(\mathbf{q}_\parallel) \tag{5.96}
$$

In the next step, we express the interaction Hamiltonian of Eq. (5.76) in terms of the bosonic and the fermionic operators that diagonalize the effective magnetic Hamiltonian of the YIG and the modified effective electron Hamiltonian of the TI respectively (see Eqs.(5.89) and (5.96)). Applying this procedure to Eq.(5.76), the interaction Hamiltonian can more compactly be rewritten as

$$
\begin{aligned}
{H'}_{1mag}^{el} = &\sum_{mn}\sum_{\mathbf{q}_\parallel,\mathbf{k}_\parallel} \Gamma_{mn}(\mathbf{k}_\parallel,\mathbf{q}_\parallel)\hat{f}_m^\dagger(\mathbf{k}_\parallel+\mathbf{q}_\parallel)\hat{f}_n(\mathbf{q}_\parallel)\bar{\beta}(\mathbf{k}_\parallel)+ \\
&\sum_{mn}\sum_{\mathbf{q}_\parallel,\mathbf{k}_\parallel} \tilde{\Gamma}_{mn}(\mathbf{k}_\parallel,\mathbf{q}_\parallel)\hat{f}_m^\dagger(\mathbf{q}_\parallel)\hat{f}_n(\mathbf{k}_\parallel+\mathbf{q}_\parallel)\bar{\beta}^\dagger(\mathbf{k}_\parallel)
\end{aligned}
\tag{5.97}
$$

where the summation over m, n is summation over the electronic bands, i.e.

$m, n = \{1,\ 2\}$. It is sufficient to know only the following scattering amplitudes:

$$
\begin{aligned}
&\Gamma_{11}(\mathbf{k}_\parallel, \mathbf{q}_\parallel) = \tfrac{1}{2}\tfrac{J_t}{g_J \mu_B}\sqrt{\tfrac{2\tilde{\mu}_0 M_s}{L^2 d}} \times \\
&\big[\sin\theta_M \left\{u(\mathbf{k}_\parallel) + v^*(\mathbf{k}_\parallel)\right\}\left\{t^*_{11}(\mathbf{k}_\parallel + \mathbf{q}_\parallel)t_{11}(\mathbf{q}_\parallel) - t^*_{21}(\mathbf{k}_\parallel + \mathbf{q}_\parallel)t_{21}(\mathbf{q}_\parallel)\right\} \\
&- \cos\theta_M \left\{u(\mathbf{k}_\parallel) + v^*(\mathbf{k}_\parallel)\right\}\left\{t^*_{11}(\mathbf{k}_\parallel + \mathbf{q}_\parallel)t_{21}(\mathbf{q}_\parallel) + t^*_{21}(\mathbf{k}_\parallel + \mathbf{q}_\parallel)t_{11}(\mathbf{q}_\parallel)\right\} \\
&+ \left\{u(\mathbf{k}_\parallel) - v^*(\mathbf{k}_\parallel)\right\}\left\{t^*_{11}(\mathbf{k}_\parallel + \mathbf{q}_\parallel)t_{21}(\mathbf{q}_\parallel) - t^*_{21}(\mathbf{k}_\parallel + \mathbf{q}_\parallel)t_{11}(\mathbf{q}_\parallel)\right\}\big] \\
&\\
&\Gamma_{21}(\mathbf{k}_\parallel, \mathbf{q}_\parallel) = \tfrac{1}{2}\tfrac{J_t}{g_J \mu_B}\sqrt{\tfrac{2\tilde{\mu}_0 M_s}{L^2 d}} \times \\
&\big[\sin\theta_M \left\{u(\mathbf{k}_\parallel) + v^*(\mathbf{k}_\parallel)\right\}\left\{t^*_{12}(\mathbf{k}_\parallel + \mathbf{q}_\parallel)t_{11}(\mathbf{q}_\parallel) - t^*_{22}(\mathbf{k}_\parallel + \mathbf{q}_\parallel)t_{21}(\mathbf{q}_\parallel)\right\} \\
&- \cos\theta_M \left\{u(\mathbf{k}_\parallel) + v^*(\mathbf{k}_\parallel)\right\}\left\{t^*_{12}(\mathbf{k}_\parallel + \mathbf{q}_\parallel)t_{21}(\mathbf{q}_\parallel) + t^*_{22}(\mathbf{k}_\parallel + \mathbf{q}_\parallel)t_{11}(\mathbf{q}_\parallel)\right\} \\
&+ \left\{u(\mathbf{k}_\parallel) - v^*(\mathbf{k}_\parallel)\right\}\left\{t^*_{12}(\mathbf{k}_\parallel + \mathbf{q}_\parallel)t_{21}(\mathbf{q}_\parallel) - t^*_{22}(\mathbf{k}_\parallel + \mathbf{q}_\parallel)t_{11}(\mathbf{q}_\parallel)\right\}\big] \\
&\\
&\Gamma_{12}(\mathbf{k}_\parallel, \mathbf{q}_\parallel) = \tfrac{1}{2}\tfrac{J_t}{g_J \mu_B}\sqrt{\tfrac{2\tilde{\mu}_0 M_s}{L^2 d}} \times \\
&\big[\sin\theta_M \left\{u(\mathbf{k}_\parallel) + v^*(\mathbf{k}_\parallel)\right\}\left\{t^*_{11}(\mathbf{k}_\parallel + \mathbf{q}_\parallel)t_{12}(\mathbf{q}_\parallel) - t^*_{21}(\mathbf{k}_\parallel + \mathbf{q}_\parallel)t_{22}(\mathbf{q}_\parallel)\right\} \\
&- \cos\theta_M \left\{u(\mathbf{k}_\parallel) + v^*(\mathbf{k}_\parallel)\right\}\left\{t^*_{11}(\mathbf{k}_\parallel + \mathbf{q}_\parallel)t_{22}(\mathbf{q}_\parallel) + t^*_{21}(\mathbf{k}_\parallel + \mathbf{q}_\parallel)t_{12}(\mathbf{q}_\parallel)\right\} \\
&+ \left\{u(\mathbf{k}_\parallel) - v^*(\mathbf{k}_\parallel)\right\}\left\{t^*_{11}(\mathbf{k}_\parallel + \mathbf{q}_\parallel)t_{22}(\mathbf{q}_\parallel) - t^*_{21}(\mathbf{k}_\parallel + \mathbf{q}_\parallel)t_{12}(\mathbf{q}_\parallel)\right\}\big] \\
&\\
&\Gamma_{22}(\mathbf{k}_\parallel, \mathbf{q}_\parallel) = \tfrac{1}{2}\tfrac{J_t}{g_J \mu_B}\sqrt{\tfrac{2\tilde{\mu}_0 M_s}{L^2 d}} \times \\
&\big[\sin\theta_M \left\{u(\mathbf{k}_\parallel) + v^*(\mathbf{k}_\parallel)\right\}\left\{t^*_{12}(\mathbf{k}_\parallel + \mathbf{q}_\parallel)t_{12}(\mathbf{q}_\parallel) - t^*_{22}(\mathbf{k}_\parallel + \mathbf{q}_\parallel)t_{22}(\mathbf{q}_\parallel)\right\} \\
&- \cos\theta_M \left\{u(\mathbf{k}_\parallel) + v^*(\mathbf{k}_\parallel)\right\}\left\{t^*_{12}(\mathbf{k}_\parallel + \mathbf{q}_\parallel)t_{22}(\mathbf{q}_\parallel) + t^*_{22}(\mathbf{k}_\parallel + \mathbf{q}_\parallel)t_{12}(\mathbf{q}_\parallel)\right\} \\
&+ \left\{u(\mathbf{k}_\parallel) - v^*(\mathbf{k}_\parallel)\right\}\left\{t^*_{12}(\mathbf{k}_\parallel + \mathbf{q}_\parallel)t_{22}(\mathbf{q}_\parallel) - t^*_{22}(\mathbf{k}_\parallel + \mathbf{q}_\parallel)t_{12}(\mathbf{q}_\parallel)\right\}\big]
\end{aligned}
\tag{5.98}
$$

where, the various parameters appearing can be straight away read off from Eqs.(5.88) and (5.95), and further, for the FMR mode we will need the $\mathbf{k}_\parallel = 0$ limit of the above amplitudes. In Eq.(5.97), there appear two types of processes: (a) magnon absorption processes (A-processes), whose scattering amplitudes are compactly denoted as $\Gamma_{mn}(\mathbf{k}_\parallel, \mathbf{q}_\parallel)$, and (b) magnon emission processes (E-processes), whose scattering amplitudes are compactly denoted as $\tilde{\Gamma}_{mn}(\mathbf{k}_\parallel, \mathbf{q}_\parallel)$. The scattering amplitudes of the two aforementioned types of

processes are related as below

$$\tilde{\Gamma}_{mn}(\mathbf{k}_{\parallel},\mathbf{q}_{\parallel})=\left[\Gamma_{nm}(\mathbf{k}_{\parallel},\mathbf{q}_{\parallel})\right]^{\dagger}\Leftrightarrow\left[\tilde{\Gamma}_{mn}(\mathbf{k}_{\parallel},\mathbf{q}_{\parallel})\right]^{\dagger}=\Gamma_{nm}(\mathbf{k}_{\parallel},\mathbf{q}_{\parallel}) \tag{5.99}$$

Saying so, knowing the scattering amplitudes of the A-processes (that were actually quoted above), one can use the last property and immediately figure out the scattering amplitudes of the E-processes. Concluding this section, it is noted that the scattering amplitudes $\Gamma_{mn}(\mathbf{k}_{\parallel},\mathbf{q}_{\parallel})$ and $\tilde{\Gamma}_{mn}(\mathbf{k}_{\parallel},\mathbf{q}_{\parallel})$ are in general complex functions of the electron and the magnon wavevectors.

5.5 Matsubara Green's function formalism (low temperature regime)

So far we have seen that to lowest order (and at low temperatures as already stressed), the interaction between the two materials consists of electron-magnon processes that do not conserve the magnon population in the YIG, as is easily seen by Eq.(5.97). Saying so, in this section we treat the interaction term at issue within the many body perturbation theory. To begin with, within the so-called Matsubara many body perturbation theory the central result is the thermodynamic and quantum averaging of a quantum mechanical operator $\hat{O}$ which is given by

$$\left\langle \hat{O}\right\rangle =\frac{\sum_{n=0}^{\infty}\frac{1}{n!}\left(-\frac{1}{\hbar}\right)^{n}\int_{0}^{\beta\hbar}d\tau_{1}...\int_{0}^{\beta\hbar}d\tau_{n}\left\langle \hat{\mathrm{T}}_{\tau}\left[\hat{\mathrm{O}}_{\mathrm{I}}(\beta\hbar)\hat{V}(\tau_{1})...\hat{V}(\tau_{n})\right]\right\rangle _{0}}{\sum_{n=0}^{\infty}\frac{1}{n!}\left(-\frac{1}{\hbar}\right)^{n}\int_{0}^{\beta\hbar}d\tau_{1}...\int_{0}^{\beta\hbar}d\tau_{n}\left\langle \hat{\mathrm{T}}_{\tau}\left[\hat{V}(\tau_{1})...\hat{V}(\tau_{n})\right]\right\rangle _{0}} \tag{5.100}$$

where $\langle(...)\rangle_{0}=Z_{0}^{-1}Tr\left[(...)\,e^{-\beta\hat{H}_{0}}\right]$, with $Z_{0}=Tr\left[e^{-\beta\hat{H}_{0}}\right]$, and $\hat{\mathrm{O}}_{\mathrm{I}}(\beta\hbar)=e^{\beta\hat{H}_{0}}\hat{O}e^{-\beta\hat{H}_{0}}$ is the operator $\hat{O}$ in the so-called interaction picture, and further,

in our case it is $\hat{V} \equiv {H'}_{1mag}^{el}$ (which is also expressed in the interaction picture). Furthermore, in the formalism we develop here, what we actually want to figure out is how the response of the YIG film to the applied microwave field (i.e. the FMR mode of the YIG) is affected by the proximity of the topological insulator (TI). Assuming that the aforementioned response can be treated within the linear response theory, one could start calculating the following set of Matsubara Green's functions

$$\chi_{\alpha\beta}(\mathbf{k}_{\parallel}, \tau - \tau') = -\mu_0 \left(- \left\langle \hat{\mathrm{T}}_{\tau} \left\{ \hat{\bar{m}}_{\alpha}(\mathbf{k}_{\parallel}, \tau) \hat{\bar{m}}_{\beta}^{\dagger}(\mathbf{k}_{\parallel}, \tau') \right\} \right\rangle \right) \tag{5.101}$$

where the various operators are defined in the Heisenberg picture, and also, α, β denote the transverse components of the magnetization field of the YIG (with respect to the local system OXYZ), and at a later stage, switch from the Matsubara Green's functions to the corresponding retarded Green's functions since it is the latter that actually appear in the linear response results. However, at temperatures much lower than the magnetic critical temperature of the YIG, where one can apply for the transverse components of the magnetization field of the YIG the approximate bosonic representation described in Eq.(5.81), the aforementioned response is a linear combination of the following set of magnonic Matsubara's Green's functions

$$\begin{aligned}
D_1(\mathbf{k}_{\parallel}, \mathbf{k'}_{\parallel}, \tau - \tau') &= - \left\langle \hat{\mathrm{T}}_{\tau} \left\{ \bar{\beta}(\mathbf{k}_{\parallel}, \tau) \bar{\beta}^{\dagger}(\mathbf{k'}_{\parallel}, \tau') \right\} \right\rangle, \\
D_2(\mathbf{k}_{\parallel}, \mathbf{k'}_{\parallel}, \tau - \tau') &= - \left\langle \hat{\mathrm{T}}_{\tau} \left\{ \bar{\beta}^{\dagger}(\mathbf{k}_{\parallel}, \tau) \bar{\beta}(\mathbf{k'}_{\parallel}, \tau') \right\} \right\rangle, \\
D_3(\mathbf{k}_{\parallel}, \mathbf{k'}_{\parallel}, \tau - \tau') &= - \left\langle \hat{\mathrm{T}}_{\tau} \left\{ \bar{\beta}^{\dagger}(\mathbf{k}_{\parallel}, \tau) \bar{\beta}^{\dagger}(\mathbf{k'}_{\parallel}, \tau') \right\} \right\rangle, \\
D_4(\mathbf{k}_{\parallel}, \mathbf{k'}_{\parallel}, \tau - \tau') &= - \left\langle \hat{\mathrm{T}}_{\tau} \left\{ \bar{\beta}(\mathbf{k}_{\parallel}, \tau) \bar{\beta}(\mathbf{k'}_{\parallel}, \tau') \right\} \right\rangle
\end{aligned} \tag{5.102}$$

with all the operators defined in the Heisenberg picture in the last equation. In the following analysis only the so-called "normal" magnonic propagators are of interest (as opposed to the "anomalous" magnonic propagators appearing in Eq.(5.102)). Within the Matsubara many body perturbation theory, the magnonic Matsubara Green's functions we're looking for are given by a perturbative expansion as below

$$\begin{aligned} &D_1(\mathbf{k}_\parallel, \mathbf{k'}_\parallel, \tau - \tau') = -\left\langle \hat{\mathrm{T}}_\tau \left\{ \bar{\beta}(\mathbf{k}_\parallel, \tau) \bar{\beta}^\dagger(\mathbf{k'}_\parallel, \tau') \right\} \right\rangle = \\ &D_1^{(0)}(\mathbf{k}_\parallel, \tau - \tau') + D_1^{(2)}(\mathbf{k}_\parallel, \mathbf{k'}_\parallel, \tau - \tau') + D_1^{(4)}(\mathbf{k}_\parallel, \mathbf{k'}_\parallel, \tau - \tau') + ... \end{aligned} \tag{5.103}$$

and similarly for the rest of the magnonic Matsubara Green's functions of interest. The zero-th order Matsubara Green's function (i.e. with the coupling between the two subsystems switched off) of the electronic subsystem is easily found to be

$$G_i^{(0)}(\mathbf{q}_\parallel, i\omega_n) = \frac{1}{i\hbar\omega_n - \varepsilon_i(\mathbf{q}_\parallel)} \tag{5.104}$$

whereas the zero-th order Matsubara Green's function of the magnonic subsystem is easily found to be

$$D^{(0)}(\mathbf{k}_\parallel, i\Omega_m) = \frac{1}{i\hbar\Omega_m - \hbar\Omega(\mathbf{k}_\parallel)} \tag{5.105}$$

where ω_n are fermionic Matsubara frequencies and Ω_m bosonic Matsubara frequencies. In the next step, we calculate the lowest order correction to the magnonic Matsubara Green's function defined in Eq.(5.103). All odd order terms of the perturbative expansion are zero, for the same reasons as in the many body perturbation theory of the electron-phonon interaction (to use a casual language, an odd number of operators cannot be paired according to

the conventional Wick's theorem since some counterparts are missing!). The aforementioned second order correction is given by

$$D_1^{(2)}(\mathbf{k}_\parallel, \mathbf{k'}_\parallel, i\Omega_\mu) = D^{(0)}(\mathbf{k}_\parallel, i\Omega_\mu)\Sigma^{(2)}_{\leftarrow\leftarrow}(\mathbf{k}_\parallel, \mathbf{k'}_\parallel, i\Omega_\mu)D^{(0)}(\mathbf{k}_\parallel, i\Omega_\mu) \tag{5.106}$$

where the so-called second order irreducible *normal* self-energy is defined as

$$\begin{aligned}\Sigma^{(2)}_{\leftarrow\leftarrow}(\mathbf{k}_\parallel, \mathbf{k'}_\parallel, i\Omega_\mu) = \delta_{\mathbf{k}_\parallel,\mathbf{k'}_\parallel} \sum_{m,n}\sum_{\mathbf{q}_\parallel} \left|\Gamma_{mn}(\mathbf{k}_\parallel, \mathbf{q}_\parallel)\right|^2 \times \\ \tfrac{1}{\beta}\sum_\nu G_m^{(0)}(\mathbf{k}_\parallel + \mathbf{q}_\parallel, i\omega_\nu + i\Omega_\mu)G_n^{(0)}(\mathbf{q}_\parallel, i\omega_\nu)\end{aligned} \tag{5.107}$$

For our case, it is the quantity defined in the last equation that is of interest from now on.

Now, within our formalism, the finite lifetime of the magnonic subsystem originates from electron-magnon scattering processes that are subject to the constraint of the conservation of the energy between the two subsystems. However, to avoid infinities in the inverse (magnon) lifetime whenever the above scattering constraint is satisfied, we proceed to ascribe a finite lifetime to the Dirac electron quasiparticles, instead of the infinite lifetime implied in Eq.(5.104), which could for instance originate from interfacial disorder effects. It is believed (actually driven by experimental results) that as far as the dynamics of the uniform ferromagnetic resonance mode is concerned, the aforementioned disorder effects are not significant. Saying so, in the footsteps of Ref.[54], after a few steps, the damping of the FMR mode of the YIG

insulator, to lowest order, is given by

$$\frac{1}{\tau_{FMR}(E_F,\eta,...)\Omega_{FMR}} \approx$$
$$\frac{1}{2\pi}\sum_{m,n}\sum_{\mathbf{q}_\parallel}\left|\Gamma_{mn}(\mathbf{k}_\parallel=0,\mathbf{q}_\parallel)\right|^2\frac{\eta}{\left(\varepsilon_m(\mathbf{q}_\parallel)-E_F\right)^2+\frac{\eta^2}{4}}\frac{\eta}{\left(\varepsilon_n(\mathbf{q}_\parallel)-E_F\right)^2+\frac{\eta^2}{4}} \tag{5.108}$$

where E_F denotes the Fermi level, η denotes the electronic quasiparticle finite lifetime and the ferromagnetic resonance frequency Ω_{FMR} is given by Eq.(5.62). Separating further intraband and interband contributions to the YIG's magnon damping leads to

$$\frac{1}{\tau_{FMR}(E_F,\eta,...)\Omega_{FMR}}\Big|_{\text{intra}} \approx$$
$$\frac{1}{2\pi}\sum_{m}\sum_{\mathbf{q}_\parallel}\left|\Gamma_{mn}(\mathbf{k}_\parallel=0,\mathbf{q}_\parallel)\right|^2\frac{\eta^2}{\left[\left(\varepsilon_m(\mathbf{q}_\parallel)-E_F\right)^2+\frac{\eta^2}{4}\right]^2} \tag{5.109}$$

and

$$\frac{1}{\tau_{FMR}(E_F,\eta,...)\Omega_{FMR}}\Big|_{\text{inter}} \approx$$
$$\frac{1}{2\pi}\sum_{m,n}\sum_{\mathbf{q}_\parallel}\left|\Gamma_{mn}(\mathbf{k}_\parallel=0,\mathbf{q}_\parallel)\right|^2\frac{\eta}{\left(\varepsilon_m(\mathbf{q}_\parallel)-E_F\right)^2+\frac{\eta^2}{4}}\frac{\eta}{\left(\varepsilon_n(\mathbf{q}_\parallel)-E_F\right)^2+\frac{\eta^2}{4}}(1-\delta_{mn}) \tag{5.110}$$

Concluding this section, it is worthwhile to mention that no vertex corrections are taken into account during the calculation of the YIG's magnon damping to lowest order, an approximation that is motivated by a reasoning completely analogous to the Migdal's argument for the vertex corrections in the electron-phonon problem (which in this case takes advantage of the small ratio of the electron-magnon exchange coupling energy scale over the Dirac electron kinetic energy (Refs.[50, 55])).

5.6 Application of the developed formalism: Enhanced damping of the FMR mode of a YIG thin film

In this last section, we apply the formalism developed previously to an experiment done by the group of Mingzhong Wu (and others) at the Colorado State University. In that experiment, the applied magnetic field is parallel to the interface between the YIG insulator and the topological insulator Bi_2Se_3 onto which the YIG is deposited. The topological insulator is about 8nm thick, which roughly corresponds to about ten quintupole layers. Roughly speaking, above four or five quintupole layers the two surfaces of the TI are decoupled from each other as assumed in the above model. The YIG thin film is about 30 nm thick, which is actually a thin film (given that experimentally thick films correspond to few up to several micrometers).

When the applied field is parallel to the interface, Eq.(5.52) dictates that the magnetization field of the YIG is also parallel to the interface (actually that is the only solution). Based on the last datum, one can further proceed to calculate the scattering amplitudes given by Eq.(5.98) under the FMR mode. Using the aforementioned scattering amplitudes as well as the electronic band structure given by Eq.(5.94), one can then calculate the contributions to the YIG's magnon damping from Eqs.(5.109) and (5.110). Below we quote only the final results since the calculation is long enough to be detailed here. Saying

so, we find that

$$\frac{1}{\tau_{FMR}(E_F,\eta,...)\Omega_{FMR}}\Big|_{\text{intra}} \approx$$
$$J_t^2 \frac{1}{4\pi^2}\left(\frac{\tilde{\mu}_0}{g_J\mu_{\text{B}}}\right)\left(\frac{M_s}{g_J\mu_{\text{B}}}\right)\frac{1}{B^2 d}\left\{\xi+\sqrt{\xi^2-1}\right\}\left\{1+\frac{2E_F}{\eta}\arctan\left(\frac{2E_F}{\eta}\right)\right\} \tag{5.111}$$

and

$$\frac{1}{\tau_{FMR}(E_F,\eta,...)\Omega_{FMR}}\Big|_{\text{inter}} \approx$$
$$J_t^2 \frac{1}{4\pi^2}\left(\frac{\tilde{\mu}_0}{g_J\mu_B}\right)\left(\frac{M_s}{g_J\mu_B}\right)\frac{1}{B^2 d}\left\{3\xi-\sqrt{\xi^2-1}\right\}\frac{\eta}{2E_F}\arctan\left(\frac{2E_F}{\eta}\right) \tag{5.112}$$

and further, the total contribution is given by

$$\frac{1}{\tau_{FMR}(E_F,\eta,...)\Omega_{FMR}} =$$
$$\frac{1}{\tau_{FMR}(E_F,\eta,...)\Omega_{FMR}}\Big|_{\text{intra}} + \frac{1}{\tau_{FMR}(E_F,\eta,...)\Omega_{FMR}}\Big|_{\text{inter}} \tag{5.113}$$

where for convenience, we've defined the following positive definite dimensionless parameter

$$\xi = \frac{H_X(0)+H_Y(0)}{2\sqrt{H_X(0)H_Y(0)}} = \frac{2\mu_0 H_0+\mu_0 M_s+H_s}{2\sqrt{(\mu_0 H_0+\mu_0 M_s+H_s)\,\mu_0 H_0}} \tag{5.114}$$

It is also not hard to verify that $\xi \geq 1 > 0$. The convention used here is that the energy is always zero at the Fermi level (following Tkachov, Ref.[60]). For instance, for a neutral TI we set $E_F = 0$, whereas for a negatively doped TI it is $E_F > 0$. For a positively doped TI is is $E_F < 0$. The electronic quasiparticle lifetime η is positive definite.

Furthermore, in the above formulae the SI units are employed. Partic-

ularly it is

$$
\begin{aligned}
&\mu_0 : vaccum\ permeability,\ \ [\mu_0] = \tfrac{eV}{m\cdot A^2} \equiv \tfrac{eV}{m\cdot (Ampere)^2} \\
&H_0 : applied\ magnetic\ field,\ \ [H_0] = \tfrac{A}{m} \equiv \tfrac{Ampere}{m} \\
&H_s > 0 : YIG\ thin\ film\ easy\ plane\ anisotropy\ parameter, \\
&\qquad [H_s] = \tfrac{eV}{moment} = \tfrac{eV}{A\cdot m^2} \equiv \tfrac{eV}{(Ampere)\cdot m^2} \\
&K_s : surface\ anisotropy\ strength\ for\ the\ YIG,\ \ [K_s] = \tfrac{eV}{m^2} \\
&M_s : saturated\ magnetic\ moment\ of\ the\ YIG\ per\ unit\ volume, \\
&\qquad [M_s] = \tfrac{moment}{m^3} = \tfrac{A\cdot m^2}{m^3} \equiv \tfrac{Ampere}{m} \\
&d :\ YIG\ film\ thickness,\ \ [d] = m \\
&\tilde{\mu}_0 : magnetic\ moment\ in\ a\ unit\ cell\ of\ the\ YIG, \\
&\qquad [\tilde{\mu}_0] = moment = A\cdot m^2 = (Ampere)\cdot m^2 \\
&g_J : Landé\ g-factor\ for\ the\ YIG\ magnetic\ moment \\
&\mu_{\rm B} : Bohr's\ magneton,\ \ [\mu_{\rm B}] = \tfrac{eV}{Tesla} \\
&J_t : electron-magnon\ exchange\ coupling,\ \ [J_t] = eV\cdot m^3 \\
&B : TI\ band\ structure\ parameter,\ \ [B] = eV\cdot m \\
&E_F : Fermi\ energy,\ \ [E_F] = eV \\
&\eta : electronic\ quasiparticle\ lifetime,\ \ [\eta] = eV
\end{aligned}
\tag{5.115}
$$

Let us now study two limiting cases for Eqs.(5.111) and (5.112). In the limit in which $|2E_F/\eta| << 1$, Eqs.(5.111) and (5.112) reduce to

$$
\begin{aligned}
&\tfrac{1}{\tau_{FMR}(E_F,\eta,...)\Omega_{FMR}}\Big|^{\rm intra}_{\left|\frac{2E_F}{\eta}\right|<<1} \approx \\
&J_t^2 \tfrac{1}{4\pi^2}\left(\tfrac{\tilde{\mu}_0}{g_J\mu_B}\right)\left(\tfrac{M_s}{g_J\mu_B}\right)\tfrac{1}{B^2 d}\left\{\xi+\sqrt{\xi^2-1}\right\}\left[1+\left(\tfrac{2E_F}{\eta}\right)^2+...\right]
\end{aligned}
\tag{5.116}
$$

and

$$
\begin{aligned}
&\tfrac{1}{\tau_{FMR}(E_F,\eta,...)\Omega_{FMR}}\Big|^{\rm inter}_{\left|\frac{2E_F}{\eta}\right|<<1} \approx \\
&J_t^2 \tfrac{1}{4\pi^2}\left(\tfrac{\tilde{\mu}_0}{g_J\mu_B}\right)\left(\tfrac{M_s}{g_J\mu_B}\right)\tfrac{1}{B^2 d}\left\{3\xi-\sqrt{\xi^2-1}\right\}\left[1-\tfrac{1}{3}\left(\tfrac{2E_F}{\eta}\right)^2+...\right]
\end{aligned}
\tag{5.117}
$$

whereby we see that there is a quadratic dependence to lowest order on the parameter $|2E_F/\eta|$. In the opposite limit, i.e. the limit in which $|2E_F/\eta| >> 1$,

Eqs.(5.111) and (5.112) reduce to

$$\frac{1}{\tau_{FMR}(E_F,\eta,...)\Omega_{FMR}}\Big|^{\text{intra}}_{\left|\frac{2E_F}{\eta}\right|>>1} \approx$$

$$\begin{cases} J_t^2 \frac{1}{4\pi^2}\left(\frac{\tilde{\mu}_0}{g_J\mu_B}\right)\left(\frac{M_s}{g_J\mu_B}\right)\frac{1}{B^2 d}\left\{\xi+\sqrt{\xi^2-1}\right\}\left\{1+\frac{\pi}{2}\frac{2E_F}{\eta}\right\}, & if \ \ \frac{2E_F}{\eta}>0 \\ J_t^2 \frac{1}{4\pi^2}\left(\frac{\tilde{\mu}_0}{g_J\mu_B}\right)\left(\frac{M_s}{g_J\mu_B}\right)\frac{1}{B^2 d}\left\{\xi+\sqrt{\xi^2-1}\right\}\left\{1-\frac{\pi}{2}\frac{2E_F}{\eta}\right\}, & if \ \ \frac{2E_F}{\eta}<0 \end{cases} \tag{5.118}$$

and also

$$\frac{1}{\tau_{FMR}(E_F,\eta,...)\Omega_{FMR}}\Big|^{\text{inter}}_{\left|\frac{2E_F}{\eta}\right|>>1} \approx$$

$$\begin{cases} J_t^2 \frac{1}{4\pi^2}\left(\frac{\tilde{\mu}_0}{g_J\mu_B}\right)\left(\frac{M_s}{g_J\mu_B}\right)\frac{1}{B^2 d}\left\{3\xi-\sqrt{\xi^2-1}\right\}\frac{\eta}{2E_F}\frac{\pi}{2}, & if \ \ \frac{2E_F}{\eta}>0 \\ -J_t^2 \frac{1}{4\pi^2}\left(\frac{\tilde{\mu}_0}{g_J\mu_B}\right)\left(\frac{M_s}{g_J\mu_B}\right)\frac{1}{B^2 d}\left\{3\xi-\sqrt{\xi^2-1}\right\}\frac{\eta}{2E_F}\frac{\pi}{2}, & if \ \ \frac{2E_F}{\eta}<0 \end{cases} \tag{5.119}$$

and from the last two equations it is easily noticed that in the aforementioned limit the intraband contribution dominates over the interband contribution, given that the former depends linearly on the parameter $|2E_F/\eta|$, whereas the latter is inversely proportional to the parameter $|2E_F/\eta|$. Furthermore, the total contribution is easily found to be

$$\frac{1}{\tau_{FMR}(E_F,\eta,...)\Omega_{FMR}}\Big|_{tot} \approx J_t^2 \frac{1}{4\pi^2}\left(\frac{\tilde{\mu}_0}{g_J\mu_B}\right)\left(\frac{M_s}{g_J\mu_B}\right)\frac{1}{B^2 d}\times$$

$$\left[\xi+\sqrt{\xi^2-1}+\left(\left\{\xi+\sqrt{\xi^2-1}\right\}\frac{2E_F}{\eta}+\left\{3\xi-\sqrt{\xi^2-1}\right\}\frac{\eta}{2E_F}\right)\tan^{-1}\left(\frac{2E_F}{\eta}\right)\right] \tag{5.120}$$

In the limit of $|2E_F/\eta| << 1$, the total YIG's magnon damping is approxi-

mately given (to lowest order) by

$$\frac{1}{\tau_{FMR}(E_F,\eta,...)\Omega_{FMR}}\Big|^{tot}_{\left|\frac{2E_F}{\eta}\right|<<1} \approx$$

$$J_t^2 \frac{1}{4\pi^2}\left(\frac{\tilde{\mu}_0}{g_J\mu_B}\right)\left(\frac{M_s}{g_J\mu_B}\right)\frac{1}{B^2 d}\left[4\xi + \left\{\xi+\sqrt{\xi^2-1}\right\}\left(\frac{2E_F}{\eta}\right)^2 + ...\right] \tag{5.121}$$

and as is seen it depends quadratically on the Fermi energy on top of a constant contribution (that would be the contribution for a neutral TI) that depends on the YIG thin film parameters (particularly on the parameter ξ defined by Eq.(5.114)). In the opposite limit of $|2E_F/\eta| >> 1$, the total YIG's magnon damping is approximately given (to lowest order) by

$$\frac{1}{\tau_{FMR}(E_F,\eta,...)\Omega_{FMR}}\Big|^{tot}_{\left|\frac{2E_F}{\eta}\right|>>1} \approx J_t^2 \frac{1}{4\pi^2}\left(\frac{\tilde{\mu}_0}{g_J\mu_B}\right)\left(\frac{M_s}{g_J\mu_B}\right)\frac{1}{B^2 d}\times$$

$$\left[\xi+\sqrt{\xi^2-1}+\left(\left\{\xi+\sqrt{\xi^2-1}\right\}\frac{2E_F}{\eta}+\left\{3\xi-\sqrt{\xi^2-1}\right\}\frac{\eta}{2E_F}\right)\frac{\pi}{2}\right], \quad if \ \ \frac{2E_F}{\eta}>0$$

$$\frac{1}{\tau_{FMR}(E_F,\eta,...)\Omega_{FMR}}\Big|^{tot}_{\left|\frac{2E_F}{\eta}\right|>>1} \approx J_t^2 \frac{1}{4\pi^2}\left(\frac{\tilde{\mu}_0}{g_J\mu_B}\right)\left(\frac{M_s}{g_J\mu_B}\right)\frac{1}{B^2 d}\times$$

$$\left[\xi+\sqrt{\xi^2-1}-\left(\left\{\xi+\sqrt{\xi^2-1}\right\}\frac{2E_F}{\eta}+\left\{3\xi-\sqrt{\xi^2-1}\right\}\frac{\eta}{2E_F}\right)\frac{\pi}{2}\right], \quad if \ \frac{2E_F}{\eta}<0 \tag{5.122}$$

and it is easily observed that the dependence on the parameter $|2E_F/\eta|$ is linear (on top of a constant contribution that depends on YIG thin film parameters). The YIG's magnon (total) damping parameter defined in Eq.(5.120) is dimensionless. From Eqs.(5.121) and (5.122), within this model, it is concluded that for a more disordered topological insulator (TI), the dependence of the YIG's magnon damping on the quasiparticle parameter $|2E_F/\eta|$ is weaker.

Let us close this section with a few remarks. As a first note, it is remarked that if all the other parameters appearing in Eqs.(5.111) to (5.113) are known, given the magnon-damping (on the LHS) one can roughly estimate the electron-magnon exchange coupling strength. In addition to that, let us stress the fact that the aforementioned results are valid as long as the electronic band structure is represented in a valid way by Eqs.(5.94). However, the general formalism developed in the previous sections is not impeded in any way (provided we are in the temperature regime stated previously) by the form of the electronic band structure, and it can be extended in a straightforward manner beyond the approximate two-band case considered above.

Bibliography

[1] W. A. Harrison. *Elementary electronic structure (Revised edition)*. World Scientific, 2004.

[2] R. Arias and D. L.Mills. Extrinsic contributions to the ferromagnetic resonance response of ultrathin films. *Journal of applied physics*, 87(9):5455–5456, 1998.

[3] R. Arias and D. L.Mills. Extrinsic contributions to the ferromagnetic resonance response of ultrathin films. *Phys. Rev. B*, 60(10):7395–7409, 1999.

[4] D. A.Smith. New mechanisms for magnetic anisotropy in localized s-state moment materials. *Journal of Magnetism and Magnetic Materials*, 1():214–225, 1976.

[5] C. Barreteau, D. Spanjaard, and M.-C. Desjonqueres. An efficient magnetic tight-binding method for transition metals and alloys. *Comptes Rendus Physique*, 17():406–429, 2015.

[6] B. A. Bernevig. *Topological insulators and topological superconductors*. Princeton, 2013.

[7] J. Chaloupka, G. Jackeli, and G. Khaliullin. Kitaev Heisenberg model on a honeycomb lattice: possible exotic phases in Iridium Oxide Na2IrO3. *Phys.Rev.Lett.*, 105(027204):1–4, 2010.

[8] J. Chaloupka, G. Jackeli, and G. Khaliullin. Zig-zag magnetic order in the Iridium Oxide Na2IrO3. *Phys.Rev.Lett.*, 110(097204):1–5, 2013.

[9] V. Cherepanov, I. Kolokolov, and V. L'vov. The saga of YIG: Spectra, thermodynamics, interaction and relaxation of magnons in a complex magnet. *Physics Reports*, 229(3):81–144, 1993.

[10] A. Chernysov, M. Overby, L. Xinyu, J. K.Furdyna, Y. Lyanda-Geller, and L. P.Rokhinson. Evidence for reversible control of magnetization in a ferromagnetic material by means of spin-orbit magnetic field. *Nature Physics*, 5():656–659, 2009.

[11] D. C.Ralph and M. D.Stiles. Spin transfer torques. *Journal of magnetism and magnetic materials*, 320():1190–1216, 2007.

[12] K. Di, V. Li Zhang, H. Siah Lim, S. Choon Ng, M. Hau Kuok, J. Yu, J. Yoon, X. Qiu, and H. Yang. Direct observation of the Dzyaloshinskii-Moriya interaction in a Pt/Co/Ni film. *Phys.Rev.Lett.*, 114(047201):047201–1–5, 2015.

[13] M. D.Stiles and A. Zangwill. Anatomy of spin-transfer torque. *Phys.Rev. B*, 66(014407):1–14, 2002.

[14] G. E.W.Bauer, E. Saitoh, and B. J.van Wees. Spin caloritronics. *Nature Materials*, 11():391–399, 2012.

[15] A. Fert and P. M.Levy. Role of anisotropic exchange interactions in determining the properties of spin-glasses. *Phys.Rev.Lett.*, 44(23):1538–1541, 1980.

[16] I. F.I.Mikhail, I. M.M.Ismail, and M. Ameen. Exact and model operators for magnon-phonon interactions in antiferromagnets. *Physica B*, 406():508–515, 2011.

[17] I. F.I.Mikhail, I. M.M.Ismail, and M. Ameen. Model calculation of thermal conductivity in antiferromagnets. *Physica B*, 476():29–35, 2015.

[18] F. Freimuth, S. Blugel, and Y. Mokrousov. Spin-orbit torques in Co/Pt(111) and Mn/W(001) magnetic bilayers from first principles. *Phys.Rev. B*, 90(174423):1–10, 2014.

[19] S. G. Dixon. Lattice thermal conductivity of antiferromagnetic insulators. *Phys.Rev.B*, 21(7):2851–1–14, 1980.

[20] A. H.MacDonald, T. Jungwirth, and M. Kasner. Shadow bands and tunneling magnetoresistance in itinerant electron ferromagnets. *arXiv preprint, arXiv:cond-mat/9801023*, 2017.

[21] A. I.Akhiezer, V. G.Bar'yakhtar, and M. I.Kaganov. Spin waves in ferromagnets and antiferromagnets,i. *Soviet Physics Uspekhi*, 3(4):567–592, 1960.

[22] D. J. Sanders and D. Walton. Effect of magnon-phonon thermal relaxation on heat transport by magnons. *Phys.Rev.B*, 15(3):1489–1494, 1977.

[23] G. Jackeli and G. Khaliullin. Mott insulators in the strong spin-orbit coupling limit: from Heisenberg to a quantum compass and Kitaev models. *Phys.Rev.Lett.*, 102(017205):1–4, 2009.

[24] M. J.Hurben and C. E.Patton. Theory of two magnon scattering microwave relaxation and ferromagnetic resonance linewidth in magnetic thin films. *Journal of applied physics*, 83(8):4344–4365, 1998.

[25] A. J.Princep, R. A.Ewings, S. Ward, S. Toth, C. Dubs, D. Prabhakaran, and A. T.Boothroyd. The final chapter in the saga of YIG. *arXiv preprint, arXiv:1705.06594*, 2017.

[26] D. Kalkstein and P. Soven. A Green's function theory of surface states. *Surface Science*, 26():85–99, 1970.

[27] M. Kataoka, O. Nakanishi, A. Yanase, and J. Kanamori. Antisymmetric spin interaction in metals. *Journal of the Physical Society of Japan*, 53(10):3624–3633, 1984.

[28] J. Kim, J. Sinha, M. Hayashi, M. Yamanouchi, S. Fukami, T. Suzuki, S. Mitani, and H. Ohno. Layer thickness dependence of the current-induced effective field vector in Ta—CoFeB—MgO. *Nature Materials*, 12():240–245, 2013.

[29] M. Koshino. Interlayer interaction in general incommensurate atomic layers. *New Journal of Physics*, 17(015014):1–10, 2015.

[30] J. Kreiger and G. Iafrate. Time evolution of bloch electrons in a homogeneous electric field. *Phys.Rev.B*, 33(8):5494–5500, 1986.

[31] A. Kreisel, P. Kopietz, P. Thanh Cong, B. Wolf, and M. Lang. Elastic constants and ultrasonic attenuation in the cone state of the frustrated antiferromagnet Cs_2CuCl_4. $Phys.Rev.B, 84(024414) : 1 - -17, 2011$.

[32] A. Kreisel, F. Sauli, L. Bartosch, and P. Kopietz. Microscopic spin wave theory for yttrium-iron garnet films. *The European Physical Journal B*, 71():56–68, 2009.

[33] H. Kurebayashi, J. Sinova, D. Fang, A. C.Irvine, T. D.Skinner, J. Wunderlich, V. Novak, R. P.Campion, B. L.Gallagher, E. K.Vehstedt, L. P.Zarbo, K. Vyborny, A. J.Ferguson, and T. Jungwirth. An antidamping spin-orbit torque originating from the berry curvature. *Nature Nanotechnology*, 9():211–217, 2014.

[34] A. L. Chernyshev and W. Brenig. Thermal conductivity in large-j two dimensional antiferromagnets: role of phonon scattering. *Phys.Rev.B*, 92(054409):1–22, 2015.

[35] P. Landeros, R. E.Arias, and D. L.Mills. Two magnon scattering in ultrathin ferromagnets: The case where the magnetization is out of plane. *Phys. Rev. B*, 77():214405–1–13, 2008.

[36] L. Liu, C.-F. Pai, Y. Li, H. W.Tseng, D. C.Ralph, and A. R.Buhrman. Spin-torque switching with the giant spin hall effect of tantalum. *Science*, 336(6081):555–558, 2012.

[37] L. M. Woods. Magnon phonon effects in ferromagnetic manganites. *Phys.Rev.B*, 65(014409):1–7, 2001.

[38] X. Ma, G. Yu, C. Tang, X. Li, C. He, J. Shi, K. L.Wang, and X. Li. Scaling of Dzyaloshinskii-Moriya interaction at heavy metal and ferromagnetic metal interfaces. *arXiv preprint, arXiv:1709.03961*, 2017.

[39] A. Manchon. A new moment for berry. *Nature Physics*, 10():340–341, 2014.

[40] A. Manchon, H. C.Koo, J. Nitta, S. M.Frolov, and R. A.Duine. New perspectives for rashba spin-orbit coupling. *Nature Materials*, 14():871–882, 2015.

[41] C. M.Bhandari and G. S.Verma. Scattering of magnons and phonons in the thermal conductivity of Yttrium Iron Garnet. *Physical Review*, 152(2):731–736, 1966.

[42] A. M.DaSilva, J. Jung, S. Adam, and A. H.MacDonald. Transport and particle-hole asymmetry in graphene on boron nitride. *Phys.Rev.B*, 91(245422):1–10, 2015.

[43] V. M.Edelstein. Spin polarization of conduction electrons induced by electric current in two-dimensional asymmetric electron systems. *Solid State Communications*, 73(3):233–235, 1990.

[44] P. M.Haney, R. A.Duine, A. S.Nunez, and A. H.MacDonald. Current induced torques in magnetic materials: Beyond spin-transfer. *Journal of magnetism and magnetic materials*, 320():1300–1311, 2008.

[45] P. M.Levy. Indirect exchange via spin-orbit coupled states. *Solid State Communications*, 7():1813–1818, 1969.

[46] P. M.Levy and A. Fert. Anisotropy induced by nonmagnetic impurities in CuMn spin-glass alloys. *Phys.Rev.B*, 23(9):4667–4690, 1981.

[47] R. M.McMichael, M. D.Stiles, P. J.Chen, and W. F.Egelhoff. Ferromagnetic resonance linewidth in thin films coupled to NiO. *Journal of applied physics*, 83(11):7037–7039, 1998.

[48] M. Montalti, A. Credi, L. Prodi, and M. T.Gandolfi. *Handbook of photochemistry*. 2006.

[49] J. H. Moon, S.-M. Seo, K.-J. Lee, K.-W. Kim, J. Ryu, H.-W. Lee, R. McMichael, and M. Stiles. Spin wave propagation in the presence of interfacial Dzyaloshinskii-Moriya interaction. *Phys.Rev.B*, 88(18):184404–1–6, 2013.

[50] S. Nakajima. On electronic specific heat of ferromagnetic rare earth metals. *Progress of Theoretical Physics*, 38(1):23–39, 1967.

[51] N. Pottier. *Non-equilibrium Statistical Physics: Linear Irreversible Processes*. Oxford Graduate Texts, 2014.

[52] A. Ruckriegel, P. Kopietz, D. A.Bozhko, A. A.Serga, and B. Hillebrands. Magneto-elastic modes and lifetime of magnons in thin yttrium-iron garnet films. *Phys. Rev. B*, 89(18):184413–1–14, 2014.

[53] L. Shi and D. A.Papaconstantopoulos. Modifications and extensions to Harrison's tight-binding theory. *Phys.Rev.B*, 70(205101):1–6, 2004.

[54] J. Sinova, T. Jungwirth, X. Liu, Y. Sasaki, J. K.Furdyna, W. A.Atkinson, and A. H.MacDonald. Magnetization relaxation in (Ga,Mn)As ferromagnetic semiconductors. *Phys. Rev. B*, 69(8):085209–1–6, 2008.

[55] V. S.Lutovinov and M. Yu.Reizer. Relaxation processes in ferromagnetic metals. *Sov. Phys. JETP*, 50(2):355–360, 1979.

[56] J. Sólyom. *Fundamentals of the physics of solids, Vol.1, Structure and Dynamics*. Springer, 2007.

[57] G. Stamokostas, P. Lapas, and G. Fiete. Thermal conductivity of local moment models with strong spin orbit coupling. *Phys.Rev.B*, 95(064410):1–26, 2017.

[58] T. Suzuki, S. Fukami, N. Ishiwate, M. Yamanouchi, S. Ikeda, N. Kasai, and H. Ohno. Current-induced effective field in perpendicularly magnetized Ta/CoFeB/MgO wire. *Appl. Phys. Lett.*, 98(142505):1–4, 2011.

[59] S. Takahashi and S. Maekawa. Spin current, spin accumulation and spin hall effects. *Sci.Technol.Adv.Mater.*, 9(014105):1–11, 2008.

[60] G. Tkachov. *Topological Insulators*. Pan Stanford Publishing, 2016.

[61] H. T.Nembach, J. M.Shaw, M. Weiler, E. Jue, and T. J.Silva. Linear relation between Heisenberg exchange and interfacial Dzyaloshinskii-Moriya interaction in metal films. *Nature Physics*, 11(10):825–829, 2015.

[62] Y. Tserkovnyak and A. Brataas. Spin pumping and magnetization dynamics in metallic multilayers. *Phys. Rev. B*, 66(224403):1–9, 2002.

[63] J. W.Davenport and M. Weinert. Electronic structure near metal-metal interfaces. *Surface Science*, 144():220–223, 1984.

[64] A. Yaniv. Electronic properties of a simple metal-metal interface. *Phys.Rev.B*, 17(10):3904–3918, 1978.

[65] A. Zangwill. *Modern Electrodynamics*. Cambridge University Press, 2013.

[66] J. Zemen, J. Masek, J. Kucera, J. A.Mol, P. Motloch, and T. Jungwirth. Comparative study of tight-binding and abinitio electronic structure calculations focused on magnetic anisotropy in ordered CoPt alloy. *Journal of Magnetism and Magnetic Materials*, 356():87–94, 2014.

[67] S. Zhang and Z. Li. Roles of nonequilibrium conduction electrons on the magnetization dynamics of ferromagnets. *Phys. Rev. Lett.*, 93(12):127204–1–4, 2004.